Zooming in on Quasar Accretion Disks using Chromatic Microlensing

by

Jeffrey A. Blackburne

B.S., California Institute of Technology (2003)

Submitted to the Department of Physics
in partial fulfillment of the requirements for the degree of
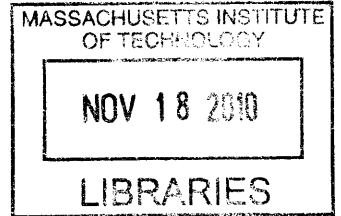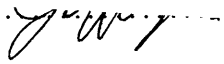
Doctor of Philosophy

at the

MASSACHUSETTS INSTITUTE OF TECHNOLOGY

September 2009

© Jeffrey A. Blackburne, MMIX. All rights reserved.

The author hereby grants to MIT permission to reproduce and distribute publicly
paper and electronic copies of this thesis document in whole or in part.

Author . . . .

Department of Physics
August 20, 2009

Certified by . . . .

Paul L. Schechter
William A. M. Burden Professor of Astrophysics
Thesis Supervisor

Accepted by . . . .

Thomas J. Greytak
Lester Wolfe Professor of Physics
Associate Department Head for Education

Zooming in on Quasar Accretion Disks
using Chromatic Microlensing

by

Jeffrey A. Blackburne

Submitted to the Department of Physics
on August 20, 2009, in partial fulfillment of the
requirements for the degree of
Doctor of Philosophy

Abstract

Observing the temperature profiles of accretion disks around black holes is a fundamental test of an important astrophysical process. However, angular resolution limitations have prevented such a measurement for distant quasars. We present a new method for determining the size of quasar accretion disks at a range of wavelengths, thus constraining their temperature profiles. The technique uses single-epoch, multi-wavelength optical and near-infrared imaging of gravitationally lensed quasars in conjunction with X-ray imaging, and takes advantage of the presence of microlensing perturbations to the magnifications of the lensed images. The dependence of these perturbations on the angular size of the source, combined with the temperature structure of quasar accretion disks, causes the flux ratio anomalies due to microlensing to appear chromatic. This allows us to probe regions of the quasar that are too small to be measured by any other technique. We apply this method to observations of 12 lensed quasars, and measure the size of the accretion disk of each in 8 broadband filters between 0.36 and 2.2 microns (in the observed frame). We find that the overall sizes are larger by factors of 3 to 30 than predicted by the standard thin accretion disk model, and that the logarithmic slope of the wavelength-dependent size is ~ 0.2 on average, much shallower than the predicted slope of 4/3. This implies that the temperature is a *steeper* function of radius than the thin disk model predicts. With this new approach to determining quasar accretion disk sizes, we are thus able to rule out the standard thin disk model as the source of the (rest-frame) ultraviolet and optical continuum in these bright quasars.

Thesis Supervisor: Paul L. Schechter
Title: William A. M. Burden Professor of Astrophysics

Acknowledgments

The heavens proclaim the glory of God.

    The skies display his craftsmanship.

Day after day they continue to speak;

    night after night they make him known.

They speak without a sound or word;

    their voice is never heard.

Yet their message has gone throughout the earth,

    and their words to all the world.

                Psalm 19:1-4 (New Living Translation)

Contents

List of Figures

List of Tables

Chapter 1

Introduction: Quasars and chromatic microlensing

Microlensing by stars in foreground lensing galaxies can substantially alter the flux ratios of quadruply lensed quasars. But the microlensing effects are greatly diminished if the quasar has an angular extent comparable to the Einstein radius of a star in the lens galaxy. The work described in this thesis takes advantage of this size discrimination provided by microlensing to measure the angular extent of quasar accretion disks. This is a crucial test of theories of quasar structure.

In this chapter, we give the requisite background about quasars, strong lensing by galaxies, and perturbations to the lensing potential such as microlensing. We also describe the structure of the thesis.

1.1 Quasars: Accretion disks and other structures

Much theoretical work has been done in the past several decades on the subject of accretion disks in quasars. The most prominent model is that of Shakura and Sunyaev [1973], who describe a solution to the equations of mass and momentum conservation featuring a geometrically thin disk of material orbiting a massive central object. The material follows roughly Keplerian orbits, but is perturbed by viscous stresses which transport angular momentum outward in the disk, while transporting the material inward. The energy released

during the infall is radiated locally, with a blackbody spectral distribution parameterized by a local temperature (the disk is taken to be optically thick). Since the material is heated as it falls further into the gravitational potential of the central object, the temperature falls with increasing radius (see Section 6.2).

Accretion disks are thought to occur in active galactic nuclei (AGN) because of the high efficiency they afford in converting the mass-energy of the infalling material to radiative energy.

Other AGN structures include regions of tenuous gas clouds that produce line emission, both broad lines and narrow; a dusty region thought to resemble a torus, which can heavily obscure the nucleus depending on the inclination angle; and in some cases a jet emerging along the axis of the disk.

Many refinements have been made to the model, including general relativistic corrections [Novikov and Thorne, 1973] and magnetic fields, which provide a possible mechanism for the viscosity via the magneto-rotational instability [Balbus and Hawley, 1991], and are almost certainly involved in the formation of jets [Lovelace, 1976].

The spectral energy distribution of quasars is remarkably broad, with roughly equal power per decade for many decades in frequency [see, e.g., Elvis et al., 1994]. In this thesis we are mostly concerned with the rest-frame ultraviolet (UV) and optical continuum, the X-ray continuum, and to a lesser extent the emission lines in the optical region and the mid-infrared (IR) continuum. The optical continuum is thought to come from the accretion disk; likewise, the mid-IR continuum comes from the dusty torus surrounding it. The emission lines arise from ionization regions distributed roughly spherically around the nucleus, at radii dependent on the local density, the ionization potential of the line, and the luminosity of the nucleus. The X-ray continuum is more of a mystery. Its spectrum is non-thermal, meaning it does not arise from the disk (the disk probably does not get hot enough). Its origin might lie in the base of a jet, or in a hot corona above the accretion disk [e.g., Haardt and Maraschi, 1991].

There is, however, not a lot of data to constrain this model for distant quasars, particularly the accretion disk model [Blaes, 2007]. Spectral fitting has not provided a definitive answer for the temperature structure of the disk, and direct imaging is not an option: at

cosmological distances (e.g., 1 Gpc), an accretion disk 1000 astronomical units (AU) in size only subtends a microarcsecond, far too small to be resolved.

We describe in this thesis a unique method for determining the size of quasar emission regions, and apply it to quasar accretion disks. The method works for quasars that are gravitationally lensed into multiple images by foreground galaxies, and takes advantage of the microlensing of the quasar images by stars in the lens galaxies.

1.2   Strong gravitational lensing and microlensing

Gravitational lensing is the term for the deflection of light by the gravitational potential. Every ray that reaches our telescopes is deflected to a small extent by the intervening mass. In this thesis we focus on quasars whose light is deflected by appreciable angles by the chance superposition of a massive foreground galaxy close to their line of sight. This manifestation of gravitational lensing is called strong lensing, and is characterized by multiple images (or *mirages*) of the background quasar. Like an optical lens, gravitational lensing can magnify or demagnify the images, though gravitational images are typically distorted as well (though in the case of quasar images, the distortion is not observable, because they are still unresolved).

1.2.1   Strong lensing theory

The most powerful treatment of the problem of gravitational lensing is the use of the Fermat time delay surface [Schneider, 1985]. The following discussion relies on the thin lens approximation (i.e., the bending occurs only along a small fraction of the light's path), and follows loosely that of Narayan and Bartelmann [1996]. As the rays of light from the background quasar traverse the gravitational potential of the foreground galaxy, their path is lengthened, and they accrue an additional delay relative to each other [the Shapiro time delay; Shapiro, 1964]. The delay is proportional to the gravitational potential of the foreground galaxy (projected onto the sky), and is added to the paraboloidal geometric time delay due to the difference in path length for a bent light path. The total delay (up to a

constant) is given by

$$\tau(\boldsymbol{\theta}) = \frac{1 + z_L}{c} \frac{D_{\mathrm{OL}} D_{\mathrm{OS}}}{D_{\mathrm{LS}}} \left[\frac{1}{2}(\boldsymbol{\theta} - \boldsymbol{\beta})^2 - \psi(\boldsymbol{\theta}) \right] \quad , \tag{1.1}$$

where z_L is the cosmological redshift of the lens, $\boldsymbol{\beta}$ is a 2D vector on the sky describing the position of the source, and D_{OL}, D_{OS}, and D_{LS} are the angular diameter distances from observer to lens, observer to source, and lens to source. The 2D gravitational potential ψ is defined as the scaled projection onto the plane of the sky of the 3D potential:

$$\psi(\boldsymbol{\theta}) \equiv \frac{D_{\mathrm{LS}}}{D_{\mathrm{OL}} D_{\mathrm{OS}}} \frac{2}{c^2} \int \Phi(D_{\mathrm{OL}}\boldsymbol{\theta}, z) dz \quad . \tag{1.2}$$

The two terms on the right hand side of Equation 1.1 are the geometric time delay and the gravitational delay, respectively. If the flux of a lensed quasar varies in time, the delay introduced by lensing will manifest in the observed variation of the images; a cross-correlation of their light curves will reveal their relative delays.

The positions of the lensed images are located at the stationary points of the Fermat time delay surface:

$$\boldsymbol{\theta} - \boldsymbol{\beta} - \boldsymbol{\nabla}_{\theta}\psi = 0 \quad . \tag{1.3}$$

A distinction may be made between images that lie at local minima of the time delay surface and those that lie at saddle points[1].

When a circularly symmetric potential is centered directly on top of a source, the distorted images merge to form an *Einstein ring*. The radius of the ring is determined by Equation 1.3, and depends on the strength of the potential and the geometric distances.

Finally, the tensor magnification of an image is given by

$$(\mathcal{M}^{-1})_{ij} = \frac{\partial \beta_i}{\partial \theta_j} = \left(\delta_{ij} - \frac{\partial^2 \psi}{\partial \theta_i \partial \theta_j} \right) \quad . \tag{1.4}$$

The above matrix is often written in terms of κ and γ, called the convergence and shear,

---

[1]There are local maxima as well near the cores of the lens galaxies, but the curvature there is so large that they are strongly demagnified; see Equation 1.4. Only one has been observed [Winn et al., 2004].

respectively. They are defined as follows:

$$\kappa(\boldsymbol{\theta}) \equiv \frac{1}{2} \nabla_\theta^2 \psi$$

$$\gamma(\boldsymbol{\theta}) \equiv \sqrt{\frac{1}{4} \left(\frac{\partial^2 \psi}{\partial \theta_1 \partial \theta_1} - \frac{\partial^2 \psi}{\partial \theta_2 \partial \theta_2} \right)^2 + \left(\frac{\partial^2 \psi}{\partial \theta_1 \partial \theta_2} \right)^2} \quad . \tag{1.5}$$

(The shear is actually a vector, but we are only concerned with its magnitude.) Notice that κ is the Laplacian of the gravitational potential; by Poisson's equation it is therefore proportional to the surface mass density. We will make use of the convergence and shear when we create microlensing magnification maps in Section 8.1; apart from that we are only concerned with the scalar magnification, which is the determinant of $\mathcal{M}$.

Equations 1.1, 1.3, and 1.4 describe the three strong lensing observables: time delays (from the potential), image positions (from the gradient of the potential), and magnifications (from its curvature).

Strong lensing is used to measure mass distributions, both of galaxies and of clusters of galaxies, and to make distance ladder-independent estimates of H_0. Its magnifying property is also used to study very distant lensed objects that would otherwise be too faint to observe. The statistics of lensing are used to constrain cosmological parameters, as well [for an exhaustive review, see Meylan et al., 2006]. In this thesis we use lensing in a different way, to study the structure of bright quasars. For this we use microlensing.

1.2.2 Flux ratio anomalies and microlensing

The lensing theory in the previous section can be combined with observations of lenses to create models for the mass distributions causing the deflection. Circular or elliptical distributions with reasonable radial profiles, in combination with external shear resulting from other massive structures near the line of sight, are able to match the positions of quasar images well, in almost all cases. But often the ratios of the images' fluxes are more difficult to reproduce [Kochanek and Dalal, 2004].

This phenomenon is most often seen in the quadruple quasars. In some fraction of lens systems, a lens galaxy is so well-aligned with a background quasar that (with the help of

21

a quadrupole moment in the potential) it produces four images of the quasar, arranged in one of a number of characteristic configurations. In Appendix A we provide images of a sample of quadruple quasars (or *quads*). Examination of the images reveals three main configurations: the *cross*, where the four images are roughly evenly spaced; the *fold*, where a pair of images are very close to one another; and the *cusp*, where three of the four images lie near each other one one side of the lens galaxy, and the fourth lies directly counter to them. The quads provide more constraints to the lens model than do doubly imaged quasars; indeed, their image positions alone are usually enough to constrain a simple model. In these cases, the flux ratios of the images can be independently compared to those predicted by the model. They are often anomalous, sometimes extravagantly so [see, e.g., Inada et al., 2003a].

There exist several possible mechanisms to explain the flux ratio anomalies, including differential extinction in the lensing galaxy (where the images are separated by the greatest physical distance), insufficient lens models, and perturbations to the lensing potential due either to dark matter subhaloes (known as millilensing) or to stars (microlensing). We will comment on these in order.

Since most lensing galaxies (including, almost certainly, all of those in our sample; see Appendex A) are red ellipticals, they are not likely to contain large amounts of dust. This is supported by the fact that X-ray spectra of lensed quasars are usually consistent with no absorption by neutral hydrogen within the lens galaxy [Pooley et al., 2007]. Additionally, propagation effects such as extinction are unable to explain the observed parity dependence of the anomalies – specifically, high-magnification saddle point image are empirically more likely to be very demagnified than minima. This parity dependence is naturally explained by substructure [Schechter and Wambsganss, 2002, Kochanek and Dalal, 2004]. For these reasons, differential extinction is not considered to be an important source of flux ratio anomalies.

Similarly, the variation in predicted flux ratios for different lens models with reasonable parameters is quite small. Dalal and Kochanek [2002] suggest error bars of 10%; Keeton et al. [2003] call this "quite conservative." For quadruple lenses in the fold configuration, a model-independent theorem states that the close pair of images will be highly magnified,

and their magnification ratio will be close to 1 [Gaudi and Petters, 2002]. Likewise, the three nearby high-magnification images in a cusp-like lens have signed magnifications[2] that add to zero; therefore, the middle image will be as bright as the two flanking it put together [Schneider and Weiss, 1992]. As we will see in the following chapters, flux ratio anomalies often violate these universal relations. So model uncertainties cannot contribute significantly to them.

The best candidate for the cause of the flux ratio anomalies is substructure within the primary lens galaxy, whether it be dark matter subhaloes or stars. Though substructure may not make a large difference in the time delay surface or its gradient, it is possible for even a (suitably located) star of $\sim 1 M_\odot$ to significantly change its curvature, and thus the magnification of an image. The difference between perturbations by subhaloes and stars is one of scale: dark matter subhaloes likely have masses between 10^3 and $10^9 M_\odot$ and Einstein radii between 0.03 and 30 milliarcseconds, whereas stars have masses averaging below $1 M_\odot$ and Einstein radii around a microarcsecond (thus the labels millilensing and microlensing, respectively). The Einstein radius of a point perturber (such as a microlens) is given by

$$
\theta_{\mathrm{Ein}} = \left(\frac{4Gm}{c^2} \frac{D_{\mathrm{LS}}}{D_{\mathrm{OL}} D_{\mathrm{OS}}} \right)^{1/2} \quad ,
\tag{1.6}
$$

where m is the mass of the perturber. The difference in scale between microlensing and millilensing leads to a difference in the time it takes for a source (moving at constant angular speed with respect to the lens) to cross the substructure Einstein radius; this time is on the order of a decade for quasar microlensing, and millenia for millilensing. It also matters when the source is extended: a dark matter subhalo will affect a greater fraction of the source than a single star will.

1.3 Chromatic microlensing and source sizes

In this thesis we report a chromatic dependence in the anomalous flux ratios of several lensed quasars. This is contrary to expectations for gravitational lensing of point sources;

---

[2]The sign of the magnification indicates the parity of the image. Saddle-point images have negative magnification.

because the geodesic equation for light is wavelength-independent, gravitational effects are achromatic. The explanation for chromatic flux ratio anomalies lies in the combination of two effects: the dependence of substructure lensing on source size, and the temperature structure of quasar accretion disks.

The Einstein ring of a perturbing mass is a measure of its area of influence. If a lensed quasar has an angular extent large compared to the Einstein radius of the perturbing masses, the effect will be washed out, since one part of the source will be magnified while another part is demagnified. So the presence of anomalous flux ratios already tells us that the source is smaller than the Einstein radius.

If millilensing is responsible for the anomalies, this is not a very strong limit. At the distance of these quasars, a milliarcsecond corresponds to a several parsecs, far larger than the accretion disk, or even the dusty torus. But microlensing can probe distances of several hundred AU, which is about the size of quasar accretion disks. Since these disks have a temperature structure, it is reasonable that longer wavelengths, originating from a larger area of the disk, should be less affected by microlensing than shorter wavelengths.

Microlensing may be distinguished from millilensing by the presence of chromatic flux ratio anomalies or by observing uncorrelated variability in the lensed images (millilensing variability operates too slowly for us to observe). Millilensing, on the other hand, is characterized by anomalous flux ratios at mid-infrared or radio wavelengths, where quasars are large enough that microlensing is ineffective. In this thesis, we operate under the assumption that the flux ratio anomalies are predominantly due to microlensing (with one exception; see Section A.2). This assumption is justified by observations, even apart from the chromatic flux ratios we report: several lenses have shown uncorrelated microlensing variability [e.g., Woźniak et al., 2000, Chartas et al., 2009, Pooley et al., 2009]. Also, mid-IR observations of lensed quasars have shown that the flux ratios match the models predictions quite well in general [Chiba et al., 2005, Minezaki et al., 2009], as expected in the case of microlensing for flux arising from the relatively large dusty torus.

No method besides microlensing is able to probe the accretion disks of distant quasars at scales as small as these. Even high-frequency very long-baseline interferometry (VLBI) [e.g., Doeleman et al., 2009] cannot reach the required resolution. Some progress has been

24

made using reverberation techniques [e.g., Kaspi et al., 2000], but only in measuring the sizes of the broad line region.

Though we focus on the effects of finite-size sources, microlensing is also able to constrain the local fraction of the surface mass density of the lens galaxy made up of stars, as opposed to smoothly distributed (presumably dark) matter. The X-ray flux ratios we describe starting in Chapter 3 are useful for this purpose, since they come from a very compact region. Using these ratios removes the need to simultaneously vary the stellar mass fraction and source size. See Schechter and Wambsganss [2004] and Pooley et al. [2009] for details on this.

1.4   Thesis structure

The structure of this thesis follows in rough chronological order the work the author (JAB) has done in the past six years, along with collaborators David Pooley (DP), Saul Rappaport (SAR), and Paul Schechter (PLS). Chapters 2 through 5 are each based on a published paper; these are Blackburne et al. [2008], Blackburne et al. [2006], Pooley et al. [2006], and Pooley et al. [2007], respectively. Chapters 6 through 9 contain material that is being prepared for publication.

Chapter 2 contains the earliest work, though its publication was delayed until after the others. It reports the discovery of HE 1113−0641, a very small-separation lens. Chapters 3 and 4 report strong anomalous flux ratios in X-rays for two lenses, and begin to explore the implications for the size of the quasars at optical wavelengths. Chapter 5 extends the analysis of the previous two chapters to a sample of ten lenses and finds that X-ray flux ratios are more anomalous than optical ones, in general.

In Chapter 6 we introduce the primary project of this thesis, the multi-wavelength optical survey designed to measure the size of twelve quasars' accretion disks as a function of wavelength. Chapter 7 describes the data we obtained, while Chapter 8 details our quantitative analysis method. In Chapter 9 we examine the results, compare them to results from the literature, and review our conclusions. Finally, in Chapter 10 we describe future work.

Throughout this thesis, we calculate distances and time delays using a geometrically flat universe with $\Omega_M = 0.3$, $\Omega_\Lambda = 0.7$, and $H_0 = 70$ km/s/Mpc.

Chapter 2

HE 1113−0641: A lensing case study

2.1 Introduction

This chapter describes the discovery of HE 1113−0641, the smallest-separation quadruply lensed quasar ever found with a ground-based optical telescope. Quad lenses are useful for studying the baryonic and dark matter components of galaxies [e.g. Schechter and Wambsganss, 2004], as well as the properties of the background accretion disk [Pooley et al., 2007, Poindexter et al., 2008] and emission line region [Keeton et al., 2006]. So each new one is significant, especially in the southern hemisphere, as there is no analog there to the Sloan Digital Sky Survey (SDSS), where many lenses are currently being found [e.g., Oguri et al., 2008b].

The exceptionally small separation of the images in this lens highlight the value of high-resolution imaging, both from the *Hubble Space Telescope* (*HST*) and from ground-based observatories. In particular, the Magellan telescopes' superior image quality enabled the discovery of this lens. The small separation has a downside, as well – the faint lens galaxy is difficult to observe, and we have little hope of measuring its redshift. And the necessity of excellent seeing makes this lens difficult to monitor. The four quasar images demonstrate flux ratio anomalies, indicating that microlensing is likely to be taking place.

Table 2.1. Observations of HE 1113−0641

Date	Instrument	Filter	Exposure	Seeing
2002 February 16	MagIC	g'	7 × 60 sec	$0\rlap{.}''52$
		i'	7 × 60 sec	$0\rlap{.}''43$
2003 January 26	MagIC	g'	1 × 60 sec	$0\rlap{.}''47$
		i'	3 × 120 sec	$0\rlap{.}''33$
2003 November 06	NICMOS	H	3 × 640 sec	$\cdots$
			1 × 704 sec	
2003 November 07	ACS/WFC	V	3 × 120 sec	$\cdots$
			2 × 480 sec	
		I	3 × 85 sec	$\cdots$
			2 × 346 sec	
			1 × 370 sec	

In Section 2.2, we report the observations made using Magellan and the *HST*. Section 2.3 describes our analysis of the data. In Section 2.4 we construct a simple model of the lensing potential, and in Section 2.5 we make a rough estimate of the lens redshift. In Section 2.6 we discuss the conclusions we can come to regarding HE 1113−0641. This chapter is adapted from Blackburne et al. [2008][1].

2.2 Observations

HE 1113−0641 was originally discovered to be a $z = 1.235$ quasar in the Hamburg/ESO digital objective prism survey [Wisotzki et al., 2000]. Based on its redshift and apparent magnitude $B = 17.01$, it was found to have a relatively high lensing probability, and was selected for a follow-up observation.

We observed the object in early 2002 and early 2003 in the Sloan g' and i' bands using the Magellan 6.5 meter telescopes. In Autumn 2003, we observed it in three bands using the Advanced Camera for Surveys (ACS) and the Near-Infrared Camera & Multi-Object Spectrometer (NICMOS) aboard the *HST*. These observations are tabulated in Table 2.1.

2.2.1 Magellan 6.5 meter imaging

HE 1113−0641 was identified as a quadruple gravitational lens on 2002 February 16 using the Baade 6.5 m telescope at the Las Campanas Observatory. Seven 60-second exposures in each of the Sloan i' and g' bands, and a single exposure in the r' band, were taken using the Magellan Instant Camera (MagIC), a 2048×2048 pixel CCD camera with a 2.4 arcminute field of view. The average seeing varied from $0\rlap{.}''43$ in i' to $0\rlap{.}''50$ in r' to $0\rlap{.}''52$ in g'. Because of the combination of mediocre seeing with the existence of only a single image in the r' band, and the absence of any corresponding images in the 2003 dataset, we did not carry out any analysis in r'.

Second-epoch images were obtained on 2003 January 26, again using MagIC, which had meanwhile been moved to the Clay telescope, 60 meters to the northwest. The three i' band images had an average seeing of $0\rlap{.}''33$, while the single g' band image had a seeing of $0\rlap{.}''47$.

The data were bias-corrected, flattened, and combined using standard techniques. The stacked 2003 i' band image may be seen in Figure 2-1.

2.2.2 *Hubble Space Telescope* imaging

On 2003 November 6 and 7, HE 1113−0641 was observed using both the NIC2 camera of NICMOS and the Wide Field channel of the ACS. The NICMOS images had 256×256 pixels and a $19\rlap{.}''2$ field of view, while those from the ACS were significantly larger, with 4096×4096 pixels filling a 3.4 arcminute field of view. Three filters were used, F160W with NICMOS and F555W and F814W with the ACS (hereafter H, V, and I, respectively). Because of the diffraction-limited quality of the images, they were not well sampled, with the width of point spread function (PSF) ranging from 1.5 pixels in H to 2.1 pixels in I.

We used the `Multidrizzle` program of Koekemoer et al. [2002a], version 2.2, to register the ACS images, clean them of cosmic rays, and combine them into a single image per filter. The drizzling process also corrects for geometric distortion arising from the design of the camera. We likewise drizzled the NICMOS images into a single image using the procedure detailed in Koekemoer et al. [2002b][2].

---

[2]The *HST* Dither Handbook [Koekemoer et al., 2002b] is available at
http://www.stsci.edu/hst/HST_overview/documents/dither_handbook
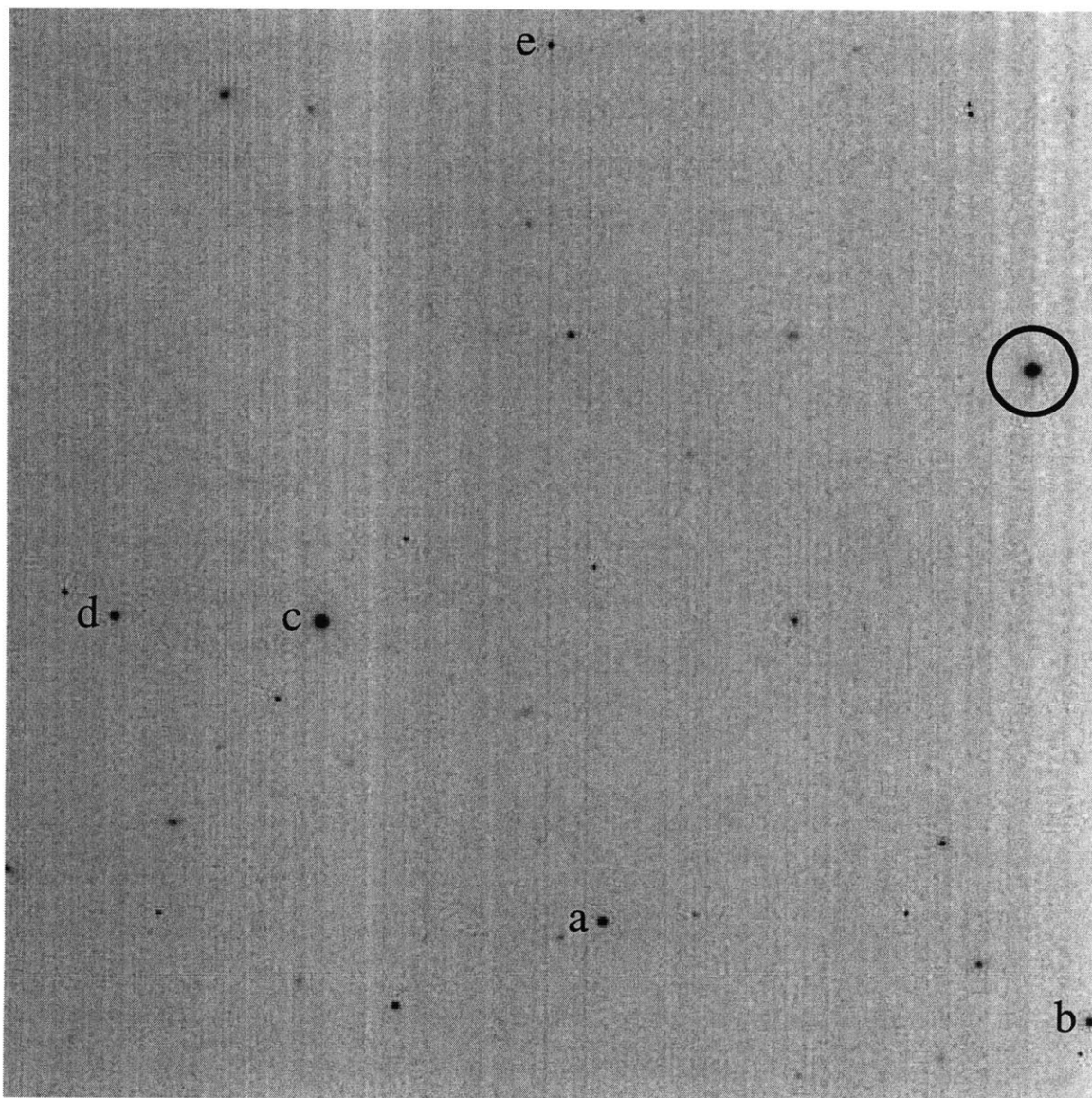
Figure 2-1 2003 Magellan i' band image of the HE 1113−0641 field, trimmed slightly and binned to 0.''276 per pixel. The image is 2.2 arcminutes on a side. The quasar is circled, and the five field stars a through e are labeled. North is up; east is to the left.

The drizzled ACS and NICMOS images of HE1113−0641 may be seen in Figure 2-2.

2.3 Analysis

The small separation of this lens, combined with the relative faintness of the lensing galaxy, complicated the task of disentangling the four quasar components and the galaxy, particularly for the ground-based data. To address this issue, we used an iterative PSF-fitting process to find the relative positions and brightnesses of the objects. First we performed a fit to each image for the relative positions of the objects, then averaged the positions thus obtained and repeated the fit, holding constant the relative positions, to determine the photometry.

We used a variant of the DoPHOT photometry package [Schechter et al., 1993] called Clumpfit to carry out the fits using a standard nonlinear least-squares algorithm. We used empirical PSFs provided by field stars for the quasar components and an elliptical pseudo-Gaussian profile [Schechter et al., 1993] for the lensing galaxy. Though this is not a physical profile choice, we found that the choice of galaxy profile had a negligible effect on the goodness of the fit. We also used DoPHOT to obtain astrometry and aperture photometry for several other stars in the wider-field (ACS and Magellan) images.

2.3.1 Magellan data

A fit consisting of four empirical PSFs (provided by a field star) was made to the stacked i' band Magellan images. This came to a total of 13 free parameters: two-dimensional position and normalization for all four objects, and the sky level. It was clear from the residual images that a small amount of leftover flux remained; indeed, that the four point sources had been over-subtracted in an attempt to compensate (see Figure 2-3). So a second fit was attempted using a model with four point sources and a circularly symmetric galaxy; however, there was not enough galaxy flux for the fit to distinguish between radial profiles or converge upon a scale size. We therefore chose a fixed-width circular pseudo-Gaussian profile for the galaxy and repeated the fit, which now had 16 free parameters. The width of the galaxy was set to the width chosen for the ACS data (see Section 2.3.2), suitably

Table 2.2. Relative Astrometry of HE 1113−0641

	B		C		D		G	
	x	y	x	y	x	y	x	y
i' (2002)	+0.515	+0.428	+0.515	−0.091	+0.148	+0.433	+0.431	+0.188
i' (2003)	+0.517	+0.424	+0.523	−0.086	+0.149	+0.432	+0.422	+0.134
V	+0.518	+0.424	+0.523	−0.085	+0.152	+0.427	$\cdots$	$\cdots$
I	+0.519	+0.422	+0.523	−0.083	+0.152	+0.429	+0.320	+0.145
H	+0.518	+0.425	+0.522	−0.083	+0.146	+0.429	+0.308	+0.169

Note. — The positive directions for x and y are west and north, respectively. All positions are measured in arcseconds, and are given relative to component A.

broadened by the PSF. This fit was able to account for the leftover flux.

The relative astrometry resulting from the 16-parameter fits in i' and other filters is listed in Table 2.2. The relative positions of the four quasar components were then weighted by the inverse of their uncertainties and averaged, yielding final values, which may be found in Table 2.5. In the case of the lensing galaxy, only the *HST* positions were averaged (see Section 2.3.2).

Once the relative astrometry had thus been determined, we repeated the fit with fixed relative positions and a fixed galaxy width. The results of this fit may be seen in Table 2.4, and residual images are in Figure 2-2.

For the g' band images, which had poorer seeing, the quasar components were too blurred for a successful fit until relative positions were fixed. The residual images of these fits may also be seen in Figure 2-2. There was no indication in the residuals of leftover flux indicative of a lens galaxy, so we conclude that we have not detected it in the g' band.

Aperture photometry was also obtained for several field stars, including those used as model PSFs. The positions of these stars, labeled a through e in Figure 2-1, may be found in Table 2.3, and their magnitudes are listed in Table 2.4.

To enable absolute flux calibration, aperture photometry was obtained for standard stars from the sample of Smith et al. [2002]. For the 2002 data we used PG 1047+003A, and for that of 2003 we used RU 152. We applied a first-order correction for atmospheric extinction

Table 2.3. Field Stars a through e

	x	y
a	−40.04	−66.50
b	+5.70	−79.16
c	−66.47	−29.91
d	−85.97	−29.07
e	−44.84	+39.90

Note. — The positive directions for x and y are west and north, respectively. All positions are measured in arcseconds, and are given relative to component A.

when calculating the zeropoints, using extinction coefficients from Table 4 of Smith et al. [2007]. It is worth noting that the Sloan $u'g'r'i'z'$ system is a broadband approximation to the (monochromatic) AB magnitude system, and is given by

$$m = -2.5 \log \frac{\int d(\log \nu) f_\nu S_\nu}{\int d(\log \nu) S_\nu} - 48.60 \quad , \tag{2.1}$$

where f_ν is the energy flux per unit frequency, and S_ν is the filter response. The system is defined by 158 standard stars, and is calibrated by synthetic spectra of BD +17°4708. The $u'g'r'i'z'$ deviates from the true AB system by less than 5% [Smith et al., 2002], and is presented in Table 2.4.

We estimate the uncertainty in the relative photometry to be 0.1 magnitudes in g' and 0.05 magnitudes in i'. Absolute photometry is less certain, with error bars a factor of 1.4 larger. With these uncertainties the data are consistent with a slight overall brightening of all four images between 2002 and 2003, probably caused by intrinsic variability of the quasar. However, they fail to convincingly demonstrate uncorrelated changes in the flux ratios over time, even when combined with *HST* data; such variations might have been

Table 2.4. HE 1113−0641 Photometry

	g' (2002)	g' (2003)	i' (2002)	i' (2003)	V	I	H	$g' - i'$ (2003)	$V - I$	$I - H$
A	18.37	18.19	18.02	17.96	18.33	18.32	18.25	+0.23	+0.00	+0.07
B	18.28	18.24	18.09	18.02	18.40	18.35	18.27	+0.22	+0.05	+0.08
C	18.53	18.39	18.46	18.37	18.64	18.61	18.74	+0.02	+0.03	−0.13
D	18.91	18.91	18.79	18.76	19.06	19.01	18.92	+0.15	+0.06	+0.08
G	⋯	⋯	22.36	22.17	⋯	22.47	21.05	⋯	⋯	+1.42
a[a]	20.63	20.70	18.08	18.05	20.16	17.86	⋯	+2.65	+2.30	⋯
b	⋯	⋯	⋯	18.39	20.66	18.04	⋯	⋯	+2.62	⋯
c	19.29	19.34	16.62	16.62	18.91	16.39	⋯	+2.72	+2.52	⋯
d	18.78	18.77	18.36	18.36	18.69	18.45	⋯	+0.41	+0.24	⋯
e	22.51	22.59	20.01	20.02	22.06	19.81	⋯	+2.57	+2.25	⋯

[a] a through e are field stars.

Note. — All magnitudes are in the Sloan $u'g'r'i'z'$ photometric system (see Section 2.3.1).
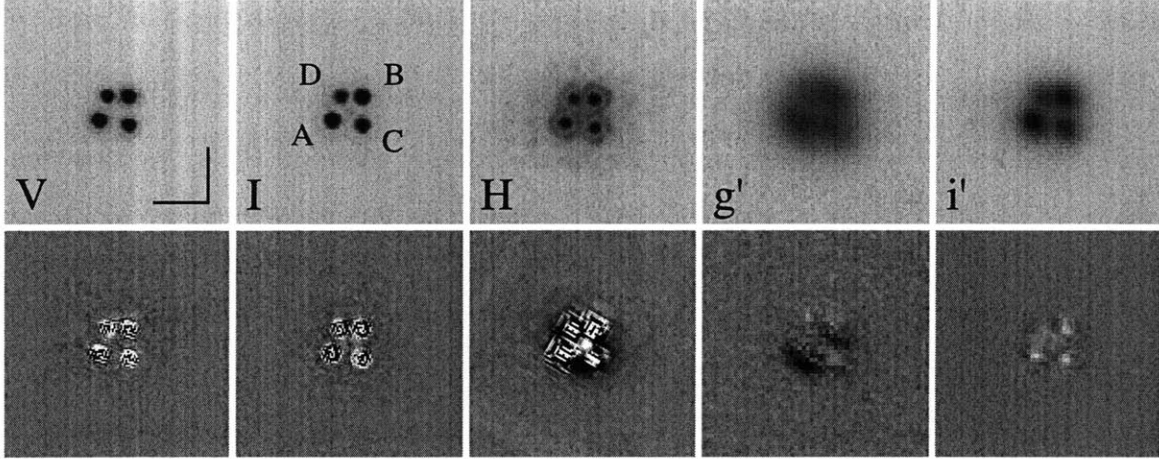
Figure 2-2 Top row: Stacked images of HE 1113−0641 from the *HST* (*V*, *I*, and *H*) and Magellan (*g′* and *i′*). Magellan data are from 2003. The images are displayed with logarithmic stretch. Bottom row: Residual images after subtraction of the best model. The images are in a linear stretch from -20σ to 20σ, where σ is the sky noise. All images are 4″.0 on a side.
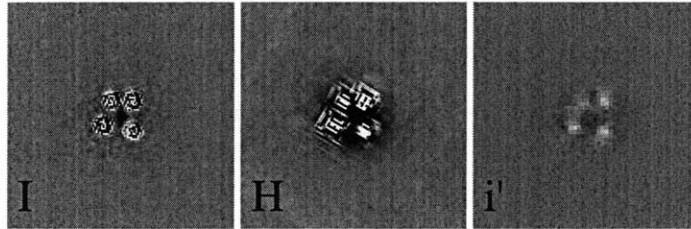
Figure 2-3 Residual images of HE 1113−0641 in the redder filters after only four point sources, and no central galaxy, have been fit and subtracted. Leftover flux from the lensing galaxy may be seen near the center. Stretch and size are equal to those of the second row of Figure 2-2.

indicative of microlensing.

Despite our use of fixed positions for the *g′* band images, there are inconsistencies in the *g′* − *i′* colors of the quasar components. It is likely that these are due to the confusion caused by mediocre seeing in the *g′* band.

There can be little doubt that the lensing galaxy has been detected in the *i′* band in both data sets. However, its size and shape remain poorly constrained. By fitting a fixed circular pseudo-Gaussian to both epochs of data, we were able to estimate its *i′* band flux, but with substantial uncertainty (0.2 magnitudes of difference between epochs). We were able to determine the position of the galaxy using *HST* data, but its size and shape remained elusive (see Section 2.3.2).

35

2.3.2 *Hubble Space Telescope* data

The *HST* images did not suffer from inadequate seeing, but rather from undersampling of the PSF, leading to complications in the interpolation of empirical PSFs. We therefore resampled the ACS images to a scale of $0\rlap{.}''03$ per pixel, and the NICMOS image to a scale of $0\rlap{.}''0375$ per pixel, when combining images.

ACS

Since the ACS PSF is known to vary across the field of view and also with time, we searched the *HST* archive for images with a suitable PSF star located close to the position of HE 1113−0641 on the chip, and obtained at a time close to 2003 November 7. In the *V* band, we used a field obtained on 2003 October 7[3], and in *I* we used a field obtained on 2003 November 25[4]. In order to minimize differences in the PSF caused by the drizzling process, we used the same Multidrizzle process on these images as on the HE 1113−0641 images. We chose PSF stars that were close to the correct position on the chip, and were not saturated. In both cases, these stars were about 1 magnitude fainter than image A.

The fits proceeded as they had in the case of the Magellan images. There was appreciable leftover flux in the *I* band, concentrated in the center of the lens system (see Figure 2-3). Since the noisy residuals of the quasar components again prevented a measurement of the lensing galaxy's radial profile or scale size, we fit it as a circular pseudo-Gaussian with a fixed width of $0\rlap{.}''35$ (broadened slightly by the ACS PSF). The width was chosen by inspection of the residual image, since the choice had little to no effect on the goodness of fit parameter. No sign of the galaxy was visible in the *V* band residual image.

Both of these fits were repeated once we had determined and fixed the relative positions. The resultant residual images are visible in Figure 2-2. The magnitudes were calibrated using AB zeropoint keywords from the *HST* data headers. The *HST* broadband flux calibration is based on synthetic spectra of four primary white dwarf stars [Bohlin, 1995], and agrees with the AB zeropoints of Smith et al. [2002] to within 3% [Bohlin and Gilliland, 2004]. The photometric data are presented in Table 2.4.

---

[3]The exposure was associated with program #9756, and started at 4:08 AM.
[4]The exposure was associated with program #9822, and started at 10:07 PM.

Astrometric measurements were made using DoPHOT on the I band image. A plate solution was found using sixteen USNO-B stars. This solution gives the position of component A as (11^{h} 16^{m} $23^{\mathrm{s}}.56$, $-6°$ $57'$ $38''.6$; J2000) to a precision of $0^{\mathrm{s}}.01$ in right ascension and $0''.1$ in declination.

NICMOS

The analysis of the NICMOS data was similar to that of the ACS data. A 2003 September 5 observation of SA 107-626 provided a model PSF[5]. In this case, the PSF star was much brighter than the quasar components.

Leftover flux from the lensing galaxy was visible in the H band image, as it had been in the I band image (see Figure 2-3). We again modeled it as a circular pseudo-Gaussian, with the same fixed width (broadened slightly by the NICMOS PSF).

A second fit was performed with the relative positions of the quasar components fixed to the averaged value. The photometry that resulted from this second fit was calibrated to the AB system using keywords from the data headers, and is visible in Table 2.4. The residual image may be seen in Figure 2-2.

2.4   Modeling the lens

Using the Lensmodel software of Keeton [2001], we modeled the lensing galaxy as a singular isothermal sphere model plus external shear. This model consists of a projected 2-dimensional lensing potential given by

$$\Psi(\boldsymbol{\theta}) = br - \frac{\gamma}{2}r^2 \cos 2(\phi - \phi_\gamma), \tag{2.2}$$

where b is the monopole Einstein radius in arcseconds, r and ϕ are the radial and angular components on the sky of the position vector $\boldsymbol{\theta}$, and γ and ϕ_γ are the strength and direction of the external shear. Note that in this convention the position of a companion mass causing a shear would be along the $\pm\phi_\gamma$ direction. (No such perturber is observed in this case,

---

[5]The exposure was associated with program #9875, and started at 4:56 AM.

consistent with the apparently small shear strength.) This model has seven free parameters, and was constrained by the averaged positions for the four components and the galaxy.

We found the best model to have a monopole Einstein radius of $0\rlap{.}''332$, with $\gamma = 0.04$ and $\phi_\gamma = 37.7$ degrees east of north. The source position was predicted to be $(x, y){=}(0\rlap{.}''308, 0\rlap{.}''151)$ relative to the position of component A, where the positive directions of x and y are west and north. Table 2.5 contains a summary of the model's predictions, compared to observed data.

The model fits the component positions very well, even with the tight constraints provided by the *HST*. It does not, however, correctly predict the flux ratios. This is in keeping with experience; optical flux anomalies can be seen in many lensed quasars [Keeton et al., 2003]. In particular, the D component, a saddle point image, is predicted to be brightest, but is observed to be the faintest, too faint by as much as a factor of 2.5. The predicted position of the lensing galaxy is $0\rlap{.}''01$ from the observed position. This is well within the estimated measurement error.

Finally, the model allows us to predict the time delays between the images, given a lens redshift. We used $z_L = 0.7$, as estimated in Section 2.5. This yields the predicted time delays seen in Table 2.5, with the maximum delay being ~ 1.5 days. We also calculated predicted time delays for $z_L = 0.4$ and $z_L = 1.0$; these changes reduced and increased (respectively) the time delays by a factor of ~ 3. This strong dependence suggests that a measurement of the time delays might constrain the lens redshift; however, the unknown radial mass profile of the lensing galaxy is likely to have a similarly strong effect on time delays.

By way of comparison, HE 0435−1223, which has a shape similar to that of HE 1113−0641 but a larger image separation, has a maximum time delay of two weeks [Kochanek et al., 2006].

2.5 Estimating the lens redshift

In order to estimate the redshift of the lensing galaxy and determine what its $I - H$ color could tell us about its morphology, we combined the results of our lens model with properties

Table 2.5.   HE 1113-0641 Astrometry & Lens Model

	Observed[a]		Predicted		Observed[b]	Predicted	Predicted
	x	y	x	y	μ	μ	Time Delays[c]
A	$0''$	$0''$	+0.002	+0.001	+16.0	+12.6	0
B	+0.518	+0.424	+0.518	+0.423	+15.7	+15.7	7.9
C	+0.522	−0.085	+0.524	−0.084	−10.2	−9.6	36.9
D	+0.150	+0.429	+0.150	+0.428	−8.6	−16.7	16.4
G	+0.313	+0.158	+0.314	+0.148	$\cdots$	$\cdots$	$\cdots$

[a]Weighted average of positions from i' band data and HST data.

[b]Flux ratios from H band data; normalized so that component B matches the model. Negative magnification denotes saddle point images.

[c]In hours.

Note. — The positive directions for x and y are west and north, respectively. All positions are measured in arcseconds.

of typical galaxies.

From the lens strength $b = 0''\!.332$ we found the line-of-sight velocity dispersion σ_L of the lens using

$$b = \frac{D_{\rm LS}}{D_{\rm OS}} \frac{4\pi\sigma_L^2}{c^2} \tag{2.3}$$

[Narayan and Bartelmann, 1996], where $D_{\rm LS}$ is the angular diameter distance from the lens to the source, and $D_{\rm OS}$ is the angular diameter distance from the observer to the source. These distances depend on both the source redshift $z_S = 1.235$ and the unknown lens redshift z_L.

By combining this equation with the Faber-Jackson relation [Faber and Jackson, 1976] for elliptical galaxies, or the Tully-Fisher relation [Tully and Fisher, 1977] for spiral galaxies, we generated a predicted observed magnitude for each filter as a function of lens redshift. The Faber-Jackson relation is given by

$$M_T^0(B) = -19.4 + 5\log h - 10(\log \sigma - 2.3) \tag{2.4}$$

39

[de Vaucouleurs and Olson, 1982], which becomes

$$M_B = -18.9 + 5 \log h - 10(\log \sigma - 2.3), \tag{2.5}$$

after applying the extinction correction $B_T - B_T^0 = 0.22$ [de Vaucouleurs et al., 1976], and with $B_J = B_T + 0.29$ [Peterson et al., 1986]. The Tully-Fisher relation is the same, but with σ replaced by circular velocity, which for an isothermal sphere is just $\sqrt{2}\sigma$.

The predicted magnitude in the i' band is given by

$$m_{i'} = M_B + DM(z_L) + K_{B,i'}(z_L) \tag{2.6}$$

where $DM(z_L)$ is the cosmological distance modulus, and $K_{B,i'}(z_L)$ is the generalized K-correction between the lensing galaxy's rest-frame B band magnitude and the observed i' band magnitude [see, e.g., Hogg et al., 2002]. To calculate the K-correction for an elliptical galaxy at each potential lens redshift, we used a spectral energy disbribution (SED) generated by the Bruzual and Charlot [2003] spectral evolution code. Our model consisted of a solar-metallicity, instantaneous starburst at a redshift of 3.0, followed by passive evolution. For a spiral galaxy, we used an empirical Scd galaxy spectrum from Coleman et al. [1980], redshifted appropriately.

The observed magnitudes of the lensing galaxy matches those predicted for an elliptical galaxy for a range of redshifts $0.4 \lesssim z \lesssim 1.0$. A spiral galaxy model also matches the H band observations, but would be brighter than observed at all redshifts in I by $\gtrsim 1$ magnitude. The galaxy's brightness and colors seem to be more consistent with an elliptical galaxy than a spiral.

In addition to this method, we estimated the probability distribution of the lensing galaxy's redshift by calculating lensing optical depth as a function of redshift, following the approach of Kochanek [1992]. We found that the median redshift was 0.66, with a 68% confidence interval of [0.41,0.88]. This is consistent with the results of the Faber-Jackson method.

2.6 Conclusions

The $z_S = 1.235$ quasar HE 1113−0641 is lensed into a cross configuration, with four components ranging from 18.0 to 18.8 magnitudes in i'. The maximum image separation is $0\rlap{.}''67$. A combination of ground-based and *HST* imaging has yielded reliable astrometry and photometry of the four quasar components of HE 1113−0641, as well as a good estimate of the position of the lensing galaxy. However, we were unable to measure the size or morphology of the galaxy. By assuming a circular pseudo-Gaussian shape and fixing a width for the galaxy, we were able to estimate its flux in the redder bands.

A singular isothermal sphere (SIS) model succeeded in matching the positions of the quasar components and of the lensing galaxy, but was unable to match the observed flux ratios. Based on what has been seen with other gravitational lenses, it seems likely that this is due to perturbations from stellar microlensing or dark matter substructure in the lens galaxy.

The redshift of the lens galaxy remains elusive, but we estimate that $z_L \sim 0.7 \pm 0.3$, based on its observed flux and colors. At this redshift, its velocity dispersion, as measured by its lensing potential, would be 180 km/s.

Because of its small separation, HE 1113−0641 will likely prove difficult to monitor using ground-based telescopes, and there is little hope for measuring a spectroscopic redshift of the lensing galaxy. Nevertheless, it is an interesting example of a small-separation lens, and may prove useful for studies that can take advantage of telescopes with very good seeing. We undertake such a study in Chapters 6 through 9.

Chapter 3

Chromatic anomalies I:

RX J1131−1231 in X-rays and

optical

3.1 Introduction

RX J1131−1231 is a rather spectacular gravitationally lensed quasar. The quasar, at a redshift of 0.658, is lensed by a nearly round elliptical galaxy at a redshift of 0.295 into a cusp configuration, with three bright images on one side of a round elliptical-type galaxy, and a counter-image on the other side. There is also a prominent ring made up of emission from the host galaxy of the quasar.

The optical flux ratios reported in the discovery paper [Sluse et al., 2003] differ significantly from the predictions of simple lens models. In this chapter, we report the results of X-ray observations made with the *Chandra X-ray Observatory* at a single epoch, and optical observations made at the Magellan telescopes at six epochs over the course of fourteen months. We find that the optical brightness of the source varied by no more than 0.3 magnitudes during this time, and continued to differ from model predictions by factors of about 2. However, the X-ray flux ratios are discrepant by factors of 3 to 9!

We discuss possible explanations for this wavelength-dependant discrepancy in the flux

ratios, and conclude that microlensing, in combination with the effects of a finite-size source, is the most likely culprit. With the exception of that of Morgan et al. [2001], which reported a strong flux ratio anomaly in the lensed quasar RX J0911+0551, this is the first work to use *Chandra* to measure flux ratio anomalies.

This chapter is adapted from Blackburne et al. [2006][1]. Section 3.2.1 was written by DP, and describes the analysis he carried out on the Chandra data. Sections 3.3.3, 3.3.4, and 3.4 were written with guidance from SAR. The remainder is the author's own work.

3.2   Observations

3.2.1   X-Ray observations

RX J1131−1231 was observed for 10.0 ks on 2004 April 12 (ObsID 4814) with the Advanced CCD Imaging Spectrometer (ACIS) on the *Chandra X-ray Observatory*. Each ACIS chip has 1024×1024 pixels and is $8\rlap{.}''3$ on a side (with a pixel size of $0\rlap{.}''49$). The PSF is both energy-dependent and position-dependent. Near the aimpoint, the half-power diameter is about $0\rlap{.}''8$ at 1 keV, broadening to about $1''$ at 8 keV. The data were taken in timed-exposure mode with an integration time of 3.14 s per frame, and the telescope aimpoint was on the back-side illuminated S3 chip. The data were telemetered to the ground in very faint mode.

The data were downloaded from the *Chandra* archive, and data reduction was performed using the CIAO 3.2.2 software provided by the *Chandra* X-ray Center[2]. The data were re-processed using the CALDB 3.1.0 set of calibration files (gain maps, quantum efficiency, quantum efficiency uniformity, effective area) including a new bad pixel list made with the acis_run_hotpix tool. The reprocessing was done without including the pixel randomization that is added during standard processing; this omission slightly improves the point spread function. The data were filtered using the standard *ASCA* grades and excluding both bad pixels and software-flagged cosmic ray events. Intervals of background flaring were searched for, but none were found.

The IDL-based software package ACIS Extract v3.79 [Broos et al., 2002] was used

---

[2]http://asc.harvard.edu

for subsequent reduction and analysis. An image of the X-ray data (see Figure 3-1) was constructed by reprojecting the events around RX J1131−1231 in the 0.5–8 keV energy range using a spatial bin size of $0\rlap{.}''16^3$. Model PSFs were produced for the images using the CIAO tool mkpsf at energies of 0.277, 1.4967, 4.51, 6.4, and 8.6 keV. The 1.4967 keV PSF was used in a maximum-likelihood reconstruction image of the data (10,000 iterations) in order to determine precise positions for each of the four lensed images.

Small apertures (about $0\rlap{.}''3$ in radius) centered on these positions were used to extract counts and spectra, and the CIAO tools mkacisrmf and mkarf were used to produce response files. ACIS Extract corrected the effective area response at each energy based on the fraction of the PSF enclosed by the extraction aperture at that energy, interpolating from the five model PSFs. The apertures enclosed roughly 30% of the PSF at 1.5 keV and roughly 25% of the PSF at 6.4 keV. These small apertures were desirable in order to reduce contamination from the other lens images, but image A still suffered some small contamination from images B and C. To correct for image A being in the wings of the PSF of both B and C, five extraction regions were placed around B and five around C at the same radial distance as A. The averages of each set of five regions were used for subtraction from A. The contribution of the cosmic X-ray background in the lens extraction regions is negligible (roughly 0.005 counts).

The spectrum of each lens image was fit in XSPEC 12.2 [Arnaud, 1996] with a powerlaw model absorbed by two components, one fixed at the Galactic column to RX J1131−1231 of $n_H = 3.64 \times 10^{20}$ cm^{-2} [Dickey and Lockman, 1990] and one allowed to vary. Acceptable fits were obtained for each image, with reduced χ^2 of 0.37, 1.3, 0.59, and 1.8 for images A, B, C, and D, respectively. For each of the images, the additional absorption components were consistent with zero, and the upper ends of the 1-σ confidence intervals were 6.0, 1.4, 2.1, and 4.4×10^{20} cm^{-2}, indicating similar (and small) absorbing columns for each image. The powerlaw indices (with 1-σ confidence intervals) were $1.21^{+0.27}_{-0.14}$, $1.23^{+0.08}_{-0.05}$, $1.63^{+0.17}_{-0.09}$, and $1.93^{+0.58}_{-0.29}$, indicating some intrinsic spectral differences (i.e., not due to absorption) among the lens images. To further quantify these differences, the spectral hardness ratio

---

[3]The satellite continuously dithers in a Lissajous pattern on the sky, requiring all images to be reprojected. Standard processing produces an image with pixels that are $0\rlap{.}''492$ on a side to match the physical CCD pixel size. ACIS Extract produces images with pixels matched to the size of those in the model PSFs.

Table 3.1. X-Ray and Optical Properties of RX J1131−1231

	X-Ray	Optical	Model
$F_B{}^a$	1.8×10^{-13}	7.5×10^{-14}	1 (+)
F_A/F_B	0.18 ± 0.04	1.10 ± 0.155	1.703 (-)
F_C/F_B	0.27 ± 0.03	0.47 ± 0.063	0.962 (+)
F_D/F_B	0.06 ± 0.01	0.17 ± 0.061	0.113 (-)
$L_B{}^b$	3.2×10^{44}	1.3×10^{44}	$\cdots$
SR(A)^c	1.05 ± 0.28	1.10; 0.86 ±0.13	$\cdots$
SR(B)^c	1.14 ± 0.09	0.96; 0.94 ±0.13	$\cdots$
SR(C)^c	0.72 ± 0.10	0.96; 0.82 ±0.13	$\cdots$
SR(D)^c	0.58 ± 0.16	0.93; 0.77 ±0.13	$\cdots$

[a]Flux in units of erg cm^{-2} s^{-1}; corrected for a magnification of 13.9, as determined from a model of the lens.

[b]Luminosity in units of erg s^{-1} for a source at $z = 0.658$ and a corresponding luminosity distance of 3840 Mpc. No k-corrections have been made.

[c]Spectral ratios in the X-ray and optical bands. X-ray ratios are defined as the observed photon flux in the 2–8 keV band to that in the 0.5–2 keV band. The first of the optical spectral ratios is for the Sloan g' band to r' band; the second is for the r' to i' bands. The optical spectral ratios are given in linear flux units.

(SR) was defined as the observed photon flux (photons cm^{-2} s^{-1}) in the 2–8 keV band to that in the 0.5–2 keV band (see Table 3.1). To characterize the intensity of each image, the unabsorbed power-law flux was integrated over 0.5–8 keV. Table 3.1 lists this flux for image B and the flux ratio for the other images.

3.2.2 Optical observations

The lens was observed at six epochs over the course of fourteen months in 2004 and 2005 at the Magellan 6.5-meter Clay telescope at Las Campanas Observatory. The observations made use of MagIC, a 2048 × 2048 direct imaging instrument with a plate scale of 0."069 per pixel and a 2.4 arcminute field of view. One epoch of observations included imaging in

three bands — Sloan g',r', and i'; the others were limited to the i' band only. The seeing on these nights varied from $0\overset{''}{.}4$ (on the night of multicolor observations) to $1\overset{''}{.}0$.

Three images from the night with the best seeing were used to produce the pseudocolor optical image shown in Figure 3-1. The g' band was mapped to blue, while r' was mapped to green and i' to red. The color stretch has been matched to the square root of the flux to bring out the faint Einstein ring.

The DoPHOT PSF-fitting photometry program was used to measure the positions and magnitudes of the four quasar components and the lensing galaxy, as well as five nearby reference stars. The presence of the Einstein ring, which has a red color and thus is especially strong in the i' band, has resulted in some additional small uncertainties, both in astrometric and photometric measurements, which are difficult to quantify. We estimate the astrometric errors at $0\overset{''}{.}01$.

The standard stars 101 207 and RU 149F [Landolt, 1992] were used to bring the multi-band observations to the AB magnitude system. The transformations from Johnson colors to Sloan AB colors were taken from Fukugita et al. [1996]. The colors thus obtained for the four quasar images are reported in Table 3.1, in linear flux units.

The five field stars were used to calibrate the i' band photometry for all six epochs to the same magnitude system as the multi-band observations. After this normalization, the magnitudes of the 5 stars had rms fluctuations of between 0.02 and 0.07 magnitudes. The magnitudes of the four quasar components thus derived are presented in Table 3.2. Because of the effects of the Einstein ring, the uncertainties are larger for these than for the reference stars; we estimate them to be 0.15 magnitudes. Within this level of uncertainty, the data are almost consistent with a steady brightness over time, although there appears to be a slight dimming trend in the last three epochs.

3.3 Discussion

3.3.1 Modeling the lens

Following the lead of Sluse et al. [2003], we used the Lensmodel software of Keeton [2001] to model the lens as a singular isothermal sphere (SIS) with an external shear. Including

Table 3.2. Optical Variability of RX J1131−1231

Date	Image A	Image B	Image C	Image D
2004 February 19	17.69	17.70	18.49	19.71
2004 February 22	17.76	17.79	18.69	19.80
2004 May 9	17.56	17.52	18.51	19.95
2004 May 26	17.54	17.58	18.48	19.64
2005 January 5	17.85	18.16	18.82	19.67
2005 April 14	18.04	18.33	18.95	19.73

Note. — All values are Sloan AB i' band magnitudes, after correction for reference stars in the same field of view.

the position of the source as well as the lens position and strength and the shear strength and direction, there were seven free parameters. We used the Magellan positions of the four lens components, which had uncertainties of $0''\!.01$, for a total of eight constraints. We did not constrain the position of the lens, in order to allow for the possibility that mass may not strictly follow the light. The fit yielded a reduced χ^2 of 1.1. The lensing mass was predicted to be $0''\!.14$ southeast of the observed galaxy position, indicating that our model is not perfect; this is typical of such simple lens models. We find the lens strength to be $1''\!.78$, and the shear to be 0.12 in a direction $73°\!.3$ west of north. These values are similar to those reported by Sluse et al. [2003] of $1''\!.82$, 0.12, and $14°\!.8$ east of north[4].

The magnifications predicted by the best fit model are -23.7, 13.9, 13.4, and -1.58 for images A, B, C, and D, respectively, with signs indicating image parity. These appear as flux ratios in Table 3.1. The C/B and A/B ratios are low by factors of $\sim$2 in the optical, and by factors of $\sim$3–9, respectively, in X-rays. The model relative intensities were used to create a simulated image as it would appear through the Magellan telescope. This image is shown in Figure 3-1. It is clear that the predicted flux ratios are different from those observed.

---

[4] A 90° offset between the two position angles is due to differing sign conventions for the shear term.

3.3.2 Genuine optical anomalies

The X-ray flux ratios clearly appear to be anomalous, but one may fairly wonder if another relatively simple lens model might fit the optical data better. Keeton et al. [2003] use the "cusp relation" (which predicts in a model-independent way that the flux of image A should be approximately the same as the sum of images B and C) to establish convincingly that a simple smooth model with an elliptical galaxy cannot explain the optical flux ratios in RX J1131−1231. A highly flattened model such as an edge-on disk might explain them, but the morphology of the galaxy and the round unbroken Einstein ring rule out this possibility.

Our own modeling efforts bore out this conclusion. We constrained the fluxes to equal the optical values and modeled the lens both as an isothermal ellipsoid with external shear, and as an isothermal sphere with another isothermal sphere off-center, to provide shear. These models did not fit nearly as well as our best fit model above, with the extra contribution to χ^2 coming nearly exclusively from the flux constraints. We also tried loosening the constraints on the positions of the images. This did improve the flux fits somewhat, but caused the positions to be fit far from their observed values.

3.3.3 Quasar variability

Another possibility for explaining the differences in the X-ray and optical flux ratio anomalies might be to invoke temporal variability in the intrinsic output of the quasar, since the observations in the two wavebands were made at different epochs – though the X-ray observation was made about half way between the second and third of the optical observations. We have shown directly that the optical flux did not undergo any major secular changes in the intensity during that year. RX J1131−1231 has a luminosity which is about midrange (on a log scale) for quasars. Therefore it *may* undergo substantial temporal variability in both its intensity and spectral slope [see, e.g., Green et al., 1993]. However, a sustained ($\gtrsim 10^4$ s) change in intensity by a factor of ∼9 within a day (the time delay difference between images A and B) would be quite unusual [Green et al., 1993]. Thus, it seems doubtful that temporal variability explains the principal flux ratio anomaly in this source.
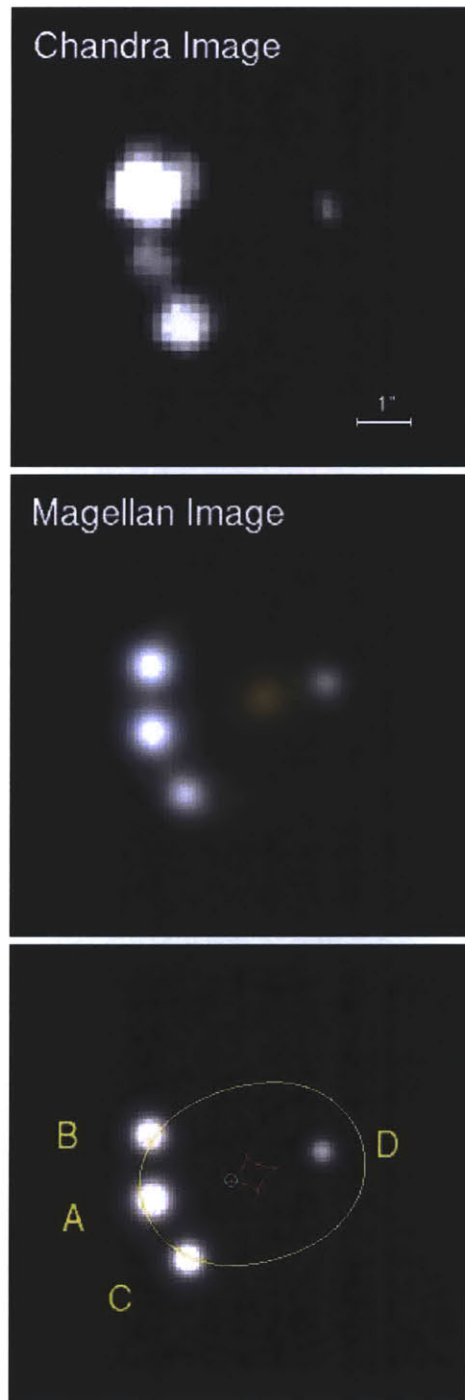
Figure 3-1 *Chandra*, Magellan, and model images (top to bottom) of RX J1131−1231. The raw *Chandra* image was convolved with a Gaussian with a width ∼70% the width of the *Chandra* PSF in order to produce a smoother appearance. The model image positions and brightnesses are from the model described in Section 3.3.1, as are the predicted source and lens positions, marked with circle and diamond-shaped caustic, respectively. Also plotted is the critical curve.

3.3.4 Anomalies due to substructure

As is the case for most anomalous quadruply lensed quasars [Kochanek and Dalal, 2004], the sense of the flux anomaly in RX J1131−1231 is to demagnify the brightest saddle point image (image A), and possibly to further magnify the brightest minimum (image B). This discrimination by image parity is expected for both micro- and millilensing [Schechter and Wambsganss, 2002, Kochanek and Dalal, 2004]. In addition, the fact that the anomaly in image A is more severe in X-rays, which originate from a smaller region than the optical light, supports microlensing rather than millilensing.

To help understand what substructure might do to the intensities of the optical and X-ray images, we estimate the ratio of the angular sizes of the emitting regions near the quasar black hole to the Einstein radius of a point object (e.g., a star) in the lensing galaxy [see also Mortonson et al., 2005]. Objects orbiting near the central black hole at radius r subtend a characteristic angle at the earth of:

$$\theta_s \simeq \frac{r}{D_{\mathrm{OS}}} = \left(\frac{r}{R_g}\right)\frac{GM_{\mathrm{BH}}}{c^2 D_{\mathrm{OS}}} \quad, \tag{3.1}$$

where M_{BH} is the black hole mass, R_g is the gravitational radius of the black hole, and D_{OS} is the angular-diameter distance to the source. By comparison, the Einstein radius of a micro- or millilensing point mass M_{ml} is

$$\theta_{\mathrm{Ein}} = \left(\frac{4GM_{\mathrm{ml}}}{c^2}\frac{D_{\mathrm{LS}}}{D_{\mathrm{OL}}D_{\mathrm{OS}}}\right)^{1/2} \quad, \tag{3.2}$$

where D_{OL} and D_{LS} are the lens and lens-to-source angular diameter distances, respectively.

We can define a dimensionless ratio of these quantities ξ, which is related to the degree to which micro- or millilensing can occur:

$$\xi \equiv \frac{\theta_s}{\theta_{\mathrm{Ein}}} = 3.5 \times 10^{-4} \left(\frac{r}{R_g}\right)\left(\frac{M_{\mathrm{BH}}}{10^8 M_{\odot}}\right)\left(\frac{M_{\mathrm{ml}}}{M_{\odot}}\right)^{-1/2}\sqrt{\frac{D_{\mathrm{OL}}(\mathrm{Gpc})}{D_{\mathrm{OS}}D_{\mathrm{LS}}}} \quad. \tag{3.3}$$

For RX J1131−1231 the above expression reduces to

$$\xi \simeq 3 \times 10^{-4} \left(\frac{r}{R_g}\right) \left(\frac{M_{\rm BH}}{10^8 M_\odot}\right) \left(\frac{M_{\rm ml}}{M_\odot}\right)^{-1/2} \quad , \tag{3.4}$$

$$\text{or,} \quad \xi \simeq 3 \left(\frac{\beta}{0.01}\right)^{-2} \left(\frac{M_{\rm BH}}{10^8 M_\odot}\right) \left(\frac{M_{\rm ml}}{M_\odot}\right)^{-1/2} \quad , \tag{3.5}$$

where β is the characteristic speed of orbiting or free-fall objects around the black hole, and we have taken $D_{\rm OS} \simeq 1400$, $D_{\rm OL} \simeq 900$, and $D_{\rm LS} \simeq 865$, all in units of Mpc.

Thus, X-ray and optical continuum emission which is emitted by the accretion disk within several hundred R_g of the black hole can be substantially microlensed (see Equation 3.4). Any broad-line emission features (with $\beta \simeq 0.01$) could be only marginally microlensed (see Equation 3.5). In contrast, any narrow-line emission region (with $\beta \simeq 10^{-3}$) would *not* be microlensed. In this study, we are limited to X-ray and continuum optical emission, both of which should be about equally microlensed.

Therefore, the clear differential in the flux ratio anomalies between the optical and X-ray bands, factors of ∼2 in the former, and ∼3–9 in the latter, presents something of a puzzle (see Section 3.4). If, on the other hand, the continuum optical emission originates farther from the center, possibly due to scattering of visible light or reprocessing of higher energy radiation, then the differential flux anomalies between X-ray and optical could be explained by microlensing. In this case we can directly estimate the size of the optical emission region as ∼ 10^4 R_g (see Equation 3.4) for a ∼10^8 $M_\odot$ black hole.

Finally, to determine if it is plausible to explain a factor of 9 demagnification using microlensing, we examined the microlensing simulations described by Schechter and Wambsganss [2002]. For a saddle-point image with a magnification of ∼20 such as image A, the probability of a demagnification a factor of 9 or greater ranges from virtually zero for a 100% stellar local projected mass density to nearly 17% for a mass density made of 10% stars and 90% smooth dark matter. We expect that at this distance from the galaxy's center, stars would make up about 15–30% of the projected mass, and so conclude that it is possible for microlensing to explain the X-ray anomaly.

3.4 Summary and conclusions

We have analyzed optical and X-ray images of the quadruple lens RX J1131−1231 and find anomalous flux ratios among the four images that are different in the optical than in the X-ray, with the more extreme anomalies being present in the X-ray band. In particular, the ratio F_A/F_B is a factor of 9.4 ± 1.7 smaller in the X-ray band that is predicted from the model image. The effects of microlensing in connection with anomalous flux ratios have been discussed extensively in the literature [see, e.g., Metcalf and Zhao, 2002, Mortonson et al., 2005]. Above, we discuss why we would nominally expect the microlensing of both the continuum optical and the X-ray images to be almost the same.

If the flux ratio anomaly differences between the X-ray and optical are ultimately resolved via microlensing, then we can turn the argument around and infer the approximate dimensions of the optical emission region [see, e.g., Mortonson et al., 2005]. First, we define $f \equiv L_{x+opt}/L_{Edd}$, where f is the fraction of the Eddington limiting luminosity that the X-ray plus optical luminosity represents. The parameter f incorporates the fact that L_{x+opt} ($\sim 5 \times 10^{44}$ ergs s^{-1}) is less than the bolometric luminosity which, in turn, is less than Eddington. The mass of the black hole can then be written as $(M_{BH} \simeq 2 \times 10^6 \ M_\odot)/f$. Equation 3.4 can then be recast as:

$$r_{opt} \simeq 10^3 R_g \left(\frac{f}{0.02} \right) \quad , \tag{3.6}$$

where r_{opt} is the size of the optical emission region, and we have taken $\xi \simeq 0.3$ in order to weaken the microlensing significantly [see, e.g., Schechter and Wambsganss, 2002, Mortonson et al., 2005], and $M_{ml} \simeq 1 \ M_\odot$.

This estimate of the size of the optical-emitting region is somewhat rough, but our methods of estimation will improve in the next few chapters.

Chapter 4

Chromatic anomalies II: PG 1115+080 in X-rays and optical

4.1 Introduction

PG 1115+080 is another example of a gravitationally lensed quasar with a flux ratio anomaly that is much stronger in X-rays than at optical wavelengths. It is the first quadruple lens discovered, and only the second overall [Weymann et al., 1980]. Its four images are in a fold configuration, which means that there is a universal relation in effect which requires the two bright merging images (the minimum A1 and the saddle point A2) to be roughly equal in brightness. Optical observations have shown non-trivial deviations from this rule, which have varied as a function of time (see Table 4.2, and references therein).

Concluding from this variability that microlensing is the cause of the low-level anomaly, Peeples et al. [2004] predict that the saddle-point image should have been demagnified by a factor of order 2 at some time within its 25-year history. But the quasar has thus far "declined to cooperate", in the words of PLS. In this chapter we report the discovery of this strong demagnification, not at optical wavelengths, but in X-rays. In Section 4.2 we describe the X-ray and optical observations and our analysis. In Section 4.3 we discuss implications for the lensing galaxy and (more to the point for this thesis) for the relative sizes of the quasar's X-ray and optical emitting regions. We summarize the results of this

chapter in Section 4.4.

This chapter is based on Pooley et al. [2006][1]. JAB wrote Sections 4.2.2 and 4.3.1, created Table 4.2 and Figure 4-4, and collaborated with DP and SAR in the writing of Sections 4.3.2, 4.3.4, and 4.4.

4.2 Observations and analysis

4.2.1 X-ray observations

PG 1115+080 was observed for 26.5 ks on 2000 Jun 02 (ObsID 363) and for 9.8 ks on 2000 Nov 03 (ObsID 1630) with ACIS aboard the *Chandra X-ray Observatory*. These observations were used by Grant et al. [2004] to study the X-ray properties of the lensing group of galaxies. The data were taken in timed-exposure mode with an integration time of 3.24 s per frame, and the telescope aimpoint was on the back-side illuminated S3 chip. The data were telemetered to the ground in faint mode.

The data were downloaded from the *Chandra* archive, and reduction was performed using the `CIAO 3.3` software provided by the *Chandra* X-ray Center[2]. The data were reprocessed using the CALDB 3.2.1 set of calibration files (gain maps, quantum efficiency, quantum efficiency uniformity, effective area) including a new bad pixel list made with the `acis_run_hotpix` tool. The reprocessing was done without including the pixel randomization that is added during standard processing. This omission slightly improves the point spread function. The data were filtered using the standard *ASCA* grades and excluding both bad pixels and software-flagged cosmic ray events. Intervals of strong background flaring were searched for, but none were found.

For each observation, an image was produced in the 0.5–8 keV band with a resolution of $0\rlap{.}''0246$ per pixel (see Figure 4-1). To determine the intensities of each lensed quasar image, a two-dimensional model consisting of four Gaussian components plus a constant background was fit to the data. The background component was fixed to a value determined from a source-free region near the lens. The relative positions of the Gaussian components

---

[1]Copyright 2006, The American Astronomical Society. Reprinted by permission.
[2]http://asc.harvard.edu

Table 4.1. X-ray and Model Flux Ratios of PG 1115+080

Ratio	ObsID 363	ObsID 1630	Model
A1/C	3.9 ± 0.3	4.3 ± 0.5	3.91
A2/C	0.6 ± 0.1	1.2 ± 0.3	3.73
B/C	1.0 ± 0.1	0.9 ± 0.1	0.67
A2/A1	0.16 ± 0.03	0.29 ± 0.08	0.96

were fixed to the separations determined from *HST* observations [Kristian et al., 1993], but the absolute position was allowed to vary. Each Gaussian was constrained to have the same full-width at half-maximum, but this value was allowed to float. The fits were performed in Sherpa [Freeman et al., 2001] using Cash statistics [Cash, 1979] and the Powell minimization method. The intensity ratios (relative to image C) are listed in Table 4.1. The best-fit full width at half-max (FWHM) was $0\rlap{.}''83 \pm 0\rlap{.}''01$ for ObsID 363 and $0\rlap{.}''80 \pm 0\rlap{.}''02$ for ObsID 1630; both consistent with the overall width of the instrumental PSF as found in the *Chandra* PSF Library [Karovska et al., 2001] supplied by the *Chandra* X-ray Center. In addition to the Gaussians, models of the form $f(r) = A[1 + (r/r_0)^2]^{-\alpha}$ were also tried; these gave similar results to the values in Table 4.1.

Based on the best fit Gaussian shape and the relative intensities, we constructed an idealized representation of the data. In Figure 4-1 we have plotted Gaussians of a common width (fwhm = $0\rlap{.}''22$), with the fitted intensities and at the fitted locations (see Table 4.1). We used the largest source width consistent (at 3σ confidence) with no blurring of the intrinsic *Chandra* PSF. A maximum likelihood deconvolution of the image is presented by Chartas et al. [2004a] and appears consistent with our "model" image.

Spectra of the quasar images were extracted using the ACIS Extract package v3.94 [Broos et al., 2002]. A single spectrum of A1 and A2 was extracted because of the significant overlap, but B and C were extracted separately. Both the *Chandra* effective area and PSF are functions of energy, and ACIS Extract corrected the effective area response for each spectrum based on the fraction of the PSF enclosed by the extraction region (at 1.5 keV, these fractions were 0.9 for A1+A2, 0.8 for B, and 0.9 for C). The spectra were grouped
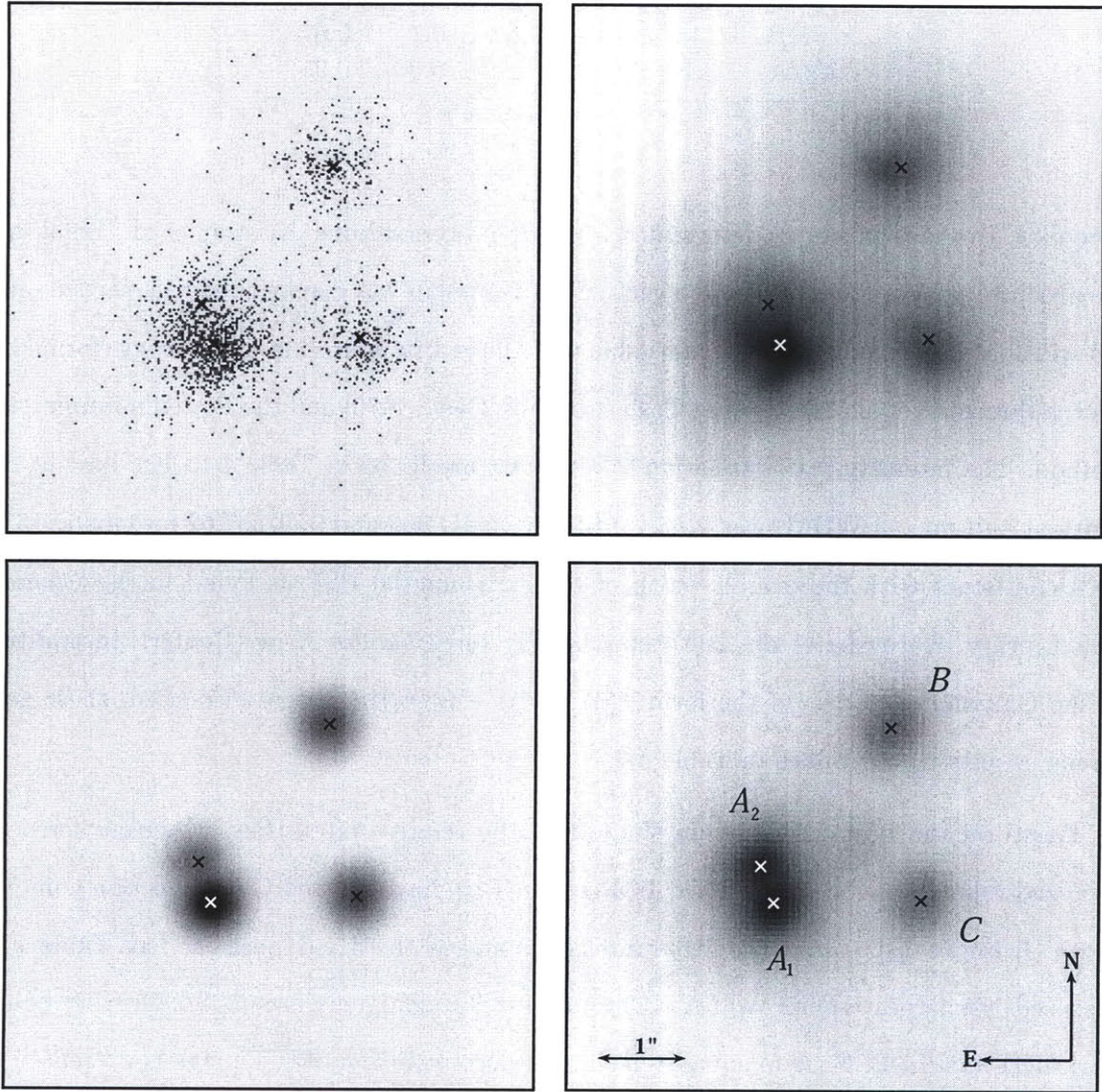
Figure 4-1 X-ray and optical images of PG 1115+080. Each image is $6'' \times 6''$. *Top left:* Raw *Chandra* data from ObsID 363 (2000 Jun 02) in the 0.5–8 keV band. *Top right:* Adaptively smoothed *Chandra* image. *Bottom left:* "Model" image based on fits to the raw *Chandra* data. *Bottom right:* Sloan i'-band Magellan image from 2005 Jun 07.
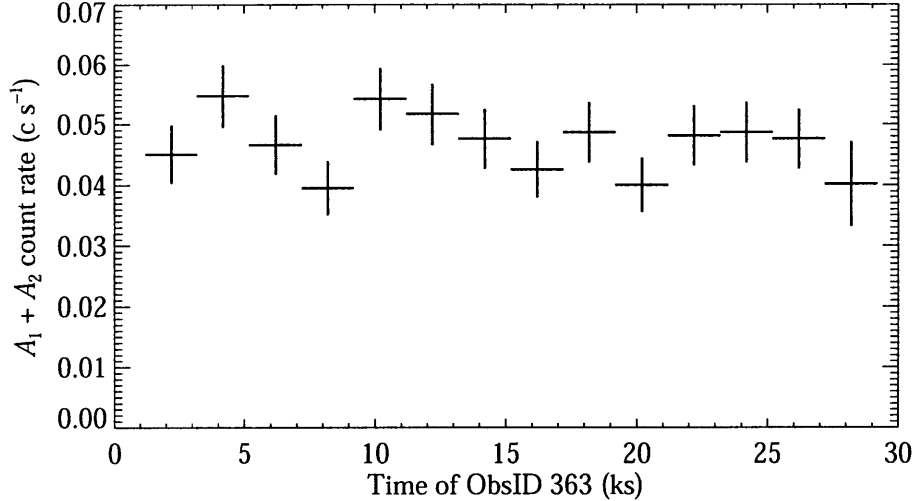
Figure 4-2 Light curve of the 0.5–8 keV count rate of A1+A2 in ObsID 363 showing a rather constant flux. Horizontal bars indicate the 2 ks time bins, and vertical bars show 1σ errors.

to contain at least ten counts per bin, and χ^2 fitting was performed in Sherpa using a simple absorbed power law model. The column density was fixed at the Galactic value of 3.56×10^{20} cm^{-2} [Dickey and Lockman, 1990]. The individual fits were all acceptable and yielded consistent results, so joint fits were performed with the power law indices tied to each other and the normalizations allowed to float. The best fit photon index for ObsID 363 is 1.57 ± 0.04 and for ObsID 1630 is 1.54 ± 0.07, which compares well with the values found from the fits of image C alone (1.55 ± 0.09 and 1.46 ± 0.08, respectively). Based on the individually fitted power laws, the unabsorbed 0.5–8 keV flux of image C is $(6.2 \pm 0.4) \times 10^{-14}$ erg cm^{-2} s^{-1} in ObsID 363 and $(6.9 \pm 0.9) \times 10^{-14}$ erg cm^{-2} s^{-1} in ObsID 1630. These serve as useful reference fluxes since image C is fairly uncontaminated by flux from the other images and is also a low-magnification minimum image and therefore less susceptible to microlensing fluctuations.

ACIS Extract was also used to obtain light curves from the above extraction regions for each observation. No significant signs of short-term variability were found within either observation; Kolmogorov-Smirnov tests showed that each light curve had a greater than 10% chance of being consistent with a constant count rate. The light curve for the A1+A2 region is plotted in Figure 4-2.

Given the time delays among the lensed images, it is fair to ask if intrinsic short-term

quasar variability combined with a time delay could masquerade as a genuine X-ray flux ratio anomaly. We can rule this out in the X-ray band for ObsID 363. The time delay between A1 and A2 from our lens model (see Section 4.3.1) is 14.5 ± 2 ks (with A1 leading). The 26.5 ks observation therefore covers 1.8 time delay cycles. If we split the observation into two equal parts, we obtain the same A1/A2 ratio as in Table 4.1. To produce this ratio as well as the constant A1+A2 lightcurve in Figure 4-2 purely by variability is highly implausible.

4.2.2 Optical observations

PG 1115+080 has been observed repeatedly with the Magellan 6.5-meter Baade and Clay telescopes at Las Campanas Observatory between 2001 March and 2006 February using MagIC. The instrument has a scale of $0\rlap{.}{''}0691$ per pixel and a 2.36 arcminute field. We present here results from three epochs for which the seeing was especially good, making the decomposition of A1 and A2 easier and less uncertain, and reducing the contamination from the lensing galaxy. Three 60-second exposures were obtained with a Johnson V filter on UT 2001 March 26. Two 60-second exposures each were obtained obtained with a Sloan i' filter on UT 2004 Feb 22 and 2005 June 07.

The data were flattened using standard procedures. ClumpFit, an empirical PSF-fitting photometry program based on DoPHOT, was used to measure fluxes and positions for the four quasar images and for the lensing galaxy. The profile for the galaxy was taken to be an elliptical pseudo-Gaussian. As we presently concern ourselves only with flux ratios, we have not put our photometry onto a standard system. The fluxes for the A1, A2 and B images are given relative to the C image, for which the microlensing fluctuations are expected to be smallest. It should be remembered that variations of 0.1 mag have been seen on a timescale of weeks and that image C leads the A images and the B image by 10 and 25 days, respectively [Schechter et al., 1997, Barkana, 1997]. The results of our photometry are given in Table 4.2, along with selected results (typically those obtained in the best seeing) from prior epochs.

We note that the flux ratios for contemporaneous observations appear to be consistent to within a few percent over the optical wavelength region. We therefore make no attempt

Table 4.2. Optical Photometry and Flux Ratios of PG 1115+080

| | | | Magnitude differences | | | Flux ratios |
UT date	Filter	FWHM	A−C	A2−C	B−C	A2/A1
1984 Mar 26[a]	B	0″.75	−1.26	−1.21	0.41	0.95 ± 0.07
1985 Mar 19[a]	V	0″.62	−1.18	−0.83	0.49	0.73 ± 0.04
1986 Feb 19[b]	V	0″.6	−1.27	−0.99	0.48	0.77 ± 0.03
1986 Feb 19[b]	B	0″.6	−1.23	−0.97	0.48	0.79 ± 0.03
1991 Mar 03[c]	F785LP	*HST*	−1.46	−1.07	0.50	0.70 ± 0.01
1991 Mar 03[c]	F555W	*HST*	−1.47	−1.02	0.50	0.66 ± 0.01
1995 Dec 20[d,e]	V	0″.85	−1.50	−1.04	0.47	0.66 ± 0.01
2001 Mar 26[e]	V	0″.56	−1.48	−1.04	0.42	0.68 ± 0.01
2004 Feb 22[e]	*i′*	0″.48	−1.40	−1.18	0.42	0.81 ± 0.01
2005 Jun 07[e]	*i′*	0″.43	−1.40	−1.19	0.42	0.81 ± 0.01
Lens Model	⋯	⋯	−1.48	−1.43	0.44	0.96

[a]Vanderriest et al. [1986]

[b]Christian et al. [1987]

[c]Kristian et al. [1993]

[d]Schechter et al. [1997]

[e]present work

to account for bandpass in presenting the present and past optical results.

4.3 Discussion

4.3.1 Modeling the lens

Using the Lensmodel software of Keeton [2001], we modeled the lensing potential as a singular isothermal sphere accompanied by a second, offset singular isothermal sphere, which provides a quadrupole moment. This choice of model was motivated by the presence of a group of galaxies to the southwest of the lensing galaxy. We used the image positions provided by the CASTLES lens survey[3] [Muñoz et al., 1998], and did not constrain the fluxes. Our best-fit model predicts an Einstein radius of 1″.0 for the primary lensing galaxy,

---

[3]http://www.cfa.harvard.edu/castles/

with a second mass having an Einstein radius of $2\rlap{.}''6$ located $12\rlap{.}''5$ away at a position angle 116° west of north. This places it close to the observed location of the associated group of galaxies. The model yields a total reduced χ^2 of 3, with the greatest contribution coming from the position of the primary lensing galaxy. The flux ratios predicted by this model are listed in Tables 4.1 and 4.2, and may be expected to vary between different plausible models of the lens on the few percent level.

4.3.2 Anomalous flux ratios and microlensing

Simple smooth analytic models [Metcalf and Zhao, 2002] predict that the A2/A1 flux ratio should be very nearly equal to unity. For our lens model, the ratio is 0.96. Chiba et al. [2005] observe a mid-infrared flux ratio of 0.93 ± 0.06, consistent with this prediction. In 1984, Vanderriest et al. [1986] measured a flux ratio of 0.95 ± 0.07, but since then, as seen in Table 4.2, the optical flux ratio has varied on a timescale of years between 0.66 and 0.81. As noted in Section 4.2.1, the contemporaneous X-ray flux ratio is less than 0.2, inconsistent not only with the predictions of the smooth models, but with the optical observations as well.

Microlensing by stars in the lensing galaxy could in principle account for such flux ratios, but only if the X-ray source is small compared to the Einstein radii of the microlensing stars. Our simple model has convergence, κ, and shear, γ, roughly equal at the image positions, with magnifications μ of $+19.9$ for the A1 image and -19.0 for the A2 image. Examples of point source magnification histograms for pairs of images very much like those in PG 1115+080 are presented by Schechter and Wambsganss [2002], with magnifications for A1 and A2 of 10 and 16, respectively. They present histograms both for the case when 100% of the convergence is due to stars and for the case when only 20% of the convergence is due to stars and the rest is due to a smooth dark component. The X-ray flux ratio rules out neither hypothesis but is considerably more likely if dark matter is present.

Until now, it was a bit of a puzzle why the optical flux anomalies had failed to deviate from unity as much as was predicted by these histograms. Now it appears that it was because the optical region is too large to be strongly microlensed (see Section 4.3.4). As Schechter and Wambsganss [2004] note, the determination of the dark matter fraction of
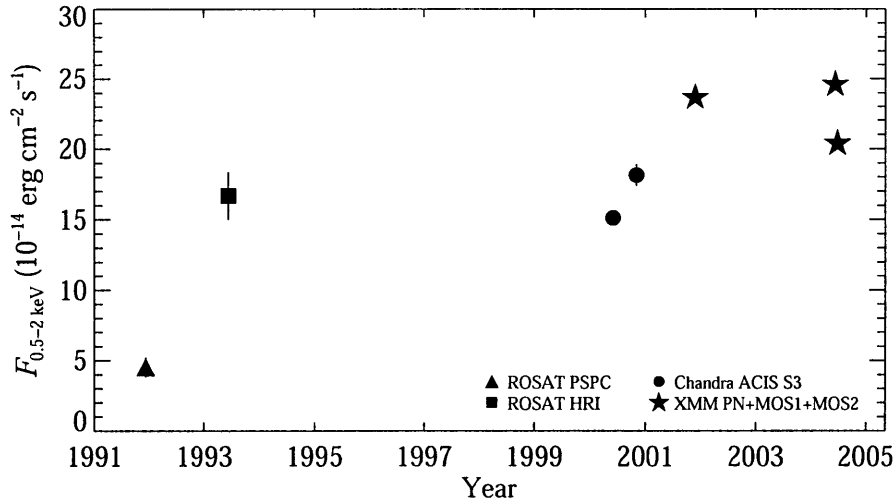
Figure 4-3 Long-term X-ray light curve of PG 1115+080 showing the combined flux of all four images. For most observations, the plotted error bars are smaller than the plotting symbols.

lensing galaxies using the statistics of flux ratio anomalies is made considerably more difficult if the source size is comparable to that of a stellar Einstein ring. It seems now that the X-ray flux ratio anomalies offer a cleaner determination of the dark matter fraction than the optical anomalies.

4.3.3 Long-term X-ray variability

According to the microlensing model for flux-ratio anomalies, discussed below, A2 is expected to brighten in X-rays on a timescale of $\sim$10 years. A follow-up study has confirmed this prediction [Pooley et al., 2009]. As A2 brightens, the unresolved flux also increases. To look for past signs of this effect, we searched the High Energy Astrophysics Science Archive Research Center, provided by NASA's Goddard Space Flight Center, for other X-ray observations of PG 1115+080 and found two *ROSAT* observations and three relevant *XMM-Newton* observations. The *ROSAT* observations and an earlier *Einstein* observation are analyzed by Chartas [2000].

The *ROSAT* count rates were converted to unabsorbed 0.5–2 keV fluxes using WebPIMMS [Mukai, 1993] with the assumptions of an absorbed power law of photon index 1.65 and a column density of 3.56×10^{20} cm^{-2}. For the *XMM* observations, we extracted spectra of

PG 1115+080 from the EPIC-PN and both EPIC-MOS detectors. We performed joint spectral fits (on all quasar images added together) in the 0.5–10 keV band for each observation with simple absorbed power laws with the column density fixed at the Galactic value. These gave acceptable fits, from which we computed the unabsorbed 0.5–2 keV fluxes. We also used our previous *Chandra* joint fits to compute the total 0.5–2 keV fluxes (from all quasar images added together) from the *Chandra* observations. The long-term X-ray light curve is shown in Figure 4-3.

From the seven measurements of the lensed flux from PG 1115+080 over the course of 12.5 years, the mean is 1.75×10^{-13} erg cm^{-2} s^{-1}, and the sample standard deviation is 6.7×10^{-14} erg cm^{-2} s^{-1}, or $\sim$40%. There is no evidence for strong short term variability from the individual lensed images in the *Chandra* data, nor is there evidence for strong short term variability within the three *XMM* observations (in which the individual images are unresolved).

As discussed above, if the demagnification of A2 is due to microlensing, the unresolved flux will rise as A2 becomes less demagnified. The observed relative X-ray fluxes of the four images A1:A2:B:C are $1 : 0.16 : 0.25 : 0.25$ (based on ObsID 363; see Table 4.1). If A2 were to rise in flux to match A1, the overall change in flux would be $\sim$50%. The recent *XMM* observations show that the X-ray flux has risen $\sim$30% since the *Chandra* observations from six years ago (Figure 4-3). However, there is an obvious degeneracy between a rise in the flux of A2 and typical quasar variability over the course of many years.

4.3.4 Sizes of quasar emission regions

The size scales of the emission regions in quasars are difficult to probe directly since they are on the microarcsecond scale or smaller. The use of reverberation methods for inferring sizes is so far limited to emission line regions, and becomes impractical for distant quasars. By contrast, microlensing directly explores angular scales of (by definition) microarcseconds and works for very distant quasars. Of the emission features of the quasar, only those which subtend smaller angles on the sky than the Einstein radius of the microlenses will exhibit strong variations in flux.

Figure 4-4 demonstrates the predictions of the standard thin disk theory for PG 1115+080.

Here we have plotted the ratio of expected angular scale for different regions of the quasar, θ_s, to the Einstein radius of a solar-mass microlens, θ_{Ein}. For ratios greater than unity, microlensing should be strongly suppressed [for a detailed analysis see Mortonson et al., 2005]. The ratio $\theta_s/\theta_{\mathrm{Ein}}$ is plotted against the assumed mass of the central black hole, M_{BH}. For every value of M_{BH} there is a corresponding Eddington luminosity which can be compared to the observed values of L_x (2.4×10^{44} erg cm^{-2} s^{-1}; 0.5–8 keV; this work) and L_{opt} (1.2×10^{45} erg cm^{-2} s^{-1}, from a sum of the V, I, awnd H band data provided by the CASTLES lens survey) for PG 1115+080 (see the top axis label). Within the $\theta_s/\theta_{\mathrm{Ein}}$ vs. M_{BH} plane we plot contours of constant size in units of R_g, the gravitational radius of the black hole (GM_{BH}/c^2). As is evident from the plot, the X-rays, which should arise deep in the gravitational potential well of the black hole, should be microlensed for any $M_{\mathrm{BH}} \lesssim 10^{10}\,M_\odot$. This is in clear agreement with the large X-ray flux ratio anomalies observed for PG 1115+080 and for two other quad lenses: RX J0911+0551 and RX J1131−1231 [Morgan et al., 2001, Blackburne et al., 2006]. By contrast, the broad-line emission region should not be microlensed, except for a lower mass black hole (i.e., $M_{\mathrm{BH}} \lesssim 3 \times 10^7\,M_\odot$). Finally, the dotted and dashed curves mark the radii within which 50% of the power in the I and V bands emerge, respectively, for a simple thin accretion disk model [e.g. Shakura and Sunyaev, 1973]. According to these curves, the optical continuum ought to be microlensed by approximately the same amount as in the X-ray band, in agreement with Mortonson et al. [2005]. But clearly it is not!

Using *HST* spectra, Popović and Chartas [2005] found that the A2/A1 ratio in the ultraviolet continuum is ~0.5 and decreases to shorter wavelengths, indicating that the UV is more severely microlensed than the optical but less microlensed than the X-rays.

Therefore, within the microlensing scenario, we can conclude that the continuum optical emission from PG 1115+080 comes from much further out than the UV, which in turn comes from further out than the X-rays. In particular, we find that the optical emission comes from a region ~3–30 times larger than expected for a thin accretion disk model (for M_{BH} in the range $3 \times 10^9 \rightarrow 10^8\,M_\odot$ and $\theta_s \sim \theta_{\mathrm{Ein}}/3$). Since L_{opt} dominates L_x in PG 1115+080 (and for many other luminous quasars), this is difficult to understand from an energetics point of view, since the energy released goes as r^{-1}. Of course the optical light could be scattered
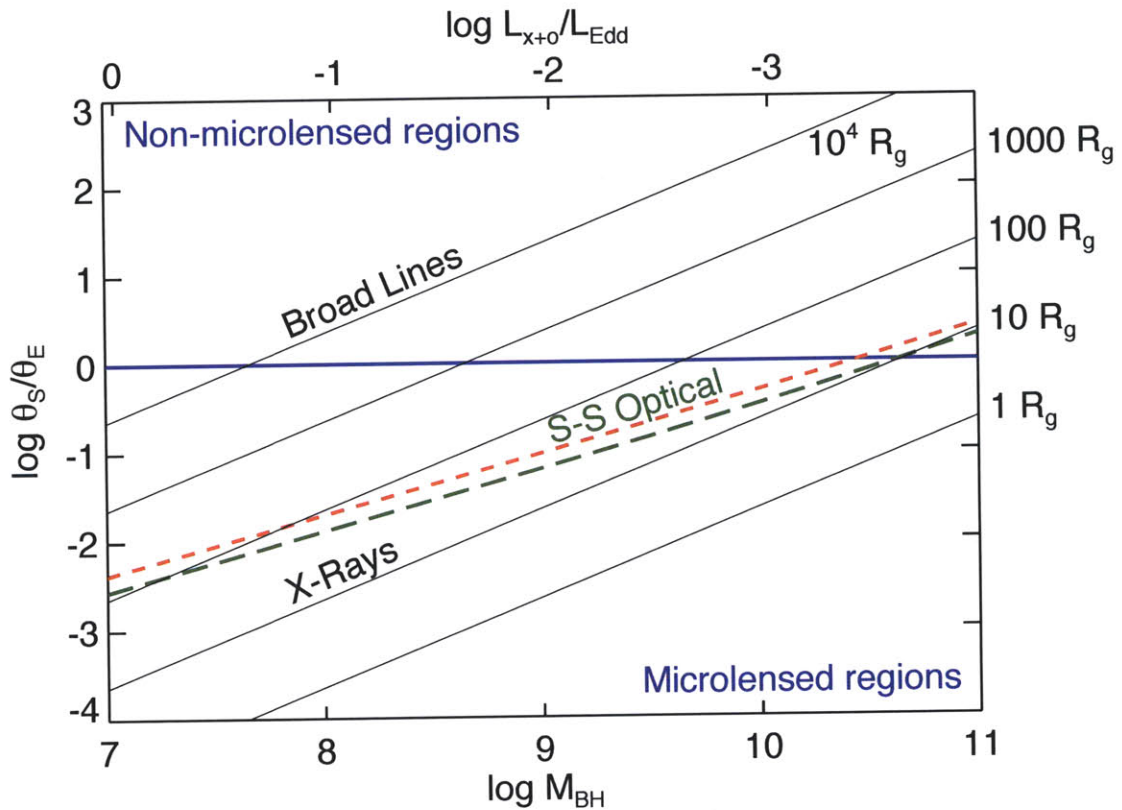
Figure 4-4 Predicted source sizes at X-ray and optical wavelengths for PG 1115+080. The blue line represents the rough boundary between regions large enough to avoid microlensing and smaller microlensed regions. The gray lines show constant size in units of gravitational radii. The expected emission regions for X-rays and broad emission lines are marked. The dashed lines denotes the prediction of the thin disk model for the half-light radius of the source in I (red) and V (green) bands. The top axis compares the measured X-ray plus optical luminosity of PG 1115+080 to the Eddington luminosity implied by the black hole mass. Both X-rays and optical disk emission are predicted to be strongly microlensed for a wide range of black hole masses.

by a large-scale plasma region; however, in that case one would expect the X-rays to be scattered as well, and hence share a similar effective emission region. Thus, while the X-ray images clearly appear to be microlensed, the bulk of the optical emission must be coming from $\sim$100–1000 R_g from the central black hole (for M_{BH} in the range $3 \times 10^9 \rightarrow 10^8 M_\odot$).

In coming to these conclusions, we have neglected special- and general-relativistic effects in the emissions from the accretion disk, except for cosmological redshift. In addition, we have followed Mortonson et al. [2005] in assuming a Kerr black hole with a large spin parameter ($a = 0.88$). This is consistent with estimates for a typical quasar [Wang et al., 2006], and implies an innermost disk radius of $2.5R_g$ and a binding energy per mass $\eta = 0.146$. We have also set the bolometric luminosity to 33% of the Eddington luminosity, as advocated by Kollmeier et al. [2006]. Neither of these parameter assumptions has a strong effect on the size of the predicted optical emission region for a thin accretion disk model.

4.4 Conclusions

We have made use of optical data collected over the past 22 years to demonstrate that the bright, close pair of lensed images of PG 1115+080 has a consistent flux ratio (A2/A1) of $\sim$0.7–0.8. X-ray observations with *Chandra*, covering two epochs separated by 5 months, indicate a much more extreme flux ratio of $\sim$0.2. Both the optical and X-ray ratios are anomalous with respect to smooth lensing models, which predict a flux ratio of 0.96. Flux ratios in the near-IR, on the other hand, match the models very well, confirming that microlensing is causing the anomalies. We used a comparison of the optical and X-ray flux ratio anomalies to show that the optical emission region is much larger (i.e., $\sim3 - 30$) than predicted by a simple thin accretion disk model.

Chapter 5

X-ray and optical anomalies in 10 lenses: Large accretion disks

5.1 Introduction

In Chapters 3 and 4 we reported very strong X-ray flux ratio anomalies in two gravitationally lensed quasars, RX J1131−1231 and PG 1115+080. We argued that microlensing was the cause of these anomalies, and that optical observations showed weaker anomalies because of the finite extent of the optical emission region. In this chapter, we carry out a systematic, uniform study of ten quadruply lensed quasars for which both optical and *Chandra* data exist, including those in the previous two chapters. The ten lensed quasars are HE 0230−2130 [Wisotzki et al., 1999], MG J0414+0534 [Hewitt et al., 1992], RX J0911+0551 [Bade et al., 1997], SDSS J0924+0219 [Inada et al., 2003a], PG 1115+080 [Weymann et al., 1980], RX J1131−1231 [Sluse et al., 2003], H 1413+117 [Magain et al., 1988], B 1422+231 [Patnaik et al., 1992], WFI J2033−4723 [Morgan et al., 2004], and Q 2237+0305 [Huchra et al., 1985].

The X-ray data are taken from the *Chandra* archive. In three cases — MG J0414+0534 [Chartas et al., 2002], H 1413+117 [Chartas et al., 2004b], and Q 2237+0305 [Dai et al., 2003] — microlensing has been invoked to explain the observed X-ray properties. In this chapter (and this thesis) we use a different approach, using the X-rays as a means to explore

the size of the optical emission regions.

In Sections 5.2 and 5.3 we describe our analysis of the X-ray and optical data, and construct simple lens models for the sample of lenses. In Section 5.4 we find that in general the X-ray flux ratios have stronger disagreements with the models than the optical ratios do, implying that the X-rays come from a more compact region than the optical. We compare the implied optical sizes to those predicted by the standard thin disk model [Shakura and Sunyaev, 1973] in Section 5.5 and find that the disks appear to be larger than the models predict by factors of $\sim 3 - 30$. We summarize our findings in Section 5.6.

This chapter is based on Pooley et al. [2007][1]. JAB wrote Section 5.3, created Tables 5.3, 5.4, and 5.6 and Figures 5-4 and 5-6, and collaborated heavily in the analysis described in Sections 5.4 through 5.6.

5.2 X-ray observations

The data were downloaded from the *Chandra* archive, and reduction was performed using the CIAO 3.3 software provided by the *Chandra* X-ray Center[2]. The data were reprocessed using the CALDB 3.2.2 set of calibration files (gain maps, quantum efficiency, quantum efficiency uniformity, effective area) including a new bad pixel list made with the acis_run_hotpix tool. The reprocessing was done without including the pixel randomization that is added during standard processing. This omission slightly improves the PSF. The data were filtered using the standard *ASCA* grades and excluding both bad pixels and software-flagged cosmic ray events. Intervals of strong background flaring were searched for, and a few were found. In all cases, the flares were mild enough that removing the intervals would have decreased the signal-to-noise of the quasar images since it would have removed substantially more source flux than background flux within the small extraction regions. Therefore, we did not remove any flaring intervals. The observation IDs, dates of observation, and exposure times are given in Table 5.1.

---

[1]Copyright 2007, The American Astronomical Society. Reprinted by permission.
[2]http://asc.harvard.edu

Table 5.1. X-ray fluxes and flux ratios for 10 lenses

Lensed Quasar			Image Flux Ratios[b]				LM unabs. $F_{0.5-8\,\mathrm{keV}}$[c]
ObsID[a]	Date	Exp. (s)	HS/HM	HS/LM	HM/LM	LS/LM	(10^{-14} erg cm^{-2} s^{-1})
HE 0230−2130			B/A	B/C	A/C	D/C	F_C
1642	2000 Oct 14.4	14 764	$0.44^{+0.08}_{-0.07}$	$0.70^{+0.13}_{-0.12}$	$1.6^{+0.2}_{-0.2}$	$0.45^{+0.08}_{-0.07}$	$5.9^{+2.8}_{-2.0}$
MG J0414+0534			A_2/A_1	A_2/B	A_1/B	C/B	F_B
417	2000 Jan 13.7	6 578	$0.82^{+0.18}_{-0.15}$	$1.9^{+0.4}_{-0.4}$	$2.3^{+0.5}_{-0.4}$	$0.25^{+0.07}_{-0.06}$	12^{+7}_{-5}
418	2000 Apr 2.9	7 437	$0.50^{+0.11}_{-0.10}$	$1.3^{+0.3}_{-0.3}$	$2.6^{+0.4}_{-0.4}$	$0.63^{+0.11}_{-0.10}$	13^{+6}_{-4}
421	2000 Aug 16.9	7 251	$0.38^{+0.12}_{-0.10}$	$0.96^{+0.38}_{-0.33}$	$2.5^{+0.5}_{-0.4}$	$0.45^{+0.09}_{-0.07}$	15^{+6}_{-5}
422	2000 Nov 16.6	7 504	$0.67^{+0.13}_{-0.12}$	$1.8^{+0.4}_{-0.4}$	$2.6^{+0.5}_{-0.4}$	$0.65^{+0.11}_{-0.10}$	14^{+9}_{-5}
1628	2001 Feb 5.1	9 020	$0.35^{+0.09}_{-0.08}$	$0.89^{+0.28}_{-0.24}$	$2.5^{+0.4}_{-0.3}$	$0.35^{+0.06}_{-0.05}$	16^{+7}_{-5}
3395	2001 Nov 9.3	28 413	$0.90^{+0.09}_{-0.08}$	$1.8^{+0.2}_{-0.2}$	$1.9^{+0.2}_{-0.2}$	$0.53^{+0.05}_{-0.05}$	13^{+3}_{-3}
3419	2002 Jan 9.0	96 664	$0.61^{+0.04}_{-0.04}$	$1.3^{+0.1}_{-0.1}$	$2.1^{+0.1}_{-0.1}$	$0.42^{+0.02}_{-0.02}$	14^{+4}_{-3}
RX J0911+0551			A/B	A/D	B/D	C/D	F_D
419	1999 Nov 2.7	28 795	$2.7^{+1.3}_{-0.8}$	$3.4^{+0.6}_{-0.5}$	$1.3^{+0.4}_{-0.4}$	$0.35^{+0.13}_{-0.11}$	$1.9^{+0.8}_{-0.6}$
1629	2000 Oct 29.8	9 826	27^{+500}_{-27}	$4.6^{+1.6}_{-1.3}$	$0.17^{+0.90}_{-0.73}$	$0.72^{+0.39}_{-0.28}$	$1.8^{+0.5}_{-0.4}$
SDSS J0924+0219			D/A	D/B	A/B	C/B	F_B
5604	2005 Feb 24.0	17 944	$0.14^{+0.07}_{-0.06}$	$0.45^{+0.25}_{-0.19}$	$3.2^{+0.8}_{-0.6}$	$0.42^{+0.19}_{-0.14}$	$1.2^{+0.8}_{-0.5}$
PG 1115+080			A_2/A_1	A_2/C	A_1/C	B/C	F_C
363	2000 Jun 2.8	26 492	$0.16^{+0.03}_{-0.03}$	$0.62^{+0.13}_{-0.12}$	$3.9^{+0.3}_{-0.3}$	$1.1^{+0.1}_{-0.1}$	$6.8^{+1.1}_{-1.0}$
1630	2000 Nov 3.3	9 826	$0.28^{+0.06}_{-0.06}$	$1.2^{+0.3}_{-0.3}$	$4.4^{+0.6}_{-0.5}$	$1.0^{+0.2}_{-0.1}$	$8.3^{+2.9}_{-2.4}$

Table 5.1

Lensed Quasar			Image Flux Ratios[b]				LM unabs. $F_{0.5-8\,\mathrm{keV}}$[c]
ObsID[a]	Date	Exp. (s)	HS/HM	HS/LM	HM/LM	LS/LM	(10^{-14} erg cm^{-2} s^{-1})
RX J1131$-$1231			A/B	A/C	B/C	D/C	F_C
4814	2004 Apr 12.2	10 047	$0.10^{+0.01}_{-0.01}$	$0.22^{+0.03}_{-0.02}$	$2.2^{+0.1}_{-0.1}$	$0.30^{+0.03}_{-0.02}$	50^{+5}_{-5}
H 1413$+$117			A/B	A/C	B/C	D/C	F_C
930	2000 Apr 19.7	38 185	$1.8^{+0.5}_{-0.4}$	$4.0^{+1.4}_{-0.9}$	$2.2^{+0.9}_{-0.6}$	$1.2^{+0.5}_{-0.3}$	$2.7^{+0.7}_{-0.6}$
5645	2005 Mar 30.1	88 863	$1.7^{+0.6}_{-0.4}$	$1.5^{+0.3}_{-0.2}$	$0.9^{+0.3}_{-0.2}$	$0.7^{+0.2}_{-0.2}$	$3.3^{+0.5}_{-0.5}$
B 1422$+$231			B/A	B/C	A/C	D/C	F_C
367	2000 Jun 1.6	28 429	$0.68^{+0.06}_{-0.05}$	$1.1^{+0.1}_{-0.1}$	$1.6^{+0.1}_{-0.1}$	$0.11^{+0.01}_{-0.01}$	37^{+6}_{-5}
1631	2001 May 21.5	10 651	$0.62^{+0.09}_{-0.08}$	$0.87^{+0.13}_{-0.12}$	$1.4^{+0.2}_{-0.2}$	$0.08^{+0.02}_{-0.02}$	40^{+12}_{-10}
4939	2004 Dec 1.6	47 729	$0.55^{+0.04}_{-0.04}$	$0.95^{+0.08}_{-0.07}$	$1.7^{+0.1}_{-0.1}$	$0.10^{+0.01}_{-0.01}$	33^{+5}_{-5}
WFI J2033$-$4723			A_2/A_1	A_2/B	A_1/B	C/B	F_B
5603	2005 Mar 10.1	15 420	$1.1^{+0.3}_{-0.2}$	$1.0^{+0.2}_{-0.2}$	$0.87^{+0.16}_{-0.14}$	$0.64^{+0.11}_{-0.10}$	$3.5^{+0.9}_{-0.8}$
Q 2237$+$0305			D/A	D/B	A/B	C/B	F_B
431	2000 Sep 6.7	30 287	$0.17^{+0.01}_{-0.01}$	$0.85^{+0.09}_{-0.08}$	$5.0^{+0.4}_{-0.3}$	$2.1^{+0.2}_{-0.2}$	$5.9^{+1.3}_{-1.1}$
1632	2001 Dec 8.8	9 538	$0.20^{+0.03}_{-0.03}$	$0.95^{+0.20}_{-0.17}$	$4.7^{+0.7}_{-0.6}$	$1.7^{+0.3}_{-0.3}$	$6.1^{+3.7}_{-2.6}$

[a]The observation identifier of the *Chandra* dataset.

[b]HS = Highly magnified Saddle point; HM = Highly magnified Minimum; LS = Less magnified Saddle point; LM = Less magnified Minimum. See Section 5.4.

[c]The unabsorbed flux of the LM image is computed from the best fit power-law model described in Section 5.2.1.

Table 5.2. Comparison of gaussian fitting to aperture extraction of SDSS 1004+4112

| Method | X-ray Image Flux Ratios | | | |
	A/B	A/C	B/C	D/C
Gaussian fit	$0.77^{+0.03}_{-0.02}$	$0.96^{+0.04}_{-0.04}$	$1.24^{+0.05}_{-0.04}$	$0.57^{+0.03}_{-0.03}$
Extraction	$0.77^{+0.03}_{-0.03}$	$0.93^{+0.04}_{-0.04}$	$1.20^{+0.05}_{-0.05}$	$0.55^{+0.03}_{-0.03}$

5.2.1 Determining X-ray flux ratios

For each observation, a sky image was produced in the 0.5–8 keV band with a sampling of $0\rlap{.}''0246$ per pixel. Because of the significant overlap of the lensed images (especially the close image pairs) in many cases, the intensities were determined by fitting to each sky image a two-dimensional model consisting of four Gaussian components plus a constant background. The background component was fixed to a value determined from a source-free region near the lens. The relative positions of the Gaussian components were fixed to the separations given in the CASTLES online database, but the absolute position was allowed to vary. Each Gaussian was constrained to have the same full-width at half-maximum (FWHM), but this value was allowed to float. The fits were performed using Cash [1979] statistics and the Powell minimization method in Sherpa [Freeman et al., 2001].

From the best fit 4-Gaussian model, the image flux ratios were calculated for the high magnification pair (saddle point and minimum; HS & HM, respectively) as well as for each image relative to the less magnified minimum (LM) image. The uncertainties on these ratios were determined with Sherpa via the `projection` command, which varies each ratio in turn along a grid of values while all other parameters are allowed to float to the new best-fit values. The results are given in Table 5.1.

Because the *Chandra* PSF is only approximately described by a Gaussian, we sought to test this method by utilizing a *Chandra* observation (ObsID 5794) of the large-separation quad SDSS 1004+4112, for which all four images are well separated[3]. We extracted counts from the 90% encircled energy region of each image, as determined by ACIS Extract v3.94

---

[3]SDSS 1004+4112 [Inada et al., 2003b] is lensed by a dark matter-dominated cluster of galaxies, and is unique enough that we did not include it in our sample of lenses.

[Broos et al., 2002], and formed a number of flux ratios. We also followed the above method of fitting Gaussians. The agreement in flux ratios is excellent (see Table 5.2).

Finally, a spectrum of the LM image was extracted for each observation with ACIS Extract and fit in Sherpa via a simple absorbed power law. The absorption consisted of a fixed Galactic component [Dickey and Lockman, 1990] plus a variable component. This simple model provided an acceptable fit in all cases, and the additional absorption component was usually consistent with zero. The 0.5–8 keV flux of the unabsorbed power law is given in Table 5.1.

5.2.2 X-ray variability

As the numbers in Table 5.1 indicate, many of the flux ratios vary to some degree for the quads that have been observed multiple times. This may be due to varying degrees of microlensing or to normal quasar variability combined with time delays among the images. In fact, variability plus a time delay could masquerade as a flux ratio anomaly. Figure 5-1 shows the X-ray lightcurves of the sum of the high magnification pair of images for each system, which are seen to be fairly constant in all systems; only small amplitude (factor of two or less) variability is observed, even in cases when the length of the observation exceeds the predicted time delay between the brightest images[4].

For the rest of the analysis, we utilized the observation with the highest signal to noise ratio for the quads observed multiple times by *Chandra*. We chose not to average over multiple epochs in order to avoid averaging out variations due to changes in microlensing. We use ObsID 3419 for MG J0414+0534, ObsID 419 for RX J0911+0551, ObsID 363 for PG 1115+080, ObsID 5645 for H 1413+117, ObsID 4939 for B 1422+231, and ObsID 431 for Q 2237+0305.

---

[4]Predictions of time delays are subject to large uncertainties, especially for pairs of images with small separations. Indeed, the time delay for RX J1131−1231 is now known to be greater than predicted by a factor of ~ 12 [Morgan et al., 2006]. This is mitigated by the fact that the optical and X-ray observations for this particular source were made on the same day.
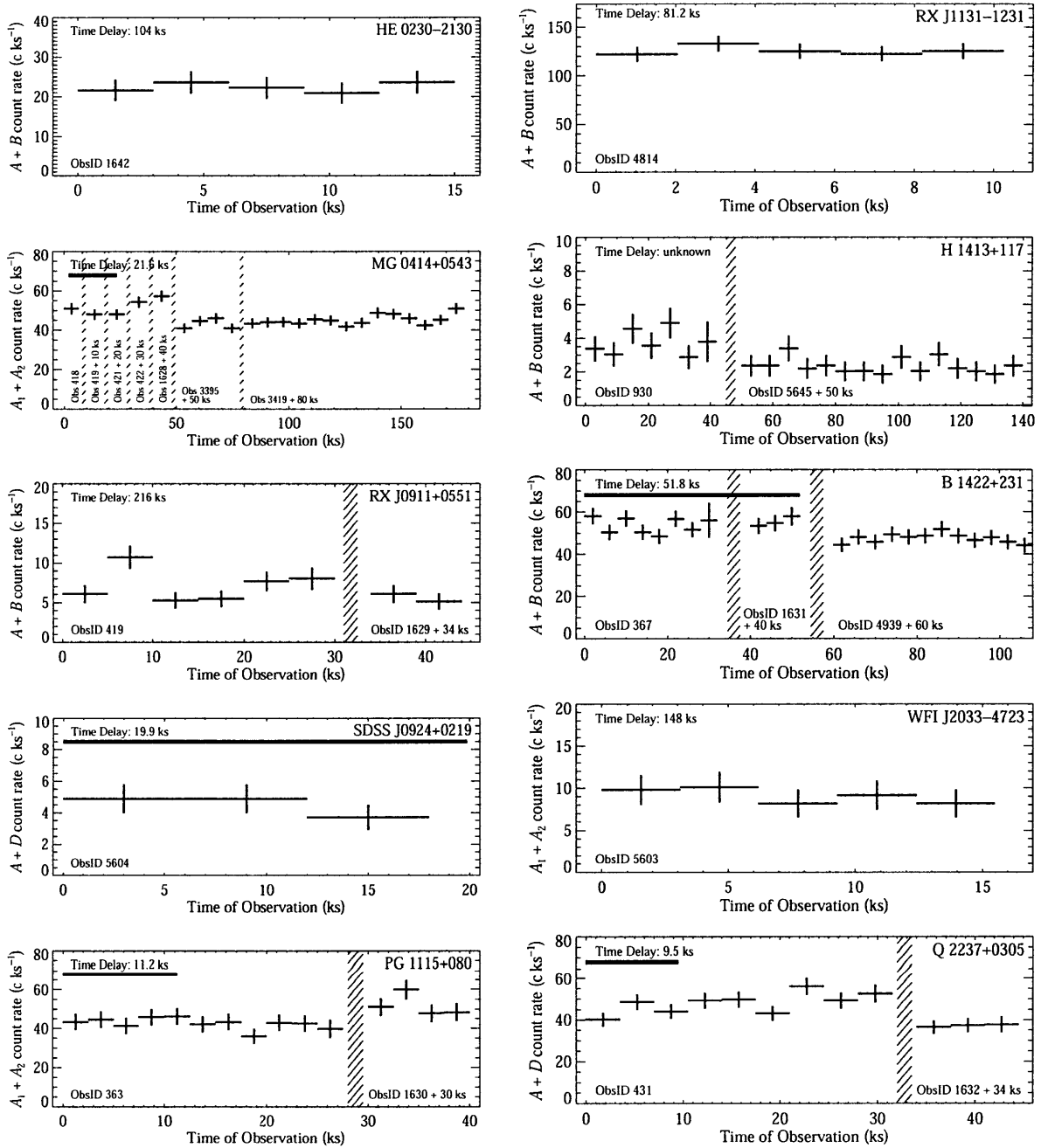
Figure 5-1 X-ray lightcurves of the high magnification pair of images in each quad. All observations in Table 5.1 were used to make these 0.5–8 keV lightcurves, with multiple observations of the same quad separated by hash marks. The time delay between the pair (from the models described in Section 5.3 and Table 5.4) is given and shown as a thick horizontal bar in the cases where it will fit on the plots.

5.3 Optical images and lens models

We turned to the existing literature for optical data with which to compare our X-ray flux ratios. For each lens, we used data near 8000 Å, either Sloan i', Cousins I, or *HST* F814W. An effort was made to choose the observations closest in time to the deepest *Chandra* observation. The dates of the observations, along with the optical bandpasses and the image magnitudes, may be found in Table 5.3. The images are arranged according to their magnifications and parity (see Section 5.4).

Under ideal circumstances, the X-ray and optical observations would have been made on the same day, in order to minimize systematic errors resulting from quasar variability and microlensing variability. But for most of these lenses, such contemporaneous observations have not been made. Three lenses have X-ray and optical observations separated by about 6 to 10 years, three by 2 to 4 years, and four by 15 months or less. One of these, RX J1131−1231, was observed in both bands on the same day [Sluse et al., 2006].

These delays between observations can add systematic uncertainty to the results. However, there are reasons to believe that their effect is not a strong one. The general lack of strong quasar variability seen in X-rays (see Section 5.2.2), coupled with the limited success of campaigns to measure lens time delays (which rely on quasar variability), suggest that quasars do not often vary by the factors that would be required to explain the flux ratio anomalies. The fact that RX J1131−1231 has an extremely strong discrepancy between X-ray and optical flux ratios despite simultaneous observations in both bands shows that time variability cannot fully explain the anomalous ratios.

We used the `Lensmodel` software of Keeton [2001], v1.06, to model each of the ten lenses as a singular isothermal sphere (SIS) with an external shear. This model has seven free parameters (lens strength, shear strength (γ) and direction (ϕ_γ), and the positions of source and lens), making it overconstrained by the ten input measurements (the positions of four images and the lensing galaxy). The position measurements were obtained from the online CASTLES database. The observed fluxes of the lens images were not used as constraints.

The models fit the image positions fairly well in all cases except that of HE 0230−2130, where the position of the D image is significantly altered by a second galaxy. Since this

Table 5.3. Optical photometry for 10 lenses

| Lensed Quasar | Optical magnitudes | | | | |
Obs. date	HS	HM	LS	LM	Filter
HE 0230−2130	B	A	D	C	
2002 Jul 29	19.22	19.02	21.21	19.59	F814W[a]
MG J0414+0534	A_2	A_1	C	B	
1994 Nov 08	21.36	20.43	22.10	21.24	F814W[a]
RX J0911+0551	A	B	C	D	
2000 Mar 02	18.38	18.64	19.36	19.66	F814W[a]
SDSS J0924+0219	D	A	C	B	
2003 Nov 19	21.59	18.69	19.86	19.52	F814W[b]
PG 1115+080	A_2	A_1	B	C	
2004 Feb 22	15.86	16.08	17.68	17.26	i'[c]
RX J1131−1231	A	B	D	C	
2004 Apr 12	17.43	17.42	19.72	18.44	I[d]
H 1413+117	A	B	D	C	
1994 Dec 22	17.77	17.84	18.15	18.06	F814W[a]
B 1422+231	B	A	D	C	
1999 Feb 06	15.85	15.88	19.68	16.41	F814W[a]
WFI J2033−4723	A_2	A_1	C	B	
2003 Aug 01	19.14	18.68	19.41	19.32	i'[e]
Q 2237+0305	D	A	C	B	
1999 Oct 20	17.39	15.92	16.77	17.21	F814W[a]

[a]See http://www.cfa.harvard.edu/castles

[b]Keeton et al. [2006]

[c]Relative magnitudes from Pooley et al. [2006]; zeropoint from this work.

[d]Sluse et al. [2006]

[e]Morgan et al. [2004]

Table 5.4. Models for 10 lenses

Quasar	$\theta_{\rm Ein}$	γ	ϕ_γ[a]	Magnification[b]				z_l	z_s
				HS	HM	LS	LM		
HE 0230−2130[c]	$\cdots$	$\cdots$	$\cdots$	−11.80	+11.50	−2.32	+6.22	0.52	2.162
MG J0414+0534	1.″20	0.13	+77.°1	−20.72	+19.07	−1.68	+5.36	0.96	2.64
RX J0911+0551	1.″11	0.32	+ 1.°1	−4.41	+8.10	−3.23	+1.77	0.77	2.80
SDSS J0924+0219	0.″88	0.04	+84.°6	−23.19	+26.78	−12.57	+10.98	0.39	1.524
PG 1115+080	1.″15	0.12	+65.°0	−13.37	+14.54	−3.02	+3.88	0.31	1.72
RX J1131−1231	1.″78	0.12	−73.°3	−23.72	+13.93	−1.58	+13.40	0.295	0.658
H 1413+117	0.″61	0.11	+21.°8	−5.17	+5.46	−3.32	+5.05	$\cdots$	2.55
B 1422+231	0.″78	0.27	−54.°6	−12.04	+8.86	−0.35	+5.69	0.34	3.62
WFI J2033−4723	1.″12	0.15	+26.°3	−6.61	+7.69	−2.20	+3.17	0.66	1.66
Q 2237+0305	0.″88	0.07	+67.°1	−9.81	+9.21	−5.32	+7.93	0.04	1.69

[a]Measured in degrees East of North.

[b]Negative magnifications signify saddle point images.

[c]HE 0230−2130 has a unique mass model with an extra companion galaxy. See text for lens parameters.

lens has an obvious strong perturbation from a companion lens galaxy, we added a second mass component to the model. Allowing its position and strength to vary, and using its measured position as a constraint, gave us eleven free parameters and twelve constraints. We found that a steeper projected profile than isothermal was required for this second mass component, so we modeled its projected mass density as a circular power-law profile with an index of −1.3. This model allows a much better fit to the data, and predicts an Einstein ring radius of 0.″79 for the main lensing galaxy and 0.″42 for the perturber, and an external shear of 0.10 in a direction 60.°1 west of north.

Parameters for the remaining lenses may be found in Table 5.4. The predicted magnifications may be expected to vary with different choices of lens models at the several percent level [Metcalf and Zhao, 2002].

Our model, in which the quadrupole term of the gravitational potential arises from an external tide, gives larger magnifications (and therefore smaller bolometric luminosities) than would a model in which the quadrupole is due to the flattening of the lens galaxy. Holder and Schechter [2003] have argued that the high ratio of quadruply lensed quasars to doubly lensed quasars can be explained if most of the quadrupole is tidal in origin.

5.4 Comparison of anomalous flux ratios: X-ray vs. optical

Figure 5-2 provides a visual guide to the optical-to-model and X-ray-to-model flux ratios of each quad. It shows representations of each system using two-dimensional Gaussians, the positions of which come from the CASTLES database. As a point of reference, the left-most frame for each quad shows Gaussians of unit amplitude. The center frame represents the optical-to-model ratio of the images, normalized by each rms (described below). The amplitude A_i of image i is given by

$$A_i = \frac{F_{\text{opt},i}/\text{rms}_{\text{opt}}}{|\mu_i|/\text{rms}_{|\mu|}} \quad , \tag{5.1}$$

where $i = 1, 2, 3, 4$, $F_{\text{opt},i}$ is the (linear) optical flux of image i, and μ_i is the image magnification from Table 5.4. The right frame gives a similar representation for the X-rays. The rms of the optical (and X-ray) observations is first computed as

$$\sqrt{\frac{1}{4} \sum_{i=1,4} (F_{\text{opt},i})^2} \quad . \tag{5.2}$$

However, because the rms can be dominated by one highly anomalous image, we remove the largest deviator and then recompute the rms. The largest deviator is defined as the image i with the maximum value of $|\log_{10}(A_{i,\text{opt}}) + \log_{10}(A_{i,\text{x-ray}})|$. This new rms is then used in eq. (1) to compute the amplitudes, the values of which are given in Table 5.5.

In every case save one, the most anomalous image was the highly magnified saddle point image. This is not surprising, since Schechter and Wambsganss [2002] have shown that microlensing is likely to affect high-magnification saddle points most strongly. In order to give the lenses a uniform treatment, we have classified the four images in each lens according to their magnifications and the local morphology of the travel-time surface. Henceforth in this thesis, "HS" will designate the highly magnified saddle-point and "HM" the highly magnified minimum. Likewise, "LS" will designate the less magnified saddle-point and "LM" the less magnified minimum.

In this work, we are most interested in the optical-to-model and X-ray-to-model ratios of the HS/HM flux ratio. The comparison between optical and X-ray ratios is shown for each
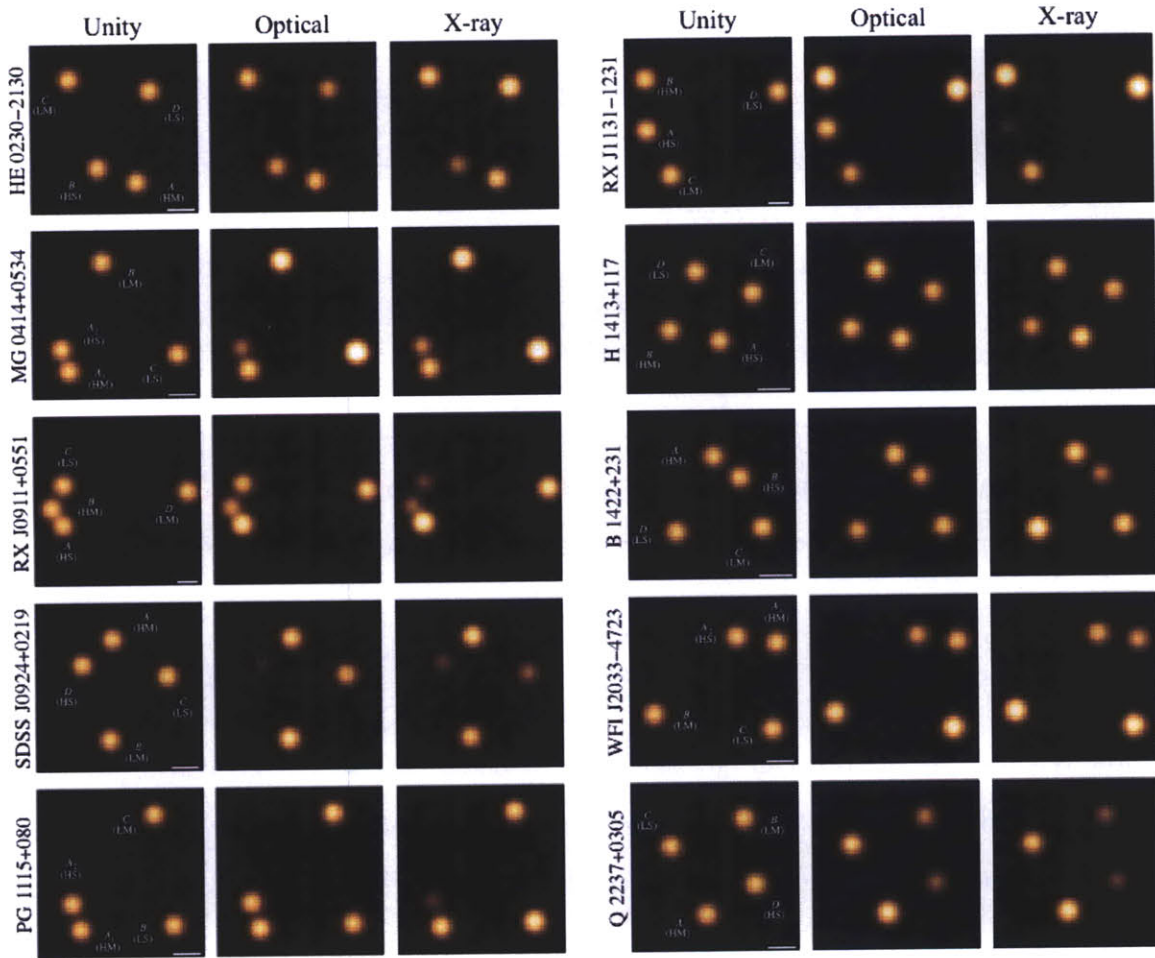
Figure 5-2 Representation of the deviations from the models in X-rays and optical. Each of the three frames for a system is constructed by placing Gaussians at the relative positions taken from the CASTLES online database. The leftmost frame in each set has the intensity of each Gaussian set to unity. In the center frame, the intensities are set to the ratio of the optical flux (normalized by the optical rms as defined by Equation 5.1) to the model flux (normalized by the model rms; see Equation 5.1). The same is done for X-rays in the rightmost frame of each set. The same color scaling is applied to every frame. For aesthetic reasons, the FWHMs of the Gaussians are a constant fraction of the frame size; a $0\overset{''}{.}5$ scale bar is shown at the bottom right of each "unity" frame, and this frame also gives the image names and image types (see Section 5.4).

Table 5.5.   Flux-to-model ratios normalized by rms

Quasar	Band	$(F_{i,\,\mathrm{obs}}/\mathrm{rms}_{\mathrm{obs}})\,/\,(|\mu_i|\,/\mathrm{rms}_{|\mu|})$ HS	HM	LS	LM
HE 0230−2130	Optical	0.76	0.94	0.62	1.02
	X-ray	0.46	1.06	1.50	1.24
MG J0414+0534	Optical	0.43	1.10	2.68	1.86
	X-ray	0.58	1.03	2.33	1.72
RX J0911+0551	Optical	1.49	0.64	0.82	1.14
	X-ray	1.76	0.36	0.24	1.29
SDSS J0924+0219	Optical	0.09	1.10	0.80	1.25
	X-ray	0.20	1.20	0.34	0.92
PG 1115+080	Optical	1.02	1.15	1.04	1.19
	X-ray	0.20	1.14	1.48	1.10
RX J1131−1231	Optical	1.03	1.76	1.87	0.72
	X-ray	0.10	1.72	2.08	0.82
H 1413+117	Optical	1.12	0.99	1.23	0.88
	X-ray	1.23	0.69	0.96	0.87
B 1422+231	Optical	0.76	1.00	0.77	0.96
	X-ray	0.49	1.22	1.78	1.10
WFI J2033−4723	Optical	0.71	0.93	1.65	1.25
	X-ray	0.84	0.65	1.66	1.81
Q 2237+0305	Optical	0.33	1.36	1.08	0.48
	X-ray	0.22	1.41	1.00	0.33

Note. — The rms values were computed from the three least anomalous images in each quad. See Section 5.4 for details.
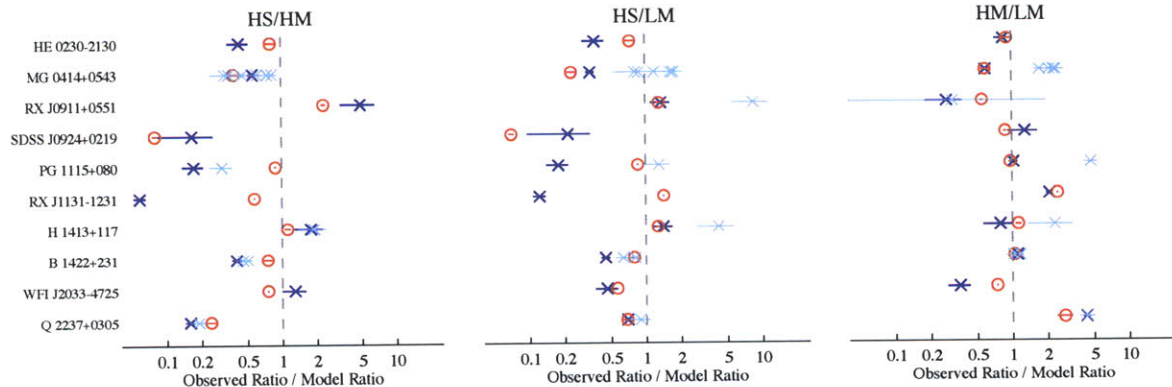
Figure 5-3 Comparison of X-ray (blue ×) and optical (red ○) ratios to lens model ratios for select image pairs for each lensed quasar. The leftmost frame shows the ratio of the highly magnified saddle point (HS) to the highly magnified minimum (HM), while the center and rightmost frame show the ratio of each of these, respectively, to the less magnified minimum (LM). The ratios for the X-ray are based on the observation with the highest signal to noise, and those for the optical are based on the observation closest in time to the chosen X-ray data. The light blue ×'s show the variation in the X-ray ratios for quads observed multiple times by *Chandra*.

quad in Figure 5-3. The first panel shows the observed HS/HM ratio relative to the model HS/HM ratio, and the second and third panels show how each of HS and HM compare to the less magnified minimum image (LM). In almost all cases, the HS/HM ratio is more extreme in X-rays than in the optical; when the observed ratio is greater then the model ratio, the X-ray ratio is greater than the optical, and, when the observed ratio is less than the model ratio, the X-ray ratio is less than the optical. The second and third panels show whether the discrepancy with the model comes from the HS or the HM image (or a combination of the two). In general, the LM image is much less susceptible to microlensing than either the HS or HM image [Kochanek and Dalal, 2004].

The group statistics for the flux ratio anomalies presented in Figure 5-3 and Table 5.5 are summarized in Figure 5-4. The error bars represent the ±rms spread in the logarithm of the flux ratios (normalized by the smooth model values) between various image pairs for our quasar sample. The black outer bars result from including all 10 quasars; the heavy blue bars result when we exclude the systems Q 2237+0305 and SDSS J0924+0219. Q 2237+0305 is excluded because the uniquely small redshift of its lensing galaxy causes the projected microlens Einstein radius to be bigger than any region of the source, while SDSS J0924+0219 might also be excluded because the source size is thought to be so small
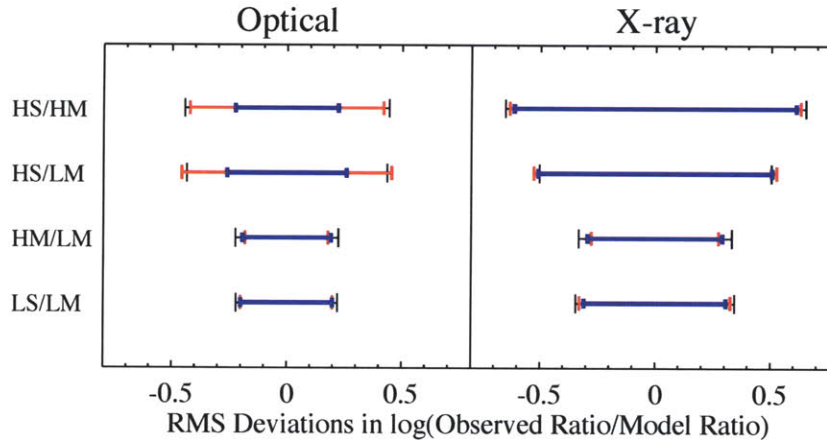
Figure 5-4 The rms of the flux ratio anomalies in the optical vs. X-ray (see Figure 5-3 and Table 5.5 for the flux ratios of individual sources). The black outer bars result from including all 10 quasars in our sample; the heavy blue bars result from excluding Q 2237+0305 and SDSS J0924+0219; the red bars result when we exclude only Q 2237+0305.

that even its broad line region is partially microlensed [Keeton et al., 2006].

It may be seen from the blue bars in this figure that the ratios of the HS to HM images deviate more (from their expected values) in the X-ray band than in the optical band by a factor of ∼2.4. The discrepancy is somewhat smaller for the HS/LM ratios at a factor of ∼1.7. The HM/LM and LS/LM ratios are not as anomalous in either band, but the X-ray ratios still have a wider range than do the optical ratios. It is on the larger anomalies in the X-ray band for the HS/HM and HS/LM ratios, as compared to those for the optical band, that we base our analysis of the size of the optically emitting regions of the accretion disks in the next section.

5.5   Sizes of quasar emission regions

For the purpose of interpreting our results, we adopt the working hypothesis that the anomalous flux ratios presented in this paper are the result of microlensing. Microlensing by stars in the lensing galaxy can account for the observed flux ratio anomalies, but only if the source is small compared to the Einstein radii of the microlensing stars. Figure 5-3 shows dramatic evidence for microlensing in the X-ray band for at least 7 of the 10 lensing systems in our study. In general, the optical emission of these same systems, while still

83

being microlensed, has less extreme flux ratio anomalies than in the X-ray band by a factor of $\sim$2 (see Figure 5-4 and the discussion above). Since the X-rays are expected to be emitted very near to the black hole, the condition for microlensing is easy to meet — the source should indeed be quite small compared to the Einstein radius of the microlensing stars. By contrast, the markedly lower degree of microlensing in the optical band implies that the size of the optical emission region in many of these sources is roughly comparable to the size of the stellar microlens Einstein radius.

Many authors have studied the effect of source size on the microlensing of quasars by intervening galaxies. Typically the results are presented as plots of microlensing light curves [e.g., Wambsganss and Paczynski, 1991] rather than rms fluctuations in the logarithm of the flux. There are no analytic techniques for estimating rms fluctuations, so one must simulate the microlensing process.

5.5.1 Microlensing simulations

Ideally we would run point source simulations for each of the 40 images in our sample, taking into account the theoretical magnification (which in turn depends upon two independent parameters, a convergence and a shear) and the fraction of baryonic matter. Each simulation would produce a magnification map, which might then be convolved with sources of different sizes, producing magnification histograms.

We undertake such an effort in Chapter 8, but for the present we can draw upon such simulations as have been carried out. In particular we use the work of Mortonson et al. [2005], who studied in detail the effect of source size on minima and saddlepoints with magnifications of +6 and −6 respectively, assuming that the convergence κ (a dimensionless surface density) is due entirely to equal mass stars and taking the shear γ to be equal to the convergence, as would be the case for an unperturbed isothermal lens. The magnifications observed for our highly magnified minima and saddlepoints are larger than this, typically by a factor of two, while our less magnified images are typically fainter than this by a factor of two. Moreover there is reason to think that the stellar component comprises only a fraction — somewhere between 1/10 and 1/2 — of the mass surface density. But in the absence of a complete set of simulations we take those of Mortonson et al. as representative.

They find that, independent of the detailed radial profile of the source, the rms logarithmic fluctuations depend only upon the ratio of the half-light radius of the source to the Einstein radius, $r_{1/2}/r_{\rm Ein}$. The rms logarithmic fluctuations decrease from their maximum value at $r_{1/2}/r_{\rm Ein} = 0$ to one half that value at $r_{1/2}/r_{\rm Ein} \approx 1/3$. Since our optical fluctuations are roughly one half the amplitude of the X-ray fluctuations (which we take to arise from a region of negligible extent) we infer that the line-of-sight projected size of the optical region is roughly $1/3$ the Einstein radius of the stars.

5.5.2 Predicted disk size: Energy considerations

To estimate a rough size for the expected region of the optical emission from quasar accretion disks, we adopt a generic thin disk model [see, e.g., Shakura and Sunyaev, 1973]. In such a model the gravitational energy release is redistributed via internal viscous stresses in such a way that, independent of the detailed nature of the origin of the viscosity, the rate of energy release per unit area of the disk at radius, r, is:

$$ \mathcal{F} = \frac{3GM\dot{M}}{8\pi r^3}\left(1 - \sqrt{\frac{r_0}{r}}\right) \tag{5.3} $$

where M, $\dot{M}$, and r_0 are the black-hole mass, accretion rate, and the inner radius of the accretion disk, respectively. Note that in this formulation neither special nor general relativistic effects are included, except implicitly via the location of r_0. In our context, such relativistic effects are unimportant in the case of a Schwarzschild black hole. Relativistic corrections, including those for accretion disks around Kerr black holes [Novikov and Thorne, 1973, Page and Thorne, 1974] are only likely to exacerbate the difficulties with understanding the size of the optical emission regions discussed below.

In the context of the thin-disk model around a Schwarzschild black hole, the fractional luminosity that emerges within a radial distance r is

$$ f_L(< r) = 3r_0 \int_{r_0}^{r}\left(1 - \sqrt{r_0/r}\right)r^{-2}dr = 1 - \frac{3}{r/r_0} + \frac{2}{\left(r/r_0\right)^{3/2}} \; . \tag{5.4} $$

The complement of this quantity, $[1 - f_L(< r)]$, i.e., the fraction of the luminosity released
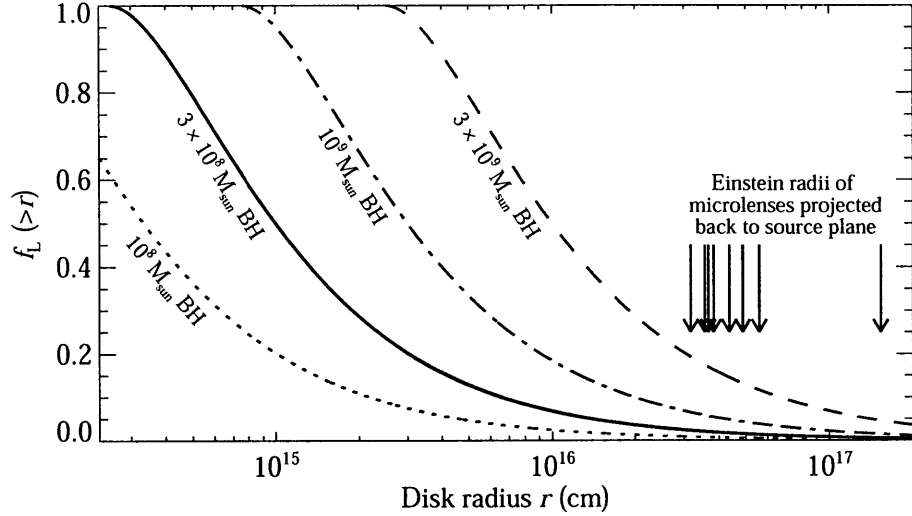
Figure 5-5 Fraction of luminosity (f_L) emitted beyond radius r in a geometrically thin accretion disk for a variety of black hole masses. The arrows indicate the physical sizes of the Einstein radii of $0.7\,M_\odot$ stars in each of the nine lensing galaxies of known redshift projected back onto the the lensed quasar.

at radii $> r$, is plotted in Figure 5-5. Here we have labeled the axis in physical units starting at $r_0 = 6GM/c^2 = 2.5 \times 10^{14}$ cm, i.e., the last stable orbit about a Schwarzschild black hole of $3 \times 10^8\,M_\odot$, an illustrative quasar mass. We also show curves for other possible black hole masses. For black holes with appreciable angular momentum, the value of r_0 moves progressively inward, and radii at which equal fractions of the luminosity are emitted do likewise.

Also overplotted on Figure 5-5 are nine arrows, one for each of our sources with known redshifts, marking the physical size of the Einstein radius of a $0.7\,M_\odot$ star in the lensing galaxy as projected back onto the lensed quasar. What we see is that the arrows are virtually all located at radii where only a tiny fraction of the quasar luminosity can emerge from the disk — at least for our fiducial black-hole mass of $3 \times 10^8\,M_\odot$. These fractional luminosity values are typically $\lesssim 2\%$ for sizes comparable to the backprojected stellar Einstein radii. Only for black-hole masses $\gtrsim 3 \times 10^9\,M_\odot$ does a significant fraction of the luminosity (i.e., $\sim$20%) originate from radial distances comparable in size to the Einstein radius. However, even then, as we showed in Pooley et al. [2006] and demonstrate below, much of this radiation should be emitted at wavelengths well beyond the optical or near IR. Given that the optical radiation (e.g., 0.4–1.5 μm) typically comprises a substantial fraction of quasar

luminosities, e.g., ~15% [Elvis et al., 1994], it appears difficult for the optical emission to be released from a thin disk at radii that are sufficiently large to allow for the partial suppression of microlensing — as observed. We further quantify this conclusion below.

5.5.3 Predicted disk size: Thin disk calculation

Figure 5-5 and Equation 5.4 imply effective *upper limits* to the size of thin accretion disks in the optical by evaluating the *bolometric* luminosity emitted within a radial distance r of the central black hole. We now proceed to compute more quantitatively how large the accretion disk is expected to appear for a fixed waveband, e.g., V, R, I. Based on the relativistic invariant I_ν/ν^3, we find the following expression for the half-light radius, $r_{1/2}$, of a thin accretion disk in a waveband centered at ν (in the Earth's frame):

$$\frac{\int_{r_0}^{r_{1/2}} \left[e^{h\nu(1+z)/kT(r)} - 1\right]^{-1} r\,dr}{\int_{r_0}^{\infty} \left[e^{h\nu(1+z)/kT(r)} - 1\right]^{-1} r\,dr} = \frac{1}{2} \quad , \tag{5.5}$$

where r_0 is the location of the inner edge of the accretion disk, and $T(r)$ is the local temperature of the accretion disk, which in the Shakura and Sunyaev [1973] model, is

$$T(r) = \left[\frac{3GM_{\mathrm{BH}}\dot{M}}{8\pi\sigma r^3}\right]^{1/4} \left(1 - \sqrt{r_0/r}\right)^{1/4} \quad . \tag{5.6}$$

In this simple picture, calculation of the half-light radius requires knowledge of three parameters: M_{BH}, $\dot{M}$, and r_0. We use primarily the optical-based method of Kaspi et al. [2000] (discussed below) to estimate the bolometric luminosity of each of the 10 sources in our sample. We also utilize the X-ray luminosity, coupled with a bolometric correction factor (also discussed below) to provide a sanity check on the Kaspi et al. [2000] approach. We further assume that all of the quasars are operating at the same fraction, $f_{\mathrm{Edd}} \simeq 1/4$, of their respective Eddington limits [Kollmeier et al., 2006]. We show below from a simple scaling argument, that our final results for $r_{1/2}$ are relatively insensitive to this choice. Finally, we assume that the radiation efficiency (rest mass to radiant energy conversion efficiency, η) of all the quasars in our sample is $\eta = 0.15$ [see, e.g., Yu and Tremaine, 2002]. For this choice of efficiency, the dimensionless black-hole spin parameter would be

$a = 0.88$ and the innermost stable orbit would be located at $r_0 \simeq 2.5R_g = 2.5GM_{\rm BH}/c^2$ [e.g., Bardeen, 1970]. However, in our simple non-relativistic disk model, we can only fix r_0, and accept whatever the non-relativistic energy release is. For $r_0 = 2.5\,R_g$ this turns out to yield an equivalent $\eta = 0.2$, which is sufficiently close to the Kerr value to provide the desired accuracy in computing $r_{1/2}$.

We summarize the computed and inferred properities of our quasar sample in Table 5.6. The second column gives the bolometric luminosity as calculated from the Kaspi et al. [2000] prescription. In this approach, $L_{\rm bol}$ is taken to be $9[\lambda F_\lambda]_{5100}4\pi d_L^2$. To estimate the 5100 Å flux in the rest frame of the quasar, we used the flux measured in the closest available broadband filter, usually the *HST* NICMOS F160W band, and extrapolated using an assumed power-law spectrum $F_\lambda \sim \lambda^{-1.7}$ [Kollmeier et al., 2006]. The third column in Table 5.6 gives an independent estimate of the bolometric luminosity for each quasar based on the measured X-ray luminosity and a bolometric correction factor of 20, as inferred from the composite AGN spectrum of Elvis et al. [1994]. The fourth column provides the black-hole mass inferred from the bolometric luminosity (in column 2) divided by the Eddington fraction, $f_{\rm Edd} = 1/4$, which then yields $L_{\rm Edd}$, and thence $M_{\rm BH}$. It should be noted that since Kollmeier et al. [2006] derive $f_{\rm Edd} = 1/4$ using the prescription of Kaspi et al. [2000], and since we follow suit, the masses we derive are independent of the dimensionless factor (of 9) in Kaspi's prescription. The error bars on the mass represent the uncertainties inferred from the $\pm$ rms (logarithmic) spread in the bolometric luminosities obtained via three different estimates: (i) the Kaspi et al. [2000] method, (ii) the X-ray luminosity, and (iii) (in 7 of the 9 cases) the mass estimate directly provided by Peng et al. [2006], which is based on a virial method involving broad-line widths and sizes of broad-line regions. The values of the half-light radius, $r_{1/2}$, computed with Equations 5.5 and 5.6 for the I band are given in the fifth column. In the sixth column are Einstein ring radii of typical $0.7M_\odot$ microlenses, projected onto the plane of the source. Finally, in the last column we give the logarithm of the ratio of the half-light radius to the microlens Einstein radius.

The results of our thin-disk estimates for the ratio $r_{1/2}/r_{\rm Ein}$ (last column of Table 5.6) are plotted in Figure 5-6. The central heavy point within each error bar is based on the black-hole mass given in column 4 of Table 5.6. The error bars on the ratio $r_{1/2}/r_{\rm Ein}$ are

Table 5.6. Properties of 10 quasars

Quasar	$L_{\text{bol,opt}}{}^{\text{a}}$ (10^{45} erg s^{-1})	$L_{\text{bol,X}}{}^{\text{b}}$ (10^{45} erg s^{-1})	log $M_{\text{BH}}{}^{\text{c}}$ ($M_\odot$)	$r_{1/2}{}^{\text{d}}$ (10^{15} cm)	$r_{1/2}{}^{\text{d}}$ (R_g)	stellar $r_{\text{Ein}}{}^{\text{e}}$ (10^{15} cm)	log $r_{1/2}/r_{\text{Ein}}$
HE 0230−2130	2.9	6.3	7.95 ± 0.24	0.93	70	43	-1.66 ± 0.16
MG J0414+0534	36	28	9.04 ± 0.17	3.8	23	31	-0.91 ± 0.11
RX J0911+0551	13	13	8.60 ± 0.18	1.9	32	35	-1.26 ± 0.12
SDSS J0924+0219	0.6	0.3	7.27 ± 0.56	0.42	152	48	-2.06 ± 0.37
PG 1115+080	11	6.6	8.53 ± 0.37	2.5	50	55	-1.35 ± 0.25
RX J1131−1231	0.80	1.3	7.39 ± 0.19	0.84	230	38	-1.65 ± 0.13
H 1413+117	56	6.5	9.24 ± 0.51	5.4	$\cdots$	$\cdots$	$\cdots$
B 1422+231	250	135	9.89 ± 0.18	13	11	47	-0.55 ± 0.12
WFI J2033−4723	5.7	3.8	8.24 ± 0.12	1.6	62	36	-1.35 ± 0.08
Q 2237+0305	32	2.7	8.99 ± 0.76	5.5	38	150	-1.43 ± 0.51

[a] Bolometric luminosities computed using $L_{\text{bol}} = 9[\lambda F_\lambda]_{5100} 4\pi d_L^2$. Computed from HM, LS, and LM images, corrected for magnification [Kaspi et al., 2000].

[b] Approximate bolometric luminosities derived from the X-ray (0.5–8 keV) luminosities (computed from LM image) with a bolometric correction factor of 20 (see Section 5.5).

[c] Calculated from the bolometric luminosities in column 2. See Section 5.5.

[d] $r_{1/2}$ is computed according to Equation 5.5 for the I band.

[e] Einstein radius of a $0.7 M_\odot$ star, projected back to the lensed quasar, in units of 10^{15} cm.
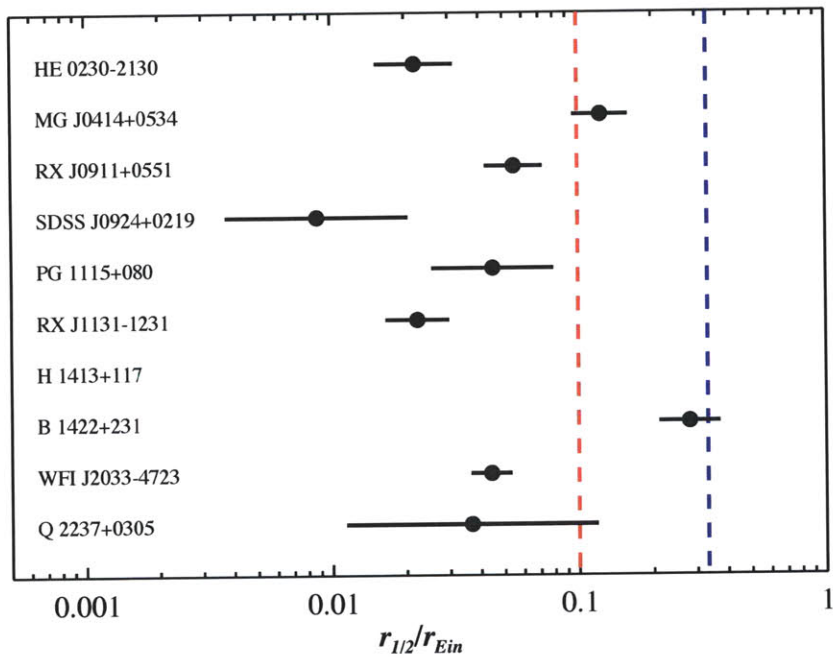
Figure 5-6 Ratio of thin-disk half-light radii to typical (0.7 M$_\odot$) microlens Einstein radii for the ten sample lenses. Estimates of the minimum value required to significantly attenuate microlensing variability are 0.1 (red) and 0.33 (blue) — see text for an explanation.

propagated from the black hole mass uncertainties given in Table 5.6. The vertical line at $r_{1/2}/r_{\mathrm{Ein}} = 1/3$ is our estimate of the ratio required to suppress microlensing in the optical band by the (logarithmic) factor of ~2 discussed in Section 5.4. The vertical line at $r_{1/2}/r_{\mathrm{Ein}} = 1/10$ represents a more conservative lower limit on $r_{1/2}/r_{\mathrm{Ein}}$ that might plausibly still be consistent with the suppressed microlensing in the optical. An inspection of Figure 5-6 shows that 7 of the 9 systems (for which $r_{1/2}/r_{\mathrm{Ein}}$ could be calculated) lie below the limit of 1/10, and therefore the disk size in the optical that we predict appears to be too small to explain the reduced microlensing. Only one of the systems, B 1422+231, has a ratio of $r_{1/2}/r_{\mathrm{Ein}}$ that slightly exceeds the 1/3 value which we think is reasonable to account for the reduced microlensing in the optical for this particular source. Note that this particular source has a flux ratio anomaly at *radio* wavelengths, an indication that millilensing is at work [Mao and Schneider, 1998].

Arguably the largest contribution to the uncertainty in the calculation of $r_{1/2}$ arises from the errors in estimating the bolometric luminosities of the quasars in our sample. We believe we can make a fairly robust estimate of the uncertainty in $r_{1/2}$ — due to the uncertainties in L_{bol} — by inspection of Figure 5-6. As discussed above, the plotted error bars are derived from the logarithmic rms scatter among the three (two) different and independent methods we have employed to infer L_{bol} (see above discussion) for 7 (2) of the sources. As Figure 5-6 indicates, the uncertainties in $r_{1/2}$ range between factors of 1.2 and 3.2, with an average value of a factor of 1.7. We take this to be a fairly reliable estimate of the uncertainty in our values for $r_{1/2}$ due to errors in estimating L_{bol}.

In our calculations leading to the set of values for $r_{1/2}/r_{\mathrm{Ein}}$ we assumed values for two key parameters of the quasars: (i) the radiative efficiency η, and (ii) the fraction $f_{\mathrm{Edd}} \equiv L_{\mathrm{bol}}/L_{\mathrm{Edd}}$. Based on a simple scaling argument, we can show how our results for $r_{1/2}$ depend on η and f_{Edd}. Equation 5.5 provides the exact definition of $r_{1/2}$ that we use. However, if we use the expression for $T(r)$ in Equation 5.6 to find the radius where $T/(1+z)$ equals $h\nu/k_B$, where ν is the center of the observation band, this is to a good approximation proportional to $r_{1/2}$. If we further neglect the factor $(1 - \sqrt{r_0/r})$ in Equation 5.6, we find

a handy scaling relation for $r_{1/2}$:

$$r_{1/2} \propto \left(M_{\mathrm{BH}}\dot{M}\right)^{1/3} \quad . \tag{5.7}$$

If we consider the bolometric luminosity to be a measured quantity for each system, then $M_{\mathrm{BH}} \propto L_{\mathrm{bol}}/f_{\mathrm{Edd}}$ and $\dot{M} \propto L_{\mathrm{bol}}/\eta$. Combining these, we can see how $r_{1/2}$ depends on the assumed parameters f_{Edd} and η:

$$r_{1/2} \propto (f_{\mathrm{Edd}}\eta)^{-1/3} \quad , \tag{5.8}$$

which is a fairly weak dependence, and not likely to lead to uncertainties in $r_{1/2}$ of more than an additional factor of ~ 2.

5.6   Summary and conclusions

We have presented a study of ten quadruply gravitationally lensed quasars for which high spatial resolution X-ray and optical data are available, paying particular attention to the differences between the observed flux ratios of the high magnification pairs of images (i.e., HS/HM) and the predicted flux ratios from smooth lensing models. The *Chandra* data were analyzed in a uniform and systematic manner, and the X-ray flux ratios were determined via two-dimensional Gaussian fits. The optical fluxes and image positions were found in the existing literature, with the bulk coming from the CASTLES project. We also modeled each lensing system as a singular isothermal sphere with external shear (except for HE 0230−2130, where a second mass component was necessary), and these simple models fit the image positions quite well.

As illustrated in Figures 5-2 through 5-4, almost all systems show evidence for an anomaly in the ratio of high-magnification saddle point and minimum images (HS/HM) as compared to the smooth model prediction. In the systems which show a pronounced anomaly, the X-rays are generally seen to be more anomalous than the optical.

For a number of reasons, we believe that the anomalous flux ratios, and the differences between these ratios in the X-ray and optical bands, are best explained by microlensing. In

previous work [Blackburne et al., 2006, Pooley et al., 2006] we have shown that extinction in the visible band and absorption of soft X-rays cannot provide the explanation. Second, we show in this study (as well as previous work) that temporal variability intrinsic to the source, in conjunction with lens time delays, also cannot, in most cases, explain the observed anomalies. Third, since images in both the X-ray and optical bands exhibit these flux ratio anomalies, but to differing degrees, no smooth lens model can reproduce these anomalies. Finally, we find that in the preponderance of systems, it is the highly magnified saddle point image (HS) whose flux is anomalous. This is in agreement with microlensing magnification distributions [Schechter and Wambsganss, 2002]. Since there is no reason for the HS location to systematically produce larger optical extinctions or X-ray absorptions, this is another argument against differential extinction/absorption being the cause of the flux ratio anomalies.

Under the hypothesis that the anomalies are produced via microlensing by stars (of typical mass 0.7 $M_\odot$) in the lensing galaxy, the implication is that the optical emitting region, which suffers rms (logarithmic) microlensing variations only half as big as those of the X-ray region, must have a typical size $\sim 1/3$ of the Einstein radius of the microlensing stars (see discussion in Section 5.5). Likewise, the X-ray emitting region, being more severely microlensed, must be substantially smaller than this.

In the context of a thin accretion disk around a black hole, the X-ray requirement is easily satisfied, as this emission likely arises from the inner parts of the disk. However, the optical emission poses something of a problem. It is generally thought to arise from a region not much larger than the X-ray region, but this is in conflict with the observed microlensing results which require larger optical emitting regions by factors of $\sim 3 - 30$ (see Figure 5-6) than are commonly accepted.

Therefore, we are left with a conundrum. Either there is a mechanism to transport the optical radiation to larger radii (and which does not affect the X-rays), or there is a missing piece of the puzzle. Regardless, we have demonstrated how the X-ray and optical observations can provide a micro-arcsecond probe of the lensed quasars, and thereby yield potentially important results.

From the work in this paper and the above discussion we draw three summary conclu-

sions:

- microlensing is the primary cause of the flux ratio anomalies.

- the optical emitting regions in the quasars involved in this study have sizes of $\sim 1/3$ of a stellar Einstein radius, i.e., $\sim$ a microarcsecond, corresponding to ~ 1000 AU.

- millilensing (e.g., by dark matter haloes) is ruled out as an explanation of the flux ratio anomalies by virtue of the above conclusion since this implies that both the X-ray and optical emission regions are small compared to the milliarcsecond scale, and should therefore be lensed by the same amount.

Chapter 6

Accretion disk structure: Introduction

6.1 Introduction

In Chapters 3 through 5 we developed the argument that the accretion disks around quasars (or at least the regions which produce UV and optical light) are in general large — large enough to significantly suppress the microlensing variability and flux ratio anomalies expected for point sources, and larger than expected from a simple Shakura-Sunyaev thin accretion disk model. In this chapter and those that follow, we build upon this foundation in two ways: we develop a quantitative method for measuring the size of a microlensed source, and we explore the dependence of the source size on wavelength within the (observer-frame) optical/IR band.

Since the publication of Pooley et al. [2007], several recent studies have used microlensing to probe the structure of individual, or a few, lenses. Some obtain a separate spectrum of each image, a feat requiring either carefully-placed slits or integral-field techniques. The lensed quasars HE 0230−2130, RX J0911+0551, SDSS J0924+0219, RX J1131−1231, and H 1413+117 have been studied in this way, and in each case the flux ratios were found to be less anomalous in the emission lines than in the continuum; this is a signature of microlensing [Keeton et al., 2006, Sluse et al., 2007, Sugai et al., 2007, Anguita et al.,

2008a]. Another study constrains the profile of the accretion disk of Q 2237+0305, using spectroscopic monitoring [Eigenbrod et al., 2008].

Other work has made use of time-series data, monitoring lensed quasars for years at a time. This technique is capable of measuring the sizes of accretion disks at the wavelengths in which the lenses are monitored, and has an advantage over single-epoch measurements in that it is able to glean information about the location of the source in the magnification map. However, it also suffers from a dependence on the unknown relative angular velocity of the source and the microlens stars. Several lensed quasars have been studied using this method; Morgan et al. [2007] used it to plot the relationship between accretion disk sizes and black hole mass. Most of the work thus far has been done in one or two broadband filters [Morgan et al., 2008a, Anguita et al., 2008b], but one study has extended the analysis to several optical/IR filters, and thus measured the temperature profile of an accretion disk [Poindexter et al., 2008]. Still other papers have combined optical monitoring data with X-ray monitoring to improve their results [Morgan et al., 2008b, Chartas et al., 2009, Dai et al., 2009].

But spectroscopy is difficult, and monitoring is expensive (especially with *Chandra*). So a few studies have used single-epoch imaging to constrain quasar structure. Agol et al. [2009] use IR measurements of Q 2237+0305 to confirm that the accretion disk and the dusty torus both contribute to the SED around 1 micron. Bate et al. [2008] and Floyd et al. [2009] use optical data nearly identical to ours to study the temperature profile of two quasars (MG J0414+0534 and SDSS J0924+0219, respectively), putting upper limits on the disk sizes and slopes.

In this work, we describe a method of analysis which allows us to measure the size of the source using single-epoch optical/IR and X-ray flux ratios. We measure flux ratios in eight optical and IR broadband filters, for twelve quadruply lensed quasars, and apply this method to them. We put constraints on the size of the accretion disks and the dependence of that size on wavelength.

Eleven of the twelve quasars were chosen from the known quadruple quasars that are observable from the southern hemisphere and have available *Chandra* data. In order to explore the dependence of size on wavelength, we needed imaging in multiple filters from

a large telescope with good image quality. The Magellan telescopes at Las Campanas Observatory fit this description, and are available to MIT astronomers; thus the focus on the southern sky. The need for *Chandra* data comes from our strategy of comparing anomalous flux ratios at X-ray wavelengths to those at optical wavelengths. *Chandra* is the only X-ray observatory with the resolution needed to separate the quasar images. Seven of these lenses are from the sample of Chapter 5 [Pooley et al., 2007]. They are HE 0230−2130, MG J0414+0534, RX J0911+0551, SDSS J0924+0219, PG 1115+080, RX J1131−1231, and WFI J2033−4723. Four do not appear in that work; their X-ray observations are more recent, and are published for the first time here. They are HE 0435−1223, HE 1113−0641, SDSS J1138+0314, and WFI J2026−4536.

The final lens, SDSS J1330+1810, was added to the sample after its discovery was reported in 2008 [Oguri et al., 2008a]. It does not have any X-ray data; our microlensing analysis of it can therefore only provide upper limits on the accretion disk size. But we do report improved positions for its quasar images and photometry in several bands (see Chapter 7).

No attempt was made to choose a "representative" sample of quasars, but there is no reason to believe that the sample is particularly biased, either. All are bright quasars at redshifts between 0.7 and 2.8, and all but MG J0414+0534 are radio-quiet. Projecting the Einstein ring of a microlens star back to the plane of the quasar results in very similar distances for all the lenses in our sample — around $4 \times 10^{16} \mathrm{cm} (m/0.7 M_\odot)^{1/2}$. We excluded the lensed quasar Q 2237+0305 because its projected Einstein ring size is much larger than the others'.

In Section 6.2 we review the predictions of the standard thin disk model for the size of the disk as a function of wavelength. The model depends on the mass of the black hole; we describe our estimates of these masses in Section 6.3.

6.2 Theory of thin accretion disks

Our analysis (see Chapter 8) yields estimated sizes for the quasar accretion disks at various wavelengths, as a fraction of the projected Einstein radius of the microlens stars. Mul-

tiplying by the Einstein radius, we arrive at a physical size. In this section we derive for comparison the size predicted by the the standard thin disk (or "alpha disk") model [Shakura and Sunyaev, 1973].

The following analysis is a slightly simplified version of that of Section 5.5.3; we have included it because the previous version was written by SAR, whereas this section is original to this thesis. We would like to lay to final rest a misconception that we have seen [e.g., in Chartas et al., 2009] regarding the theoretical accretion disk sizes we calculated in Section 5.5. It has been stated that our sizes were calculated using the observed flux and assuming the disk radiates like a blackbody at an assumed temperature. This is *not* what we did; we performed the full thin-disk analysis, as presented below. The only differences are in our estimates of the black hole masses (see Section 6.3) and a slight streamlining of the treatment (neglecting the correction factor in Equation 6.1 and using the rest wavelength).

The salient feature of the thin disk model for our purposes is its temperature profile, which is famously independent of the unknown α parameter which parameterizes the viscosity, and after which the model is named.

$$T_{\mathrm{eff}}(r) = \left[\frac{3GM_{\mathrm{BH}}\dot{M}}{8\pi\sigma_B r^3}\right]^{1/4} \left(1 - \sqrt{r_0/r}\right)^{1/4} \quad , \qquad (6.1)$$

where M_{BH} is the black hole mass, $\dot{M}$ is the mass accretion rate, σ_B is the Stefan-Boltzmann constant, and r_0 is the innermost radius of the accretion disk (generally considered to be the innermost stable circular orbit). This equation is the same as Equation 5.3. For the remainder of this chapter we will ignore the factor $[1 - (r_0/r)^{1/2}]^{1/4}$, because the optical emission regions of interest lie at a sufficient distance from the innermost radius r_0 that the factor is essentially unity (see Figure 6-1). This approximation simplifies our analysis; now the effective temperature of the disk is simply a power law in radius.

We define a wavelength-dependent scale size r_λ such that the blackbody described by $T_{\mathrm{eff}}(r_\lambda)$ peaks at λ (we neglect the numerical factor in Wien's Law):

$$r_\lambda \equiv \left[\frac{3GM_{\mathrm{BH}}\dot{M}}{8\pi\sigma_B \left(h_P c/\lambda_{\mathrm{rest}} k_B\right)^4}\right]^{1/3} = \left[\frac{45GM_{\mathrm{BH}}\dot{M}\lambda_{\mathrm{rest}}^4}{16\pi^6 h_P c^2}\right]^{1/3} \quad , \qquad (6.2)$$

where h_P is Planck's constant. This radius is only intended as a rough scale, but the $\lambda_{\text{rest}}^{4/3}$ dependence of the size of the disk is already apparent in this definition.

Based on the findings of Mortonson et al. [2005], we have parameterized our analysis of the data using the half-light radius of the disk at various wavelengths. To find the theoretical prediction for the half-light radius, we must integrate the flux from the inner edge of the disk out, and stop when the flux is half the total flux of the disk:

$$\frac{\int_{r_0}^{r_{1/2}} \left[\exp[h_P c/\lambda_{\text{rest}} k_B T(r)] - 1\right]^{-1} r\, dr}{\int_{r_0}^{\infty} \left[\exp[h_P c/\lambda_{\text{rest}} k_B T(r)] - 1\right]^{-1} r\, dr} = \frac{\int_{r_0}^{r_{1/2}} \left[\exp[(r/r_\lambda)^{3/4}] - 1\right]^{-1} r\, dr}{\int_{r_0}^{\infty} \left[\exp[(r/r_\lambda)^{3/4}] - 1\right]^{-1} r\, dr} = \frac{1}{2} \qquad (6.3)$$

(see Equation 5.5). We performed the integration numerically, setting the lower bound of the integral to zero, and found that $r_{1/2}(\lambda_{\text{rest}}) = 2.44 r_\lambda$. Setting the lower limit to zero has a very small effect on this result if (as with these lensed quasars) r_λ is much larger than the inner radius of the disk. Indeed, there is only a 6% change if we dial $r_{1/2}$ all the way down to $10 r_0$.

It only remains to determine the black hole mass M and the mass accretion rate $\dot{M}$. We express the latter in terms of the fraction of the Eddington luminosity at which the quasar is emitting:

$$f_{\text{Edd}} \equiv \frac{L_{\text{bol}}}{L_{\text{Edd}}} = \frac{\eta \dot{M} c \sigma_T}{4\pi G M_{\text{BH}} m_p} \quad , \qquad (6.4)$$

where σ_T is the Thomson scattering cross-section, m_p is the proton mass, and η is the efficiency of the accretion disk in converting the infalling mass to energy. In thin disks around rotating black holes, η is thought to be around 0.15 [Yu and Tremaine, 2002]. Thus

$$r_{1/2} = 2.44 \left[\frac{45 G^2 M_{\text{BH}}^2 m_p f_{\text{Edd}} \lambda_{\text{rest}}^4}{4\pi^5 h_P c^3 \sigma_T \eta}\right]^{1/3} \sqrt{\cos i}$$

$$= \left(1.68 \times 10^{16} \text{cm}\right) \left(\frac{M_{\text{BH}}}{10^9 M_\odot}\right)^{2/3} \left(\frac{f_{\text{Edd}}}{\eta}\right)^{1/3} \left(\frac{\lambda_{\text{rest}}}{\mu\text{m}}\right)^{4/3} \qquad (6.5)$$

(we have included a factor of $\sqrt{\cos i}$ to account for the inclination of the disk with respect to our line of sight, and set it to a reasonable average value of $2^{-1/2}$ in the second line).

For this analysis we follow Pooley et al. [2007] (see also Chapter 5) in adopting an Eddington fraction of 0.25 for our sample of quasars [Kollmeier et al., 2006]. The impact
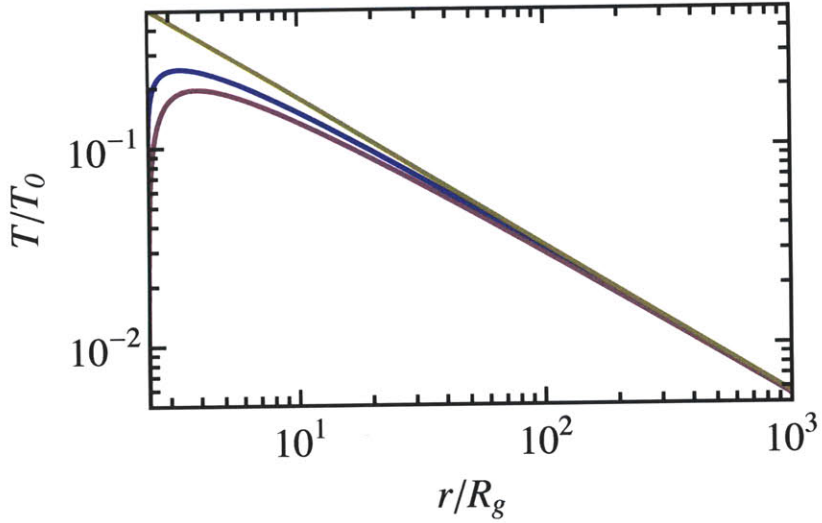
Figure 6-1 Comparison of effective temperature curves for three simple models for accretion disks. Top curve: $r^{-3/4}$ power law. Middle curve: Shakura and Sunyaev [1973] model. Bottom curve: Relativistic Novikov and Thorne [1973] model. The spin parameter a/M has been set to 0.88. Changing it does not qualitatively change the curves; its primary effect is to move the inner edge of the disk.

of this approximation is mitigated by of the weak dependence of $r_{1/2}$ on f_{Edd}.

In order to ensure that our model is applicable in the disk regions we are interested in, we compare the temperature profile of our simple power-law model to the Shakura-Sunyaev disk and to the fully relativistic Novikov and Thorne [1973] model in Figure 6-1. For all values of the black hole spin parameter a/M_{BH}, the error in our power-law model is less than 1% at radii greater than 50 gravitational radii. This region is where we measure the optical disk size. Note that in Figure 6-1,

$$T_0 = \left[\frac{3GM_{\mathrm{BH}}\dot{M}}{8\pi\sigma_B R_g^3}\right]^{1/4} . \tag{6.6}$$

6.3 Determining the black hole masses

There are two methods for estimating the mass of a supermassive black hole. The first is to measure the quasar's luminosity and apply an assumption about its Eddington fraction. The second is to measure the width of the broad emission lines in the quasar's spectrum, with the idea that the Doppler broadening of the lines is due to the Keplerian motion of the

emitting gas around the black hole. The latter virial method requires an estimate of the distance of the gas from the central object; for quasars this is normally obtained using an empirical relationship between the luminosity of the object and the size of the broad line region, calibrated by reverberation mapping of nearby AGN [Vestergaard, 2002].

The virial method has become very popular, and is generally regarded as more accurate than the use of the bolometric luminosity. Indeed, in our case the latter method must estimate not only the bolometric correction, but one or more lensing magnifications, since the unlensed source is impossible to observe. For this reason, we adopt where we can the virial estimates that exist of the black hole masses of our lensed quasars. Peng et al. [2006] use the virial method to estimate the masses of 6 of our sample: MG J0414+0534, HE 0435−1223, RX J0911+0551, SDSS J0924+0219, PG 1115+080, and RX J1131−1231. Morgan et al. [2007] make use of these estimates, and use the same method to estimate the mass of SDSS J1138+0314. Of the remaining quasars in our sample, HE 0230−2130 and WFI J2033−4723 have mass estimates in Pooley et al. [2007, see Chapter 5] based on their optical and X-ray luminosities.

For the remaining quasars (HE 1113−0641, SDSS J1330+1810, and WFI J2026−4536) we use bolometric luminosities to estimate the black hole masses, in exactly the same way as Pooley et al. [2007] did. To get a bolometric luminosity via optical wavelengths, we take the *HST* NICMOS F160W ($\approx H$, 1.6 microns) magnification-corrected magnitude of the LM image from the CASTLES database and convert it to a flux at the central wavelength of that filter. We then extrapolate to the redshifted analogue of (rest-frame) 5100 Å using an assumed power-law spectrum $f_\lambda \sim \lambda^{-1.7}$ [Kollmeier et al., 2006]. We use this flux in the formula

$$L_{\mathrm{bol}} = 9[\lambda f_\lambda]_{5100\text{Å}} 4\pi d_L \qquad (6.7)$$

where d_L is the luminosity distance of the quasar [Kaspi et al., 2000]. Our second approach was to multiply the $0.3 - 8$ keV X-ray flux (see Section 7.1) by a bolometric correction factor of 20 [Elvis et al., 1994].

Table 6.1 lists all of these black hole mass estimates. We visually compare the virial mass estimates to those calculated using bolometric luminosities in Figure 6-2. The luminosity

Table 6.1.   Black hole Mass Estimates

Quasar	$L_{bol,opt}$ $(10^{46}$ erg/s$)$	$L_{bol,X}$ $(10^{46}$ erg/s$)$	$M_{BH,opt}$ $(10^9 M_\odot)$	$M_{BH,vir}$ $(10^9 M_\odot)$
HE 0230−2130	0.29	0.63	0.092	$\cdots$
MG J0414+0534	3.6	2.8	1.1	1.82
HE 0435−1223	0.38[a]	0.46[a]	0.12	0.50
RX J0911+0551	1.3	1.3	0.41	0.80
SDSS J0924+0219	0.06	0.03	0.019	0.11
HE 1113−0641	0.27[a]	0.10[a]	0.087	$\cdots$
PG 1115+080	1.1	0.66	0.35	0.92/1.23[b]
RX J1131−1231	0.08	0.13	0.025	0.06
SDSS J1138+0314	0.38[a]	0.25[a]	0.12	0.04[c]
SDSS J1330+1810	4.7[a]	$\cdots$	1.5	$\cdots$
WFI J2026−4536	2.5[a]	1.1[a]	0.79	$\cdots$
WFI J2033−4723	0.57	0.38	0.18	$\cdots$

[a]This work.

[b]Two values are from the C IV and Mg II lines, respectively. We adopt the Mg II value.

[c]Morgan et al. [2007]

Note. — Unless otherwised indicated, bolometric luminosity estimates are from Pooley et al. [2007] and virial mass estimates are from Peng et al. [2006].
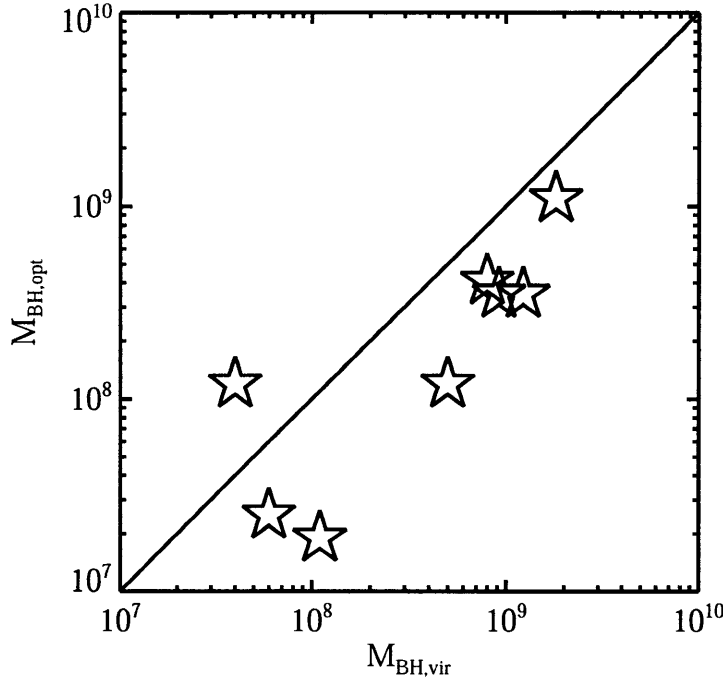
Figure 6-2 Comparison of virial mass estimates from Peng et al. [2006] to those estimated using the bolometric luminosity method of Pooley et al. [2007]. See Section 6.3 and Table 6.1. The solid line represents a 1:1 correspondence; it is not a fit.

masses are systematically smaller than the virial masses, by factors of $\sim$ 3; this could lead to under-predictions of the accretion disk size by factors of $\sim$ 2 for the lenses in which we use the bolometric mass estimate (in the absence of a virial estimate). This systematic bias is a little surprising, since the bolometric luminosity technique we are using is calibrated using the virial method [Kollmeier et al., 2006]. It may be partially due to a bias in our magnification correction, but it is difficult to imagine that we have systematically overestimated magnifications by a factor of three.

6.4 Putting it all together

With mass estimates in hand (or, rather, in Table 6.1), and adopted values of 0.25 and 0.15 for the Eddington fraction f_{Edd} and accretion efficiency η, respectively, we can predict with no free parameters what the projected size of the accretion disk should be as a function of

wavelength, according to the thin disk model (see Equation 6.5). Though the black hole masses are uncertain by factors of ~ 3, and the Eddington fraction and accretion efficiency are uncertain as well, the relatively weak dependence of $r_{1/2}$ on these parameters ensures that the predictions are secure to within a factor of ~ 3. In Chapter 9 we will compare these predictions to our measurements. But first, we describe the data in Chapter 7 and our new quantitative analysis method in Chapter 8.

Chapter 7

Accretion Disk Structure: X-ray and optical/infrared data

7.1 X-ray observations

The X-ray flux ratios for this survey all come from the *Chandra X-ray Observatory*; its resolution allows us to distinuguish the four quasar images. For five of the lenses among our sample (specifically HE 0230−2130, MG J0414+0534, RX J0911+0551, SDSS J0924+0219, and WFI J2033−4723) we adopt the X-ray flux ratios reported in Pooley et al. [2007]. For PG 1115+080 we adopt the X-ray flux ratios from Pooley et al. [2009]; they are more contemporaneous with our optical/IR observations. For the same reason, for RX J1131−1231 we use observations reported by Chartas et al. [2009]. Specifically, we use the 2007 February 13 observation (for comparison with MagIC data) and the 2007 April 16 observation (for comparison with PANIC data). We also make use of X-ray flux ratios for four other lenses: HE 0435−1223, HE 1113−0641, SDSS J1138+0314, and WFI J2026−4536. These come from recent *Chandra* observations, which are reported in an upcoming paper [Pooley et al., 2009, in preparation]. For these four, as well as RX J1131−1231, we have performed an analysis nearly identical to that described in Section 5.2 [Pooley, 2009, private communication]. The remaining lens, SDSS J1330+1810, has no X-ray observations.

Three of the four new X-ray lenses posed special challenges while fitting. In the cases

Table 7.1. X-ray fluxes and flux ratios

Quasar			Image Flux Ratios[b]			LM unabs. $F_{0.5-8\,\mathrm{keV}}$[c]
ObsID[a]	Date	Exp. (s)	HS/LM	HM/LM	LS/LM	$(10^{-14}\ \mathrm{erg\ cm^{-2}\ s^{-1}})$
HE 0230−2130			B/C	A/C	D/C	F_C
1642	2000 Oct 14	14 764	$0.70^{+0.13}_{-0.12}$	$1.6^{+0.2}_{-0.2}$	$0.45^{+0.08}_{-0.07}$	$\cdots$
MG J0414+0534			A2/B	A1/B	C/B	F_B
3419	2002 Jan 9	96 664	$1.3^{+0.1}_{-0.1}$	$2.1^{+0.1}_{-0.1}$	$0.42^{+0.02}_{-0.02}$	$\cdots$
HE 0435−1223			B/C	A/C	D/C	F_C
7761	2006 Dec 17	10 130	$0.99^{+0.15}_{-0.15}$	$2.6^{+0.3}_{-0.3}$	$0.96^{+0.14}_{-0.14}$	$3.3^{+0.7}_{-0.7}$
RX J0911+0551			A/D	B/D	C/D	F_D
419	1999 Nov 3	28 795	$3.4^{+0.6}_{-0.5}$	$1.3^{+0.4}_{-0.4}$	$0.35^{+0.13}_{-0.11}$	$\cdots$
SDSS J0924+0219			D/B	A/B	C/B	F_B
5604	2005 Feb 24	17 944	$0.45^{+0.25}_{-0.19}$	$3.2^{+0.8}_{-0.6}$	$0.42^{+0.19}_{-0.14}$	$\cdots$
HE 1113−0641			D/A	B/A	C/A	F_A
7760	2007 Jan 28	15 180	$0.78^{+0.32}_{-0.32}$	$0.63^{+0.41}_{-0.41}$	$0.20^{+0.16}_{-0.16}$	$7.4^{+2.2}_{-2.2}$
PG 1115+080			A2/C	A1/C	B/C	F_C
7757	2008 Jan 31	28 800	$0.62^{+0.13}_{-0.12}$	$3.9^{+0.3}_{-0.3}$	$1.1^{+0.1}_{-0.1}$	$\cdots$
RX J1131−1231			A/C	B/C	D/C	F_C
7787	2007 Feb 13	5 190	$5.53^{+0.38}_{-0.38}$	$3.09^{+0.23}_{-0.23}$	$0.61^{+0.06}_{-0.06}$	$\cdots$
7789	2007 Apr 16	5 190	$5.43^{+0.36}_{-0.36}$	$2.87^{+0.20}_{-0.20}$	$0.37^{+0.04}_{-0.04}$	$\cdots$
SDSS J1138+0314			D/C	A/C	B/C	F_C
7759	2007 Feb 13	19 080	$1.3^{+0.6}_{-0.5}$	$3.2^{+1.0}_{-1.0}$	$1.0^{+0.4}_{-0.4}$	$1.4^{+0.5}_{-0.5}$
WFI J2026−4536			A2/B	A1/B	C/B	F_B
7758	2007 Jun 28	10 170	$2.0^{+1.7}_{-1.0}$	$5.8^{+1.8}_{-1.7}$	$0.40^{+0.06}_{-0.15}$	$5.3^{+1.2}_{-1.2}$
WFI J2033−4723			A2/B	A1/B	C/B	F_B
5603	2005 Mar 10	15 420	$1.0^{+0.2}_{-0.2}$	$0.87^{+0.16}_{-0.14}$	$0.64^{+0.11}_{-0.10}$	$\cdots$

[a]The observation identifier of the *Chandra* dataset.

[b]HS = Highly magnified Saddle point; HM = Highly magnified Minimum; LS = Less magnified Saddle point; LM = Less magnified Minimum. See Section 5.4.

[c]The unabsorbed flux of the LM image is computed from the best fit power-law model described in Section 5.2.1. We only report new measurements here; see Table 5.1.

106

of HE 1113−0641, SDSS J1138+0314, and WFI J2026−4536, the least-squares optimization settled on a PSF larger than for any of the other observations. We fixed the width of the PSF in these cases to the average of the other X-ray PSFs. The flux in image A2 of WFI J2026−4536 was very sensitive to the PSF, so we allocated a generous 1.5 magnitudes of uncertainty to its flux ratio, added in quadrature to the other sources of uncertainty (see Section 7.4.2).

Table 7.1 summarizes the *Chandra* observations and the flux ratios measured.

7.2   Optical observations

Between 2007 February and 2008 May, we undertook an optical observing campaign to obtain multi-band, contemporaneous images of our sample of lenses. At IR wavelengths, we used the J, H, and K_s filters with Persson's Auxiliary Nasmyth Infrared Camera (PANIC), on the 6.5-meter Baade telescope at Las Campanas. In the optical, we used the Sloan $u'g'r'i'z'$ filters with MagIC, which was on the neighboring Clay telescope when we began our campaign, but was moved to Baade while the observations were still underway. This change of location allowed us to use both instruments during the same observing run, and even during the same night! MagIC and PANIC have fields of view $2\!.'4$ and $2\!.'1$ on a side, respectively, large enough for each image to include stars appropriate for use as PSF templates. The instruments' pixel scales are $0\!.''069$ and $0\!.''125$ pixels, which more than adequately sample the PSF. The details of the observations are listed in Table 7.2. The author carried out most of the observations.

During our 2007 September observing run, MagIC was offline for an upgrade, so we instead used the the Inamori Magellan Areal Camera System (IMACS) in its imaging mode. With its f/4 camera, the instrument has a pixel scale of $0\!.''11$ and a $15\!.'5$ field of view, but in order to reduce the readout time we used only a subraster $2\!.'2$ on a side. We used this instrument for our observations of HE 0230−2130, MG J0414+0534, and HE 0435−1223.

The images were bias-corrected, flattened, and corrected for cosmic rays using standard techniques. Where multiple exposures were obtained, they were combined, so that we ended up with a single image per filter per lensed quasar.

Table 7.2. Optical observations

Quasar	Date	Instrument	Filters	Exposures (s)	Seeing ($''$)
HE 0230−2130	2007 Sept 16	IMACS	$u'g'r'i'z'$	720; 240; 240; 240; 480	0.43
	2007 July 29	PANIC	JHK_s	540; 540; 540	0.64
MG J0414+0534	2007 Sept 21	IMACS	$r'i'z'$	360; 240; 480	0.67
	2007 Sept 22	PANIC	JHK_s	810; 720; 720	0.76
HE 0435−1223	2007 Sept 16	IMACS	$u'g'r'i'z'$	720; 240; 240; 270; 480	0.67
	2007 Sept 22	PANIC	JHK_s	810; 1080; 1080	1.06
RX J0911+0551	2007 Feb 13	MagIC	$g'r'i'z'$	240; 240; 300; 480	0.70
	2007 Feb 14	MagIC	u'	720	0.63
	2007 Apr 7	PANIC	JHK_s	540; 405; 405	0.72
SDSS J0924+0219	2007 Feb 13	MagIC	$u'g'r'i'z'$	720; 240; 240; 180; 480	0.61
	2007 Apr 7	PANIC	JHK_s	540; 540; 540	0.64
HE 1113−0641	2007 Feb 14	MagIC	$g'r'i'z'$	240; 180; 120; 240	0.49
	2007 Apr 7	PANIC	JHK_s	450; 450; 450	0.45
PG 1115+080	2008 Feb 1	MagIC	$g'r'i'z'$	120; 120; 150; 240	0.55
	2008 Feb 2	MagIC	u'	720	0.87
	2008 Feb 4	PANIC	JHK_s	540; 540; 540	0.56
RX J1131−1231	2007 Feb 13	MagIC	$u'g'r'i'z'$	480; 120; 120; 120; 240	0.65
	2007 Apr 6	PANIC	JHK_s	486; 405; 405	0.76
SDSS J1138+0314	2007 Feb 13	MagIC	$u'g'r'i'z'$	1080; 480; 480; 360; 960	0.75
	2007 Apr 8	PANIC	JHK_s	540; 540; 540	0.47
SDSS J1330+1810	2008 Feb 1	MagIC	$u'g'r'i'z'$	360; 120; 120; 150; 240	0.53
	2008 Feb 3	PANIC	JHK_s	540; 540; 540	0.68
WFI J2026−4536	2008 May 13	MagIC	$u'g'r'i'z'$	720; 240; 240; 360; 480	0.54
	2008 May 12	PANIC	JHK_s	135; 135; 90	0.43
WFI J2033−4723	2007 June 15	MagIC	$u'g'r'i'z'$	720; 240; 120; 300; 480	0.88
	2007 July 4	PANIC	JHK_s	135; 135; 90	0.51

Because of the small separations of the lensed quasar images in our sample, we observed only under the best atmospheric seeing conditions. The excellent image quality at the Magellan telescopes was crucial to the success of our survey. The i'- and J-band seeing is reported in Table 7.2, which outlines the optical/IR observations obtained for this work. The seeing in the other filters was roughly consistent with the rule of thumb: FWHM $\propto \lambda^{-1/5}$.

Because we are primarily interested in the flux *ratios* of lensed quasars (indeed, we cannot measure absolute magnifications), we did not, in general, obtain images of standard stars for the purpose of calibrating our photometry. In the case of SDSS J1330+1810, however, we did observe standard stars in the optical bands, so we report (in Section 7.3) calibrated photometry for this lens. We also estimate the photometric zero point in the J and K_s bands, based on images taken the same night which contain several calibrated

2MASS sources.

7.3 Optical and infrared photometry

Despite the high quality of our data, careful PSF subtraction was necessary to disentangle the compact clumps of point sources and lens galaxies that make up our sample. For each image, we used a non-linear least-squares fitting technique to simultaneously fit the positions and relative fluxes of the 4 quasar components and the lens galaxy.

For lenses that presented no obvious difficulty (such as a blended pair of merging quasar components), we performed a simultaneous fit to the images in all filters, with the relative positions of the quasar components and the lens galaxy allowed to vary, but constrained to be the same in all filters. The amplitudes of the quasar components were completely free to vary. The best-fit positions were consistent in every case with the *HST* positions listed on the CASTLES website.

In cases where merging pairs (or triples) would have caused strong correlations between positions and flux ratios, we fixed the relative positions of the quasar components and the lensing galaxy to the CASTLES positions.

RX J1131$-$1231 required special treatment. Because of its very bright Einstein ring, the quasar components were over-subtracted by the least-squares minimizer, especially at the longer wavelengths. So we performed a second fit to this system's r' through K_s data, fixing all of the quasar fluxes to values that resulted in residuals that looked like an unbroken Einstein ring. Though it was completely ad-hoc, we think that this "chi-by-eye" technique gave flux ratios less affected by systematic errors. Section 7.4.1 describes our method for estimating the uncertainty of these flux ratios.

In all cases we modeled the lensing galaxy as a 2D "pseudo-Gaussian" function, with a full-width at half-max as a fixed parameter. The width was chosen using a trial-and-error technique, examining the residuals by eye. (Because of the frequent presence of a faint Einstein ring due to the quasar's host galaxy, least-squares minimization often overestimated the width). Because the lens galaxy nearly always had a low signal-to-noise ratio compared to the quasar images, the goodness of the fit was insensitive to this approximation. The

Table 7.3. Differential astrometry for SDSS J1330+1810

Image	x	y
A	-1.258 ± 0.01	-1.168 ± 0.01
B	-0.839 ± 0.01	-1.190 ± 0.01
C	$\equiv 0$	$\equiv 0$
D	-1.488 ± 0.01	0.444 ± 0.01
G	-1.037 ± 0.02	-0.195 ± 0.02

Note. — Positive x and y point west and north, respectively.

galaxies were mostly round, but for the few exceptions we treated the axis ratio and position angle as we did the width.

The fitted fluxes of the lens galaxies are uncalibrated, and therefore of little interest; we do not report them. SDSS J1330+1810 is the exception to this rule; because it was discovered relatively recently, and because observing conditions were photometric on the night it was observed, we observed standard stars in all bands but H, for the purpose of calibrating its fluxes. The calibrated magnitudes of this lens galaxy are reported in Table 7.4. The optical calibration relies on aperture photometry of the standard stars SA 107-351 (for u') and G163-50 (for $g'r'i'z'$), and places the fluxes on the Sloan $u'g'r'i'z'$ system, which closely approximates the monochromatic AB system [Smith et al., 2002]. The IR flux calibration makes use of a field containing several 2MASS sources; we performed aperture photometry on them and compared their measured magnitudes to those reported in the NASA/IPAC Infrared Science Archive[1] to obtain photometric zero points. This places our calibrated J and K_s fluxes on the 2MASS photometric system [Cohen et al., 2003].

The lack of HST positions for SDSS J1330+1810, combined with the relative brightness and elliptical shape of the lensing galaxy, made it a special challenge. In order to get the shape of the galaxy right, we adopted an iterative approach. First we fixed the galaxy parameters to reasonable guesses and fit the positions and fluxes of the quasar components,

---

[1]http://irsa.ipac.caltech.edu

Table 7.4. Photometry for SDSS J1330+1810

Filter	HM	HS	LM	LS	
	A − C	B − C	C	D − C	G
u'	-0.75 ± 0.06	$+0.27 \pm 0.06$	19.69 ± 0.06	$+1.70 \pm 0.08$	$\cdots$
g'	-0.79 ± 0.06	$+0.17 \pm 0.06$	20.99 ± 0.06	$+1.78 \pm 0.08$	25.08 ± 0.11
r'	-0.86 ± 0.06	-0.18 ± 0.06	20.57 ± 0.06	$+1.63 \pm 0.08$	23.48 ± 0.11
i'	-0.90 ± 0.03	-0.13 ± 0.03	21.07 ± 0.06	$+1.71 \pm 0.06$	23.26 ± 0.10
z'	-0.88 ± 0.04	-0.12 ± 0.04	21.55 ± 0.06	$+1.95 \pm 0.11$	23.46 ± 0.10
J	-0.85 ± 0.07	-0.18 ± 0.08	18.88 ± 0.06	$+1.34 \pm 0.14$	18.94 ± 0.10
H	-0.84 ± 0.07	-0.24 ± 0.08	$\cdots$	$+1.54 \pm 0.18$	$\cdots$
K_s	-0.89 ± 0.07	-0.36 ± 0.08	17.78 ± 0.06	$+2.29 \pm 0.55$	17.13 ± 0.10

Note. — Optical magnitudes for image C and lens galaxy G are calibrated to the $u'g'r'i'z'$ system, while J and K_s magnitudes are calibrated to the 2MASS system. All values are in magnitudes.

subtracting them from the image. To the residual image (which contained only the lens galaxy) we then fit a single elliptical pseudo-Gaussian [Schechter et al., 1993], with all parameters allowed to vary. The best-fit FWHM of the galaxy was $1\rlap{.}''0$ along the major axis; the axis ratio and position angle were 0.67 and $24\rlap{.}°5$ east of north. Finally, we fit the original image again, fixing the galaxy shape parameters to the best-fit values, in order to find the quasar positions and fluxes. The results are consistent with those of Oguri et al. [2008a], but have higher precision; they are reported in Tables 7.3 (astrometry) and 7.4 (photometry).

We used nearby bright (but not saturated) stars in each frame as PSF templates in our fitting.

For each lens, the transformation between pixel coordinates and sky coordinates was determined by fitting the star positions in our i' and J band images to the USNO-B catalog. On average, there were $\sim 10 - 15$ objects for each fit. The pixel scale and rotation angle thus determined for i' and J were assumed to apply to the remaining MagIC/IMACS data and PANIC data, respectively.

Relative photometry for all the lenses in our sample (except SDSS J1330+1810) is listed

in Table 7.5. We also list the calculated rms deviation of the flux ratios in each filter from those predicted by the lens models. This number is an indication of how anomalous the flux ratios are. For comparison with the optical flux ratios, we also list the X-ray and predicted model ratios, in magnitudes.

Table 7.5. Relative photometry for the rest of the lenses

Quasar	Filter	HM	HS	LM	LS	rms[a]
HE 0230−2130		A	B	C	D	
	u'	0 ± 0.00	$+0.26 \pm 0.06$	$+0.97 \pm 0.05$	$+2.60 \pm 0.17$	0.17
	g'	0 ± 0.00	$+0.25 \pm 0.06$	$+0.69 \pm 0.05$	$+2.41 \pm 0.14$	0.14
	r'	0 ± 0.00	$+0.23 \pm 0.05$	$+0.62 \pm 0.05$	$+2.44 \pm 0.20$	0.17
	i'	0 ± 0.00	$+0.17 \pm 0.02$	$+0.58 \pm 0.02$	$+2.37 \pm 0.37$	0.15
	z'	0 ± 0.00	$+0.12 \pm 0.06$	$+0.55 \pm 0.06$	$+2.95 \pm 0.64$	0.38
	J	0 ± 0.00	$+0.15 \pm 0.02$	$+0.54 \pm 0.02$	$+2.64 \pm 0.95$	0.26
	H	0 ± 0.00	$+0.12 \pm 0.06$	$+0.50 \pm 0.06$	$+2.74 \pm 1.21$	0.31
	K_s	0 ± 0.00	$+0.07 \pm 0.05$	$+0.50 \pm 0.06$	$+3.48 \pm 1.66$	0.62
MG J0414+0534		A1	A2	B	C	
	r'	$+0.20 \pm 0.40$	$+0.30 \pm 0.38$	0 ± 0.02	$+0.41 \pm 0.21$	0.89
	i'	-0.40 ± 0.15	$+0.13 \pm 0.29$	0 ± 0.02	$+1.05 \pm 0.19$	0.52
	z'	-0.65 ± 0.06	-0.01 ± 0.10	0 ± 0.02	$+1.01 \pm 0.09$	0.45
	J	-0.93 ± 0.01	-0.42 ± 0.02	0 ± 0.02	$+0.96 \pm 0.05$	0.29
	H	-0.84 ± 0.05	-0.84 ± 0.06	0 ± 0.02	$+0.96 \pm 0.07$	0.19
	K_s	-1.01 ± 0.01	-0.86 ± 0.01	0 ± 0.02	$+0.94 \pm 0.05$	0.15
HE 0435−1223		C	B	A	D	
	u'	$+0.94 \pm 0.03$	$+1.00 \pm 0.04$	0 ± 0.00	$+0.90 \pm 0.04$	0.45
	g'	$+0.73 \pm 0.05$	$+0.78 \pm 0.05$	0 ± 0.00	$+0.86 \pm 0.06$	0.35
	r'	$+0.69 \pm 0.03$	$+0.70 \pm 0.04$	0 ± 0.00	$+0.85 \pm 0.04$	0.32
	i'	$+0.58 \pm 0.05$	$+0.65 \pm 0.06$	0 ± 0.00	$+0.81 \pm 0.06$	0.29
	z'	$+0.57 \pm 0.03$	$+0.61 \pm 0.04$	0 ± 0.00	$+0.87 \pm 0.04$	0.27
	J	$+0.53 \pm 0.05$	$+0.54 \pm 0.05$	0 ± 0.00	$+0.84 \pm 0.06$	0.25
	H	$+0.49 \pm 0.05$	$+0.51 \pm 0.06$	0 ± 0.00	$+0.84 \pm 0.06$	0.24
	K_s	$+0.41 \pm 0.02$	$+0.42 \pm 0.02$	0 ± 0.00	$+0.84 \pm 0.03$	0.20
RX J0911+0551		B	A	D	C	
	u'	$+0.39 \pm 0.03$	0 ± 0.00	$+1.64 \pm 0.09$	$+1.28 \pm 0.03$	0.45
	g'	$+0.19 \pm 0.10$	0 ± 0.00	$+1.15 \pm 0.13$	$+1.09 \pm 0.10$	0.45
	r'	$+0.25 \pm 0.05$	0 ± 0.00	$+1.31 \pm 0.10$	$+1.09 \pm 0.05$	0.43
	i'	$+0.17 \pm 0.05$	0 ± 0.00	$+1.22 \pm 0.10$	$+0.97 \pm 0.05$	0.40
	z'	$+0.13 \pm 0.02$	0 ± 0.00	$+1.16 \pm 0.09$	$+0.85 \pm 0.02$	0.38
	J	$+0.03 \pm 0.03$	0 ± 0.00	$+1.07 \pm 0.09$	$+0.71 \pm 0.03$	0.34
	H	$+0.11 \pm 0.03$	0 ± 0.00	$+1.03 \pm 0.10$	$+0.73 \pm 0.04$	0.38
	K_s	-0.11 ± 0.04	0 ± 0.00	$+0.93 \pm 0.10$	$+0.69 \pm 0.05$	0.35

Table 7.5

Quasar	Filter	HM	HS	LM	LS	rms[a]
SDSS J0924+0219		A	D	B	C	
	u'	0 ± 0.00	$+1.68 \pm 0.51$	$+1.47 \pm 0.06$	$+2.64 \pm 0.51$	0.71
	g'	0 ± 0.00	$+2.78 \pm 0.08$	$+1.53 \pm 0.05$	$+2.59 \pm 0.06$	1.00
	r'	0 ± 0.00	$+2.97 \pm 0.05$	$+1.43 \pm 0.01$	$+2.41 \pm 0.02$	1.07
	i'	0 ± 0.00	$+2.98 \pm 0.08$	$+1.36 \pm 0.05$	$+2.28 \pm 0.06$	1.08
	z'	0 ± 0.00	$+2.86 \pm 0.08$	$+1.35 \pm 0.02$	$+2.27 \pm 0.04$	1.03
	J	0 ± 0.00	$+2.25 \pm 0.10$	$+1.15 \pm 0.06$	$+1.88 \pm 0.08$	0.81
	H	0 ± 0.00	$+2.12 \pm 0.12$	$+1.12 \pm 0.06$	$+1.65 \pm 0.08$	0.76
	K_s	0 ± 0.00	$+1.90 \pm 0.10$	$+1.02 \pm 0.04$	$+1.40 \pm 0.06$	0.69
HE 1113−0641		B	D	A	C	
	g'	$+0.20 \pm 0.05$	$+0.87 \pm 0.05$	0 ± 0.00	$+0.42 \pm 0.05$	0.46
	r'	$+0.14 \pm 0.05$	$+0.75 \pm 0.05$	0 ± 0.00	$+0.54 \pm 0.05$	0.39
	i'	$+0.11 \pm 0.01$	$+0.76 \pm 0.01$	0 ± 0.00	$+0.52 \pm 0.01$	0.40
	z'	$+0.13 \pm 0.01$	$+0.96 \pm 0.02$	0 ± 0.00	$+0.44 \pm 0.01$	0.49
	J	$+0.18 \pm 0.01$	$+0.96 \pm 0.02$	0 ± 0.00	$+0.38 \pm 0.01$	0.50
	H	$+0.14 \pm 0.01$	$+0.77 \pm 0.02$	0 ± 0.00	$+0.42 \pm 0.02$	0.42
	K_s	$+0.11 \pm 0.02$	$+0.68 \pm 0.02$	0 ± 0.00	$+0.47 \pm 0.02$	0.37
PG 1115+080		A1	A2	C	B	
	u'	-1.51 ± 0.05	-0.86 ± 0.05	0 ± 0.02	$+0.36 \pm 0.05$	0.26
	g'	-1.44 ± 0.05	-1.30 ± 0.05	0 ± 0.02	$+0.30 \pm 0.05$	0.10
	r'	-1.41 ± 0.01	-1.24 ± 0.01	0 ± 0.02	$+0.35 \pm 0.02$	0.10
	i'	-1.41 ± 0.05	-1.23 ± 0.05	0 ± 0.02	$+0.39 \pm 0.05$	0.09
	z'	-1.39 ± 0.01	-1.23 ± 0.01	0 ± 0.02	$+0.39 \pm 0.02$	0.09
	J	-1.42 ± 0.05	-1.19 ± 0.05	0 ± 0.02	$+0.41 \pm 0.05$	0.10
	H	-1.45 ± 0.05	-1.18 ± 0.05	0 ± 0.02	$+0.35 \pm 0.06$	0.13
	K_s	-1.41 ± 0.03	-1.17 ± 0.03	0 ± 0.02	$+0.48 \pm 0.06$	0.10
RX J1131−1231		B	A	C	D	
	u'	-1.29 ± 0.02	-1.74 ± 0.03	0 ± 0.01	$+0.63 \pm 0.08$	0.74
	g'	-1.06 ± 0.05	-1.52 ± 0.05	0 ± 0.01	$+0.94 \pm 0.09$	0.62
	r'	-1.10 ± 0.04	-1.55 ± 0.06	0 ± 0.01	$+1.00 \pm 0.11$	0.61
	i'	-1.00 ± 0.10	-1.46 ± 0.12	0 ± 0.01	$+0.97 \pm 0.10$	0.61
	z'	-0.90 ± 0.08	-1.33 ± 0.11	0 ± 0.01	$+1.00 \pm 0.08$	0.61
	J	-0.78 ± 0.17	-1.21 ± 0.23	0 ± 0.01	$+0.75 \pm 0.12$	0.71
	H	-0.64 ± 0.18	-1.04 ± 0.22	0 ± 0.01	$+0.65 \pm 0.15$	0.77
	K_s	-0.51 ± 0.12	-1.12 ± 0.20	0 ± 0.01	$+0.97 \pm 0.18$	0.64

Table 7.5

Quasar	Filter	HM	HS	LM	LS	rms[a]
SDSS J1138+0314		A	D	C	B	
	u'	0 ± 0.05	$+1.98 \pm 0.10$	$+1.70 \pm 0.07$	$+1.35 \pm 0.07$	0.72
	g'	0 ± 0.05	$+1.17 \pm 0.10$	$+1.28 \pm 0.10$	$+1.33 \pm 0.10$	0.42
	r'	0 ± 0.05	$+1.29 \pm 0.05$	$+1.27 \pm 0.05$	$+1.38 \pm 0.05$	0.45
	i'	0 ± 0.05	$+1.36 \pm 0.02$	$+1.28 \pm 0.01$	$+1.37 \pm 0.02$	0.47
	z'	0 ± 0.05	$+1.17 \pm 0.06$	$+1.19 \pm 0.05$	$+1.25 \pm 0.06$	0.41
	J	0 ± 0.05	$+1.33 \pm 0.03$	$+1.16 \pm 0.02$	$+1.40 \pm 0.03$	0.45
	H	0 ± 0.05	$+1.26 \pm 0.07$	$+1.06 \pm 0.06$	$+1.34 \pm 0.07$	0.42
	K_s	0 ± 0.05	$+0.83 \pm 0.07$	$+0.89 \pm 0.07$	$+1.24 \pm 0.08$	0.27
WFI J2026$-$4536		A1	A2	B	C	
	u'	-0.61 ± 0.01	-1.30 ± 0.01	0 ± 0.02	$+0.19 \pm 0.01$	0.34
	g'	-0.99 ± 0.05	-1.27 ± 0.05	0 ± 0.02	$+0.22 \pm 0.05$	0.20
	r'	-1.25 ± 0.05	-1.21 ± 0.05	0 ± 0.02	$+0.22 \pm 0.05$	0.12
	i'	-1.36 ± 0.01	-1.17 ± 0.01	0 ± 0.02	$+0.09 \pm 0.01$	0.06
	z'	-1.38 ± 0.05	-1.13 ± 0.05	0 ± 0.02	$+0.25 \pm 0.05$	0.12
	J	-1.53 ± 0.01	-1.11 ± 0.01	0 ± 0.02	$+0.29 \pm 0.01$	0.18
	H	-1.50 ± 0.07	-0.90 ± 0.07	0 ± 0.02	$+0.30 \pm 0.05$	0.19
	K_s	-1.49 ± 0.05	-0.77 ± 0.05	0 ± 0.02	$+0.24 \pm 0.05$	0.22
WFI J2033$-$4723		A1	A2	B	C	
	u'	-0.41 ± 0.03	$+0.06 \pm 0.04$	0 ± 0.04	$+0.69 \pm 0.06$	0.07
	g'	-0.52 ± 0.05	$+0.14 \pm 0.06$	0 ± 0.04	$+0.48 \pm 0.06$	0.06
	r'	-0.51 ± 0.01	$+0.05 \pm 0.02$	0 ± 0.04	$+0.38 \pm 0.04$	0.05
	i'	-0.54 ± 0.05	-0.05 ± 0.06	0 ± 0.04	$+0.24 \pm 0.06$	0.10
	z'	-0.52 ± 0.03	-0.05 ± 0.04	0 ± 0.04	$+0.29 \pm 0.06$	0.08
	J	-0.60 ± 0.05	-0.12 ± 0.05	0 ± 0.04	$+0.17 \pm 0.06$	0.12
	H	-0.58 ± 0.06	-0.13 ± 0.06	0 ± 0.04	$+0.15 \pm 0.07$	0.13
	K_s	-0.58 ± 0.03	-0.09 ± 0.04	0 ± 0.04	$+0.11 \pm 0.05$	0.14

[a]Minimum root-mean-square deviation of the four image fluxes from the model prediction, in magnitudes.

7.4 Uncertainty estimation

Aside from statistical measurement uncertainty in the flux ratios, systematic errors may arise from several directions. At optical and IR wavelengths, quasar emission lines, quasar variability, or contamination from a lens galaxy or an Einstein ring may contribute. In X-rays, quasar variability is again a factor, and delays between X-ray and optical/IR observations combine with microlensing variability to contribute additional uncertainty.

7.4.1 Optical uncertainties

Quasar emission lines are thought to come from a region too large to be strongly affected by microlensing[2] [Schneider and Wambsganss, 1990]. Therefore the presence of emission line flux in our broadband measurements will cause errors if we assume we are measuring the continuum from the accretion disk. The strength and effect of these errors is very difficult to predict. In lieu of a full treatment, we allocated a 5% (0.05-magnitude) uncertainty in our flux ratios for filters into which one of the following lines has been redshifted: CIV, CIII], MgII, Hβ, or Hα. (This is roughly the percentage of the broadband flux within the filter taken up by one of these lines, in general.) Occasionally, Lyα falls in a filter, or there are two emission lines present; in these cases we allocated 0.1 magnitudes of uncertainty.

The multiple images of a strongly lensed quasar arrive with relative delays of hours to weeks because of the different paths taken by their light. Quasar variability can conspire with these time delays to mimic flux ratio anomalies. We do not expect this to be a very strong effect, because the most interesting anomalies tend to happen in pairs of images will small relative time delays. In order to quantify the effect, we extrapolated the empirical quasar variability structure function in Figure 18 of de Vries et al. [2005] using a power law: $\log(S(\tau)) = 0.8 - 0.65\log(\tau)$. This gave us an estimated standard deviation S for the quasar brightness (in magnitudes) as a function of time delay τ.

Time delays have been measured for five of the lenses in our sample. For HE0435$-$1223, RXJ0911+0551, PG1115+080, RXJ1131$-$1231, and WFIJ2033$-$4723, we used, respectively, the time delays reported by Kochanek et al. [2006], Hjorth et al. [2002], Barkana

---

[2]Some degree of broad line emission microlensing has been observed, however [e.g., Keeton et al., 2006].

[1997], Morgan et al. [2006], and Vuissoz et al. [2008]. For the remaining lenses we used the time delays predicted by our lens model (see Section 7.5). In the cases of HE 1113–0641 and WFI J2026–4536, the lens redshift is unknown, so we used $z_L = 0.7$. The resulting quasar variability uncertainties were only significant for a few quasar images (e.g., image D in RX J1131–1231 or RX J0911+0551).

Finally, a few of our lenses present special observational challenges to those who would measure their flux ratios. HE 0230–2130 is one such lens, as its image D is only $0\rlap{.}''4$ from a bright companion to the main lens galaxy. We added in quadrature an extra error equal to the change in measured brightness if 25% of the galaxy light were attributed to the quasar image. This ranged from 0.1 magnitudes in g' to 1.6 magnitudes in K_s. RX J1131–1231 is another example; its bright Einstein ring, which is due to the quasar's host galaxy, causes the PSF fitting routine to over-subtract the quasar. We fit the brightnesses of the quasar components by hand (see Section 7.3), and estimated the uncertainties as half the difference between our estimates and those of the fit. In addition, we allocated some uncertainty to images that were only marginally detected (e.g., SDSS J0924+0219 images C and D in the u' band).

For each flux ratio in each filter, we added in quadrature the uncertainties, both statistical (measurement error) and systematic (broad emission lines, quasar variability, microlensing variability, and blending with other emission). The results may be seen in Table 7.5.

7.4.2   X-ray uncertainties

Like the optical flux ratios, the X-ray ratios had uncertainties due to measurement noise and the blending of close pairs; in this case both errors were generally larger because the X-ray observations have fewer photons, and a broader PSF. There were also contributions from intrinsic quasar variability, as before. But the X-ray ratios had an additional source of error, because unlike the optical/IR ratios, they were not measured contemporaneously with the other wavelengths.

Crucial to our analysis is the assumption that the arrangement of the source and the microlenses is the same for all wavelengths. But when observations are not contempora-

neous, the source and the microlenses have the opportunity to reconfigure themselves. To estimate the magnitude of this effect, we again used a structure function; this time it was not empirical, but was derived from microlensing magnification maps (see our description of these maps in Section 8.1). For each image, we chose the appropriate map (with a mass fraction in stars of 0.1) and ran 1000 tracks across it, in random directions, measuring the RMS variation in the log of the magnification as a function of distance moved.

The conversion to a structure function (with a time delay on the abscissa instead of a distance) required the transverse velocity of the source relative to the lens. We added four velocity components in quadrature: the velocity dispersion of the stars in the lens galaxy (as estimated by our lens model), the tangential component of the velocity of the sun relative to the rest frame of the cosmic microwave background (CMB), and the two peculiar velocities of the quasar and the lens galaxy [as estimated using equation 14.10 of Peebles, 1980]:

$$
v_\perp^2 = \left(\frac{\sqrt{2\sigma_L^2}}{(1+z_L)} \frac{D_{OS}}{D_{OL}} \right)^2 + \left((370\text{km/s}) \sin\alpha \frac{D_{LS}}{D_{OL}} \right)^2
$$
$$
+ \left(\frac{\sqrt{2}(235\text{km/s})}{(1+z_S)^{3/2}} \frac{f(z_S)}{f(0)} \right)^2 + \left(\frac{\sqrt{2}(235\text{km/s})}{(1+z_L)^{3/2}} \frac{f(z_L)}{f(0)} \frac{D_{OS}}{D_{OL}} \right)^2 \quad , \tag{7.1}
$$

where D_{OL}, D_{OS}, and D_{LS} are angular diameter distances from observer to lens, observer to source, and lens to source, respectively; we use these distances to project all velocities to the source plane. The angle α is the angle between the sun's velocity with respect to the CMB rest frame and the line of sight to the lens, and $f(z)$ is the cosmological growth factor (we approximate it as $f \propto \Omega_M(z)^{0.6}$). The numerical factors for the CMB dipole velocity and present-day galaxy velocity dispersion we have taken from Lineweaver et al. [1996] and Kochanek [2004], respectively. The stellar velocity dispersion σ_L of the lens we estimate from the monopole component of our lens model (see Section 7.5) using the relation [Narayan and Bartelmann, 1996]

$$
b = 4\pi \frac{\sigma_L^2}{c^2} \frac{D_{LS}}{D_{OS}} \quad . \tag{7.2}
$$

All velocities are corrected for cosmological time dilation. Factors of $\sqrt{2}$ convert one-

dimensional velocity dispersions to two dimensions.

Multiplying this estimated source speed by the delay between our optical/IR observations and their X-ray counterparts, we determined the distance traveled by the source along the map, and from the structure function read off the predicted error in our X-ray flux ratio.

For each X-ray flux ratio, we added in quadrature the uncertainty contributions from measurement errors, intrinsic quasar variability, and microlensing variability. The resulting uncertainties are quoted in Table 7.5. In general, the largest contributions came from microlensing variability, though measurement errors were also substantial in some cases. As in the optical case, the uncertainty due to quasar variability is relatively insignificant.

7.5 Modeling the lenses

We used the `Lensmodel` program [Keeton, 2001] to create models of each lens. The models were constrained by the positions of the four lensed images, and that of the lensing galaxy, a total of ten constraints. We did not use fluxes for constraints, since most of our lenses suffer from flux ratio anomalies. Nor did we use time delays.

Positions for the quasar images and lens galaxies came from the CASTLES survey.

Our default model consisted of a singular isothermal sphere for the lensing galaxy, with a quadrupole component of the potential provided by a constant external shear. With the position of the lens fixed, this model has five free parameters: the monopole strength of the lens, the magnitude and direction of the shear, and the position of the source.

In some cases, such as HE 0435−1223, this simple model fit the image positions well. But in several cases the χ^2 goodness-of-fit was poor enough to warrant further sophistication. In these cases, we made changes to the model motivated by the appearance of the lens galaxy.

The lensing galaxy of HE 0230−2130 has a prominent companion, located close to image D. We modeled this companion as a second isothermal sphere, fixing its position to its *HST* measured value but allowing its mass to vary (because its position was fixed, we did not need to steepen its density profile, as in Section 5.3). Despite only adding one free parameter to the model, this addition improved the fit considerably.

We followed a similar strategy when modeling MG J0414+0534, RX J0911+0551, and

119

WFI J2033−4723, each of which displays a faint smudge in its *HST* image which is arguably a satellite to the lens galaxy. Adding secondary lenses at the positions of the smudges improved the fits to acceptable levels.

The lens galaxy in PG 1115+080 does not have a nearby companion, but is a member of a small galaxy group centered to the southwest of the lens. We explicitly modeled the group as a second isothermal sphere for this lens. We parameterized its position using polar coordinates, and allowed its mass and distance from the main galaxy to vary while fixing its position angle to that of the brightest galaxy in the group. We did not include an external shear in this fit.

Finally, the lens galaxy in SDSS J1330+1810 displays significant ellipticity. In this case we used an isothermal ellipsoid instead of including an external shear. We allowed the ellipticity and position angle to vary, along with the galaxy position, for a total of seven free parameters. Since there are no *HST* data for this lens, we used our measured image positions for constraints (see Section 7.3 and Table 7.3). SDSS J1330+1810 was the only lens system where an isothermal ellipsoid made for a better fit than an isothermal sphere with external shear.

We used the local convergence κ and shear γ predicted at the image positions by these models to generate our microlensing magnification maps (see Section 8.1). We also used the magnifications implied by κ and γ to contrast with our measured flux ratios. These magnifications are listed in Table 7.6. We note that in the case of MG J0414+0534, we did not contrast our measured flux ratios with the magnifications predicted by our model, but with the mid-IR fluxes reported by Minezaki et al. [2009] (see Section A.2).

The salient features of our best-fit models are listed in Table 7.6. Though these models are very simple, they should be sufficient for our purposes, because of the relative insensitivity of flux ratio predictions to "reasonable" variations in lensing potentials [Metcalf and Zhao, 2002]. Because there is some variation in the predicted flux ratios with different models, we allocated a model uncertainty to our flux ratios at a level of 0.03 magnitudes for merging cusp or fold images and 0.05 magnitudes for the other images. These uncertainties were added in quadrature to the other uncertainties described in Section 7.4.

Table 7.6. Lens model parameters

Quasar	Primary lens			Secondary lens			Linear Magnification			
	b	γ	ϕ_γ[a]	b_2	x_2[b]	y_2[b]	HM	HS	LM	LS
HE 0230−2130	0."87	0.11	−60.°0	0."33	− 0.283	+0.974	+9.42	−9.65	+4.95	−1.35
MG J0414+0534	1."14	0.11	+74.°6	0."12	− 0.385	+1.457	+22.9	−24.2	+6.23	−3.11
HE 0435−1223	1."20	0.078	−13.°8	$\cdots$	$\cdots$	$\cdots$	+7.49	−7.90	+7.14	−4.73
RX J0911+0551	0."97	0.27	+ 7.°2	0."24	− 0.754	+0.665	+11.0	−5.96	+1.97	−4.99
SDSS J0924+0219	0."87	0.063	+84.°8	$\cdots$	$\cdots$	$\cdots$	+14.9	−13.0	+6.62	−6.55
HE 1113−0641	0."33	0.040	+37.°7	$\cdots$	$\cdots$	$\cdots$	+15.8	−16.7	+12.6	−9.59
PG 1115+080	1."03	$\cdots$	$\cdots$	2."57	−10.866	−5.300	+19.7	−18.9	+5.09	−3.37
RX J1131−1231	1."86	0.16	−73.°6	$\cdots$	$\cdots$	$\cdots$	+13.2	−22.7	+12.6	−1.05
SDSS J1138+0314	0."67	0.10	+32.°6	$\cdots$	$\cdots$	$\cdots$	+7.17	−6.68	+5.17	−3.64
SDSS J1330+1810	0."94	0.16[c]	−32.°2[c]	$\cdots$	$\cdots$	$\cdots$	+27.1	−27.2	+8.41	−5.50
WFI J2026−4536	0."66	0.11	−90.°0	$\cdots$	$\cdots$	$\cdots$	+13.7	−11.5	+3.78	−4.01
WFI J2033−4723	1."07	0.11	+36.°0	0."25	+ 0.229	+2.02	+6.04	−3.80	+3.88	−2.46

[a]All angles are measured in degrees east of north.

[b]Position of secondary galaxy, relative to main lensing galaxy, in arcseconds. The positive directions of x and y are west and north, respectively.

[c]Ellipticity and position angle of the lens galaxy.

Chapter 8

Accretion disk structure:

Estimating disk sizes

We have developed a quantitative method for estimating the angular size of the quasar accretion disk, using our measured flux ratios, at a range of wavelengths. At UV and optical rest wavelengths, the disk must be small enough that microlensing is able to produce the observed flux ratio anomalies, but large enough to attenuate the stronger X-ray anomalies.

8.1   Microlensing magnification maps

To simulate the microlensing of a finite-size source, we use magnification maps created using the inverse ray-tracing technique of Wambsganss et al. [1990]. Each of the four images in each lens has a convergence κ and a shear γ which determine its magnification; these are specified by the model of the lens (see Section 7.5). The convergence is proportional to the surface mass density along the line of sight. To create a magnification map, we divide up the convergence into a part due to smoothly-distributed matter (e.g. dark matter) and a part due to point masses (baryonic matter in stars). We vary the mass fraction allotted to stars in logarithmic steps between 1.47% and 100% to create for each quasar image a family of 12 magnification maps, holding the total convergence fixed.

We specify a broken power-law as the mass function for the microlens stars. Between $0.08\,M_\odot$ and $0.5\,M_\odot$, its logarithmic slope is -1.8; above $0.5\,M_\odot$ it steepens to -2.7. This
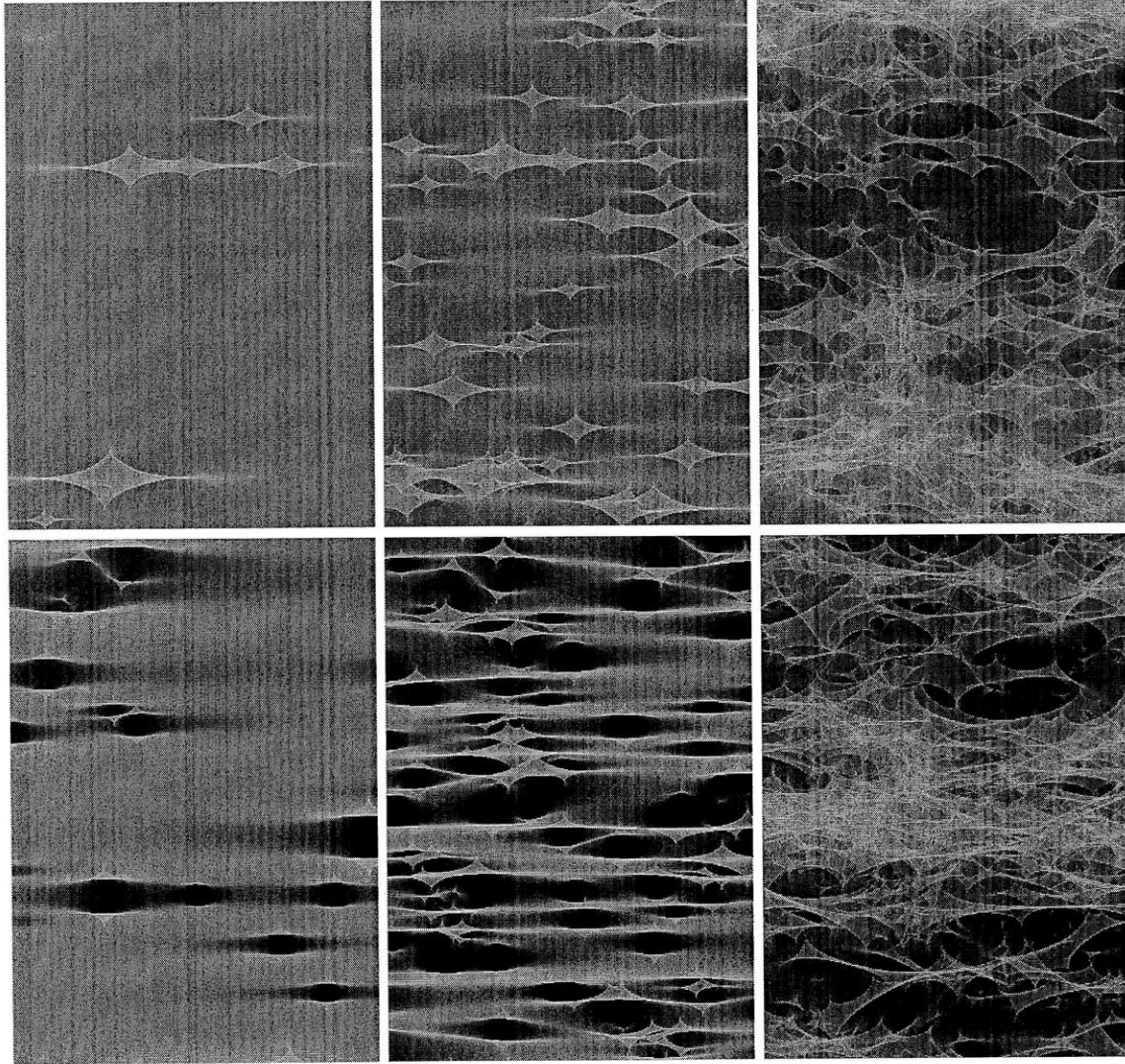
Figure 8-1 Examples of microlensing magnification maps. Top row: positive parity (minimum) image. Bottom row: negative parity (saddle point) image. The first column has 1.5% of the surface mass density in stars; the second 10%, and the third column 100%. The grayscale extends from 3 magnitudes of demagnification (black) to 3 magnitudes of magnification (white). The regions shown are 4.5×6.5 solar-mass Einstein radii. The stars are scattered randomly across the sky, and their masses are drawn from our broken power law mass function (see Section 8.1).
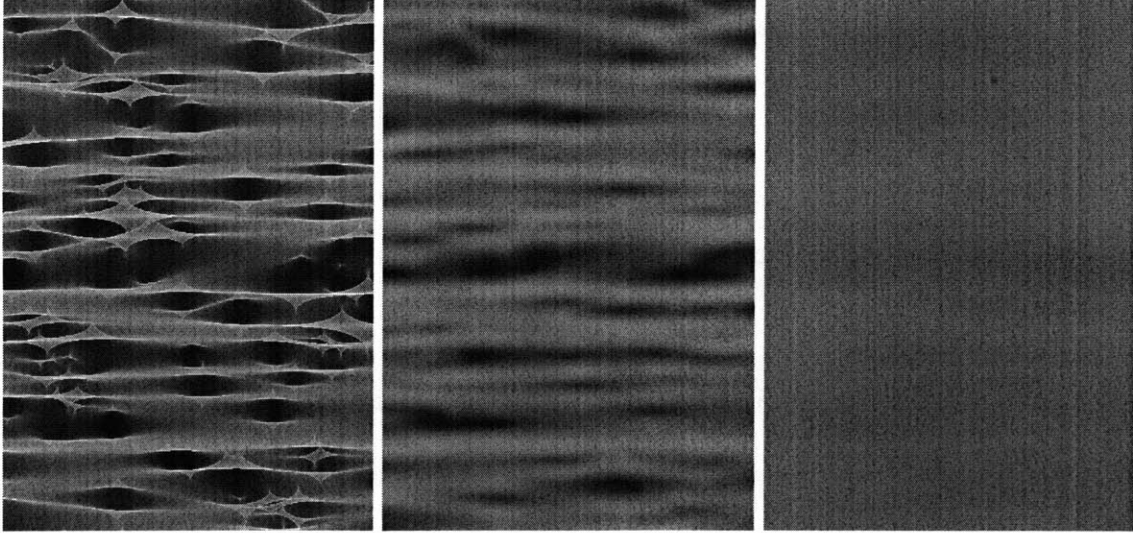
Figure 8-2 Example of the effect of convolving a map with a finite-size source. Left: No convolution. Middle: Convolution with a source with half-light radius $10^{-0.8}$ times the size of a solar-mass Einstein radius. Right: Convolution with a source with a half-light radius equal to a solar-mass Einstein radius. Dimensions and grayscale are identical to those of Figure 8-1.

mass function is very similar to that of Kroupa [2001]. We cut off the mass function at $1.5\,M_\odot$, because the stellar populations in these early-type lens galaxies are typically old. With this mass function, the average microlens mass is $\langle m \rangle = 0.247\,M_\odot$.

Each map provides the deviation in the magnification of its quasar image from that produced by a smooth mass distribution, as a function of the position of the source. They are 2000 pixels on a side; this is 20 times the Einstein radius of a solar-mass microlens star. When projected back to the quasar, the side length is $\sim 5 \times 10^{17}$ cm for our sample (the exact number depends on the redshifts of the lens and the quasar). The pixel size is thus $\sim 2.5 \times 10^{14}$ cm, or a few gravitational radii for a $10^9 M_\odot$ black hole. This is much smaller than the size of the optical accretion disk. Some examples of these magnification maps are provided in Figure 8-1.

We convolve these magnification maps with circular Gaussian kernels of varying half-light radii, to represent the smoothing effect of a finite source brightness distribution. Mortonson et al. [2005] showed that microlensing variations are mainly sensitive to the half-light radius of a source rather than the details of its radial profile, so a Gaussian shape was deemed sufficient. Our product is then a family of magnification maps for each quasar

image with two parameters: the stellar mass fraction and the half-light radius of the source. We marginalize over the former in the next section, as a detailed investigation of the ratio of stellar to dark matter in the lens galaxies is outside the scope of this thesis [but see Pooley et al., 2009]. The effect of the convolution is to blur the map and reduce its dynamic range; this is demonstrated on an example map in Figure 8-2.

8.2 A Bayesian estimation method using optical flux ratios

A suitably normalized histogram of a magnification map is an estimate of the probability distribution for deviations from the macrolensing model magnification. Figure 8-3 shows four such magnification histograms, one for each image in SDSS J1330+1810, for a particular source size and stellar mass fraction. The abscissa of these plots denotes the microlensing deviation from the model in magnitudes. We use 16 bins per magnitude in this figure, and also throughout the remainder of our analysis. Atop the histograms have been plotted vertical lines, indicating the observed deviation from the model in the i' band.

Though we have plotted four vertical lines in Figure 8-3, we have only actually measured three magnification ratios among the four images. Thus, the "center of mass" position of the four lines is unknown. In Figure 8-3 it is set to zero, but in reality the four lines are free to slide from side to side in formation. Each position corresponds to a distinct value of the source quasar luminosity.

As the half-light radius of the source increases, the histograms will become narrower. As this brings each vertical line (representing an observed data point) farther into the wings of its associated probability distribution, the likelihood of this source size will fall. We use a Bayesian method to find these likelihoods. Assuming a uniform prior probability distribution for source size,

$$\mathcal{L}(\text{size}|\text{data}) \propto P(\text{data}|\text{size}) \quad . \tag{8.1}$$

To find the total probability of observing the flux ratios that we do, we must marginalize over the unknown quasar luminosity. To do this, we shift the four histograms horizontally,
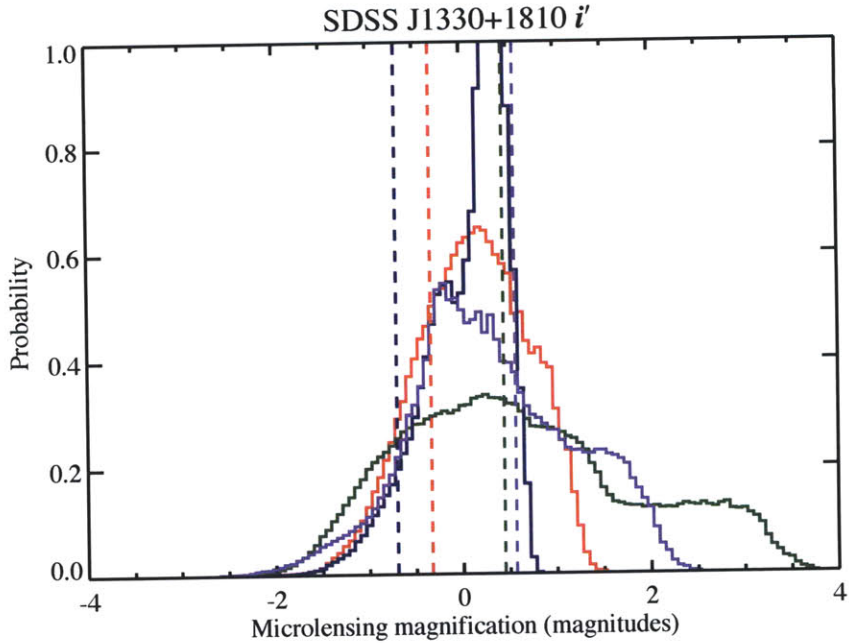
Figure 8-3 Histograms derived from magnification maps for the four images of SDSS J1330+1810, with a source size 10% of a solar-mass Einstein radius. Images A, B, C, and D are red, green, blue, and purple, respectively. Flux ratios from our i' band data have been overplotted in dotted lines. The abscissa denotes deviation from the predicted flux ratios; if the dotted lines all fell at zero, the lens would have no flux ratio anomaly. Magnifications are in magnitudes, so positive numbers denote demagnification.
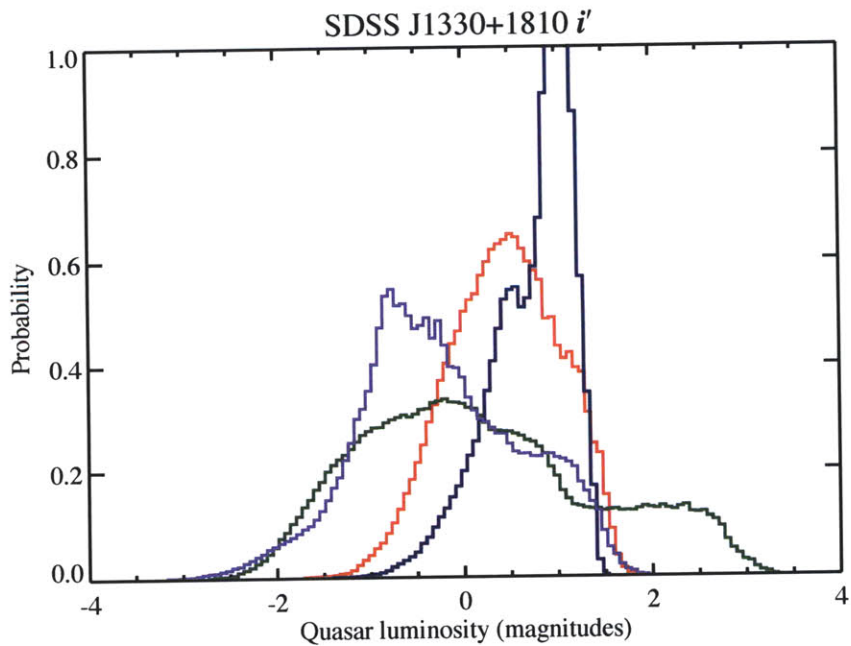
Figure 8-4 Histograms identical to those in Figure 8-3, but shifted so that the observed magnifications line up. The abscissa now denotes quasar luminosity (in magnitudes relative to some arbitrary standard); see Section 8.2 for an explanation.
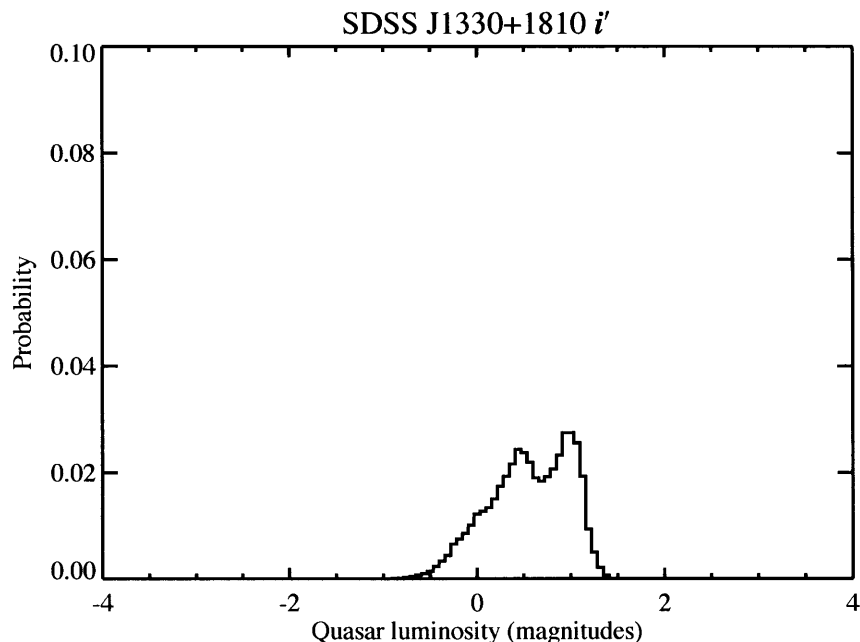
Figure 8-5 Product of the four shifted histograms in Figure 8-4. The total area under this curve is the probability of observing flux ratios we did, given the source size we chose (see Figure 8-3).

together with their associated measurements, until the vertical lines fall atop one another. The shifted versions of the four histograms in Figure 8-3 are shown in Figure 8-4. We then multiply the four shifted histograms to obtain a single "product histogram" (shown in Figure 8-5). This is mathematically equivalent to marching the vertical lines across the four original histograms in lockstep, bin by bin, and tallying the product of the bins occupied by lines. For this reason, in Figures 8-4 and 8-5 the abscissa denotes quasar luminosity rather than microlensing magnification. To find the total probability of observing these particular flux ratios, we integrate under the product histogram. This process is repeated for several source sizes, in order to find the right hand side of Equation 8.1 for each. The resulting list of probabilities serves as a relative likelihood distribution for the source size.

Since each bin in the product histogram corresponds to a different quasar luminosity, we impose a weighting when integrating under it, to account for the scarcity of bright quasars relative to fainter quasars. For our weighting function we take a power law with slope -2.95; this is the slope (for bright quasars) of a redshift-independent quasar luminosity function estimated by Richards et al. [2006].
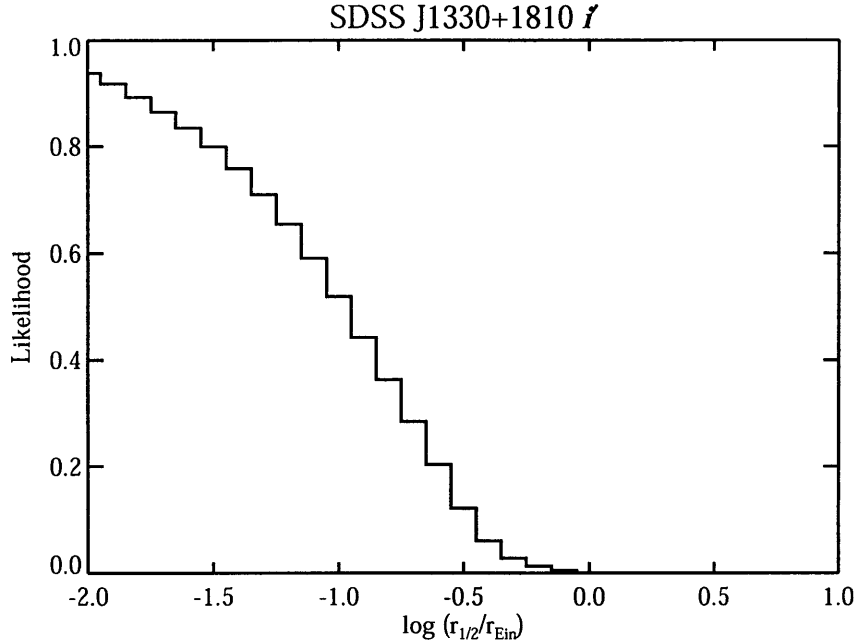
Figure 8-6 Likelihood distribution for the size of SDSS J1330+1810, using the i' band data. The histograms were convolved with the measurement uncertainties, and the quasar luminosity function was used as a weighting factor when integrating the product of the histograms. A logarithmic prior was used. See Appendix B for the complete set of likelihood distributions.

It is worth noting that because our source sizes are equally spaced in logarithmic space, our prior is a logarithmic one, that is, uniform in log space. For completeness, we also use a linear prior; this simply involves multiplying the likelihood distribution by a power law of slope 1.

We repeat this technique for each of the 12 stellar mass fractions and take a weighted average of the resulting likelihood distributions. The weights are a measure of how likely we view each stellar mass fraction to be; we interpolated them from the values shown in Figure 6 of Pooley et al. [2009].

Figure 8-6 shows the likelihood distribution resulting from the use of this technique on the i' band flux ratios of SDSS J1330+1810. (More accurately, this figure shows the result of the refinements in Section 8.3). The results for the rest of the filters are given in Appendix B.

Examination of Figure 8-6 demonstrates the ability of this method to rule out large sizes (i.e., greater than an Einstein radius). This decrease in likelihood to zero occurs when two

of the shifted histograms become narrow enough that they no longer overlap at all; at this point the likelihood is zero.

There is no such decrease for small source radii. This is to be expected on a common-sense basis, since the optical flux ratio anomalies simply indicate that the source is undergoing microlensing. To set a lower limit on the size, we must discern why the observed anomalies are not stronger than they are — finite-size attenuation, or simply the fact than the source at the time of observation fell by chance in a non-extreme region of the magnification map? Though some size discrimination is possible by comparing the likelihood distributions derived from blue filters versus red filters, the ability to rule out very small sizes will only come from comparing the optical likelihood distributions to those derived from X-ray observations (see Section 8.4).

8.3   Taking uncertainties into account

This technique treats the measured flux ratios as perfectly known quantities. They determine the distance by which the magnification histograms are shifted before being multiplied together. The width of the final likelihood distribution for the source size is the result of the width of the microlensing histograms (i.e., the statistical nature of quasar microlensing).

However, there are significant uncertainties in our measured flux ratios. The various sources of uncertainty are discussed in detail in Section 7.4, but they include measurement uncertainties, confusion of close pairs of images, lensing time delays, emission line contamination, and non-contemporaneous observations. The upshot is that the uncertainties on our flux ratios range from a few percent to factors of 2 or more.

The effect of uncertainties is to broaden the spikes representing the measured flux ratios into Gaussians. We must now consider a range of possible shifts for the four histograms. The easiest way to do this is to convolve the histograms with Gaussian kernels representing the uncertainties in the shifts. It may be illuminating to think of this as "adding the variances" due to uncertainties to those due to the width of the histograms. Because the histograms are broadened by the convolution, they overlap more than they did previously, causing the likelihood distribution for source size to widen as well.

130

8.4 Adding X-ray flux ratios to the mix

SDSS J1330+1810, the lens we chose for the examples in the previous section, is unique among our sample of lenses in that it has never been observed in X-rays. But for the remainder we have at least one measurement of the X-ray flux ratios. In general, these flux ratios deviate from smooth lens model predictions more strongly than do the optical ratios, leading us to believe that the X-ray emitting region is much smaller than the optical emitting region [Pooley et al., 2007, see Chapter 5].

We again wish to find the value of the right hand side of Equation 8.1, but this time, we want the probability of observing *both* the X-ray and optical flux ratios simultaneously, given a source size. Because we estimate that the X-rays originate from a very compact region, we assume the X-ray ratios are drawn from the original (unconvolved) magnification distribution. Then, for each source size, we construct a two-dimensional histogram, as follows. Let O be the magnitudes by which the optical flux deviates from the model-predicted value, and X be the same in X-rays. Then we tally each pixel in a bin whose two coordinates O and X are given by the pixel's value in the convolved map and its value in the unconvolved map, respectively. This histogram, after appropriate scaling, is the joint probability distribution for the optical and X-ray microlensing magnifications; it is the 2D generalization of the histogram in Section 8.2. Two such histograms, corresponding to images A1 and A2 of PG 1115+080, are shown in Figure 8-7.

The rest of the analysis proceeds much like the 1D case. The joint distributions for the four components of a given lens are shifted in two dimensions by their measured flux ratios and multiplied together to obtain the product distribution, which is then summed to obtain the likelihood for the current source size.

For very small source sizes, the two maps from which each histogram is constructed are nearly identical, so the histogram lies nearly along the line $X = O$. So for this source size to be assigned any significant likelihood, the optical and X-ray shifts must be the same. As the source size increases, the histogram's extent in the O direction decreases, until it is nearly aligned with the X axis. In this case, the optical shifts must be nearly zero for the likelihood to be appreciable. This evolution of the 2D histogram is shown in Figure 8-8.
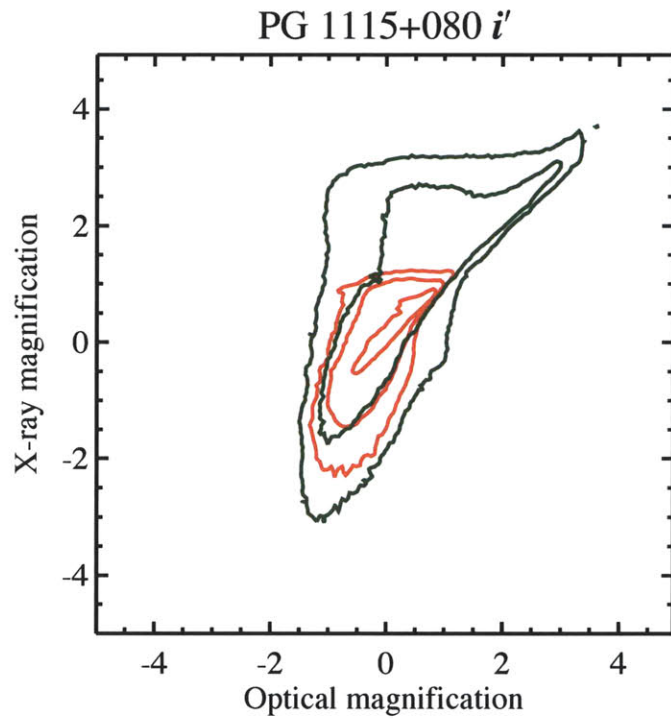
Figure 8-7 Two-dimensional histograms derived from pairs of magnification maps for PG 1115+080, for a compact X-ray source and an optical source 10% the size of a solar-mass Einstein radius. Red: image A1. Green: image A2. Images B and C are suppressed for clarity. The histograms are already shifted according to the observed flux ratios. The axes signify deviation from the predicted magnification, in magnitudes; positive numbers denote demagnification.
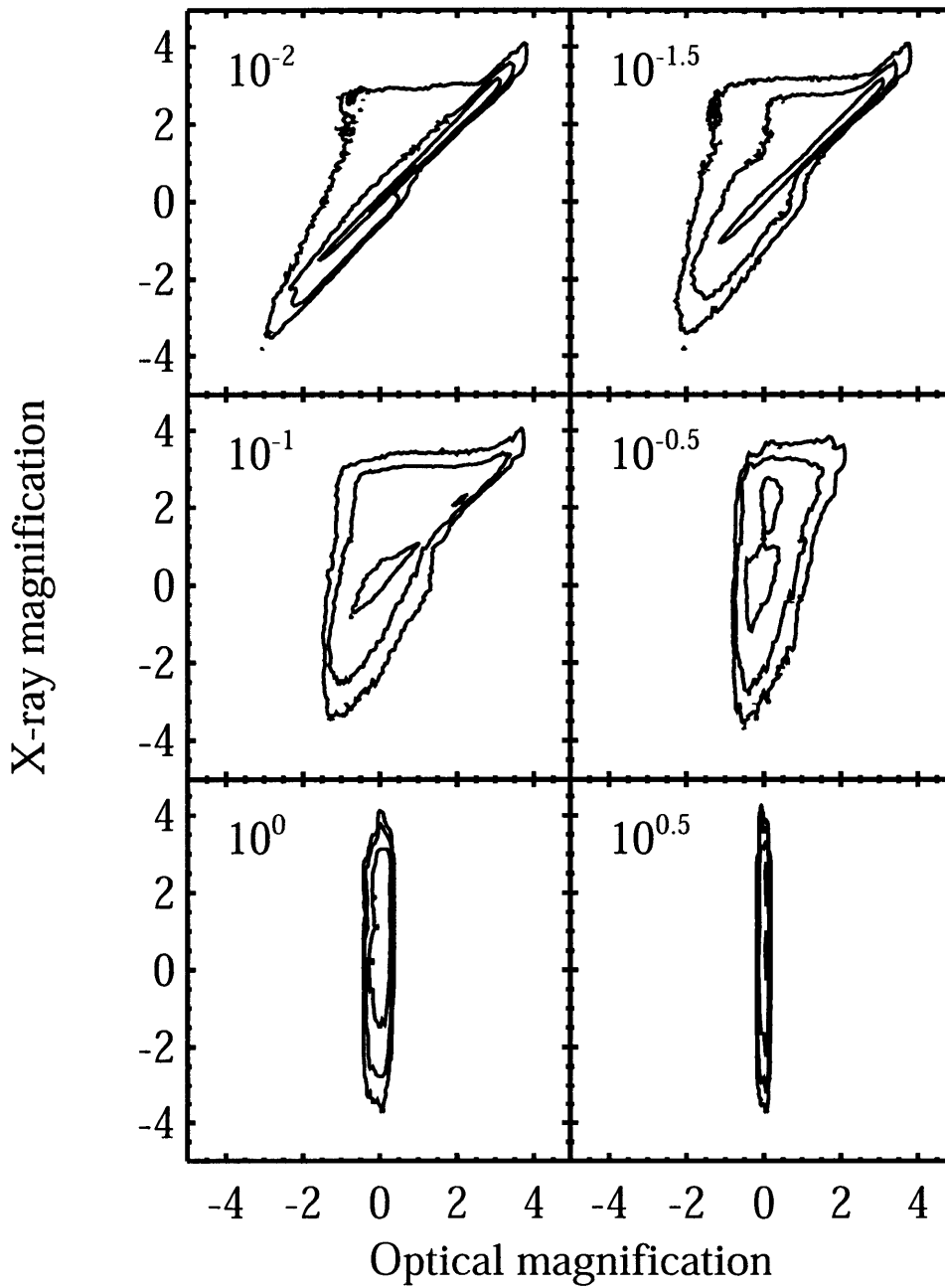
Figure 8-8 Two-dimensional histogram for image A2 of PG 1115+080. On the horizonal axis is microlensing magnification at optical wavelengths, in magnitudes. On the vertical axis is X-ray microlensing magnification. Contours are logarithmically spaced. At the top left of each plot is the half-light radius of the optical source, in units of a solar-mass Einstein radius. As the optical source gets larger, the histogram narrows in the horizontal direction.

133

In section 8.2 we applied a weighting function to account for the quasar luminosity function. Here we expand this treatment to include not only the luminosity function, but the correlation between X-ray and optical flux in quasars.

The first component of our new weighting function enforces the correlation between optical and X-ray quasar luminosities usually parameterized using

$$\alpha_{OX} \equiv 0.3838 \log(L_{2\,\mathrm{keV}}/L_{2500\text{Å}}) \quad . \tag{8.2}$$

According to Gibson et al. [2008], $\alpha_{OX} = -0.217 \log(L_{2500\text{Å}})$ plus a constant. This implies that $X = 0.4346O$ plus a constant. Their scatter in α_{OX} is about 0.1, corresponding to 0.65 magnitudes. So we construct a band centered on a line with a slope of 0.4346 in the OX plane, with a Gaussian cross-section. In order to be conservative, we double the scatter and set the width of the Gaussian to correspond to $\sigma = 1.3$ magnitudes. The intercept of the line we adjust so that the line falls on the "center of mass" of the product histogram.

The second component of our weighting function accounts for the quasar luminosity function. In Section 8.2 we used a power-law with slope -2.95. We recycle this luminosity function now, and apply it in the direction along the line of correlation. Note that the luminosity function for X-ray selected bright quasars has the very similar slope of -2.8, according to Silverman et al. [2008].

We multiply the product histogram by both of these weighting functions before integrating it. They take the luminosity function into account, and ensure that scenarios with a large optical luminosity and a small X-ray luminosity, and vice versa, are suppressed.

This technique is effective at ruling out very small sizes for the optical emitting region. Indeed, the likelihood of an optical point source must be zero unless the optical and X-ray flux ratios are identical (or at least consistent).

As before, we iterate this technique over magnification maps representing a variety of stellar mass fractions, and marginalize the likelihood distributions.

8.5 Uncertainties revisited

A new wrinkle presents itself once we start considering the uncertainties in the X-ray flux ratios. Because the size estimates in all the optical/IR filters depend on the same X-ray flux ratios, their errors (that is, the widths of the likelihood distributions) are correlated.

To properly treat the correlations in the source size likelihood distributions, we use a Monte Carlo method to determine the covariances between the sizes in various filters. Instead of convolving our two-dimensional histograms with the measurement errors, we calculate the most likely size for each filter, for each of a sample of 1000 sets of flux ratios from the normal distributions implied by our measurement errors. This allows us to construct the covariance matrix C, where $C_{ij} = \mathrm{Cov}(r_{1/2,i}, r_{1/2,j})$ and i and j are filter indices. The diagonal elements of the matrix are, of course, simply the variances of the half-light radii due to measurement uncertainty.

To this covariance matrix we add the variance due to the intrinsic width of the two-dimensional histograms:

$$\mathcal{W}^{-1} = C + S \quad , \tag{8.3}$$

where $S_{ij} = \left(\sigma^i_{\mathrm{hist}}\right)^2$ for $i = j$ and $S_{ij} = 0$ otherwise. In turn, $\left(\sigma^i_{\mathrm{hist}}\right)^2$ is the variance in the half-light radius in the ith filter due to the width of the histograms; it is derived from the 68% confidence interval of the original (no measurement uncertainty) likelihood distribution. We have written the left hand side of Equation 8.2 as an inverse, so that $\mathcal{W}$ is the weight matrix used in the least-squares fit in Equation 9.3.

8.6 Source size as a function of wavelength

After running the Monte Carlo error propagation described in the last section and calculating the covariance matrix for the uncertainties on the source half-light radii, we averaged for each filter the 1000 likelihood distributions representing different realizations of the measured flux ratios. An example of this final distribution is shown in Figure 8-9; the full sample, with linear and logarithmic priors, is given in Appendix B.

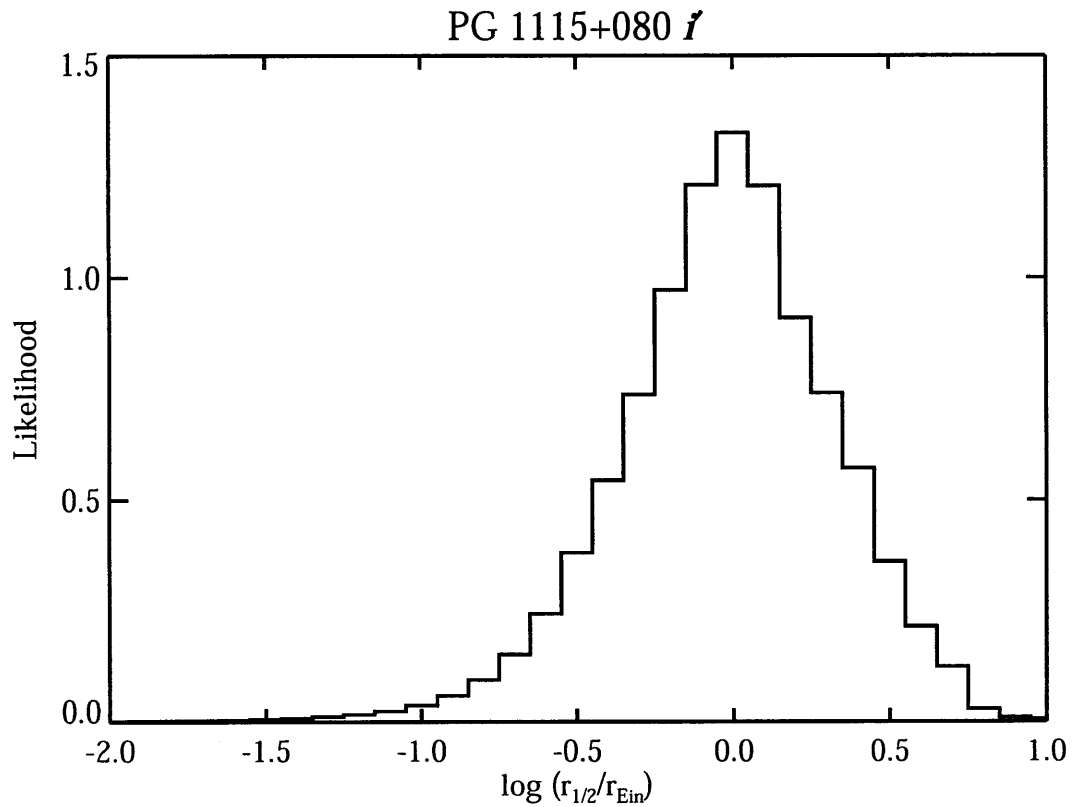In the next chapter we describe how we interpret these likelihood distributions, including

Figure 8-9 Likelihood distribution for the size of PG 1115+080 in the i' band, resulting from considering both i' band and X-ray flux ratios. The Monte Carlo method described in Section 8.5 was used to account for measurement uncertainties. A logarithmic prior was used. See Appendix B for the complete set of likelihood distributions.

fitting power-law models to the disk size as a function of wavelength.

8.7 An alternative analysis method

Our analysis takes advantage of the fact that the flux ratios in a given optical/IR filter and those in X-rays are simultaneously different, both from each other, and from the model predictions. We create two-dimensional histograms to serve as joint probability distributions. But because we compare the X-rays to each filter in turn, correlated errors arise in our size estimates. We must then use a Monte Carlo method to characterize the correlations.

The covariances we calculated in Section 8.5 are moments of the full nine-dimensional joint probability distribution for the flux ratios in 8 optical/IR bands and one X-ray band. This suggests an alternative strategy for analyzing the flux ratios: generalize from two dimensions to nine, creating a 9D histogram for each quasar image from an ensemble of nine magnification maps, one unsmoothed (for the X-ray magnification) and the others smoothed by various sizes. The sizes would be chosen by fixing a size offset and power-law slope with wavelength (the same two parameters for which we fit in the next chapter).

The 9D histograms would then be convolved with measurement errors (no need for Monte Carlo techniques), shifted, and multiplied, and the product summed (with the appropriate weighting for luminosity function, etc.). The resulting number would be the relative likelihood of the size and slope chosen when constructing the histograms. A new size and slope would then be chosen, and the process would be repeated.

This method would not give rise to correlated errors in the size estimates. The end result would be a two-dimensional likelihood distribution for the size of the accretion disk and the slope with wavelength.

In practice, we have not been able to carry out this analysis due to computational limitations. The limiting step is the convolution of the histogram with Gaussian measurement errors. In nine dimensions, the computational and (more importantly) storage requirements are beyond our reach at this time.

Chapter 9

Accretion disk structure: Results and conclusions

Chapter 8 described how we measured the half-light radius of the accretion disk of each lens in our sample, at a variety of wavelengths. In this chapter, we compare these measurements with the predictions of the standard thin disk theory (see Section 6.2) and with similar measurements reported elsewhere.

9.1   Determining the source sizes

The likelihood distributions produced in the previous chapter are all in units of $r_{1/2}/r_{\mathrm{Ein}}$, where r_{Ein} is the Einstein radius of a solar mass microlens in the lensing galaxy, projected back to the source plane (see Equation 1.6). From this point on, we multiply our size estimates by this scaling factor. If we have seriously misestimated the mass function of the stars in the lensing galaxy, this scaling will introduce a systematic shift in the physical sizes; a rule of thumb is that the scaling is proportional to the square root of the average mass divided by the Hubble constant:

$$r_{1/2} \propto \left(\frac{\langle m \rangle}{h_{70}} \right)^{1/2} \quad . \tag{9.1}$$

In Figures 9-1 through 9-12 we plot the half-light radius of the accretion disks as a

function of rest wavelength. The medians and modes of the likelihood distributions are plotted as squares and crosses, respectively. The error bars come from the covariance matrix C and the width of the likelihood distributions (see Section 8.5).

For each lens we fit a power law to the medians of the distributions:

$$r_{1/2} = r_{1/2,\text{central}} \left(\frac{\lambda}{\lambda_{\text{central}}} \right)^{\nu} \quad , \tag{9.2}$$

where λ_{central} is the geometric mean of our observed wavelengths, corrected for cosmological redshift, and $r_{1/2,\text{central}}$ is the half-light radius of the source at that wavelength. Since the errors on the medians are correlated, we minimize the statistic

$$\chi^2 = (\mathbf{y} - \mathbf{m})^{\text{T}} \cdot \mathcal{W} \cdot (\mathbf{y} - \mathbf{m}) \quad , \tag{9.3}$$

where $\mathbf{y}$ and $\mathbf{m}$ are the data and the power-law model, respectively, and $\mathcal{W}$ is the weight matrix defined in Equation 8.2. The best-fit power law is plotted in Figures 9-1 through 9-12 as a dashed line. The parameters thus determined are listed in Table 9.1.

Finally, we plot the prediction of the standard thin disk model as a solid line in these figures. This prediction comes from Equation 6.5, where we use 0.25 for f_{Edd}, 0.15 for η, and the values from Table 6.1 for M_{BH} (we use the virial estimates where possible, and fall back on the estimates based on bolometric luminosity). There are no free parameters, so it is not a fit.

The choice of prior has a small effect on the disk size measurements. In general, the linear prior favors larger sizes than the logarithmic prior does. This is to be expected, since it is more heavily weighted at larger sizes. In general, the difference in $r_{1/2}$ is ~ 0.2 dex. The measured slope is unaffected by the choice of prior, in most cases (the exception being HE 0230−2130). Since a logarithmic prior seems more appropriate for the disk size, we focus on these results.

9.2 Comparison with the thin disk prediction

9.2.1 Disk size as a function of wavelength

For all of the lenses in our sample, the measured overall sizes are larger than predicted by the thin disk model, by factors ranging from ~ 2 to more than 30. The logarithm of this factor is listed for each quasar in Table 9.1. Comparing the logarithmic offset to our errors in $\log(r_{1/2})$, we see that we have ruled out the thin disk normalization by at least 3σ in all cases except MG J0414+0534, and as many as 10σ in some cases. This result is completely consistent with that of Pooley et al. [2007], though our current analysis method is more quantitative.

The average offset between $r_{1/2,\text{central}}$ and the thin disk prediction at the same wavelength is 0.89 dex — a factor of 7.5. A chi-square test yields a χ^2 of 36 per degree of freedom when comparing the measured sizes to expected sizes.

With the exception of MG J0414+0534, all of our quasars show power-law slopes ν flatter than the expected $\lambda^{4/3}$ dependence by 1.2 to 2.6σ or more. Even though these do not individually rule out the thin disk slope at high significance, the combination of ten out of eleven lenses makes a convincing case that quasar accretion disks have slopes flatter than 4/3. Treating the measurement for each quasar as an independent constraint, the average value of ν is 0.20 (if we exclude HE 0230−2130, MG J0414+0534, and WFI J2033−4723, the average slope rises to 0.31). Running a chi-square test on all eleven lenses, we find that comparing the slopes to the expected 4/3 yields a χ^2 of 5.5 per degree of freedom. It is worth noting that nearly all of our measured slopes are consistent with $\nu = 0$ — an accretion disk with size independent of wavelength!

Since the temperature profile is given by $T_{\text{eff}} \propto r^{-1/\nu}$, our result implies that the effective disk temperature is a steeply falling function of radius.

MG J0414+0534 is the one quasar with a slope ν consistent with 4/3. It is intriguing that the same quasar that matches the thin disk size prediction is also consistent when it comes to slope. MG J0414+0534 is also the only radio-loud quasar in our sample. It is perhaps too early for such speculation, but it may be that this quasar is in a different accretion state from the rest of our sample.

Two lenses present an interesting puzzle: both HE 0230−2130 and WFI J2033−4723 seem to decrease in size with wavelength. This result does not seem to arise from a flaw in our analysis method, since the flux ratios themselves become more anomalous with wavelength, implying a smaller source size (see Table 7.5). It cannot be due to microlensing variability, since the optical/IR measurements are coeval. It is difficult to imagine a physical scenario where this takes place; it seems very unlikely, purely on energy grounds, that the disk would be hotter (i.e., bluer) at large sizes than at small sizes. Further observation of these lenses at a range of wavelengths will shed more light on this question.

9.2.2 Disk size as a function of black hole mass

In Figure 9-13 we plot the dependence of the disk's half-light radius on black hole mass at fixed rest wavelength, using 11 of our 12 lenses (we excluded SDSS J1330+1810). We choose 2500 Å for our wavelength in order to match that used by Morgan et al. [2007]. We use the best-fit power law from Section 9.1 to find the 2500 Å size; Morgan et al. [2007] had to extrapolate from single-wavelength measurements. Like this previous study, we find the expected $r_{1/2} \propto M_{\mathrm{BH}}^{2/3}$ dependence (see Equation 6.5). However, our results disagree with those of Morgan et al. [2007] when it comes to the normalization of the relation — where they find agreement with thin disk models, we find an overall offset of one order of magnitude. The only quasar that is consistent with the prediction is MG J0414+0534.

The best-fit slope for $r_{1/2}$ versus M_{BH} is 0.42 ± 0.09. The χ^2 value per degree of freedom for this fit is 6.1, indicating that there is some scatter (though this high value is partially due to unmodeled errors in the black hole mass estimates).

9.2.3 Ruling out systematic errors

The discrepancy between our results and the expectations of the thin disk model obliges us to ensure that our analysis method is not affected by systematic errors. Perhaps an unforeseen systematic has crept in, causing a bias toward larger disks or a flatter dependence of size on wavelength. The latter is very plausible: if the microlenses happen to be arranged so that the microlensing anomaly of a quasar image is near zero, its flux ratio will be fairly independent of wavelength. Of course, this would have to happen to all four of the images

Table 9.1. Best-fit parameters for disk size vs. wavelength

Quasar	λ_{central}[a] (angstroms)	Logarithmic Prior $\log(r_{1/2,\,\text{central}})$	$\log(r_{1/2}/r_{\text{pred}})$	ν	Linear Prior $\log(r_{1/2,\,\text{central}})$	$\log(r_{1/2}/r_{\text{pred}})$	ν
HE 0230−2130	2763	16.17 ± 0.19	$+1.31$	-0.80 ± 0.64	16.68 ± 0.18	$+1.82$	-0.25 ± 0.63
MG J0414+0534	3075	15.90 ± 0.19	$+0.11$	$+1.50 \pm 0.84$	16.10 ± 0.16	$+0.31$	$+1.49 \pm 0.74$
HE 0435−1223	3250	16.09 ± 0.19	$+0.64$	$+0.67 \pm 0.55$	16.37 ± 0.16	$+0.93$	$+0.55 \pm 0.49$
RX J0911+0551	2299	15.09 ± 0.16	$+0.71$	$+0.23 \pm 0.43$	16.29 ± 0.18	$+0.90$	$+0.24 \pm 0.46$
SDSS J0924+0219	3462	15.79 ± 0.16	$+0.75$	$+0.17 \pm 0.49$	15.97 ± 0.13	$+0.92$	$+0.19 \pm 0.42$
HE 1113−0641	4438	15.86 ± 0.18	$+0.74$	$+0.05 \pm 0.49$	16.03 ± 0.11	$+0.91$	$+0.05 \pm 0.38$
PG 1115+080	3212	16.72 ± 0.12	$+1.02$	$+0.40 \pm 0.45$	16.90 ± 0.11	$+1.20$	$+0.45 \pm 0.39$
RX J1131−1231	5270	15.55 ± 0.14	$+0.43$	$+0.40 \pm 0.50$	15.80 ± 0.12	$+0.69$	$+0.20 \pm 0.46$
SDSS J1138+0314	2540	16.01 ± 0.19	$+1.44$	$+0.41 \pm 0.54$	16.26 ± 0.16	$+1.68$	$+0.43 \pm 0.45$
WFI J2026−4536	2705	16.52 ± 0.15	$+1.04$	$+0.27 \pm 0.53$	16.68 ± 0.12	$+1.20$	$+0.17 \pm 0.42$
WFI J2033−4723	3285	16.71 ± 0.16	$+1.55$	-0.63 ± 0.52	16.91 ± 0.13	$+1.75$	-0.67 ± 0.41

[a] λ_{central} is the geometric average of the rest wavelengths of our observations.

in a given lens system to affect our analysis, but such an occurrence could very well cause the flattening we see.

To test this possibility, we ran a small-scale Monte Carlo simulation. We generated 30 sets of fake flux ratios from the magnification maps designed for PG 1115+080, using the maps with 10% of the mass in stars. The source profile used to generate the flux ratios followed the expectations of the thin disk model. We then ran our analysis on the fake flux ratios and examined the results. On average, the correct slope was recovered — the mean slope was 1.17, and the χ^2 per degree of freedom was 0.98. This tells us that the observed discrepancy in ν is real. We did find a small systematic offset in the size normalization; the measured sizes were about 0.3 dex larger than the input sizes. This slightly reduces the significance of the measured average offset, but does not eliminate it.

9.3 Comparison with other work

A few other studies have measured or put limits on quasar accretion disk profiles using microlensing. In this section, we compare our results to theirs.

Bate et al. [2008] put an upper limit on the half-light radius of the disk of MG J0414+0534 in the (observed) r' band of 1.8×10^{16} cm. This is consistent with our result; our r'-band size measurement is about 3×10^{15} cm. They also constrain the slope ν to be between 0.77 and 2.67 (at 95% confidence), consistent with the predictions of the thin disk model, and consistent with our measurement. The reason for our improved measurement, particularly of the half-light radius, is our use of X-ray flux ratios.

Floyd et al. [2009] repeat this analysis using measurements of SDSS J0924+0219. They place an upper limit on the u'-band size of the disk of 3.04×10^{16} cm; this is again consistent with our u'-band size of 1×10^{16} cm. They put an upper limit of 1.34 on ν at 95% confidence; this agrees with our value of 0.17.

Poindexter et al. [2008] use time-domain measurements of the doubly lensed quasar HE 1104−1805 at a variety of wavelengths to constrain the structure of its accretion disk. They measure a B-band radius of 6.7×10^{15} cm and a power-law slope $1/\nu$ of 0.61. Their results are consistent with the predictions of the standard thin disk. Since this lens is not

in our sample, we cannot directly compare size measurements. However, their work does disagree with ours on the applicability of the thin disk model.

Finally, Eigenbrod et al. [2008] use spectrophotometric monitoring of Q 2237+0305 to measure the accretion disk profile. Their results are dependent on the prior chosen for the relative angular velocity of the quasar and the microlensing stars. They adopt a prior which yields a disk profile consistent both in slope and normalization to the thin disk model, but a different value of the velocity could yield a much larger disk with a flatter profile similar to our results.

9.4 Conclusions

The work in Chapters 6 through 9 was motivated by our observation in Chapters 3 through 5 of a general chromatic dependence in the flux ratio anomalies due to microlensing. Specifically, the anomalies are more pronounced in X-rays than they are at optical wavelengths. In this work we have found that chromatic microlensing can be observed between optical and near-IR broadband filters, and not only by comparing X-rays and optical wavelengths.

We have adopted a "snapshot" observational strategy, which does not depend on monitoring observations and is thus much more economical in its use of telescope time. This has enabled observation at a range of wavelengths between 3600 Å and 2.2 microns, and allowed us to work with a sample of 12 lensed quasars, roughly tripling at a stroke the sample of quasars with microlensing data on the disk profile.

We have developed a method for combining X-ray flux ratios with those at our optical/IR wavelengths to set both upper and lower limits on the size of the accretion disk of each quasar as a function of wavelength. This measurement is so far only possible using microlensing, and it puts direct constraints on accretion models for quasars.

We have found that in most cases the thin accretion disk model [Shakura and Sunyaev, 1973, Novikov and Thorne, 1973] correctly predicts the dependence of the size of the disk at 2500 Å on the black hole mass, but underpredicts the absolute size of the disk at this wavelength by factors of ~ 10. The measured sizes are also inconsistent in the aggregate with the predicted $\lambda^{4/3}$ dependence on wavelength, preferring a much flatter logarithmic

slope around 0.2 (though the individual measurement errors and the scatter are fairly large). The temperature profile slope is the inverse of the slope, so our observations imply a steeper temperature profile than expected.

Systematic underestimates of black hole masses, underestimates of Eddington fraction, or underestimates of the accretion efficiency could be responsible for the discrepancy in size (though not the slope). However, they would have to be very large errors — factors of ~ 30 in black hole mass, or ~ 1000 in Eddington fraction or accretion efficiency. If we have overestimated the average mass of the stellar microlenses by a factor of ~ 100, then our conversion from angular to spatial units is suspect, but we doubt that this is the case, with $\langle m \rangle = 0.25$. In all, it appears that the rest frame UV and optical emission from bright quasars does not, in general, originate in a standard thin disk, but from something larger, with a temperature profile steeper than $r^{-3/4}$.
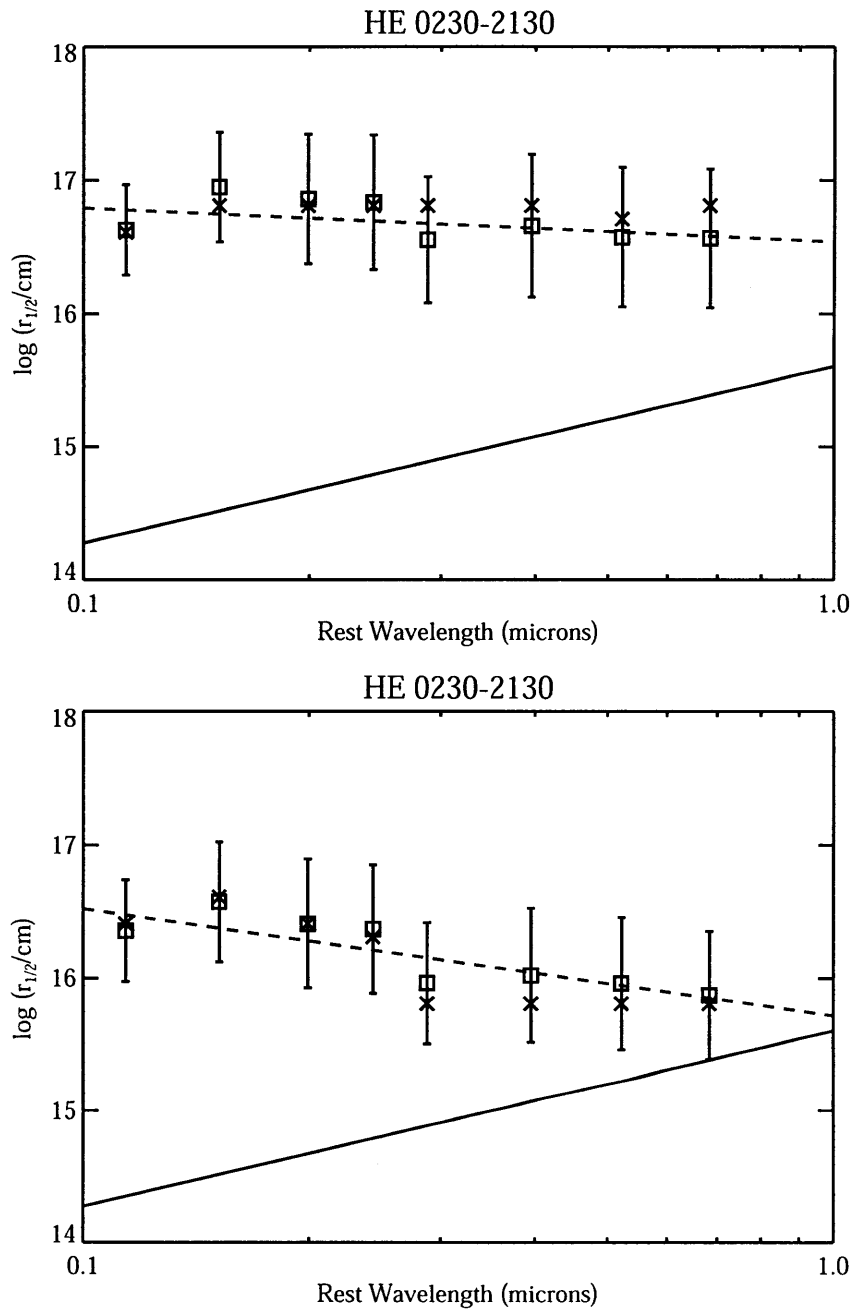
Figure 9-1 Estimated half-light radius of HE 0230−2130 as a function of wavelength. Solid line predicts the radius predicted by the thin disk model. Top panel: Linear prior. Bottom panel: Logarithmic prior.
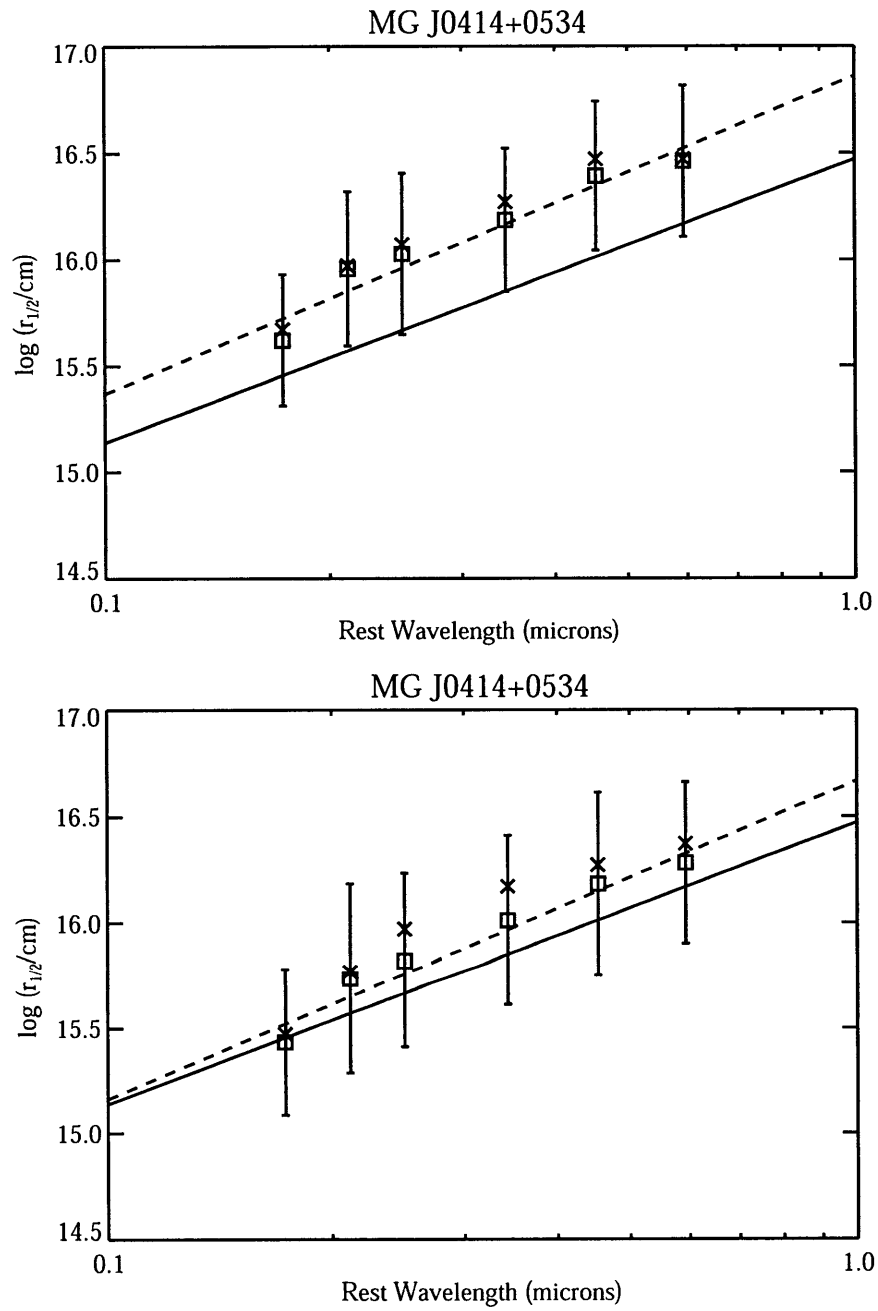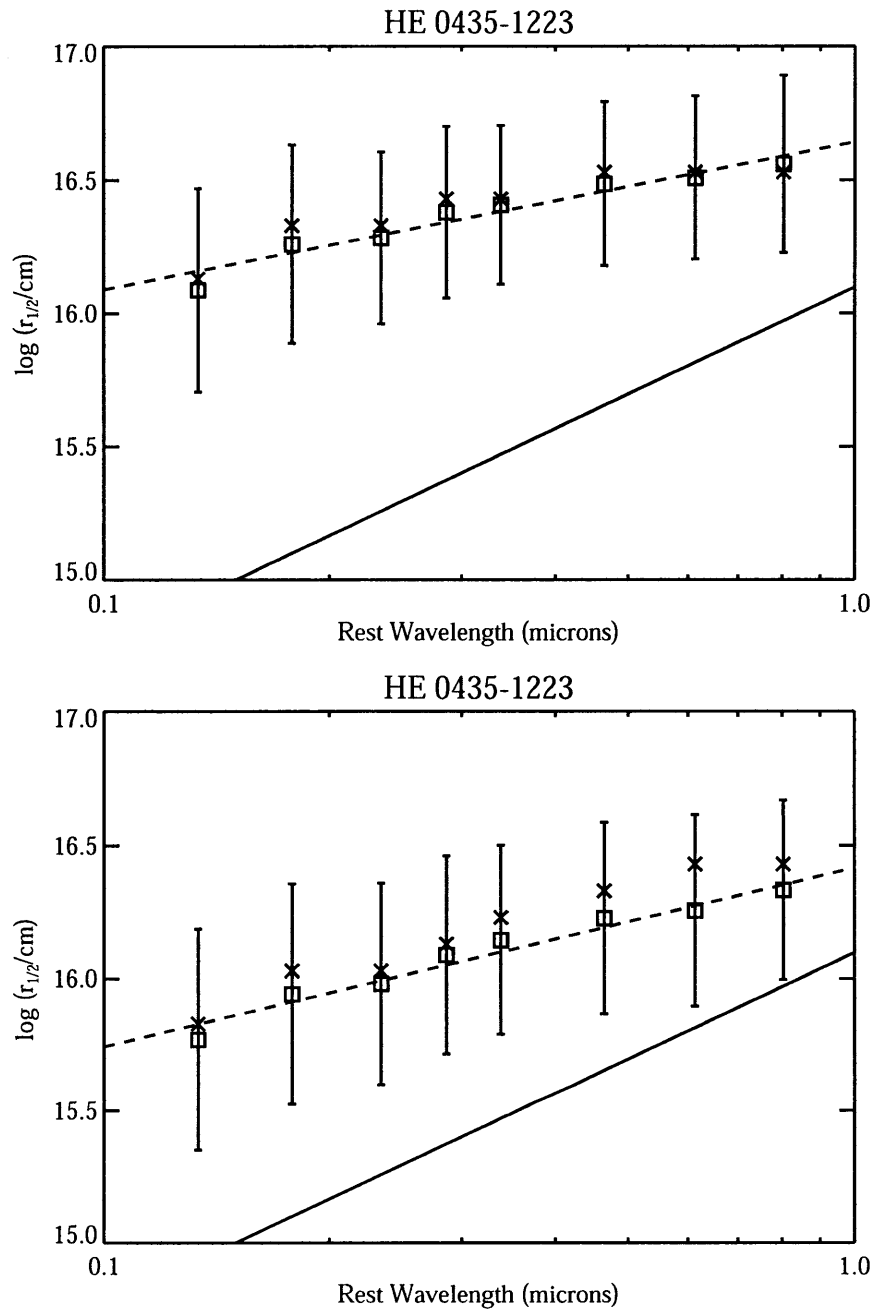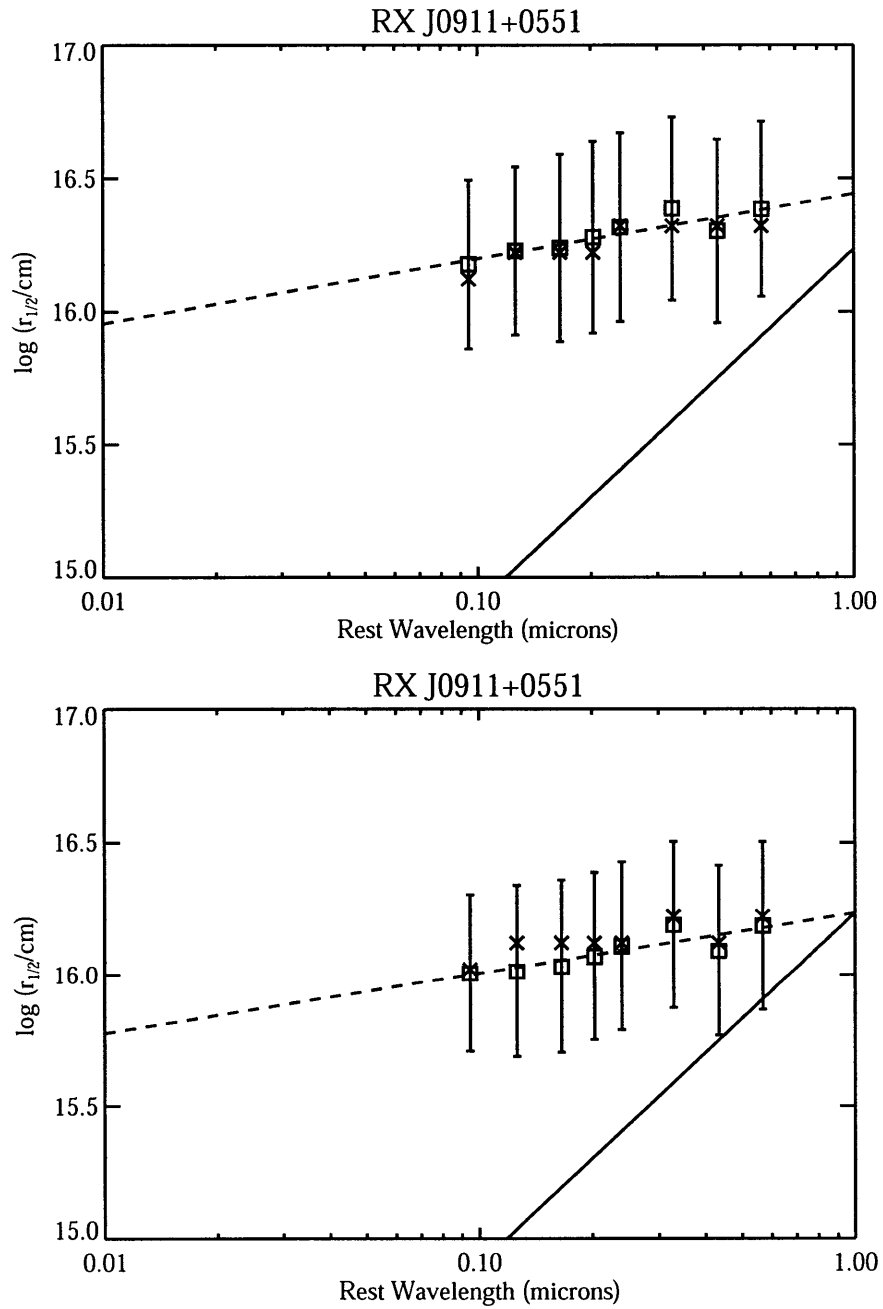
Figure 9-2 Estimated half-light radius of MG J0414+0534 as a function of wavelength. Solid line predicts the radius predicted by the thin disk model. Top panel: Linear prior. Bottom panel: Logarithmic prior.
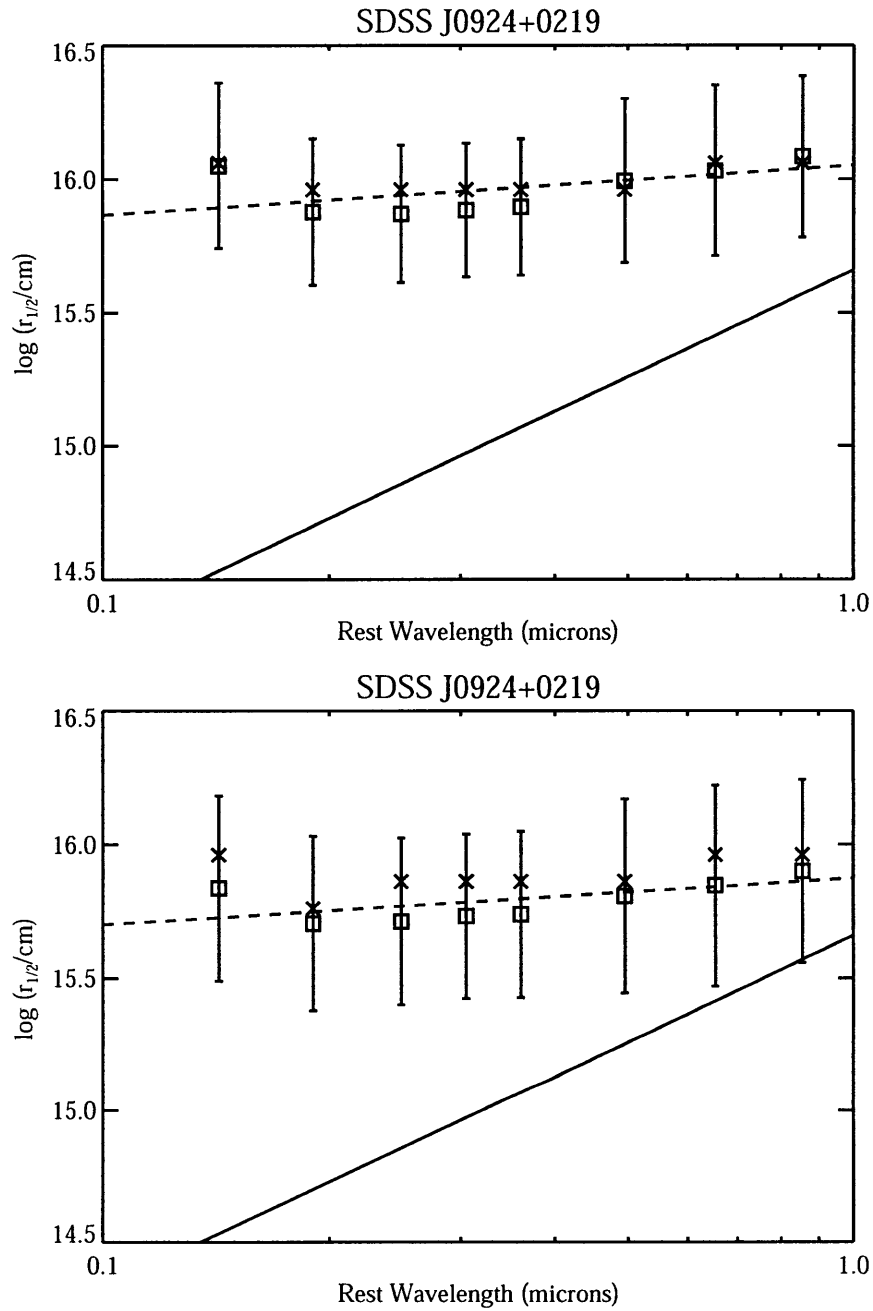
Figure 9-3 Estimated half-light radius of HE 0435−1223 as a function of wavelength. Solid line predicts the radius predicted by the thin disk model. Top panel: Linear prior. Bottom panel: Logarithmic prior.

Figure 9-4 Estimated half-light radius of RX J0911+0551 as a function of wavelength. Solid line predicts the radius predicted by the thin disk model. Top panel: Linear prior. Bottom panel: Logarithmic prior.
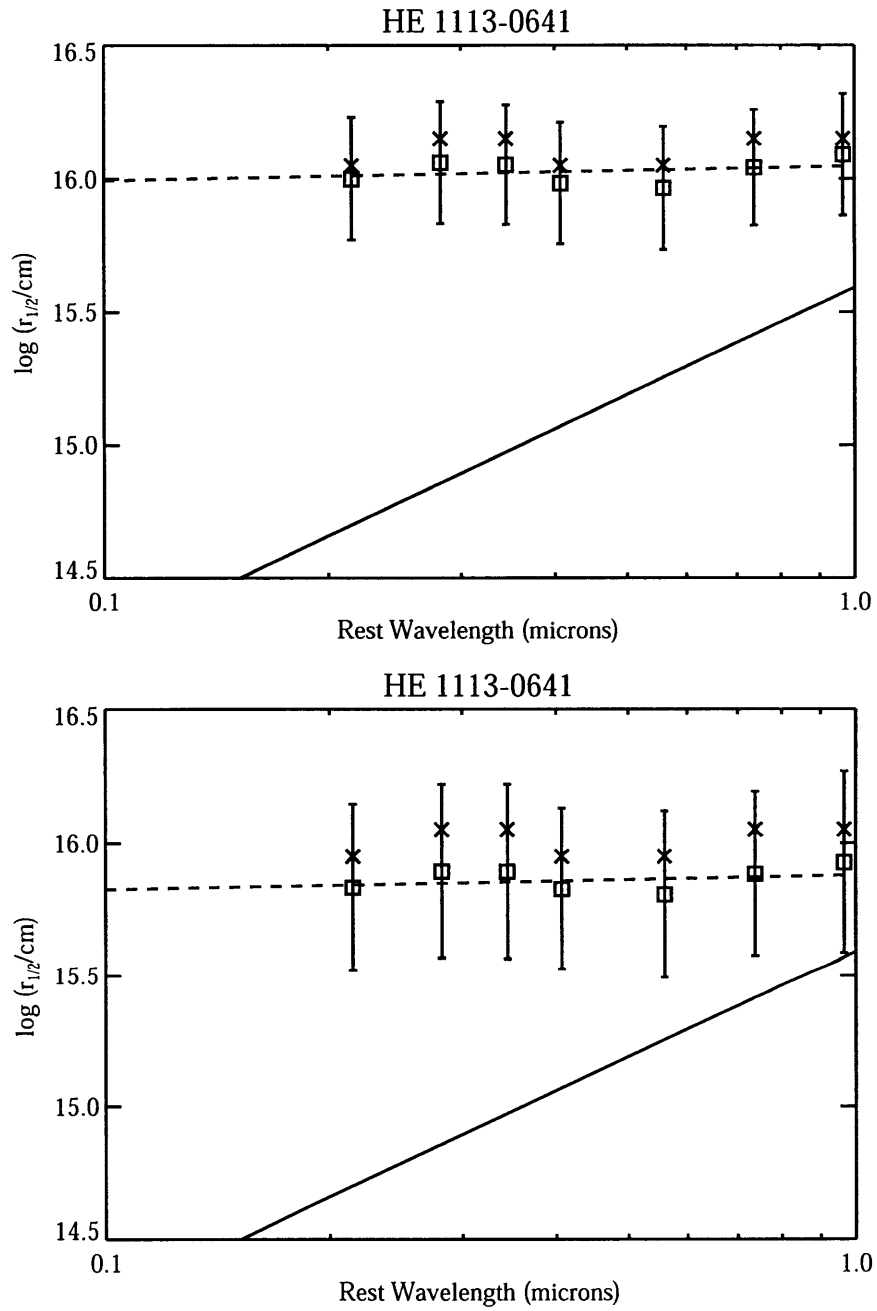
150

Figure 9-5 Estimated half-light radius of SDSS J0924+0219 as a function of wavelength. Solid line predicts the radius predicted by the thin disk model. Top panel: Linear prior. Bottom panel: Logarithmic prior.

Figure 9-6 Estimated half-light radius of HE 1113−0641 as a function of wavelength. Solid line predicts the radius predicted by the thin disk model. Top panel: Linear prior. Bottom panel: Logarithmic prior.
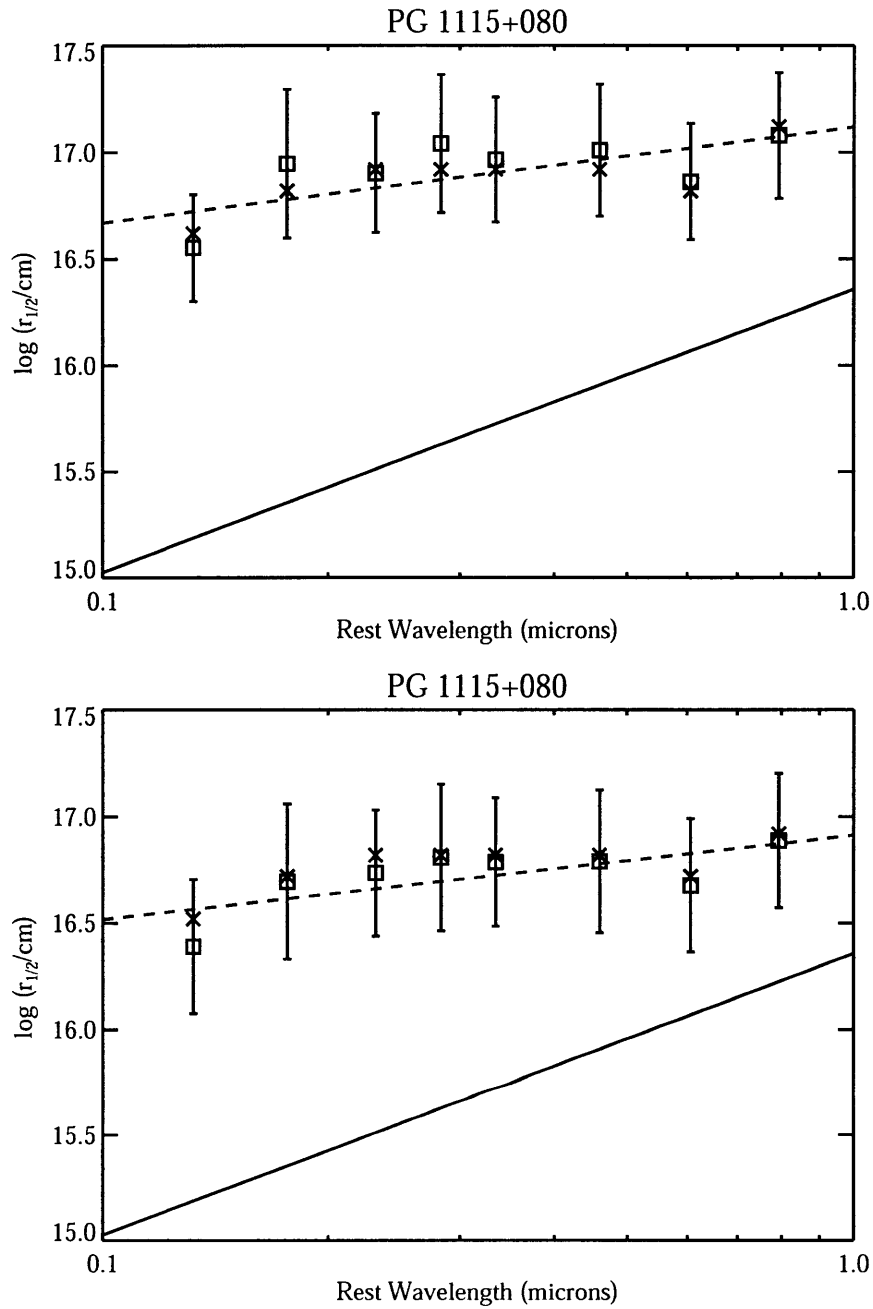
Figure 9-7 Estimated half-light radius of PG 1115+080 as a function of wavelength. Solid line predicts the radius predicted by the thin disk model. Top panel: Linear prior. Bottom panel: Logarithmic prior.
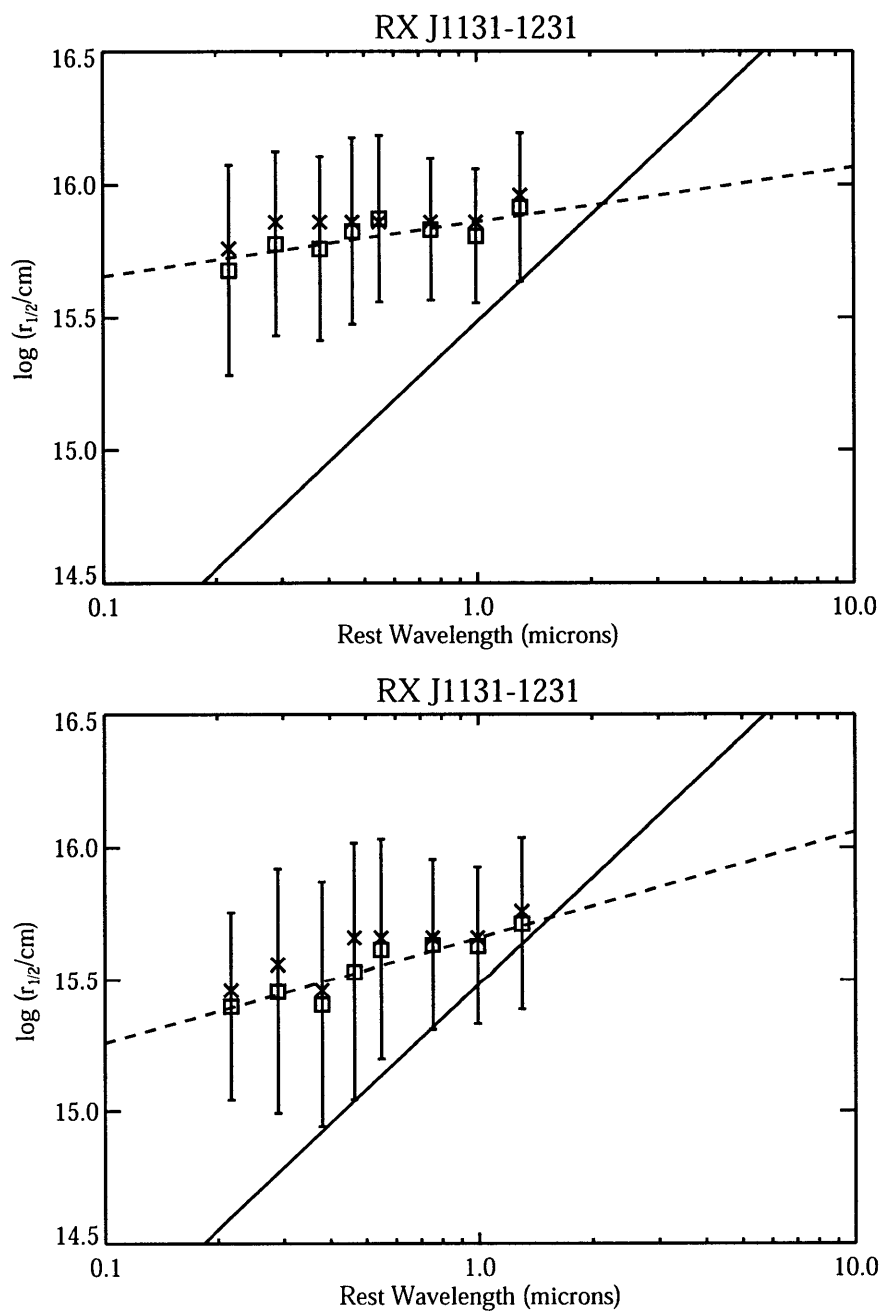
Figure 9-8 Estimated half-light radius of RX J1131−1231 as a function of wavelength. Solid line predicts the radius predicted by the thin disk model. Top panel: Linear prior. Bottom panel: Logarithmic prior.
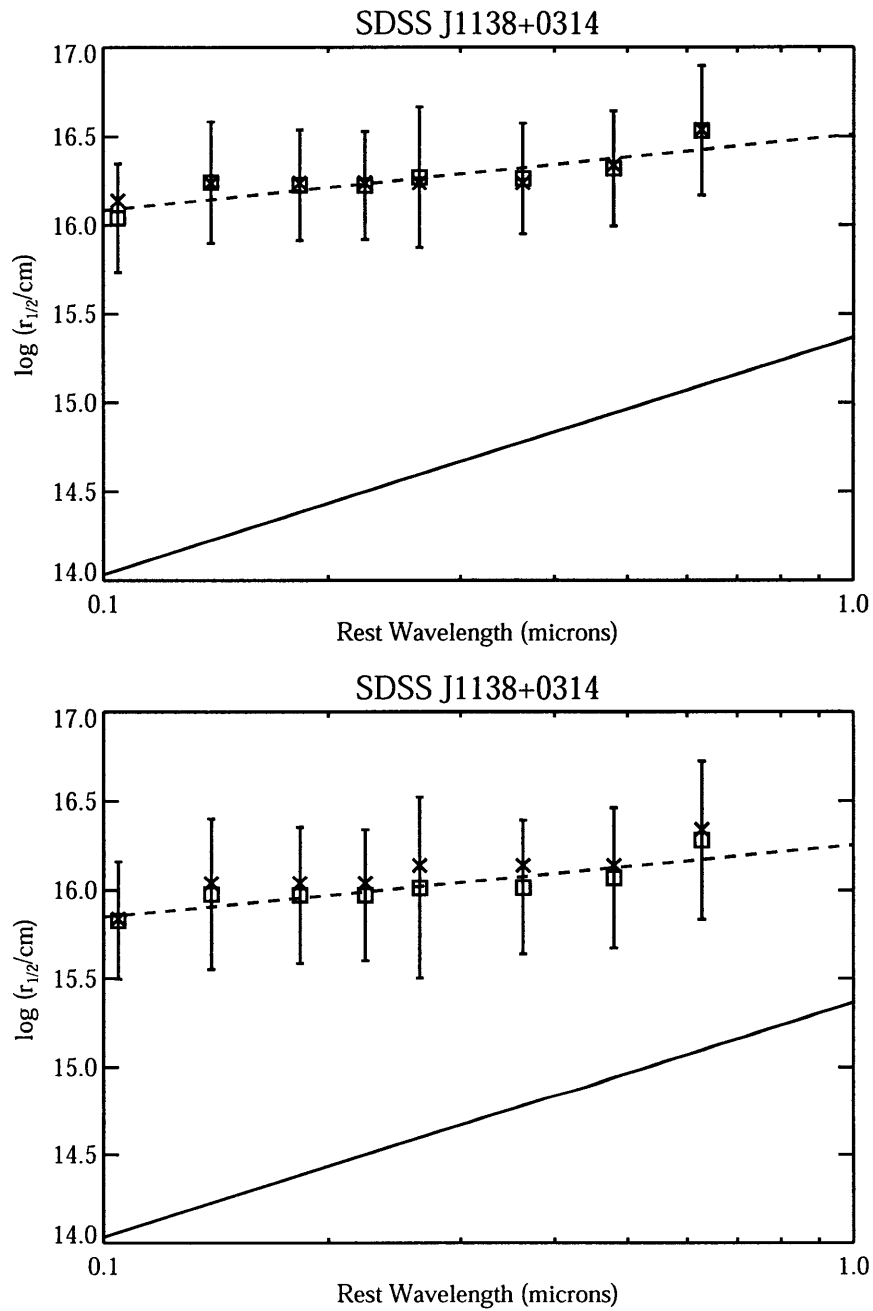
Figure 9-9 Estimated half-light radius of SDSS J1138+0314 as a function of wavelength. Solid line predicts the radius predicted by the thin disk model. Top panel: Linear prior. Bottom panel: Logarithmic prior.
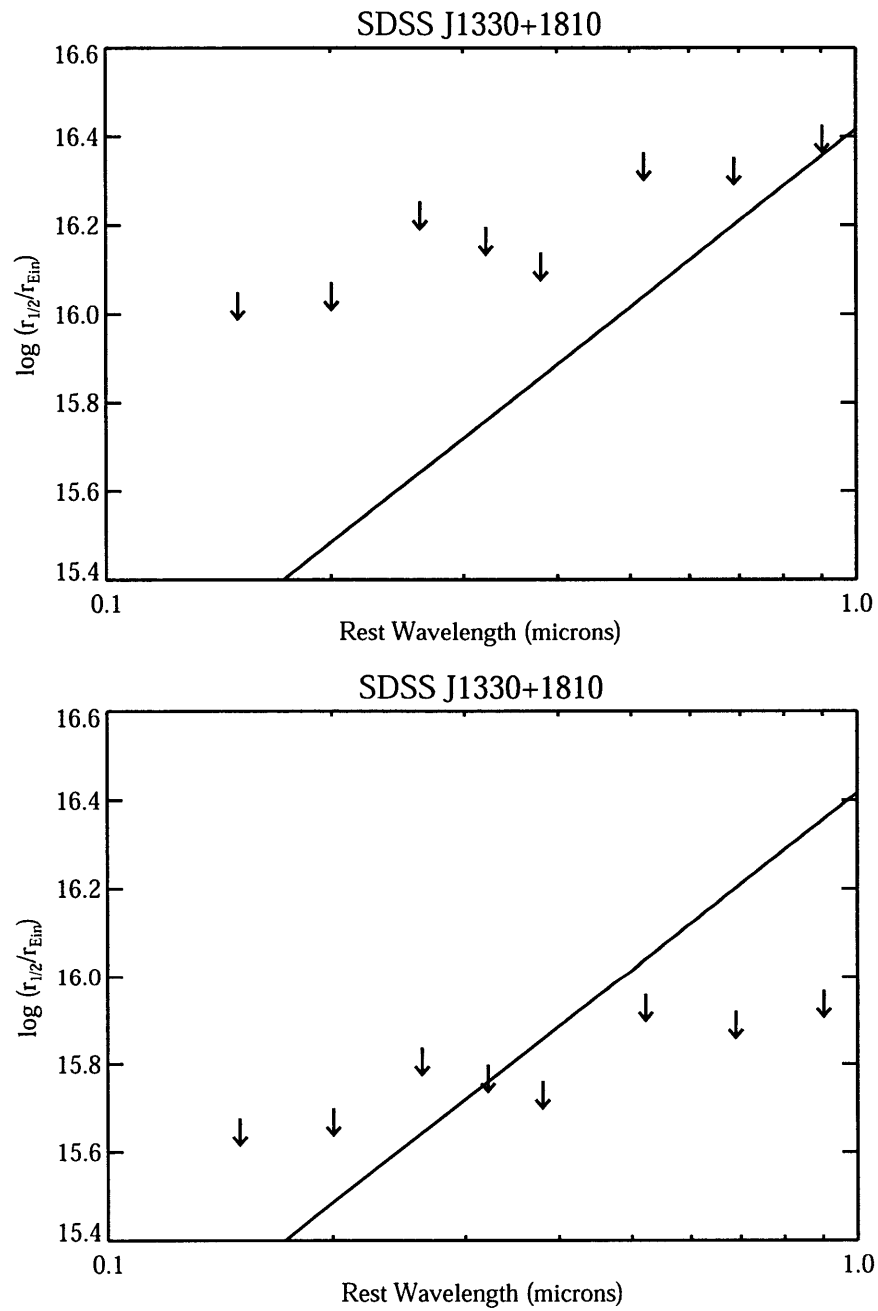
Figure 9-10 Upper limits on the half-light radius of SDSS J1330+1810 as a function of wavelength. Solid line predicts the radius predicted by the thin disk model. Top panel: Linear prior. Bottom panel: Logarithmic prior.

Figure 9-11 Estimated half-light radius of WFI J2026—4536 as a function of wavelength. Solid line predicts the radius predicted by the thin disk model. Top panel: Linear prior. Bottom panel: Logarithmic prior.
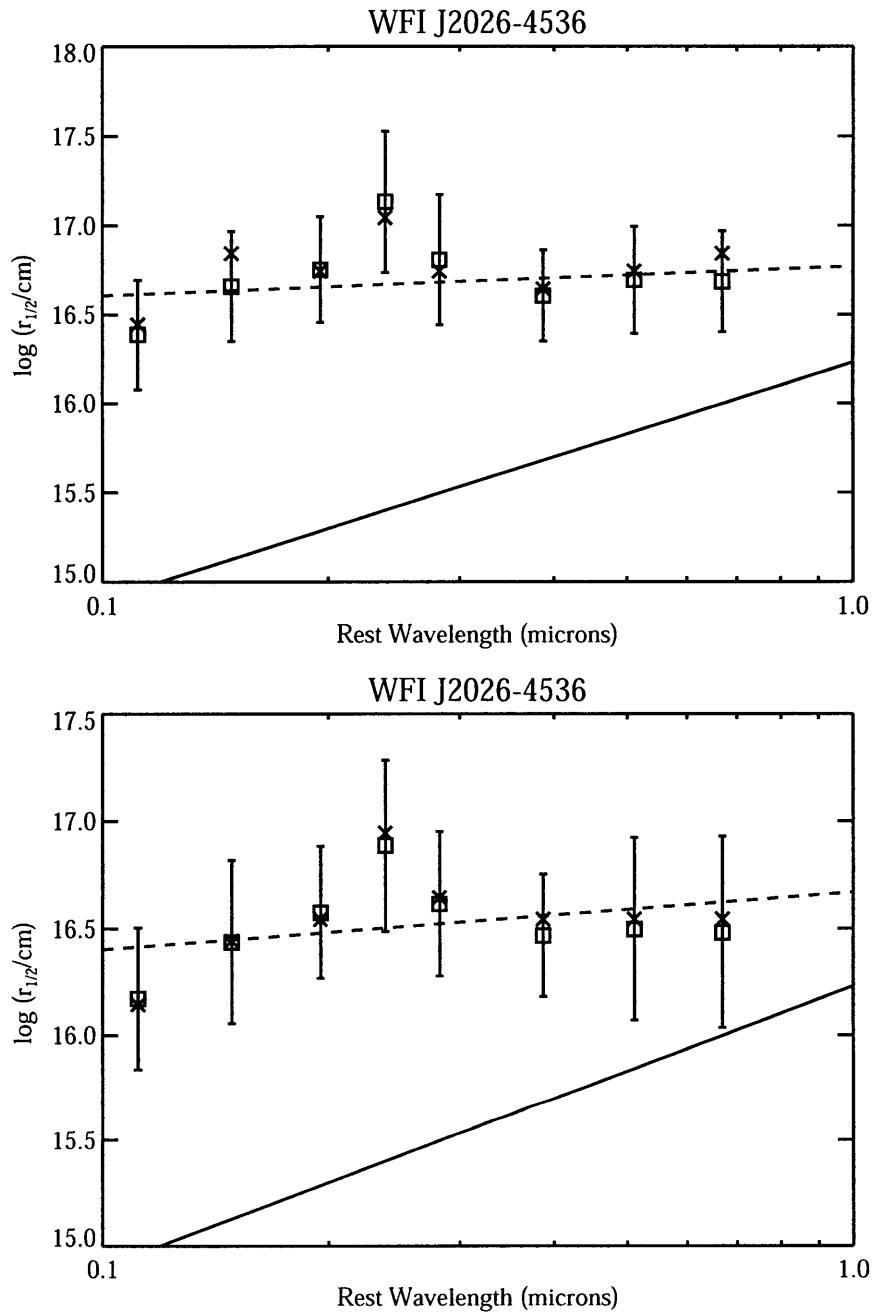
Figure 9-12 Estimated half-light radius of WFI J2033—4723 as a function of wavelength. Solid line predicts the radius predicted by the thin disk model. Top panel: Linear prior. Bottom panel: Logarithmic prior.
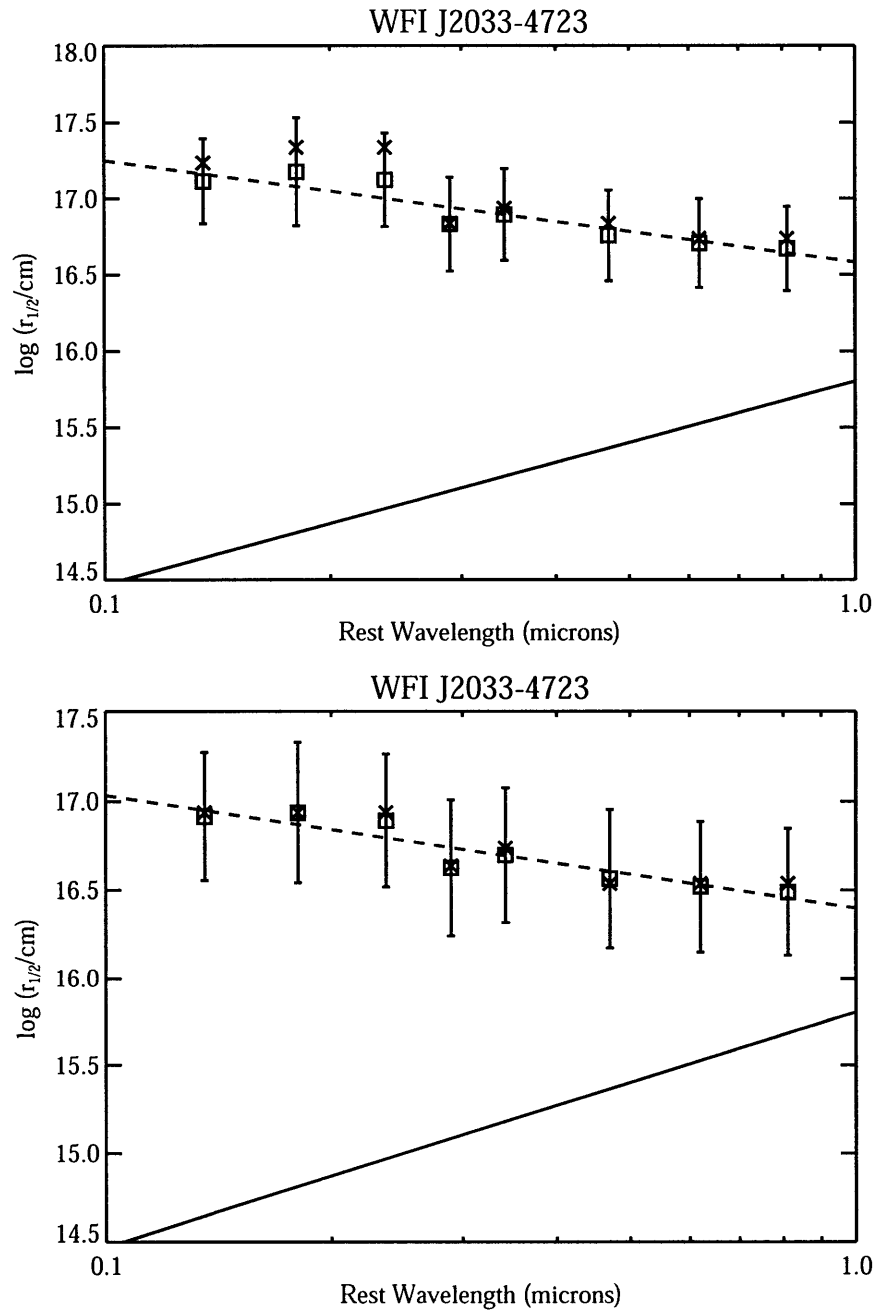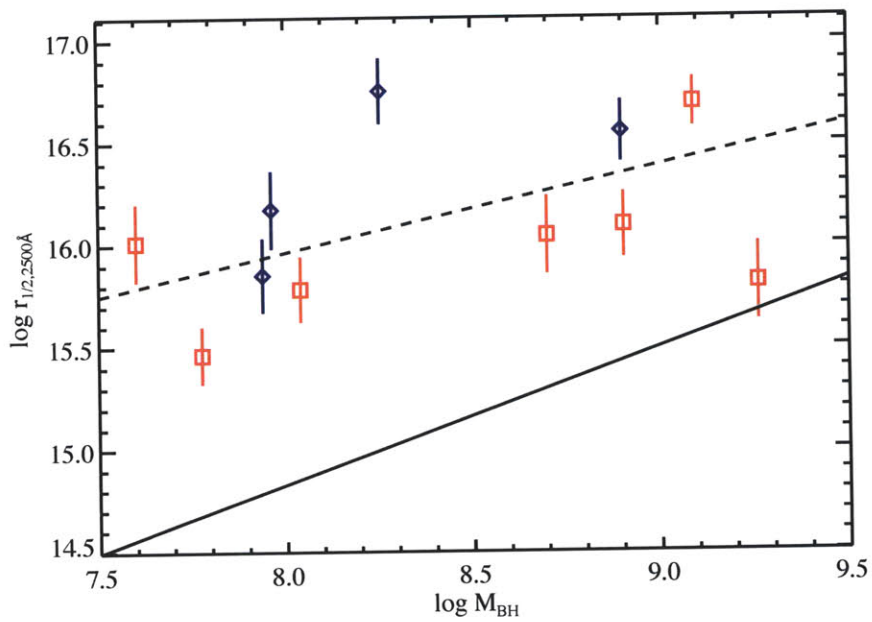
158

Figure 9-13 Half-light radius at a rest wavelength of 2500 Å, as a function of black hole mass. The solid line is the prediction of the thin disk model, while the dotted line is the best fit to the data. Black hole masses estimated using the virial method are plotted as red squares; those estimated using bolometric luminosity are plotted as blue diamonds. Black hole masses have (unplotted) uncertainties of $\sim$0.3 dex.

Chapter 10

Epilogue: Future work

10.1 Reduce uncertainties

As we mentioned in Section 8.3, the width of our source size likelihood distributions results both from the intrinsic width of the magnification histograms and from the uncertainties in our flux ratios. Of these, the former is unavoidable without extending our observing strategy into the time domain. It is very possible, however, to improve our error bars by working to decrease the latter.

The largest contribution to the uncertainties in most of our flux ratios was due to the delay between the X-ray and optical observations. In the future, it is entirely reasonable to schedule multi-wavelength observations of lensed quasars to coincide with *Chandra* observations.

10.2 Complementary observation styles

The single-epoch multi-wavelength analysis method developed in this thesis is complementary to time-domain methods such as that described in Kochanek [2004]. The time-domain style of observation allows us to rule out parts of the microlensing magnification map, reducing the uncertainty stemming from the width of the histograms. This method is best-suited to single-band observations, because it is relatively expensive in telescope time. But combining multi-epoch, single-wavelength observations with occasional multi-wavelength obser-

vations (e.g. when a *Chandra* observation is scheduled) should give us the best of both methods, allowing us to measure quasar sizes at different wavelengths while also gaining the reduced uncertainties characteristic of the time-domain method.

10.3 Spectroscopy

Quasar emission lines contaminate our broadband measurements. Their emission comes from a larger region than the accretion disk, so their flux anomalies should be smaller than the surrounding continuum. But it will be possible in the future to apply our analysis method to spectroscopic data as well. Spectroscopic data will allow us to refine our continuum measurements by subtracting line emission. But even more exciting is the possibility of measuring the sizes of the line emission regions by measuring their flux ratios. These sizes can be combined with the line widths to make a virial estimate of the black hole mass. Currently these estimates are made using an empirical relation between continuum luminosity and size, calibrated by local reverberation mapping measurements [Vestergaard, 2002]. Direct measurement of a few lensed quasars' broad emission line region sizes would allow us to sidestep this relation for those quasars, and may allow us to improve its calibration for high-redshift quasars in general.

Though spectroscopic work has shown that the emission lines are usually less anomalous than the continuum, flux ratio anomalies have been observed [Keeton et al., 2006, Sluse et al., 2007]. This indicates that it is reasonable to be optimistic about our chances of making this measurement.

Appendix A

Catalog of gravitational lenses used in this thesis

In this appendix we list the fifteen quadruply lensed quasars that we analyze in this thesis. Twelve of the fifteen are in the sample of Chapters 6 through 9; we display postage-stamp images of these lenses in the filters we observed them in, along with residual images from our PSF subtraction. The other three lenses appear in Chapter 5. For these three lenses we reproduce an image from the CASTLES survey.

We also describe each lens briefly, and cite the paper reporting its discovery.

A.1 HE 0230−2130

The quasar HE 0230−2130, at redshift $z_S = 2.162$, is lensed into a fold configuration by a pair of galaxies at redshift $z_L = 0.52$ [Wisotzki et al., 1999]. Image D lies very close to the secondary galaxy.
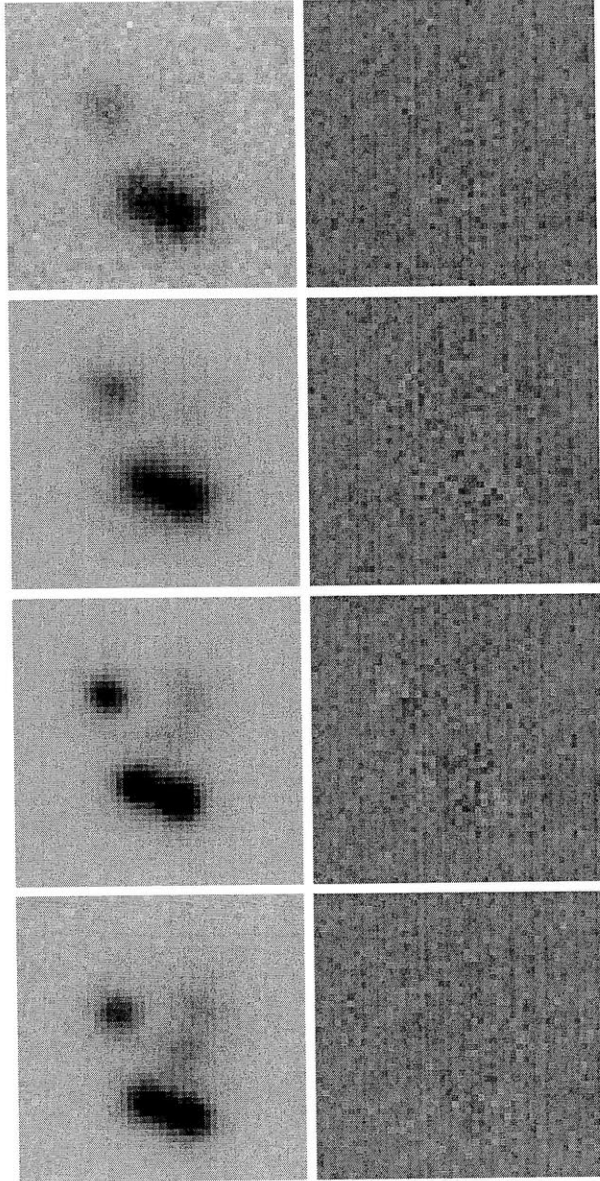
Figure A-1 Postage-stamp images of HE 0230−2130 in $u'g'r'i'$ (top to bottom). Left: original image. Right: residuals after nonlinear least-squares fit. In the residual images, the grayscale stretch is set to $\pm 20\sigma$ of the sky level.
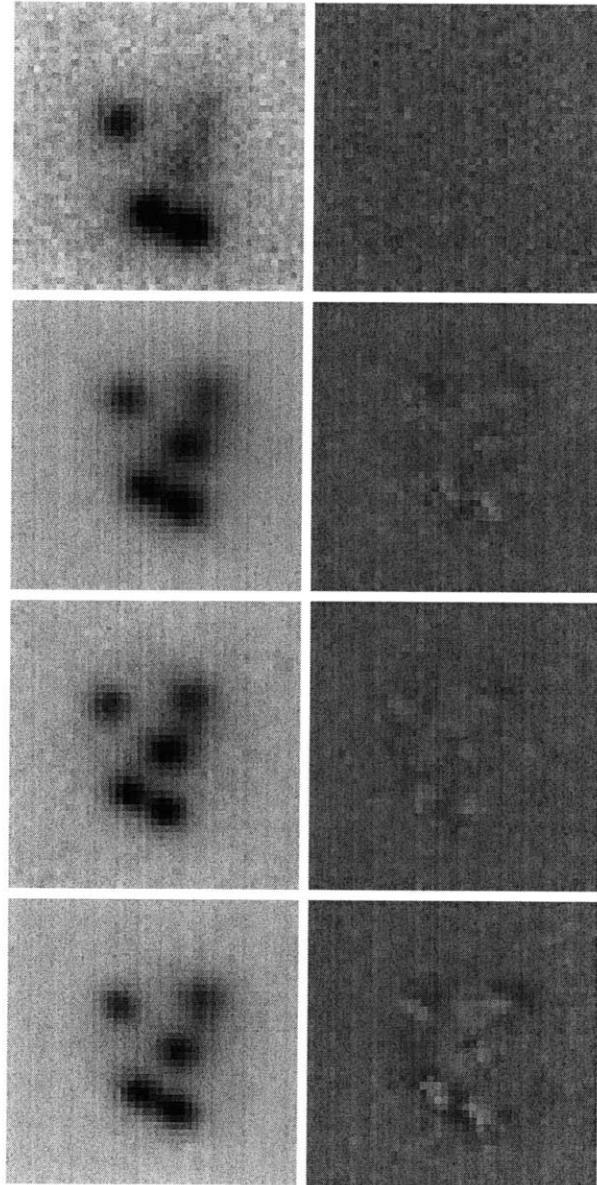
Figure A-1 (cont'd) Postage-stamp images of HE 0230−2130 in $z'JHK$ (top to bottom). Left: original image. Right: residuals after nonlinear least-squares fit. In the residual images, the grayscale stretch is set to $\pm 20\sigma$ of the sky level.

A.2 MG J0414+0534

The $z_S = 2.64$ quasar MG J0414+0534 is lensed by a $z_L = 0.96$ galaxy into a fold configuration [Hewitt et al., 1992]. It is the only radio-loud quasar in our sample, and has very red optical colors, probably due to extinction intrinsic to the source [Falco et al., 1997]. In addition, it is the only one with clear evidence for *millilensing* – its mid-IR flux ratios show a distinct anomaly [Minezaki et al., 2009]. In our analysis of this lens, we have adopted these mid-IR fluxes as our microlensing-free fluxes, instead of those predicted by the lens model.
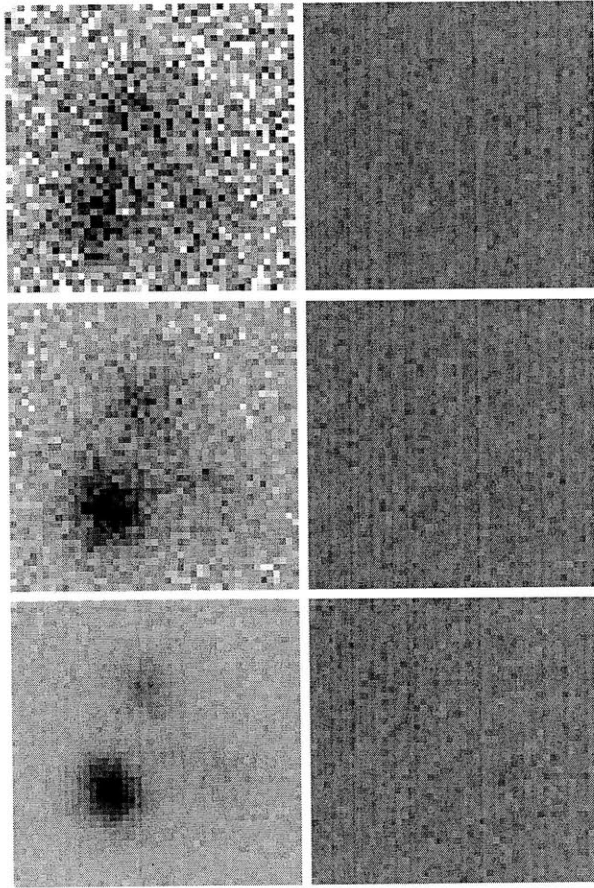

Figure A-2 Postage-stamp images of MG J0414+0534 in $r'i'z'$ (top to bottom). Left: original image. Right: residuals after nonlinear least-squares fit. In the residual images, the grayscale stretch is set to $\pm 20\sigma$ of the sky level.
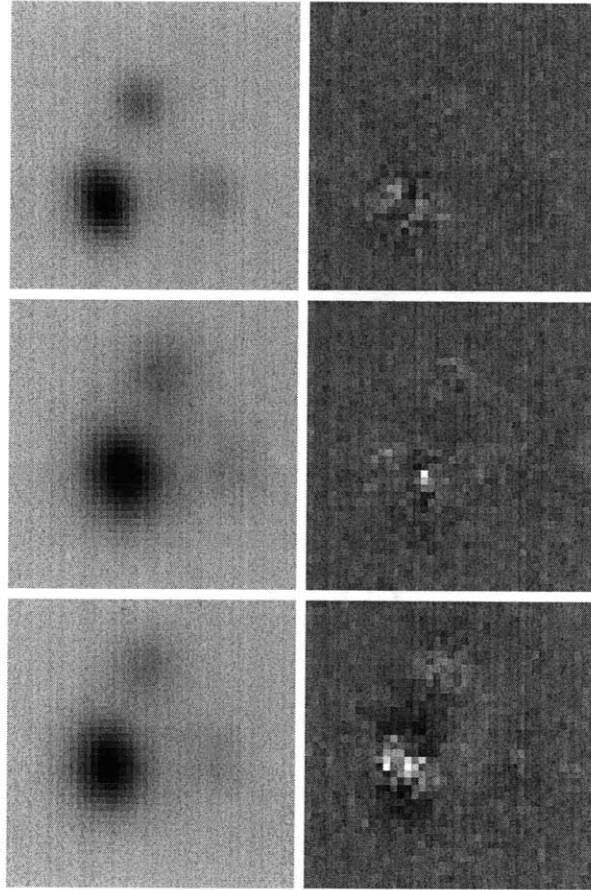
Figure A-2 (cont'd) Postage-stamp images of MG J0414+0534 in JHK (top to bottom). Left: original image. Right: residuals after nonlinear least-squares fit. In the residual images, the grayscale stretch is set to $\pm 20\sigma$ of the sky level.

A.3 HE 0435−1223

The $z_S = 1.689$ quasar HE 0435−1223 is lensed into a cross shape by a galaxy at $z_L = 0.46$ [Wisotzki et al., 2002].
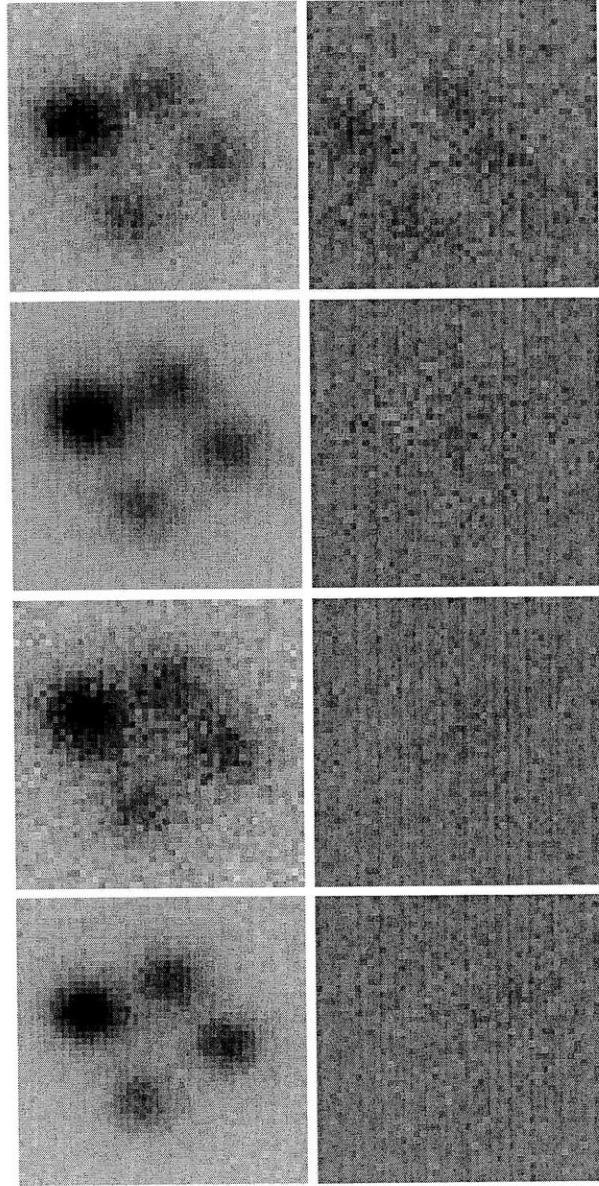

Figure A-3 Postage-stamp images of HE 0435−1223 in $u'g'r'i'$ (top to bottom). Left: original image. Right: residuals after nonlinear least-squares fit. In the residual images, the grayscale stretch is set to $\pm 20\sigma$ of the sky level.

Figure A-3 (cont'd) Postage-stamp images of HE 0435−1223 in $z'JHK$ (top to bottom). Left: original image. Right: residuals after nonlinear least-squares fit. In the residual images, the grayscale stretch is set to $\pm 20\sigma$ of the sky level.
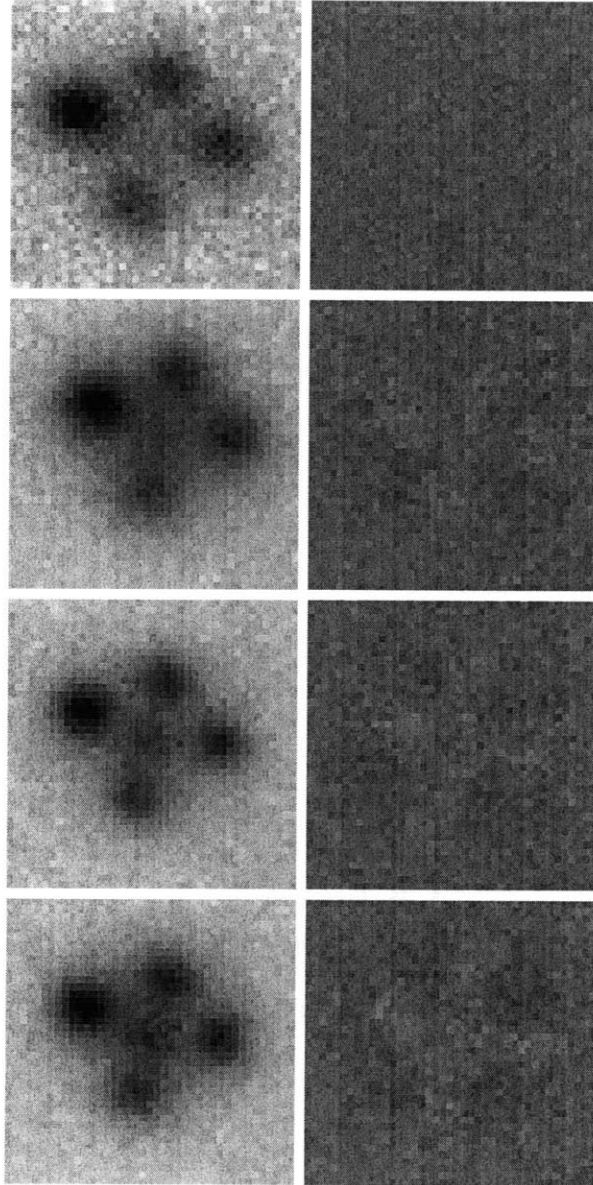
A.4   RX J0911+0551

The quasar RX J0911+0551, at redshift $z_S = 2.80$, is lensed by a galaxy at redshift $z_L = 0.77$ into a cusp configuration [Bade et al., 1997].
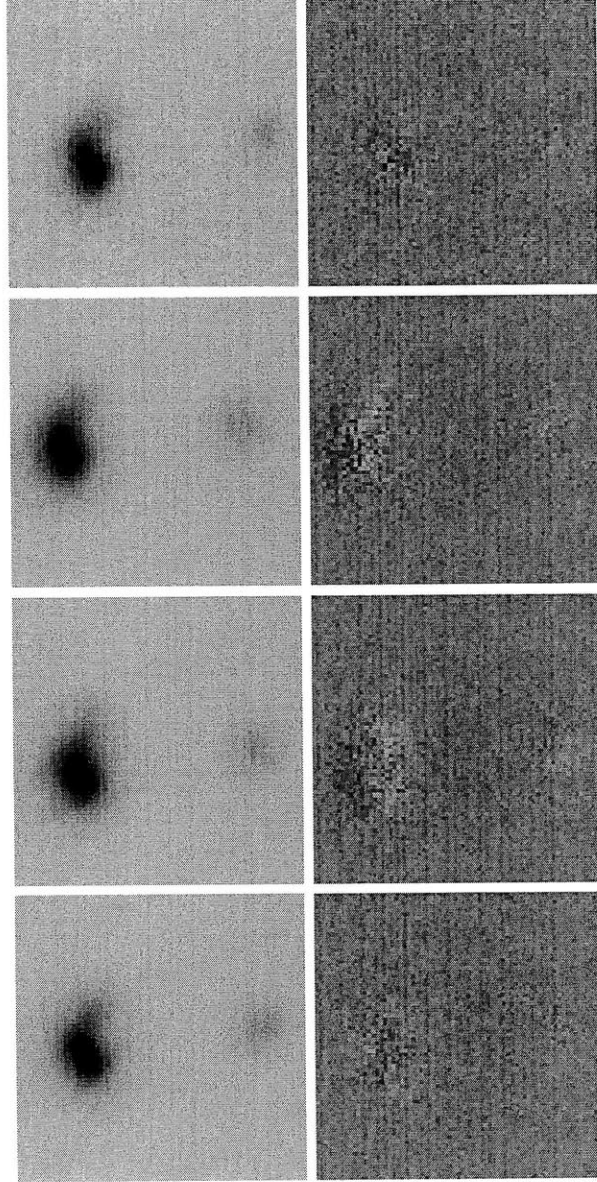

Figure A-4 Postage-stamp images of RX J0911+0551 in $u'g'r'i'$ (top to bottom). Left: original image. Right: residuals after nonlinear least-squares fit. In the residual images, the grayscale stretch is set to $\pm 20\sigma$ of the sky level.
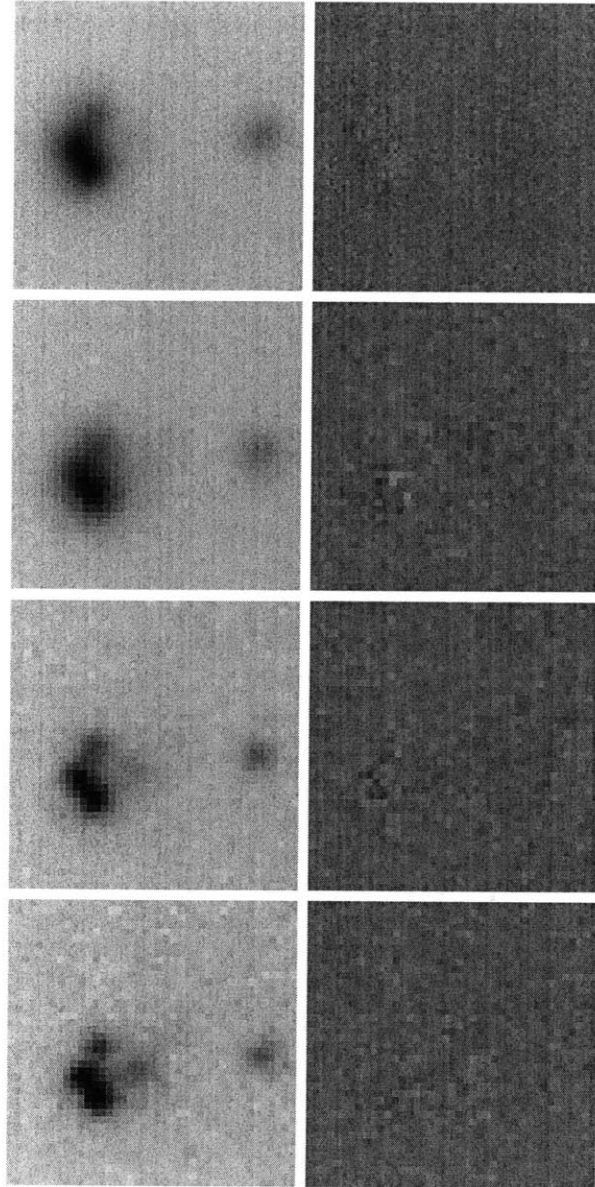
Figure A-4 (cont'd) Postage-stamp images of RX J0911+0551 in $z'JHK$ (top to bottom). Left: original image. Right: residuals after nonlinear least-squares fit. In the residual images, the grayscale stretch is set to $\pm20\sigma$ of the sky level.

A.5 SDSS J0924+0219

SDSS J0924+0219 is a quasar at redshift $z_S = 1.524$ which is lensed into a fold configuration by a galaxy at redshift $z_L = 0.39$ Inada et al. [2003a]. It is notoriously the most anomalous lensed quasar, as its image D, which as part of a merging pair of images ought to be bright, is demagnified by an order of magnitude at optical wavelengths.
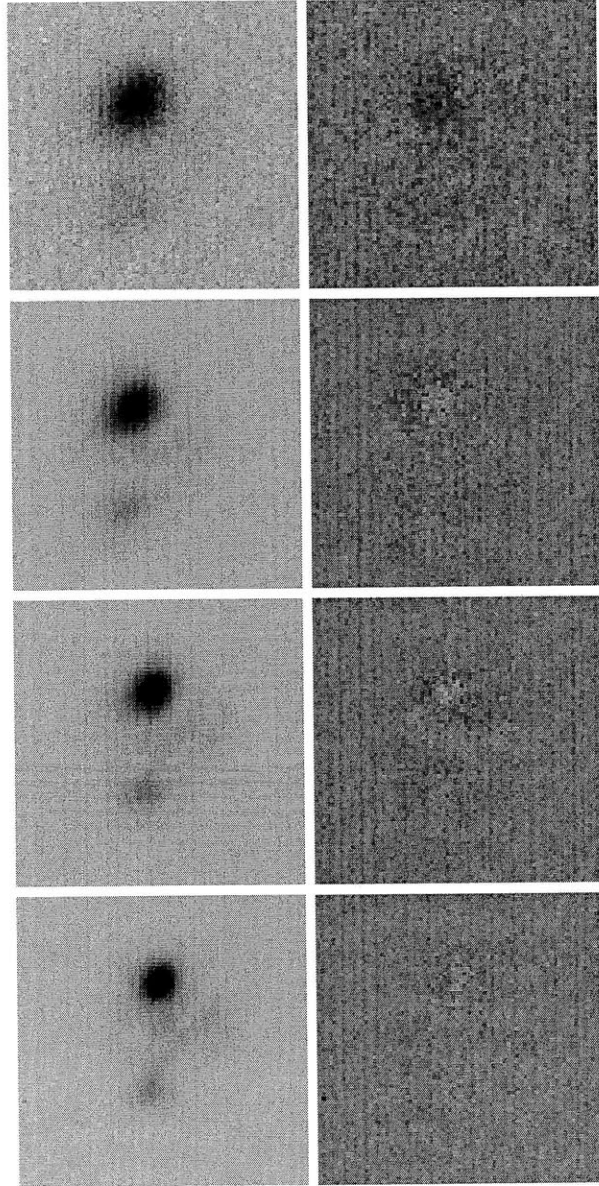

Figure A-5 Postage-stamp images of SDSS J0924+0219 in $u'g'r'i'$ (top to bottom). Left: original image. Right: residuals after nonlinear least-squares fit. In the residual images, the grayscale stretch is set to $\pm 20\sigma$ of the sky level.

172

Figure A-5 (cont'd) Postage-stamp images of SDSS J0924+0219 in $z'JHK$ (top to bottom). Left: original image. Right: residuals after nonlinear least-squares fit. In the residual images, the grayscale stretch is set to $\pm 20\sigma$ of the sky level.

A.6 HE 1113−0641

The quasar HE 1113−0641, at redshift $z_S = 1.235$, is lensed into a cross configuration by a foreground galaxy of unknown redshift [Blackburne et al., 2008]. We estimate the lens redshift to be $z_L \sim 0.7$ (see Chapter 2).

Figure A-6 Postage-stamp images of HE 1113−0641 in $g'r'i'$ (top to bottom). Left: original image. Right: residuals after nonlinear least-squares fit. In the residual images, the grayscale stretch is set to $\pm 20\sigma$ of the sky level.
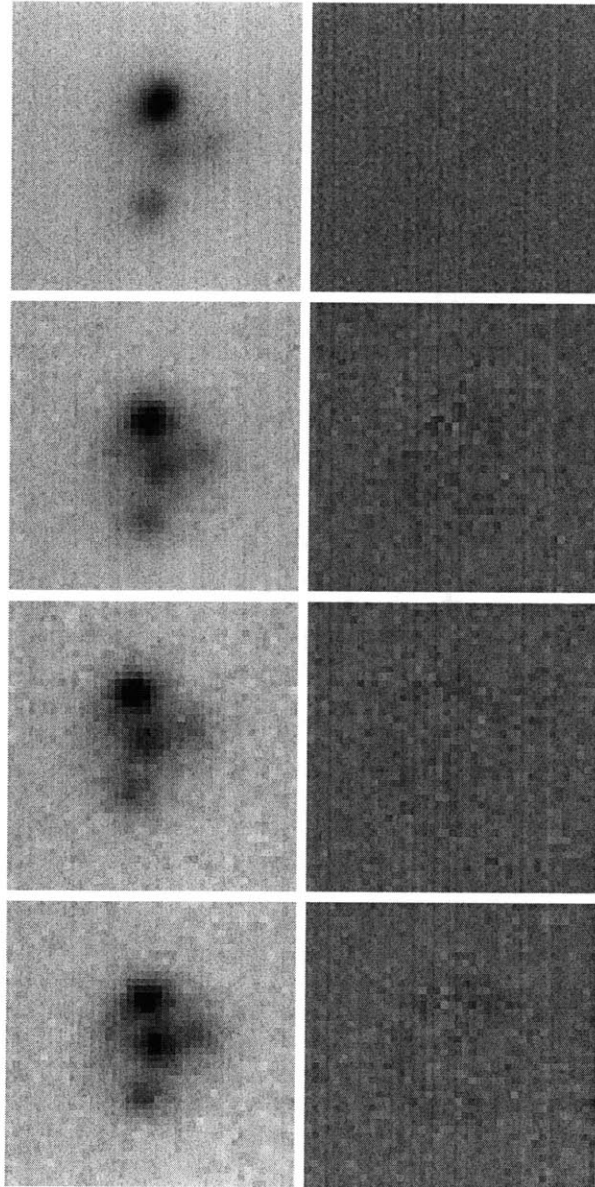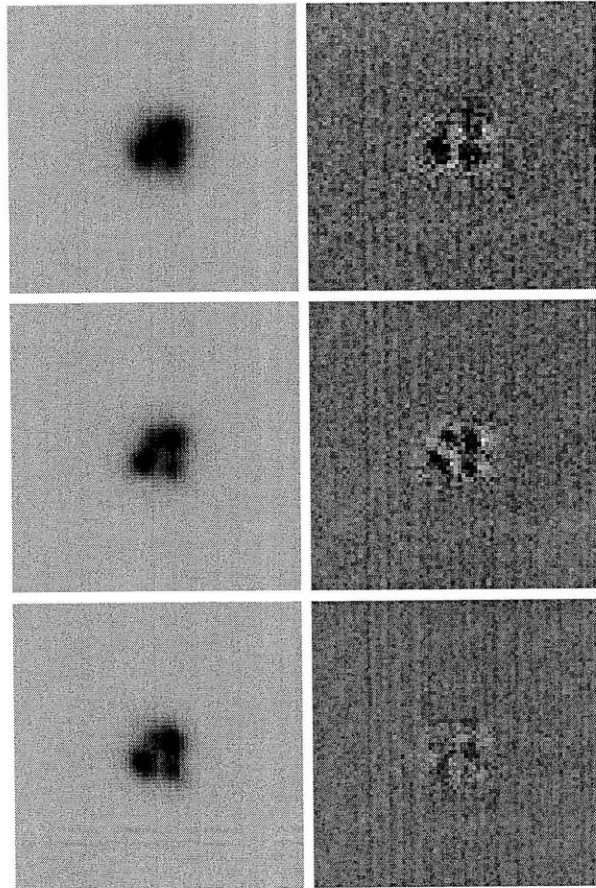
Figure A-6 (cont'd) Postage-stamp images of HE 1113−0641 in $z'JHK$ (top to bottom). Left: original image. Right: residuals after nonlinear least-squares fit. In the residual images, the grayscale stretch is set to $\pm 20\sigma$ of the sky level.

A.7   PG 1115+080

PG 1115+080, at a redshift of $z_S = 1.72$, is lensed into a fold configuration by a foreground galaxy at redshift $z_L = 0.31$. It was the first quadruple quasar to be discovered [Weymann et al., 1980].

Figure A-7 Postage-stamp images of PG 1115+080 in $u'g'r'i'$ (top to bottom). Left: original image. Right: residuals after nonlinear least-squares fit. In the residual images, the grayscale stretch is set to $\pm 20\sigma$ of the sky level.
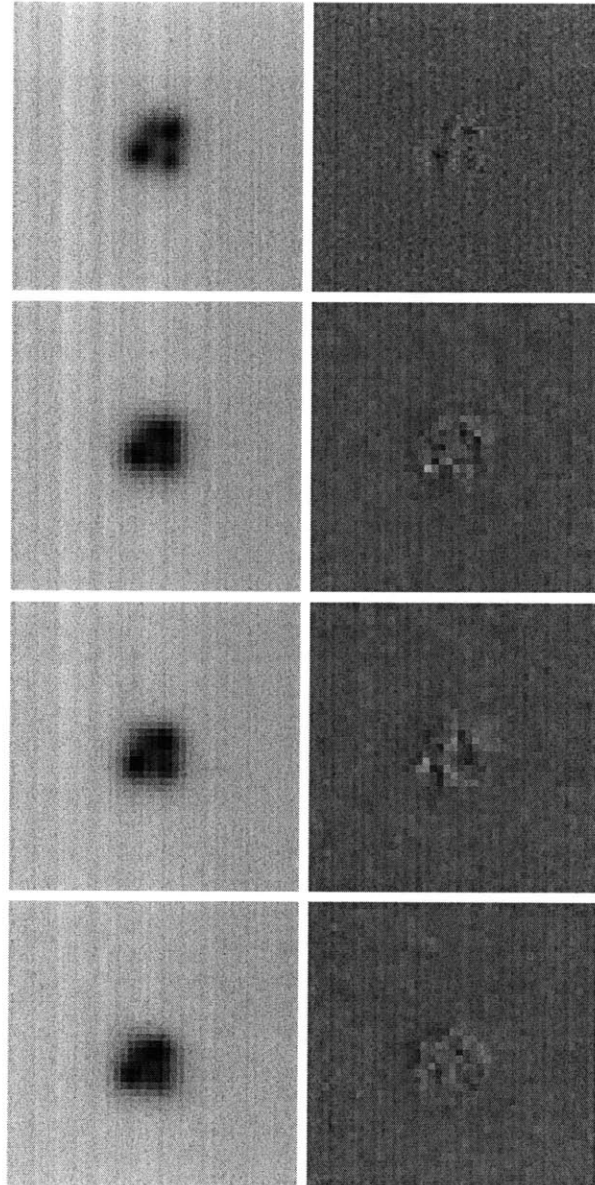
Figure A-7 (cont'd) Postage-stamp images of PG 1115+080 in $z'JHK$ (top to bottom).
Left: original image. Right: residuals after nonlinear least-squares fit. In the residual
images, the grayscale stretch is set to $\pm20\sigma$ of the sky level.

A.8 RX J1131−1231

At redshift $z_S = 0.658$, RX J1131−1231 is the lowest-redshift lensed quasar in our sample.

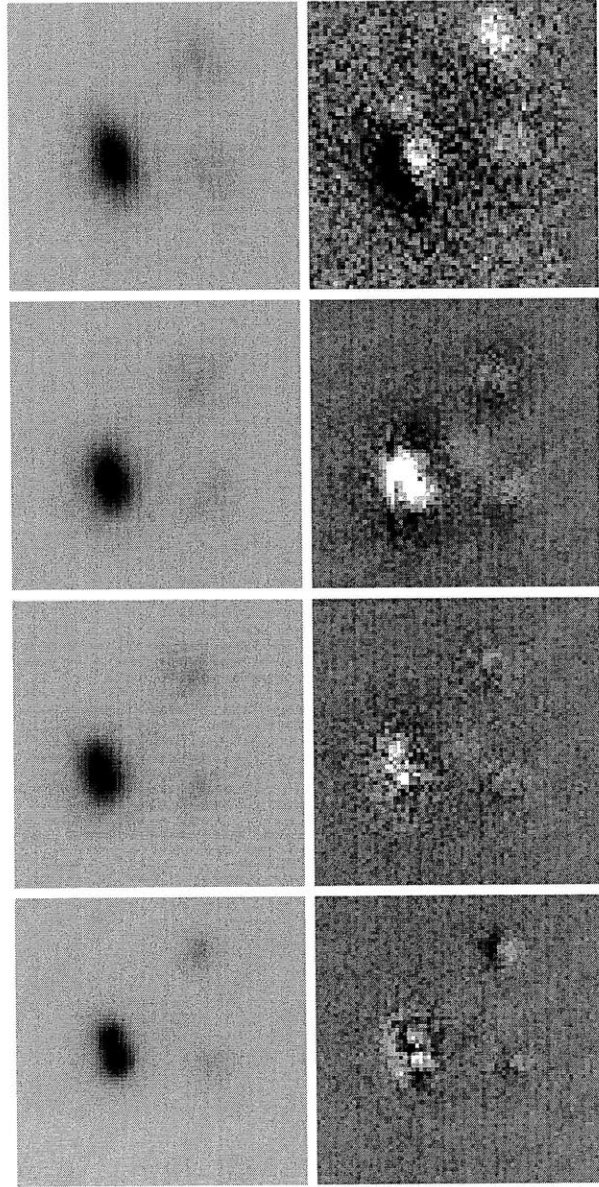Its lens galaxy is at redshift $z_L = 0.295$ [Sluse et al., 2003].

Figure A-8 Postage-stamp images of RX J1131−1231 in $u'g'r'i'$ (top to bottom). Left: original image. Center: residuals after nonlinear least-squares fit. Right: residuals after manually fixing the fluxes ("chi-by-eye").

Figure A-8 (cont'd) Postage-stamp images of RX J1131−1231 in $z'JHK$ (top to bottom). Left: original image. Center: residuals after nonlinear least-squares fit. Right: residuals after manually fixing the fluxes ("chi-by-eye"). In the residual images, the grayscale stretch is set to $\pm 20\sigma$ of the sky level.

A.9 SDSS J1138+0314

The $z_S = 2.44$ quasar SDSS J1138+0314 is lensed by a galaxy at redshift $z_L = 0.45$ into a cross configuration [Eigenbrod et al., 2006].

Figure A-9 Postage-stamp images of SDSS J1138+0314 in $u'g'r'i'$ (top to bottom). Left: original image. Right: residuals after nonlinear least-squares fit. In the residual images, the grayscale stretch is set to $\pm20\sigma$ of the sky level.
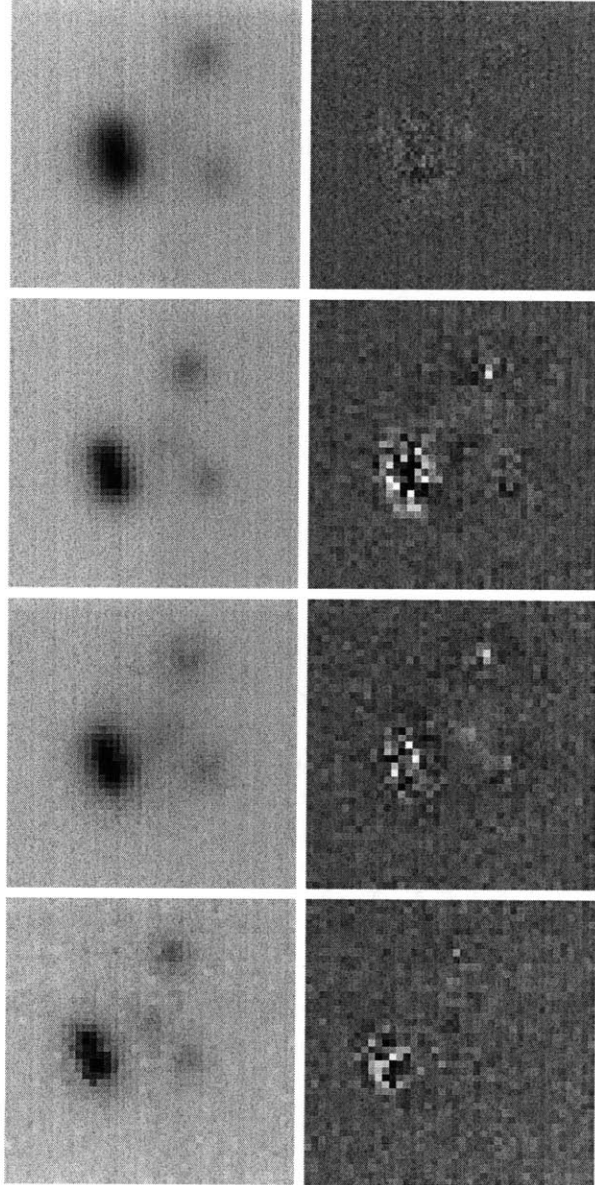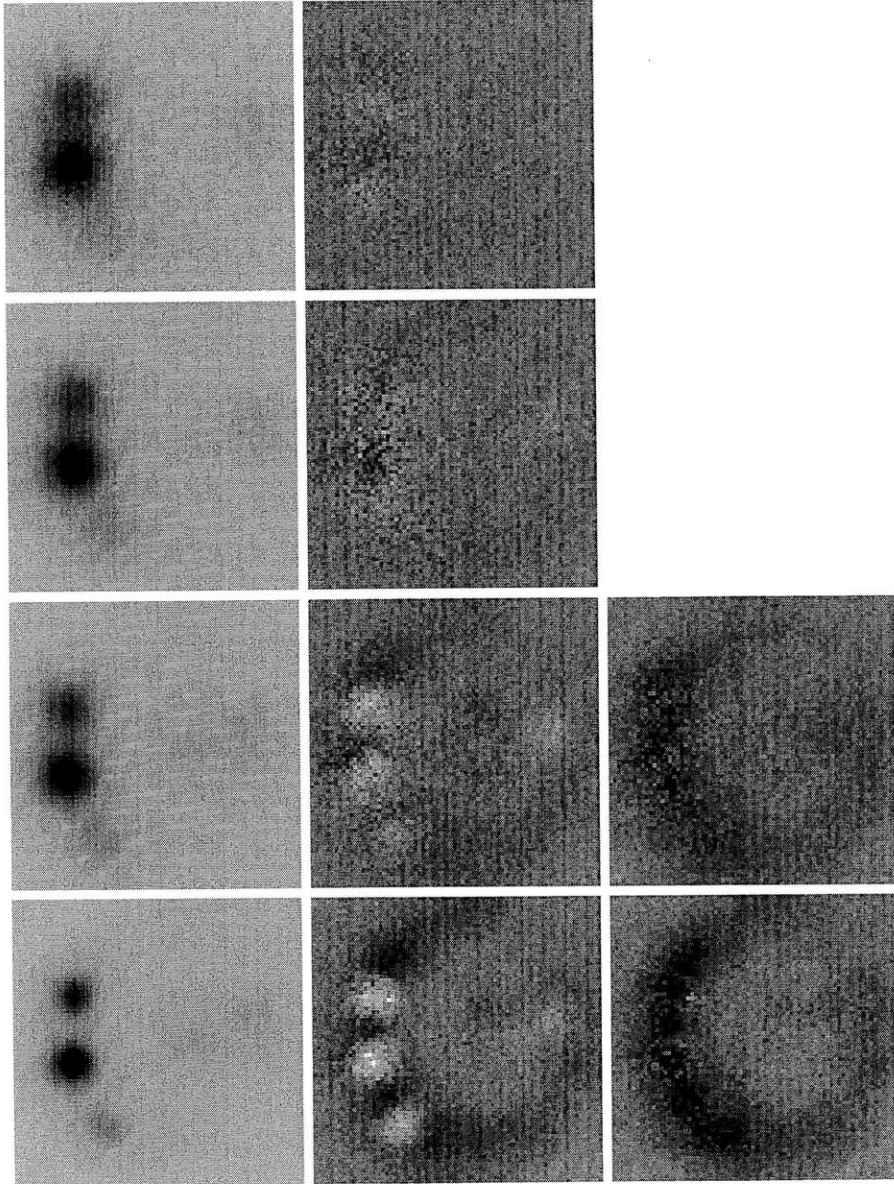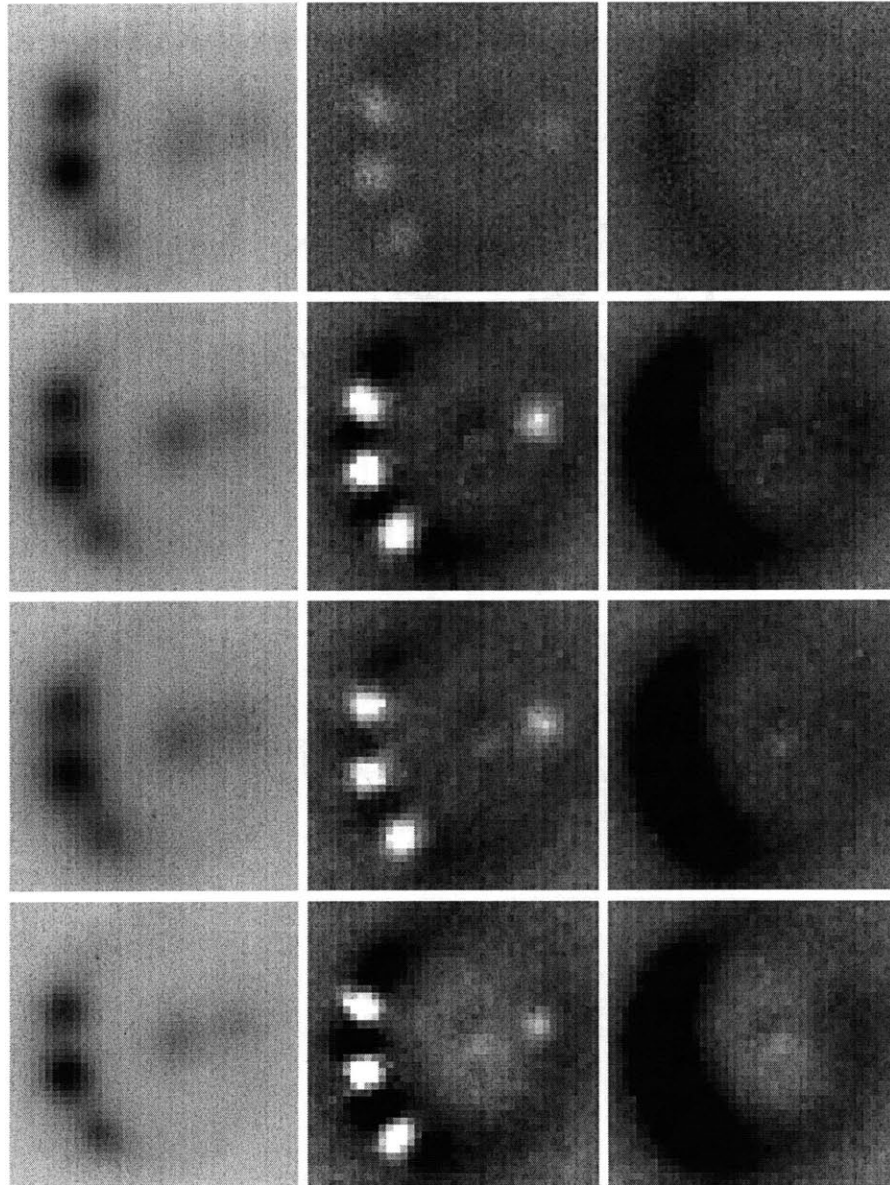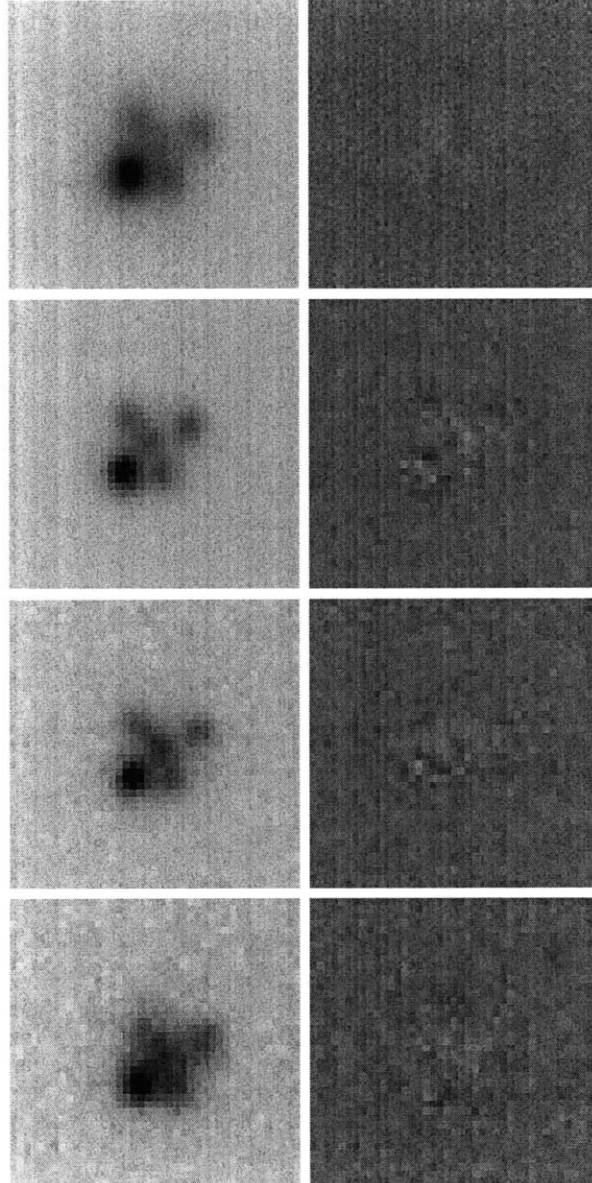
Figure A-9 (cont'd) Postage-stamp images of SDSS J1138+0314 in $z'JHK$ (top to bottom). Left: original image. Right: residuals after nonlinear least-squares fit. In the residual images, the grayscale stretch is set to $\pm 20\sigma$ of the sky level.

A.10   SDSS J1330+1810

The $z_S = 1.393$ quasar SDSS J1330+1810 is lensed into a fold configuration by a bright elliptical galaxy at redshift $z_L = 0.373$ [Oguri et al., 2008a]. It is alone among our sample in that it has not yet been observed at X-ray wavelengths.
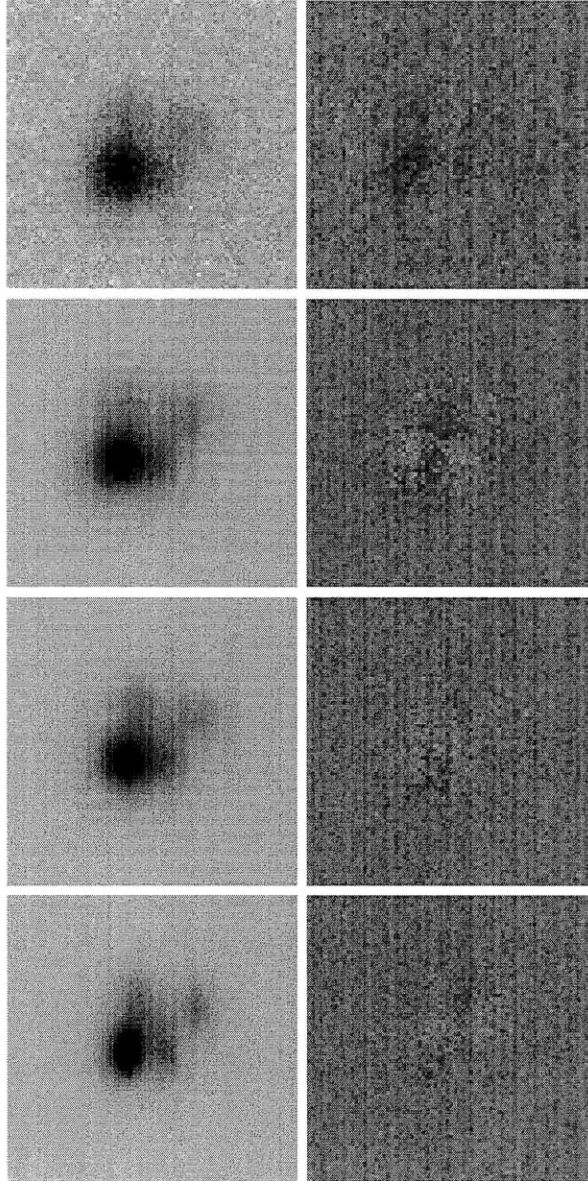

Figure A-10 Postage-stamp images of SDSS J1330+1810 in $u'g'r'i'$ (top to bottom). Left: original image. Right: residuals after nonlinear least-squares fit. In the residual images, the grayscale stretch is set to $\pm 20\sigma$ of the sky level.

Figure A-10 (cont'd) Postage-stamp images of SDSS J1330+1810 in $z'JHK$ (top to bottom). Left: original image. Right: residuals after nonlinear least-squares fit. In the residual images, the grayscale stretch is set to $\pm 20\sigma$ of the sky level.
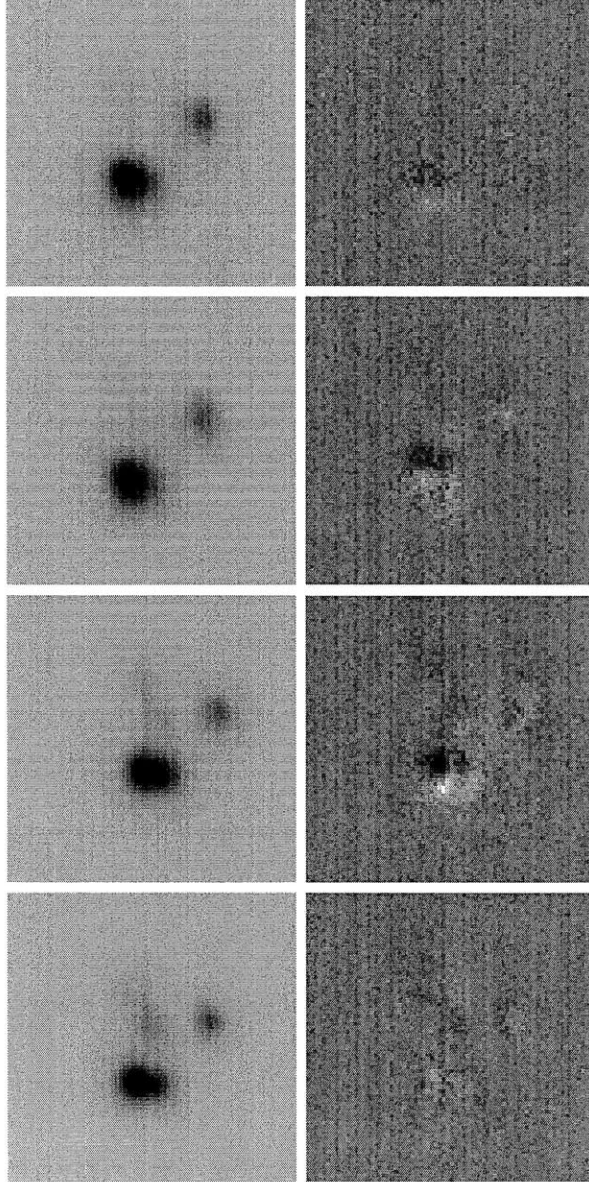
A.11   H 1413+117

The $z_S = 2.55$ quasar H 1413+117 is lensed by a galaxy at unknown redshift into a cross configuration [Magain et al., 1988]. No original optical data on this lens are included in this thesis, though its X-ray fluxes are reported in Chapter 5. A picture of the lens may be found on the CASTLES web site[1].

A.12   B 1422+231

B 1422+231, at redshift $z_S = 3.62$, is lensed into a cusp configuration by a galaxy at redshift $z_L = 0.34$ [Patnaik et al., 1992]. We do not report any original optical data for this lens, though its X-ray fluxes are reported in Chapter 5. B 1422+231 is a radio-loud quasar, and its radio fluxes are anomalous, indicating that it is affected by millilensing by dark matter substructure [Mao and Schneider, 1998]. A picture of this lens may be found on the CASTLES web site.

---

[1] http://www.cfa.harvard.edu/castles/

A.13 WFI J2026−4536

At redshift $z_S = 2.23$, WFI J2026−4536 is lensed into a compact fold configuration by a galaxy of unknown redshift [Morgan et al., 2004]. In our analysis, we estimate its redshift to be 0.7; this introduces only a small amount of uncertainty into our size measurements, since the stellar Einstein ring radius depends weakly on z_L.

Figure A-11 Postage-stamp images of WFI J2026−4536 in $u'g'r'i'$ (top to bottom). Left: original image. Right: residuals after nonlinear least-squares fit. In the residual images, the grayscale stretch is set to $\pm 20\sigma$ of the sky level.
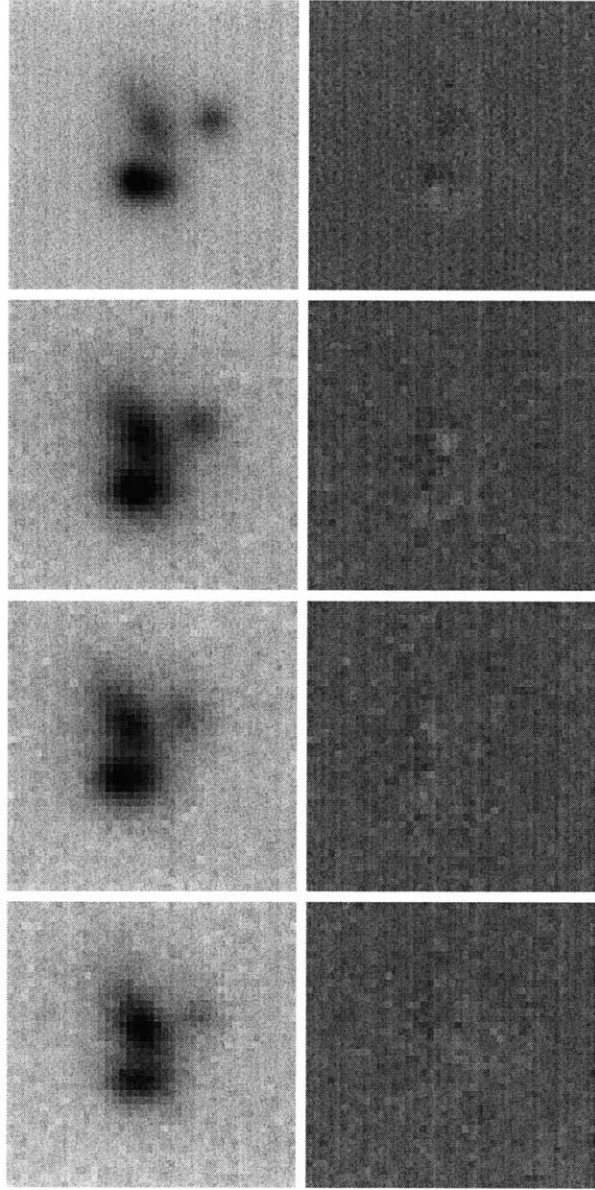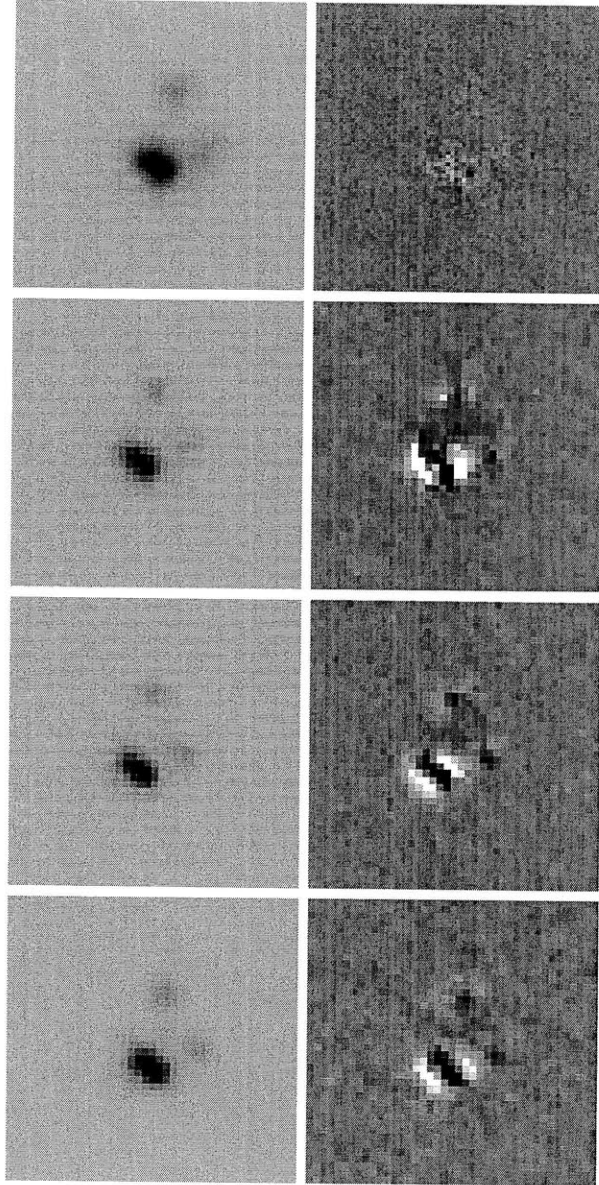
Figure A-11 (cont'd) Postage-stamp images of WFI J2026$-$4536 in $z'JHK$ (top to bottom). Left: original image. Right: residuals after nonlinear least-squares fit. In the residual images, the grayscale stretch is set to $\pm 20\sigma$ of the sky level.

A.14 WFI J2033−4723

The quasar WFI J2033−4723, at redshift $z_S = 1.66$, is lensed by a $z_L = 0.66$ galaxy into a fold configuration [Morgan et al., 2004].
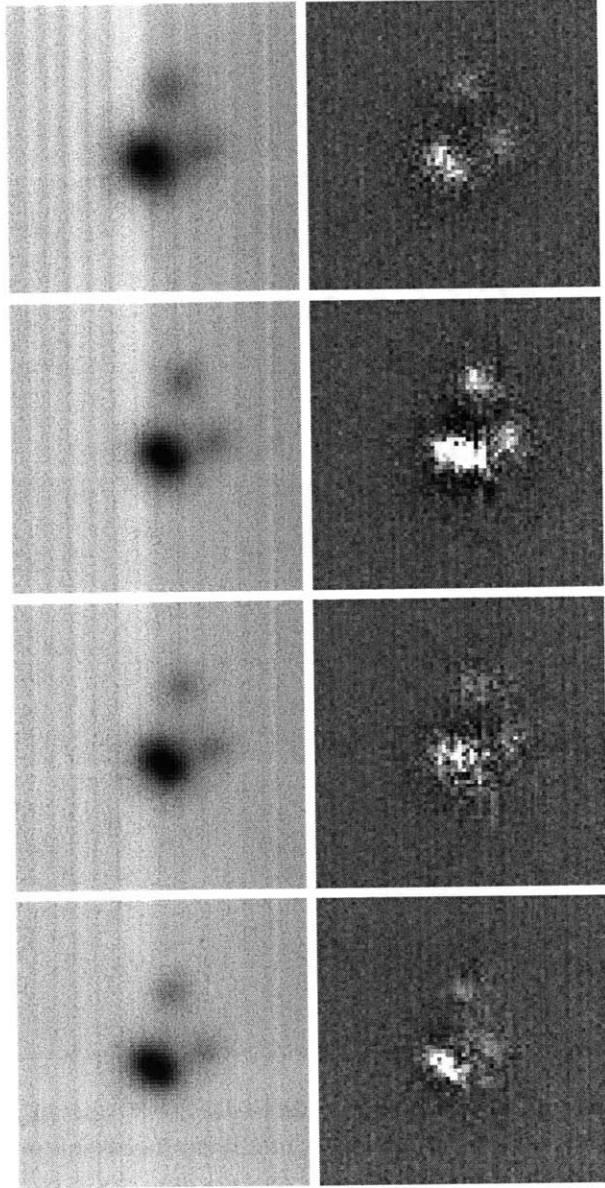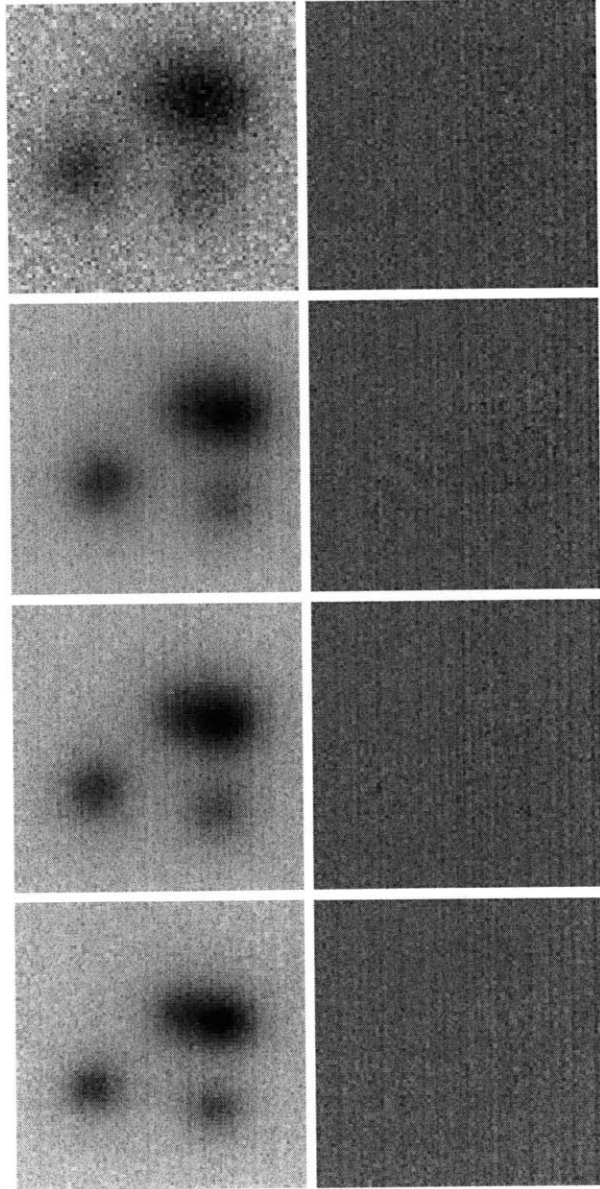

Figure A-12 Postage-stamp images of WFI J2033−4723 in $u'g'r'i'$ (top to bottom). Left: original image. Right: residuals after nonlinear least-squares fit. In the residual images, the grayscale stretch is set to $\pm 20\sigma$ of the sky level.
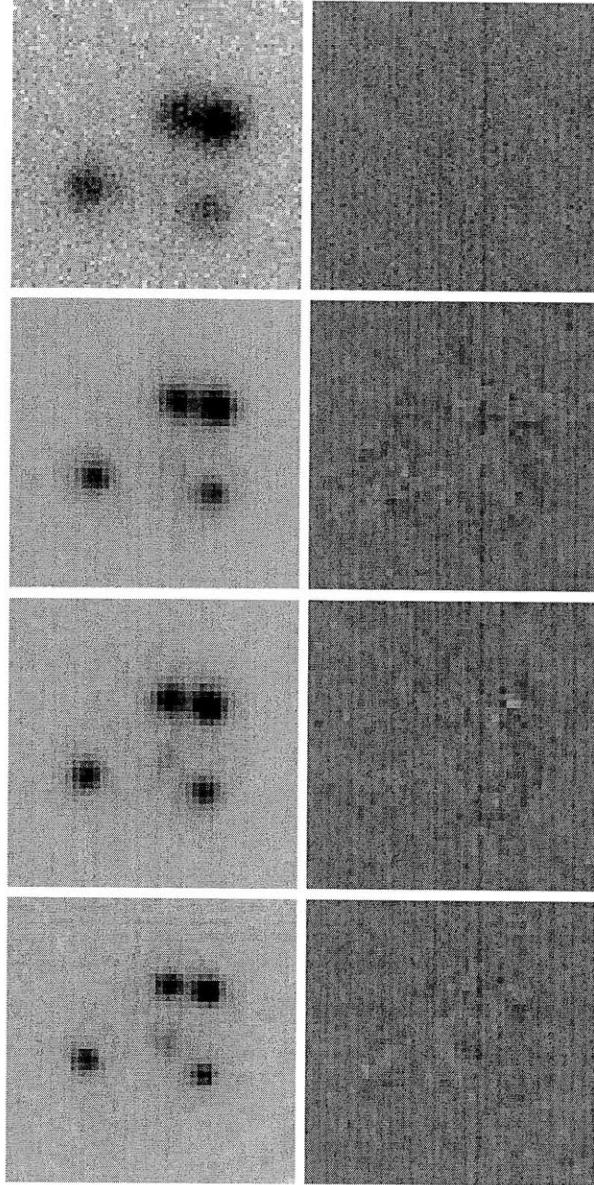
Figure A-12 (cont'd) Postage-stamp images of WFI J2033−4723 in $z'JHK$ (top to bottom). Left: original image. Right: residuals after nonlinear least-squares fit. In the residual images, the grayscale stretch is set to $\pm20\sigma$ of the sky level.

A.15   Q 2237+0305

The $z_S = 1.69$ quasar Q 2237+0305 is lensed into a cross configuration by a lens galaxy at a redshift $z_L = 0.04$ [Huchra et al., 1985]. The low redshift of the lens galaxy causes the Einstein crossing time to be much less than for the other lenses; for this reason microlensing has been observed many times in this system [e.g., Woźniak et al., 2000]. Another result of the low lens redshift is that the projected size of the Einstein radius in the source plane is a factor of ~ 3 greater than the other lenses. We do not report any original optical data for this lens, though its X-ray fluxes are reported in Chapter 5. A picture of the lens system may be found on the CASTLES web site.

Appendix B

Likelihood distributions for the accretion disk sizes

This appendix contains plots of all the likelihood distributions we calculated. Most lenses have sixteen each, since we have eight filters and a choice of linear or logarithmic priors.

Figure B-1 Likelihood distributions for the half-light radius of HE 0230−2130 in the $u'g'r'i'$ filters, as a fraction of a $1M_\odot$ Einstein radius. Left column: logarithmic prior. Right column: Linear prior.

Figure B-1 (cont'd) Likelihood distributions for the half-light radius of HE 0230−2130 in the $z'JHK_s$ filters, as a fraction of a $1M_\odot$ Einstein radius. Left column: logarithmic prior. Right column: Linear prior.

193

Figure B-2 Likelihood distributions for the half-light radius of MG J0414+0534 in the $r'i'z'$ filters, as a fraction of a $1M_\odot$ Einstein radius. Left column: logarithmic prior. Right column: Linear prior.

Figure B-2 (cont'd) Likelihood distributions for the half-light radius of MG J0414+0534 in the JHK_s filters, as a fraction of a $1M_\odot$ Einstein radius. Left column: logarithmic prior. Right column: Linear prior.

Figure B-3 Likelihood distributions for the half-light radius of HE 0435−1223 in the $u'g'r'i'$ filters, as a fraction of a $1M_\odot$ Einstein radius. Left column: logarithmic prior. Right column: Linear prior.

Figure B-3 (cont'd) Likelihood distributions for the half-light radius of HE 0435−1223 in the $z'JHK_s$ filters, as a fraction of a $1M_\odot$ Einstein radius. Left column: logarithmic prior. Right column: Linear prior.
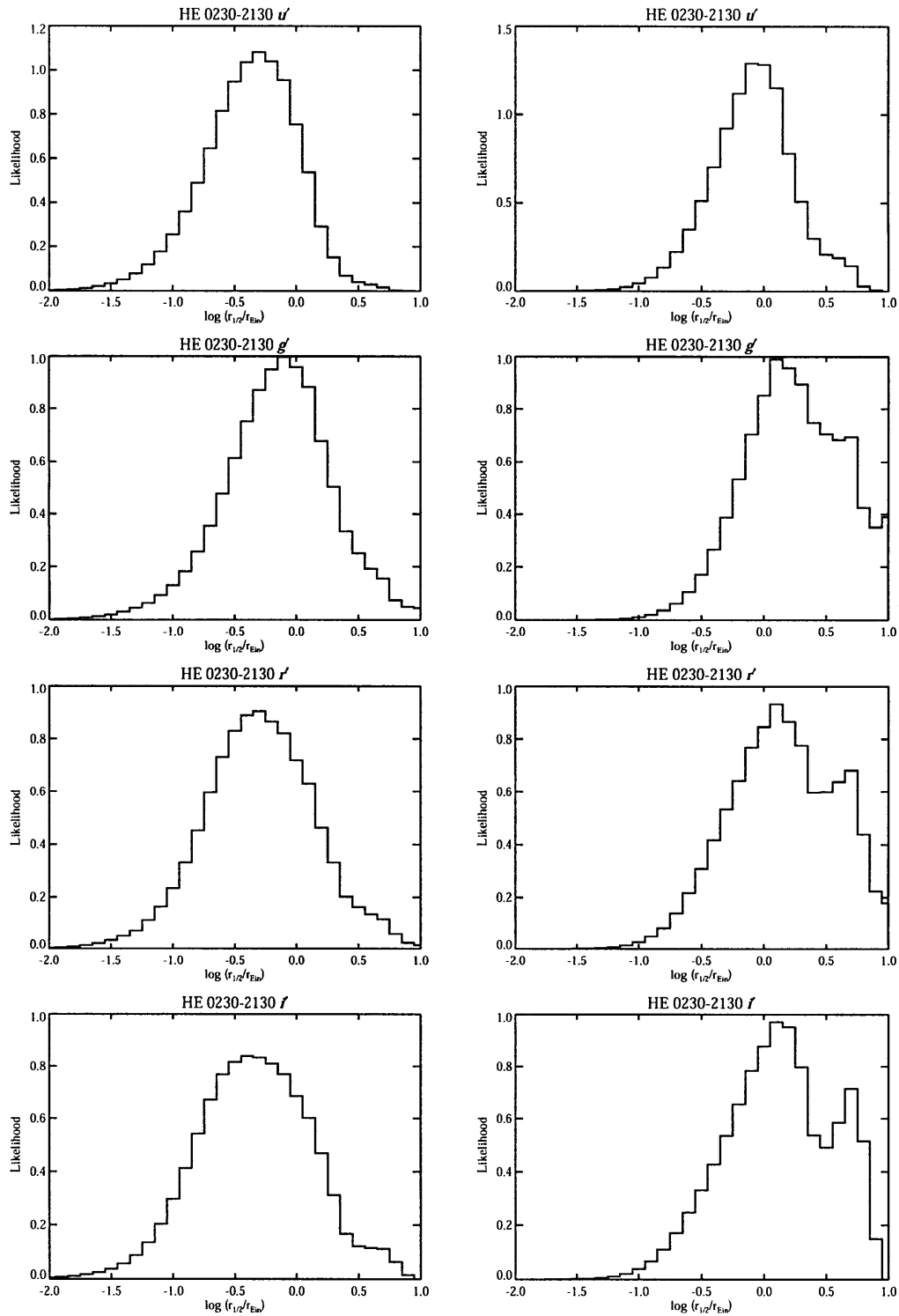
Figure B-4 Likelihood distributions for the half-light radius of RX J0911+0551 in the $u'g'r'i'$ filters, as a fraction of a $1M_\odot$ Einstein radius. Left column: logarithmic prior. Right column: Linear prior.

Figure B-4 (cont'd) Likelihood distributions for the half-light radius of RX J0911+0551 in the $z'JHK_s$ filters, as a fraction of a $1M_\odot$ Einstein radius. Left column: logarithmic prior. Right column: Linear prior.

199

Figure B-5 Likelihood distributions for the half-light radius of SDSS J0924+0219 in the $u'g'r'i'$ filters, as a fraction of a $1M_\odot$ Einstein radius. Left column: logarithmic prior. Right column: Linear prior.
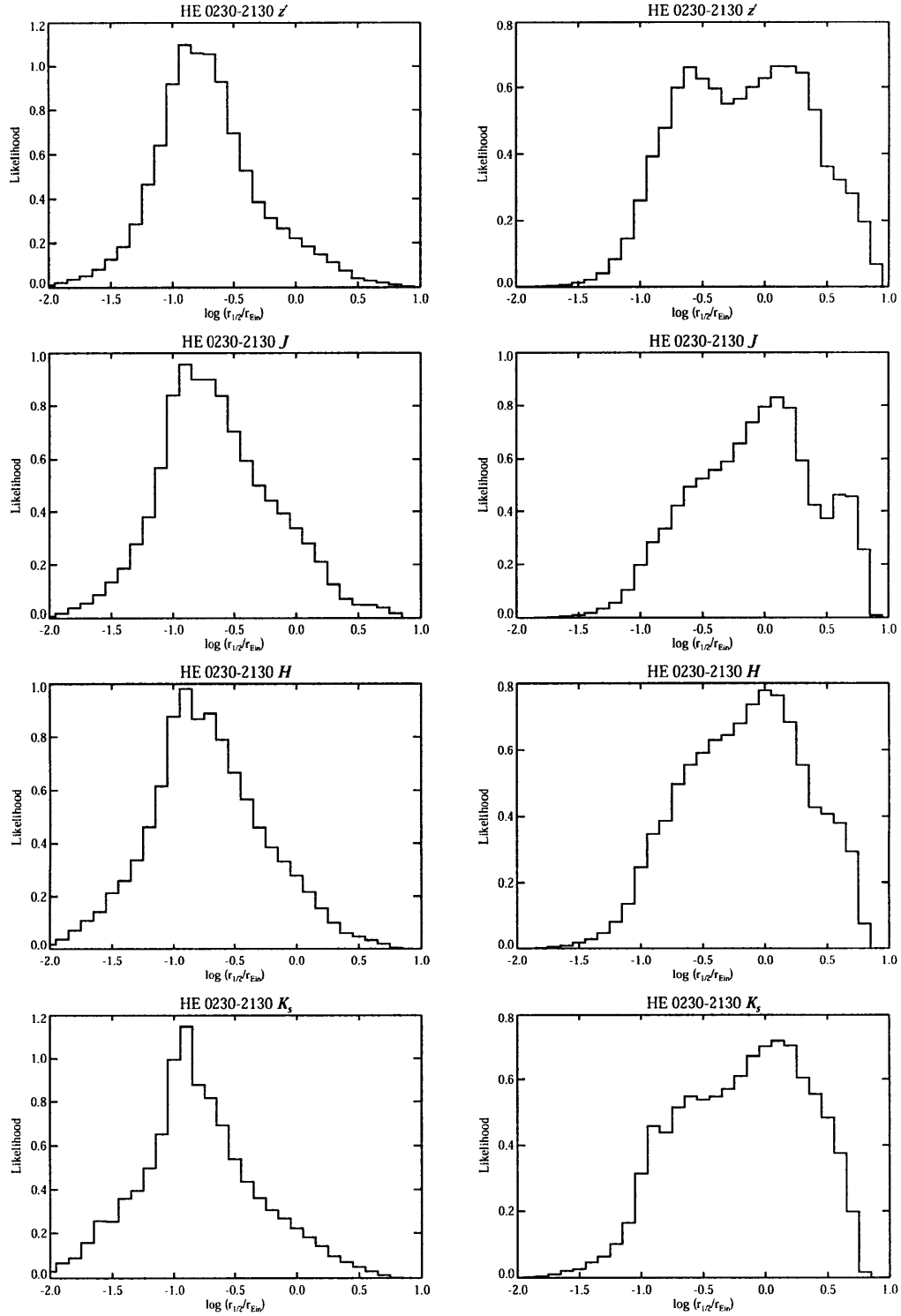
Figure B-5 (cont'd) Likelihood distributions for the half-light radius of SDSS J0924+0219 in the $z'JHK_s$ filters, as a fraction of a $1M_\odot$ Einstein radius. Left column: logarithmic prior. Right column: Linear prior.

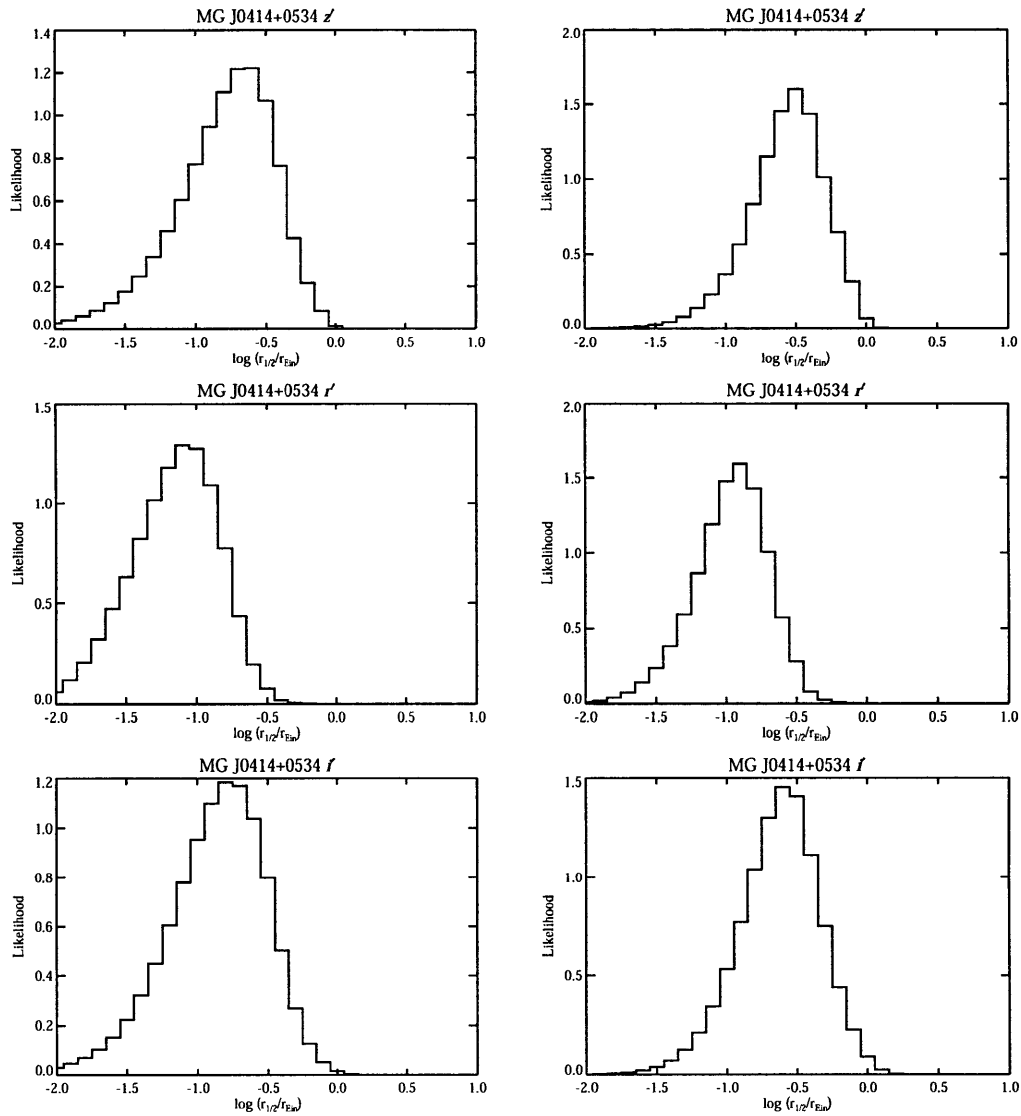Figure B-6 Likelihood distributions for the half-light radius of HE 1113−0641 in the $g'r'i'z'$ filters, as a fraction of a $1M_\odot$ Einstein radius. Left column: logarithmic prior. Right column: Linear prior.
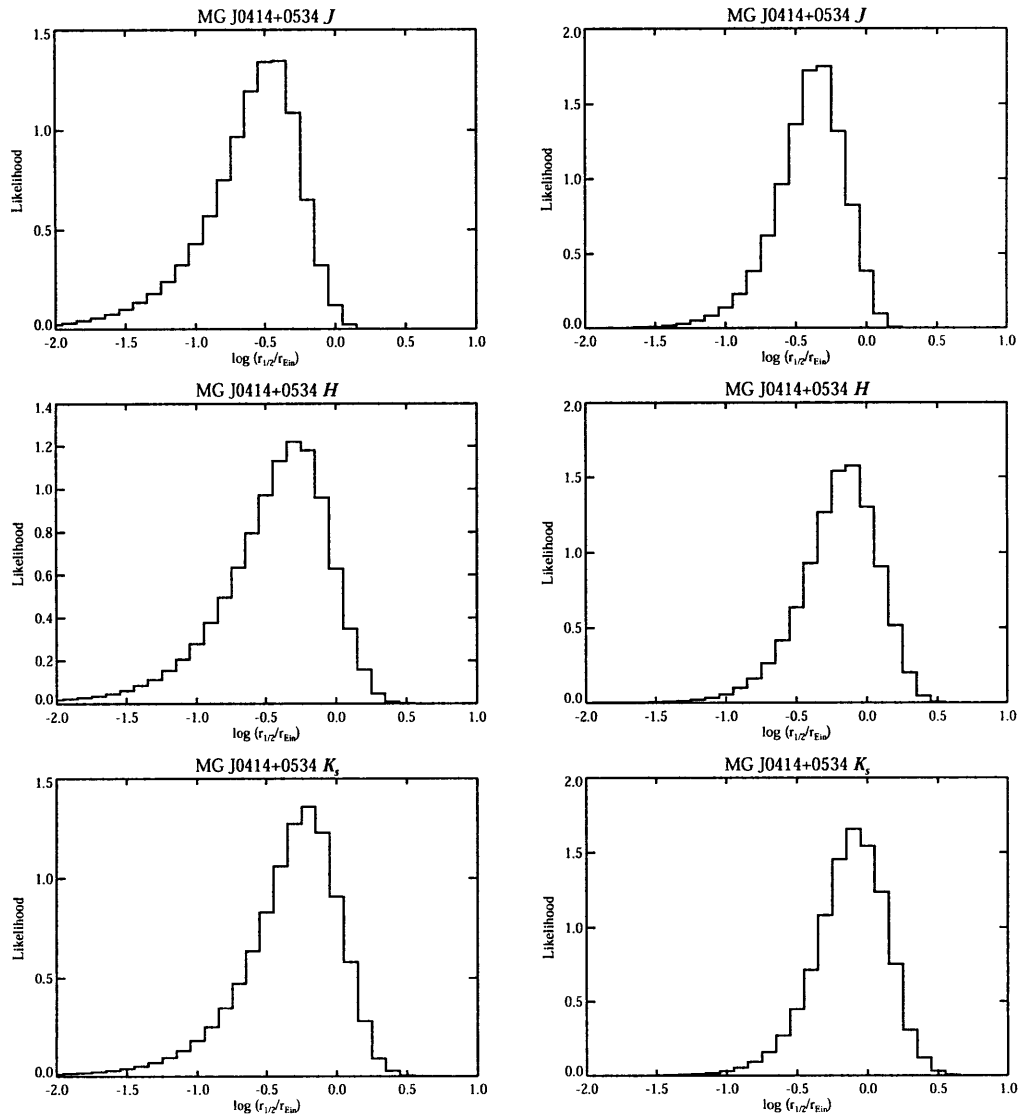
Figure B-6 (cont'd) Likelihood distributions for the half-light radius of HE 1113−0641 in the JHK_s filters, as a fraction of a $1M_\odot$ Einstein radius. Left column: logarithmic prior. Right column: Linear prior.
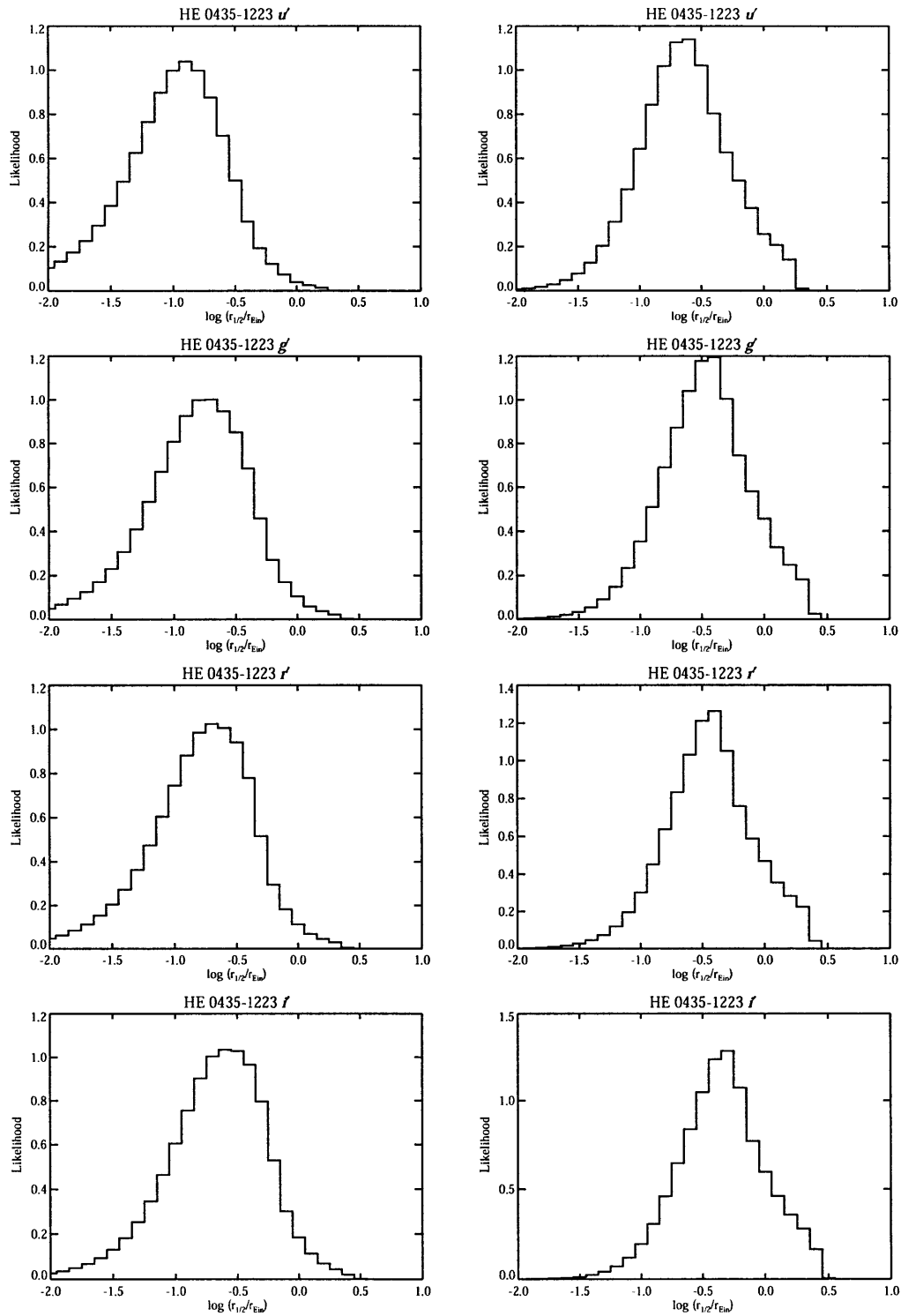
203
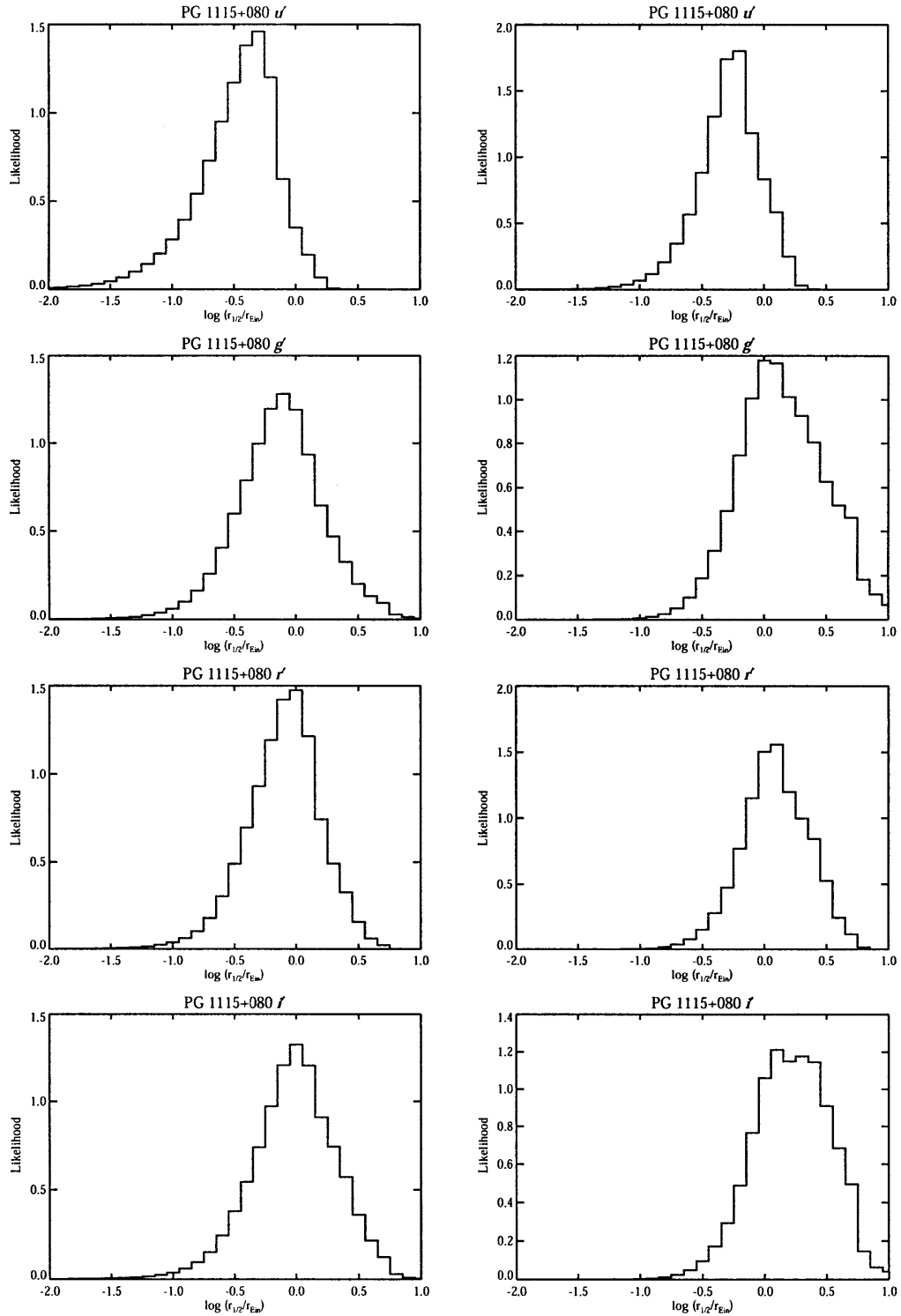
Figure B-7 Likelihood distributions for the half-light radius of PG 1115+080 in the $u'g'r'i'$ filters, as a fraction of a $1M_\odot$ Einstein radius. Left column: logarithmic prior. Right column: Linear prior.
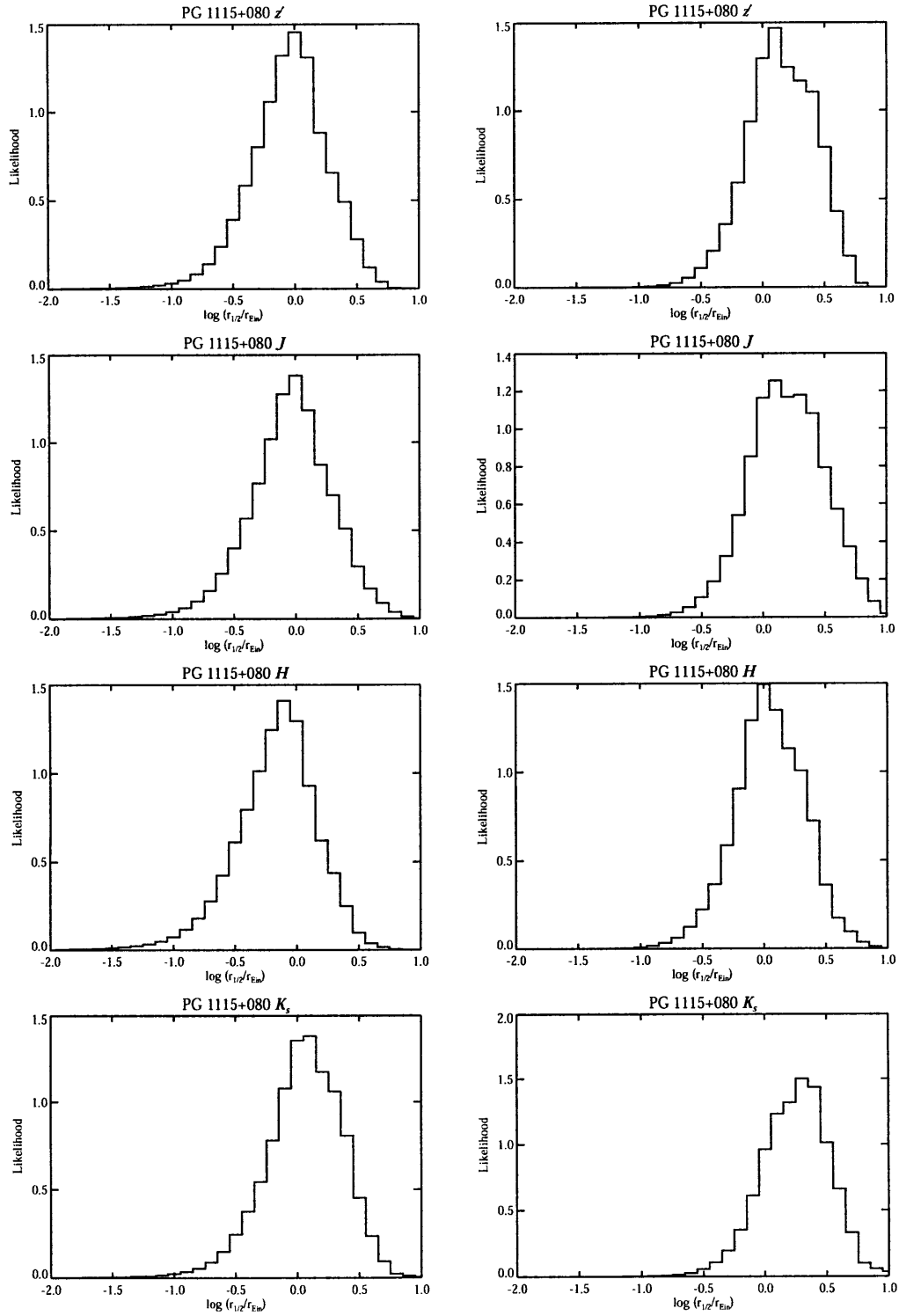
Figure B-7 (cont'd) Likelihood distributions for the half-light radius of PG 1115+080 in the $z'JHK_s$ filters, as a fraction of a $1M_\odot$ Einstein radius. Left column: logarithmic prior. Right column: Linear prior.
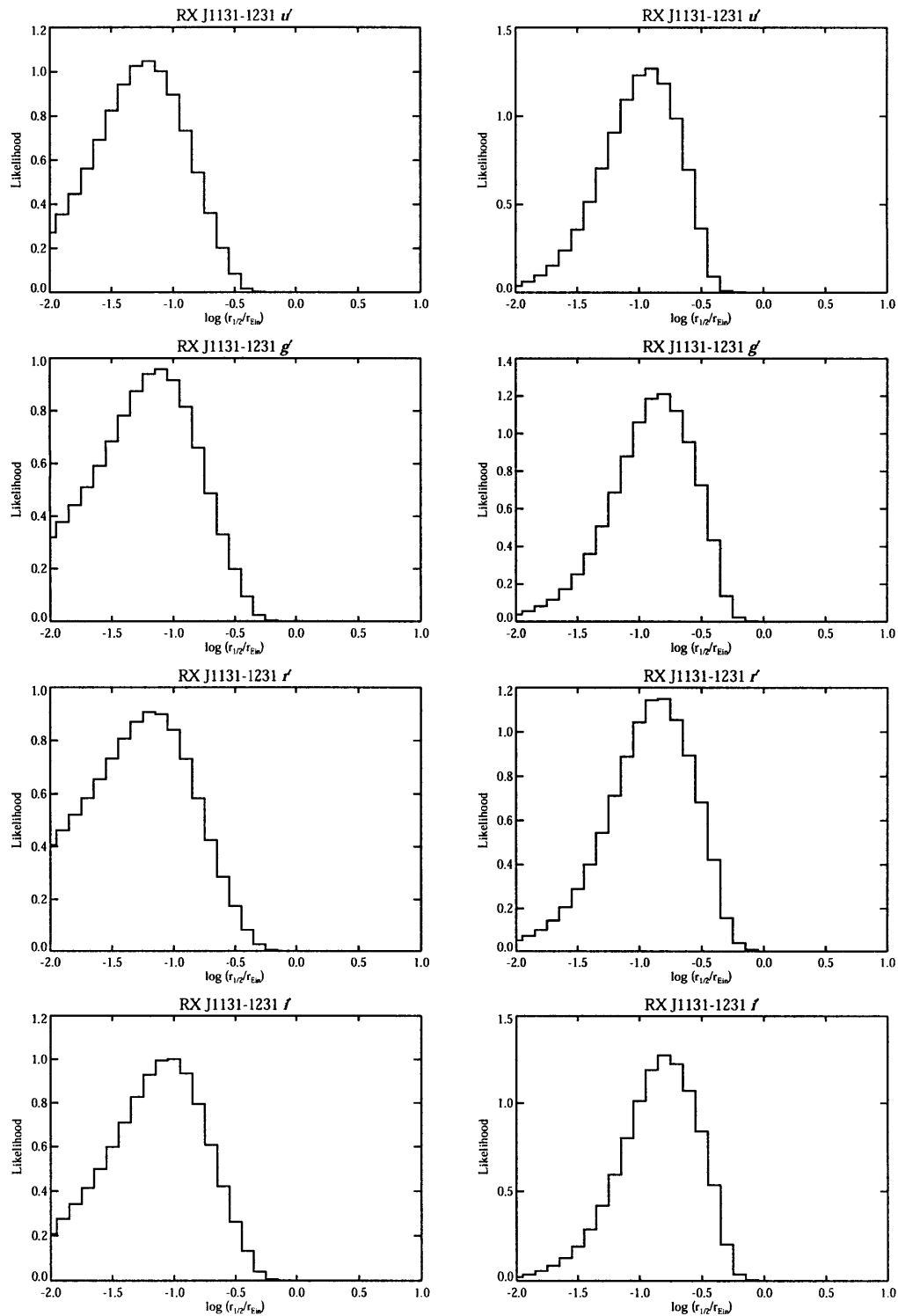
Figure B-8 Likelihood distributions for the half-light radius of RX J1131−1231 in the $u'g'r'i'$ filters, as a fraction of a $1 M_\odot$ Einstein radius. Left column: logarithmic prior. Right column: Linear prior.
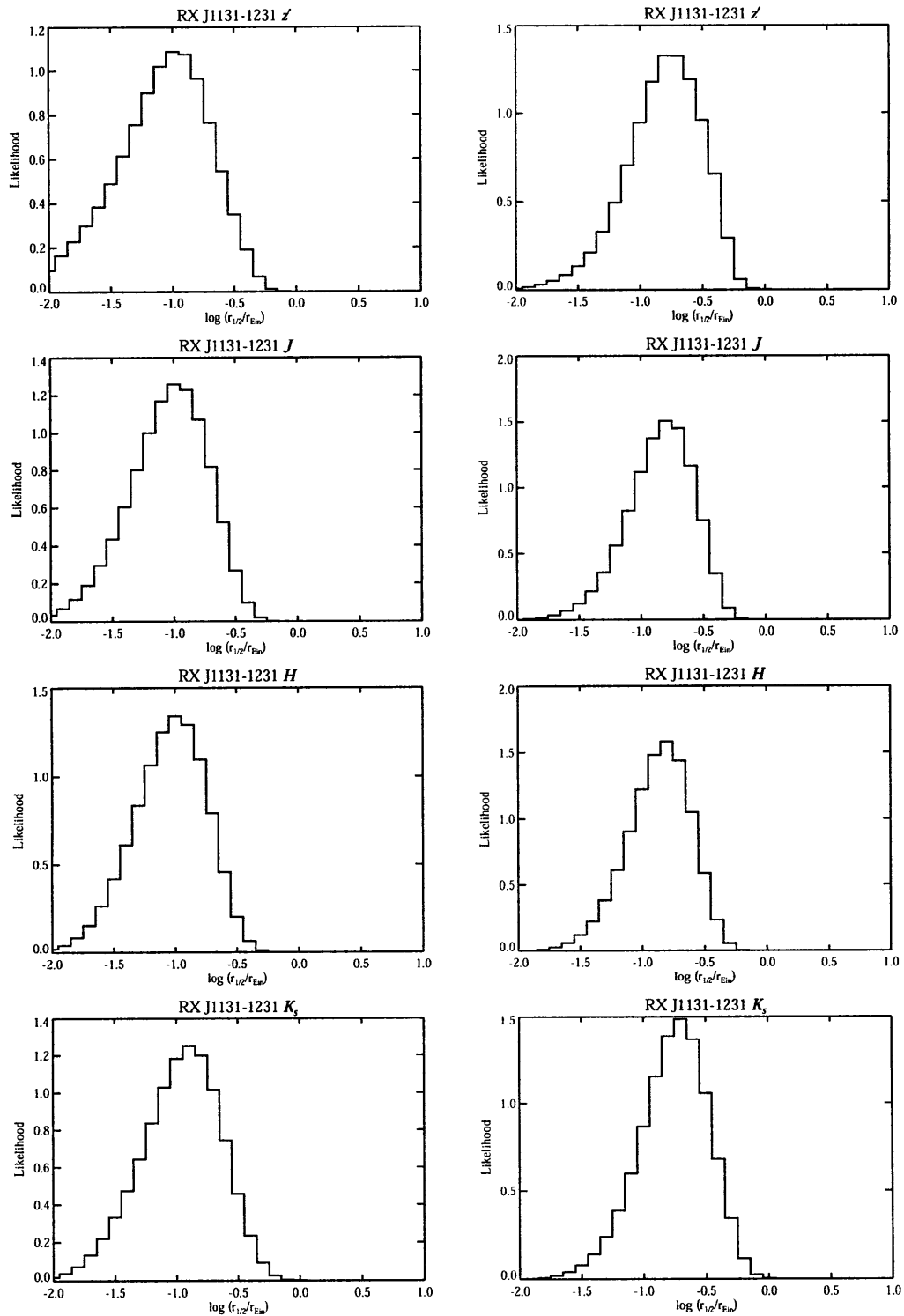
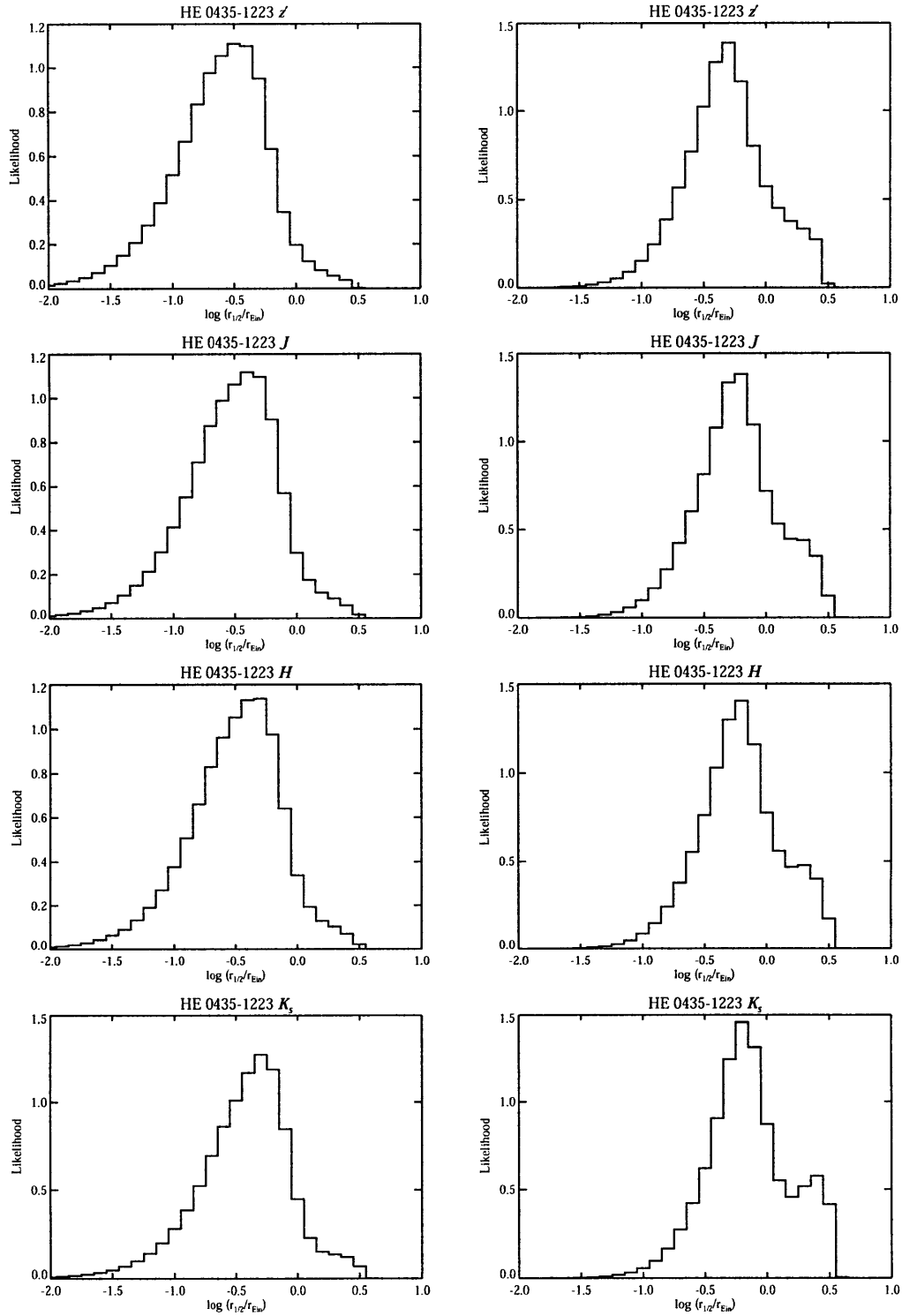Figure B-8 (cont'd) Likelihood distributions for the half-light radius of RX J1131−1231 in the $z'JHK_s$ filters, as a fraction of a $1M_\odot$ Einstein radius. Left column: logarithmic prior. Right column: Linear prior.
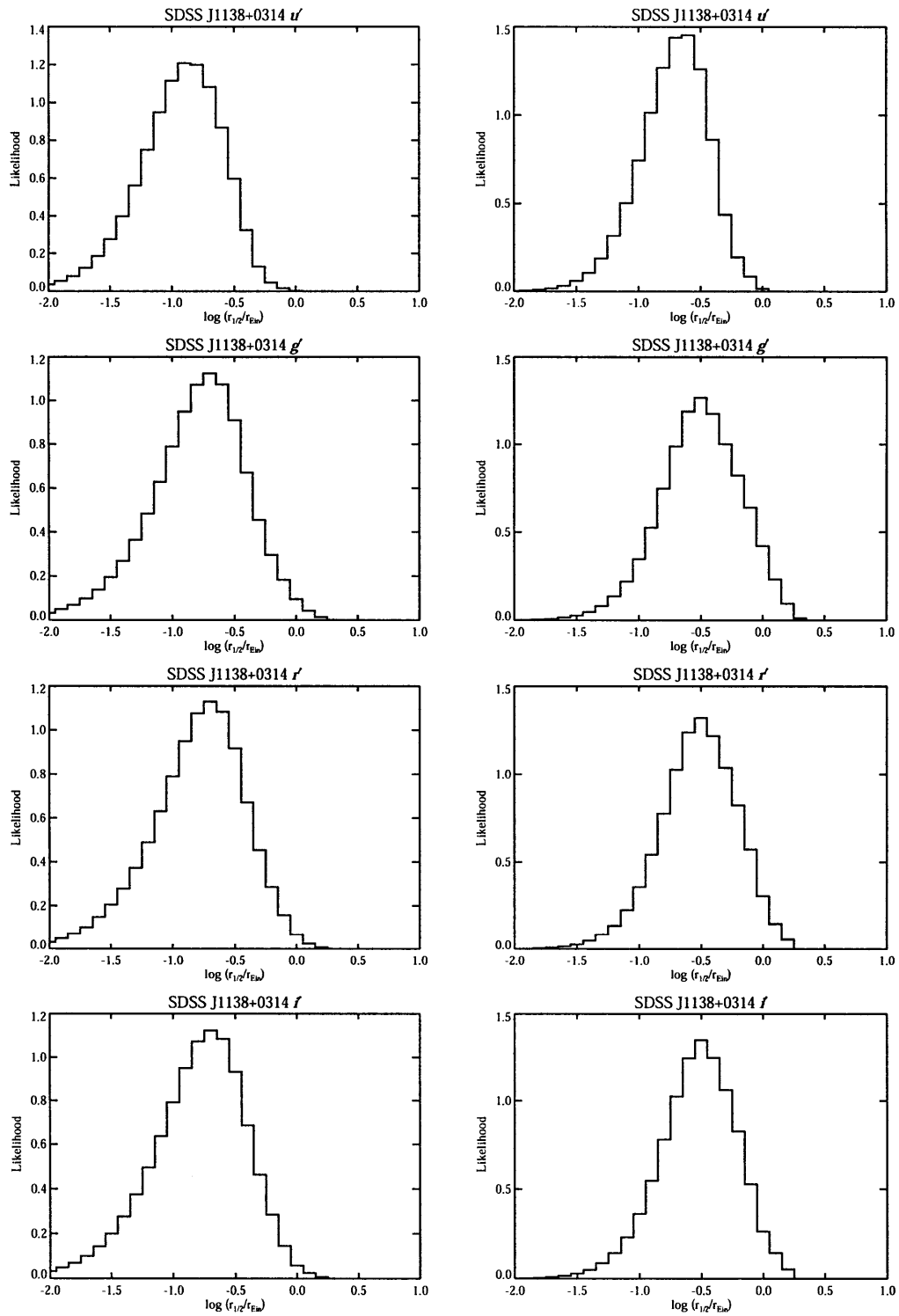
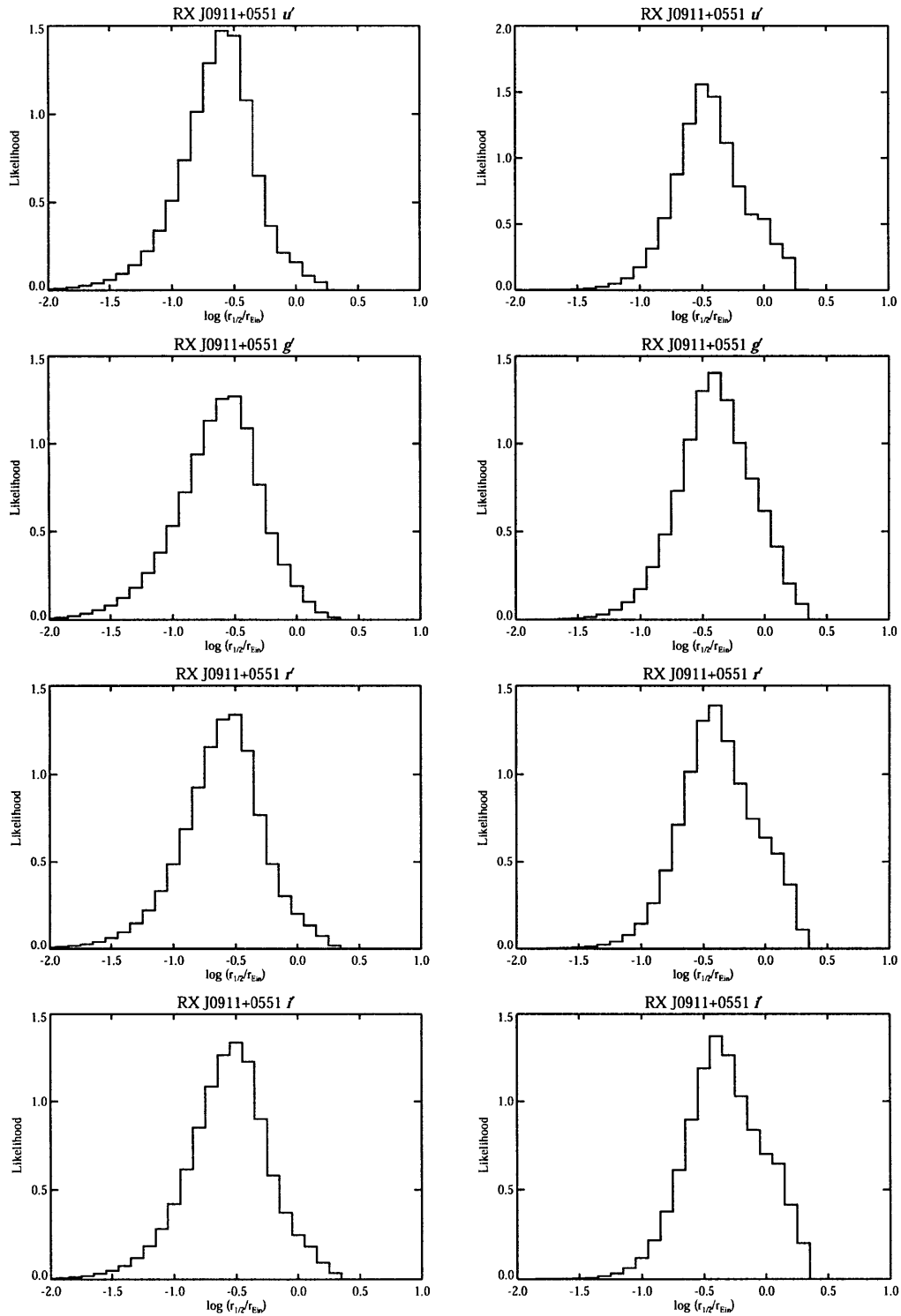Figure B-9 Likelihood distributions for the half-light radius of SDSS J1138+0314 in the $u'g'r'i'$ filters, as a fraction of a $1M_\odot$ Einstein radius. Left column: logarithmic prior. Right column: Linear prior.
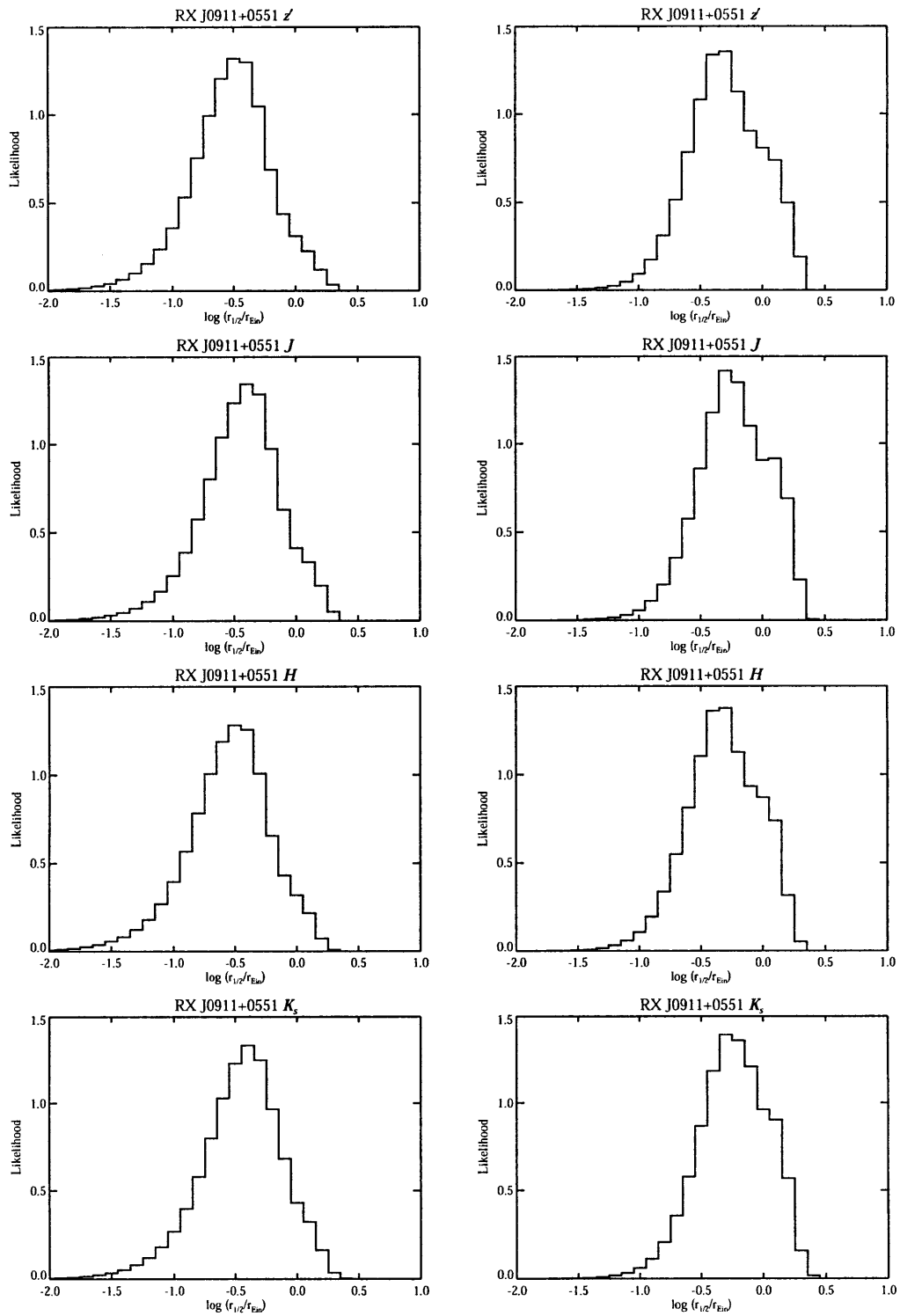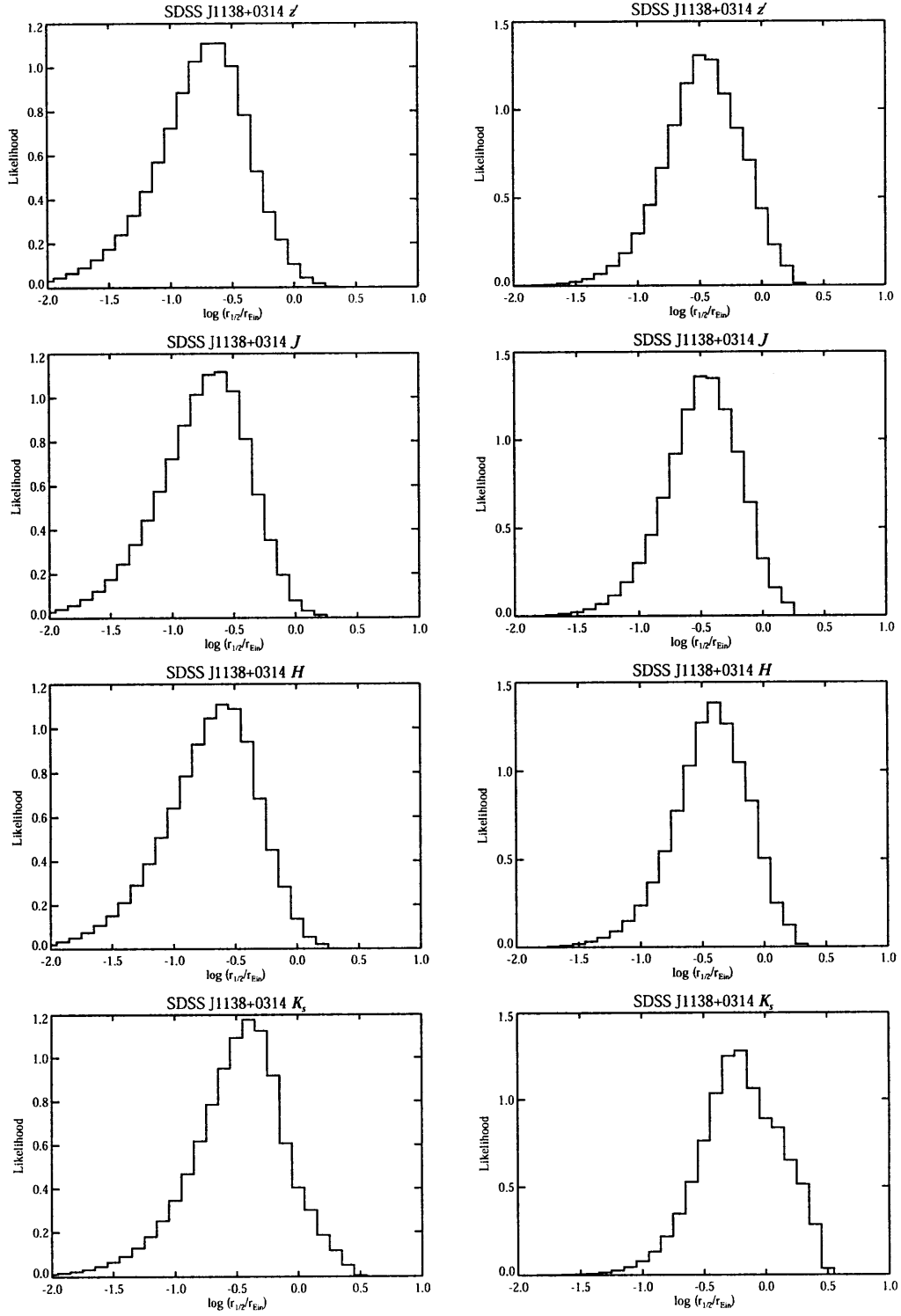
Figure B-9 (cont'd) Likelihood distributions for the half-light radius of SDSS J1138+0314 in the $z'JHK_s$ filters, as a fraction of a $1M_\odot$ Einstein radius. Left column: logarithmic prior. Right column: Linear prior.
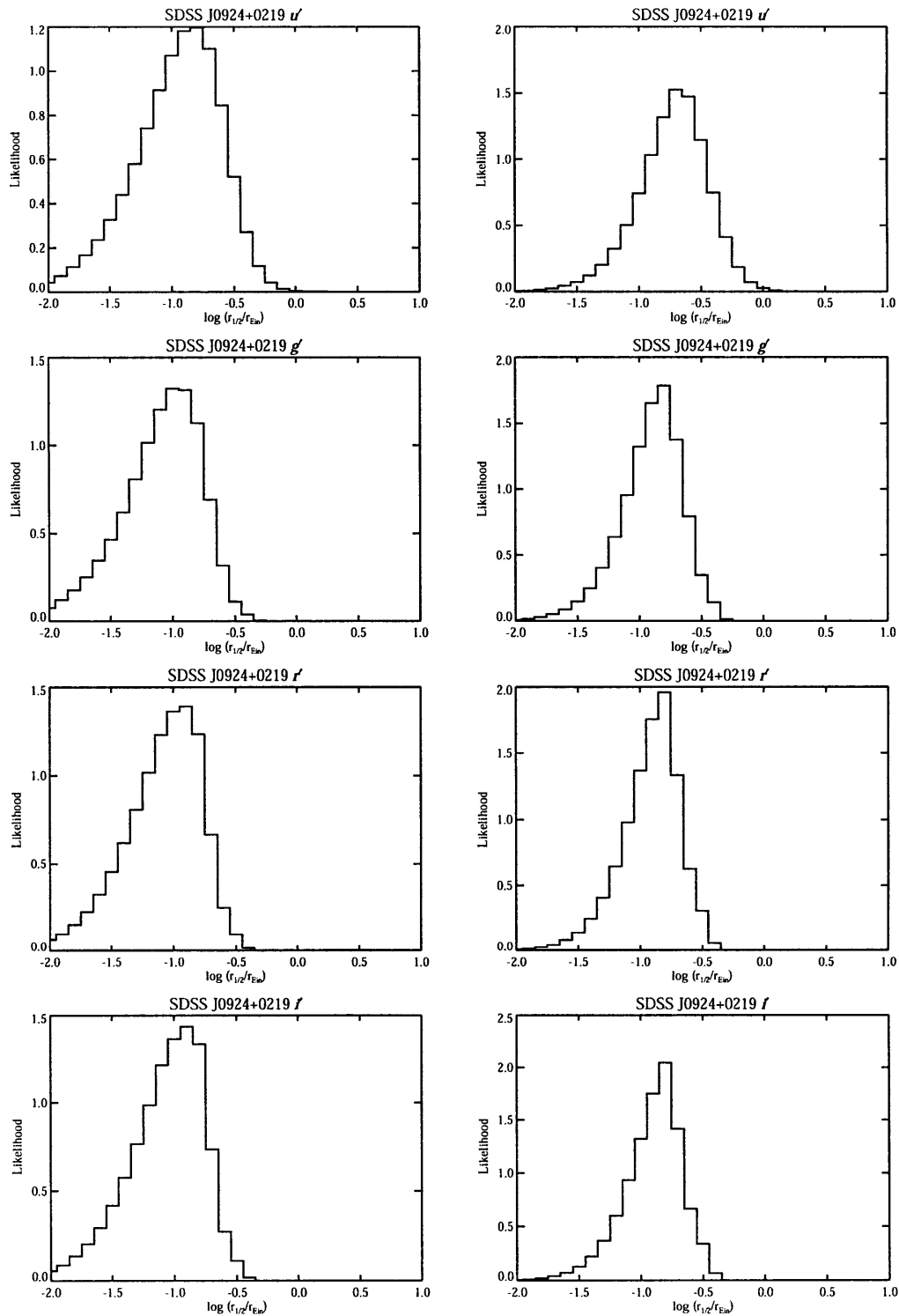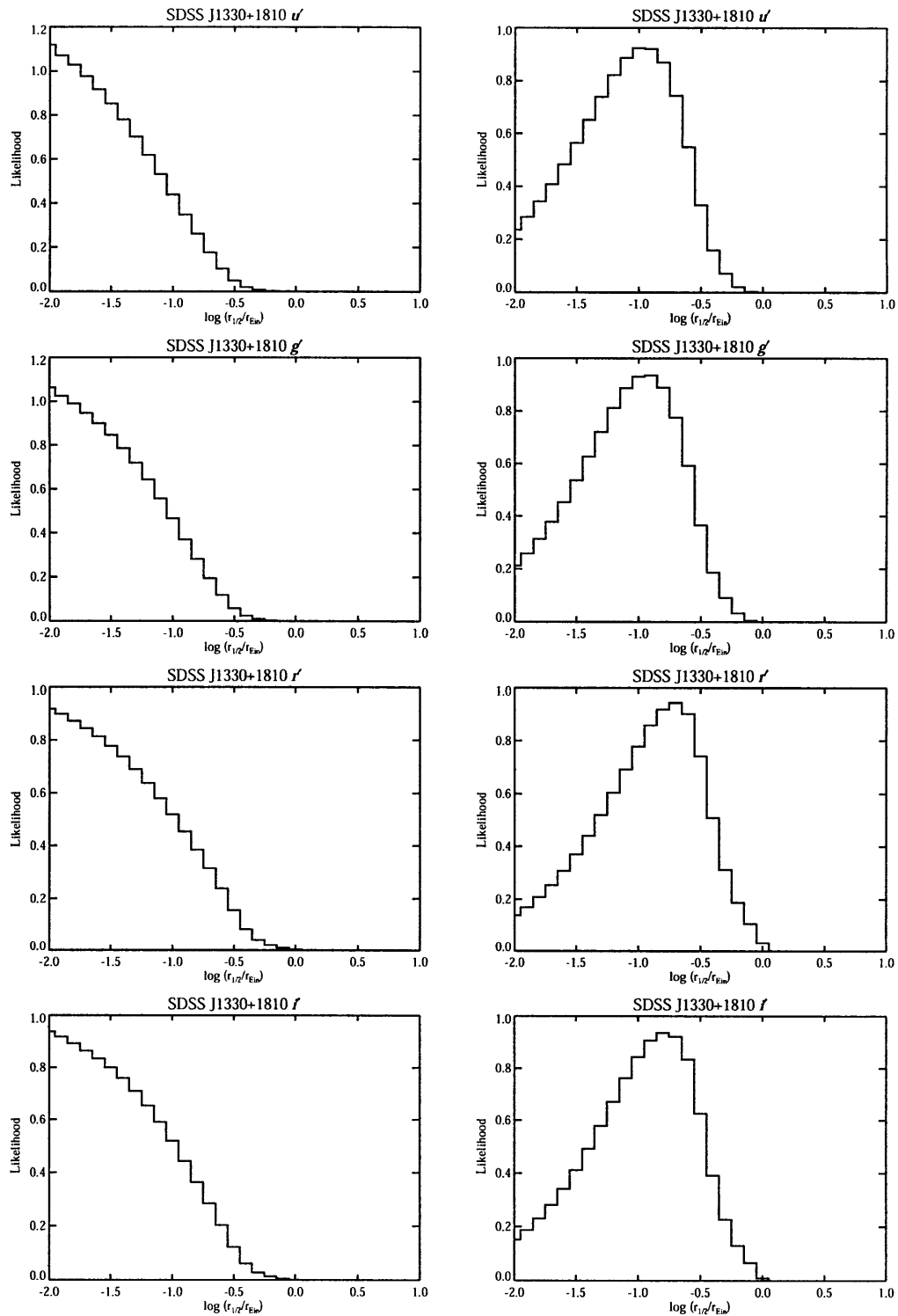
Figure B-10 Likelihood distributions for the half-light radius of SDSS J1330+1810 in the $u'g'r'i'$ filters, as a fraction of a $1M_\odot$ Einstein radius. Left column: logarithmic prior. Right column: Linear prior.
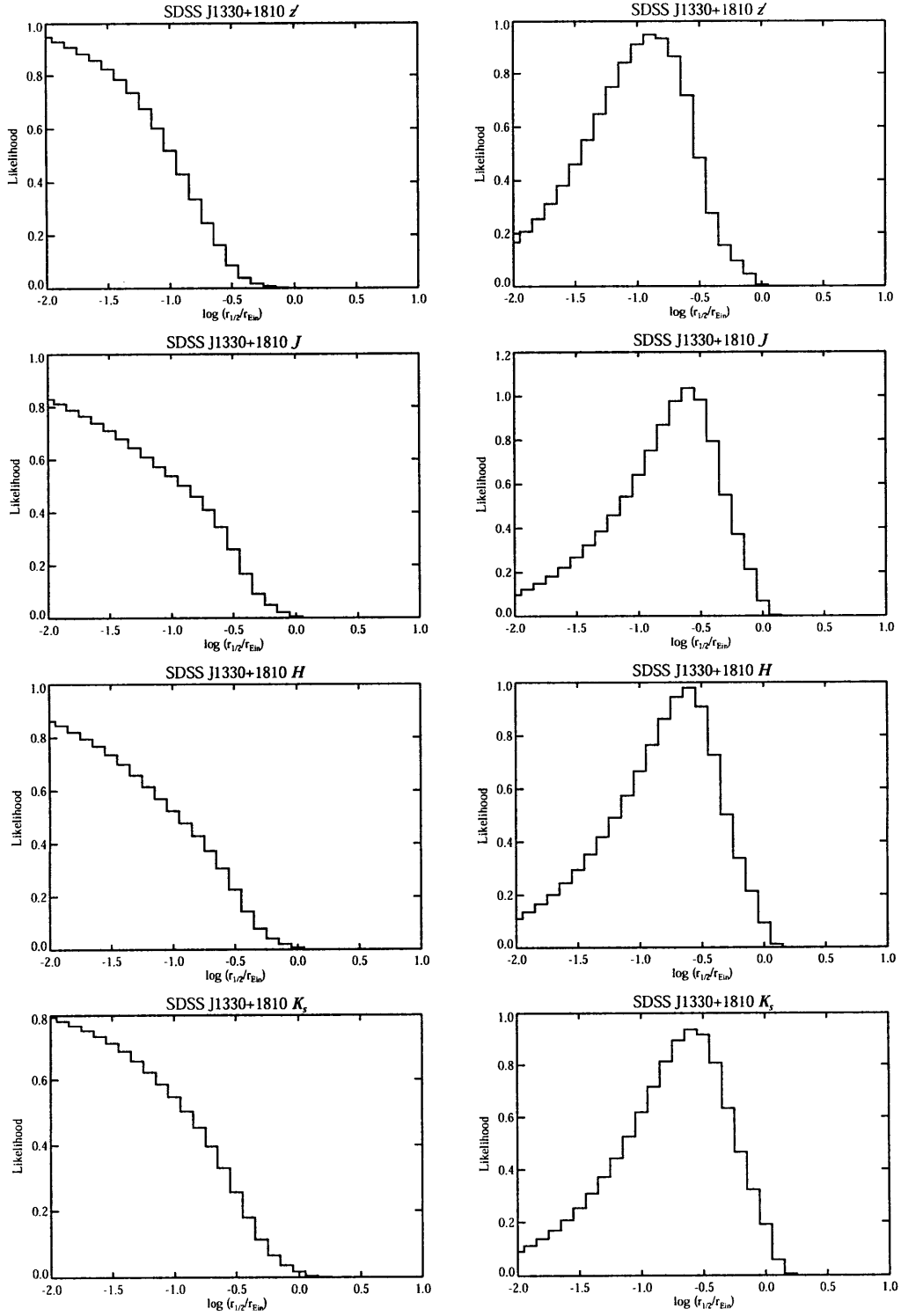
Figure B-10 (cont'd) Likelihood distributions for the half-light radius of SDSS J1330+1810 in the $z'JHK_s$ filters, as a fraction of a $1M_\odot$ Einstein radius. Left column: logarithmic prior. Right column: Linear prior.
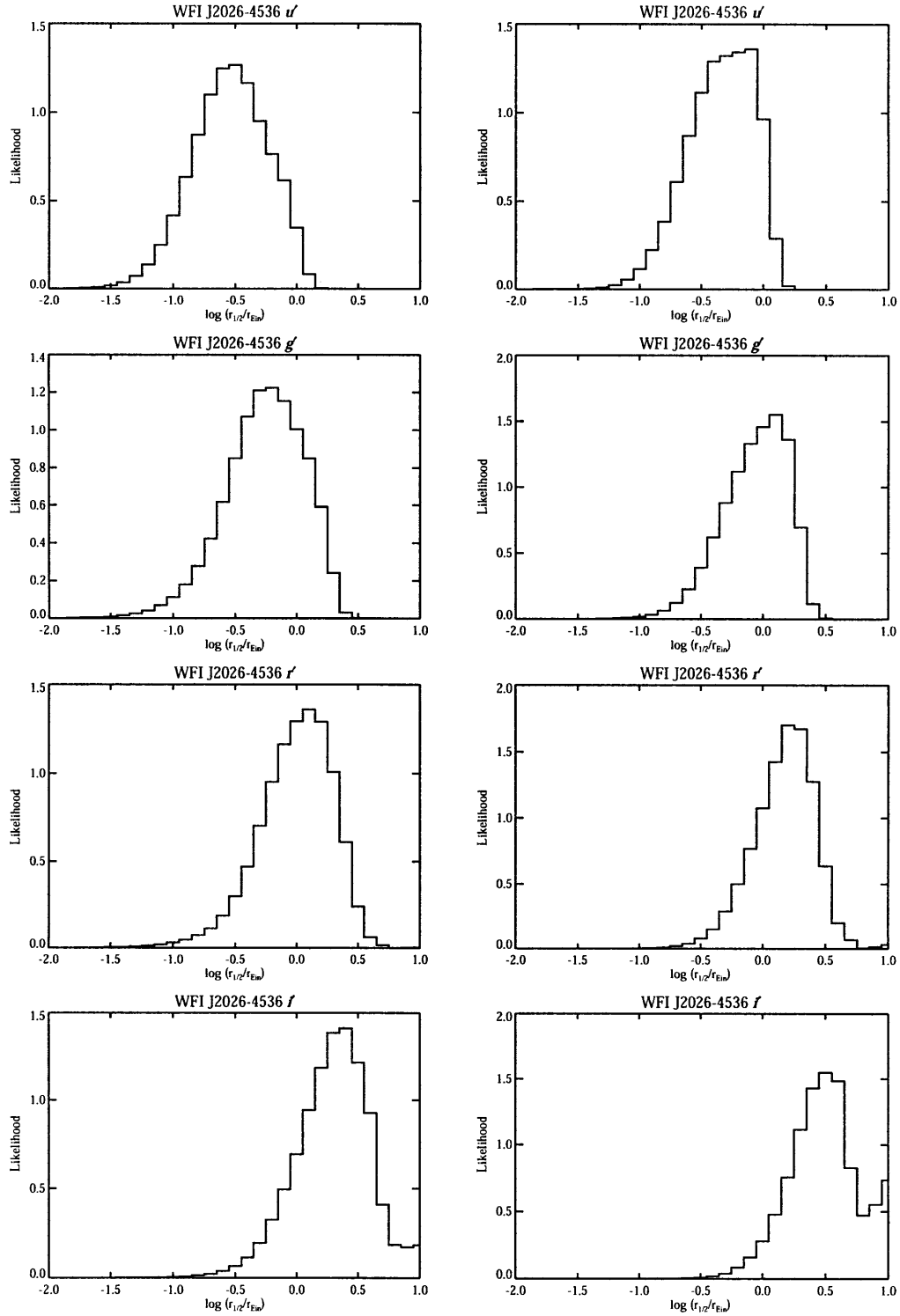
Figure B-11 Likelihood distributions for the half-light radius of WFI J2026−4536 in the $u'g'r'i'$ filters, as a fraction of a $1M_\odot$ Einstein radius. Left column: logarithmic prior. Right column: Linear prior.
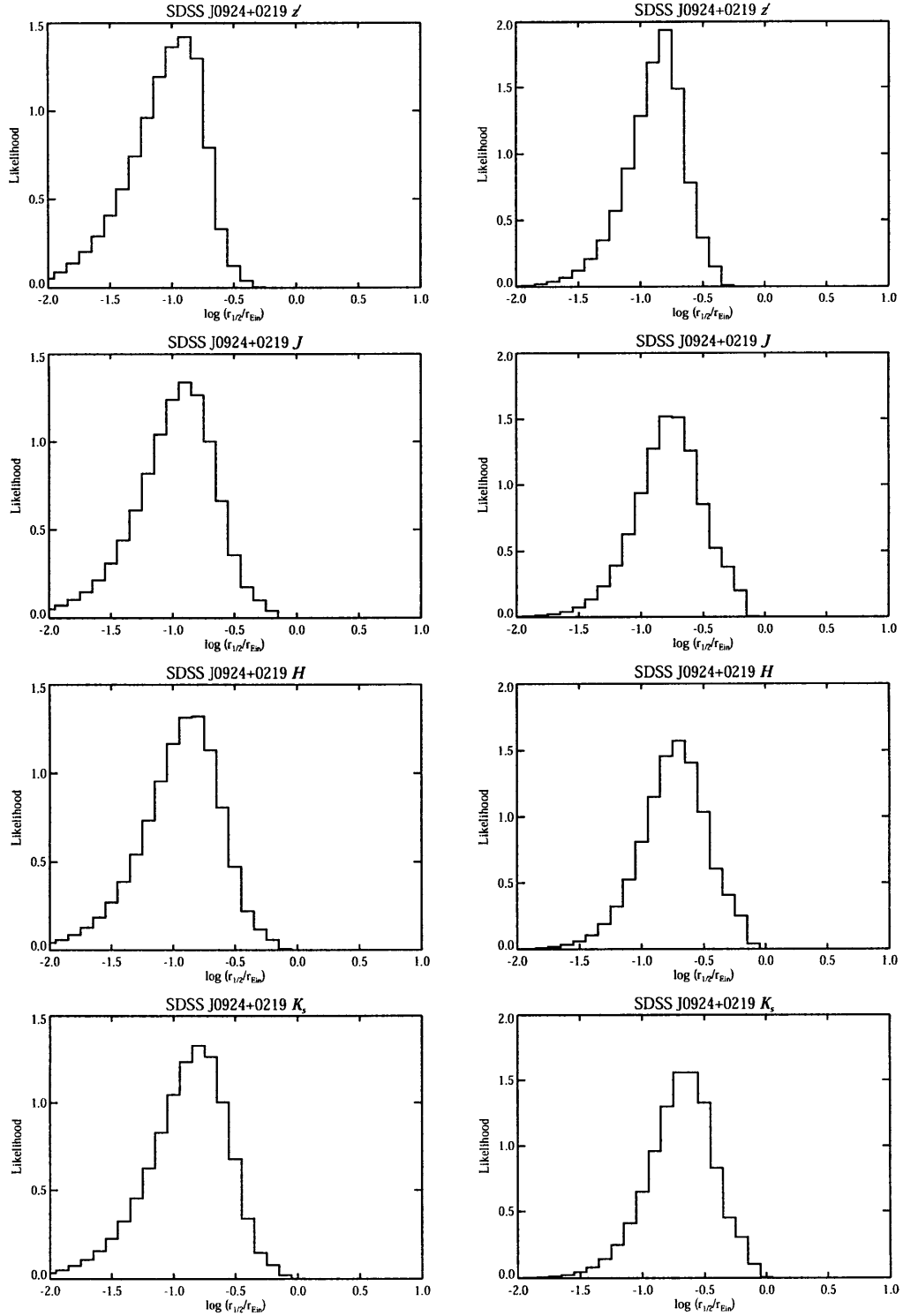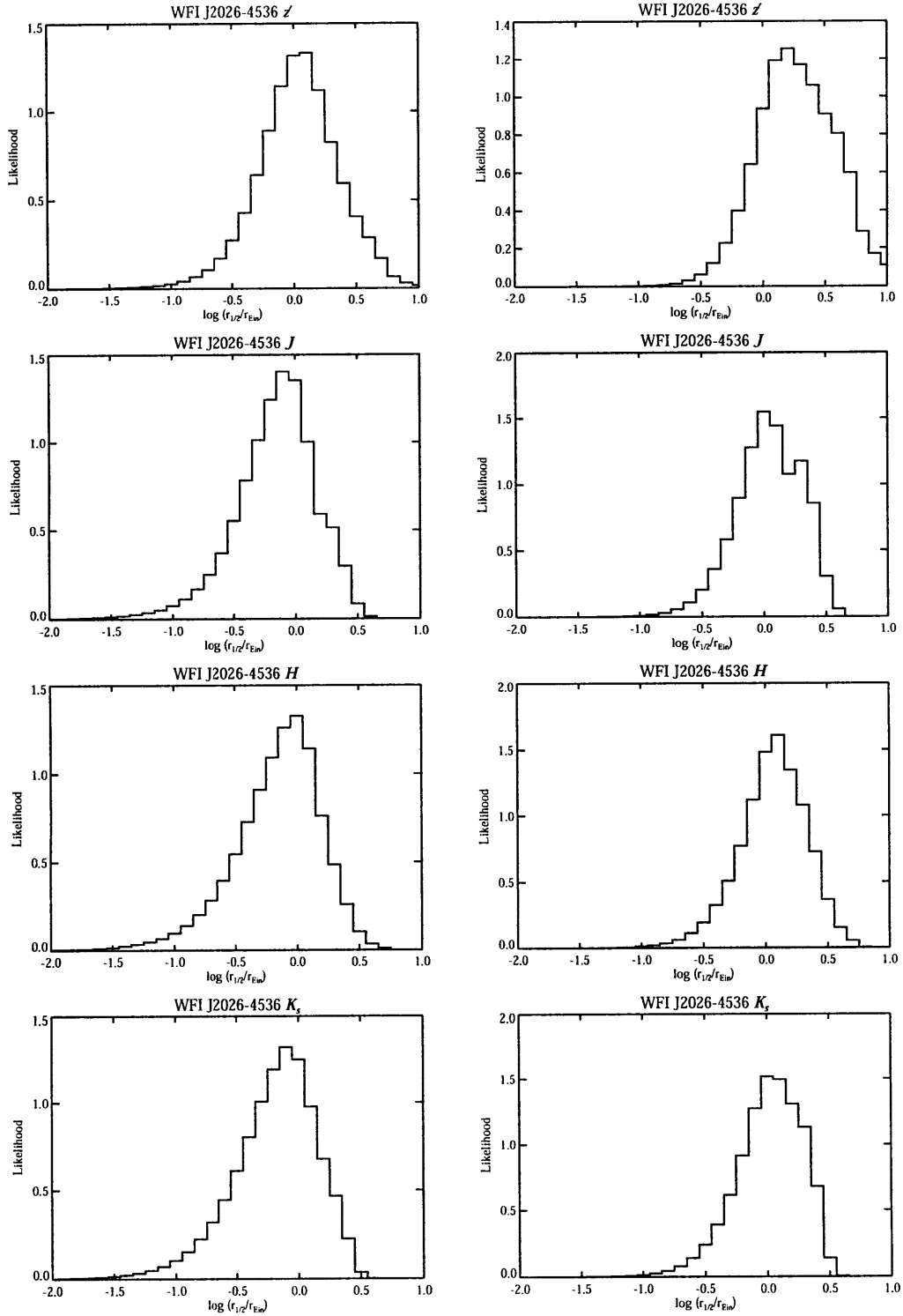
Figure B-11 (cont'd) Likelihood distributions for the half-light radius of WFI J2026−4536 in the $z'JHK_s$ filters, as a fraction of a $1M_\odot$ Einstein radius. Left column: logarithmic prior. Right column: Linear prior.
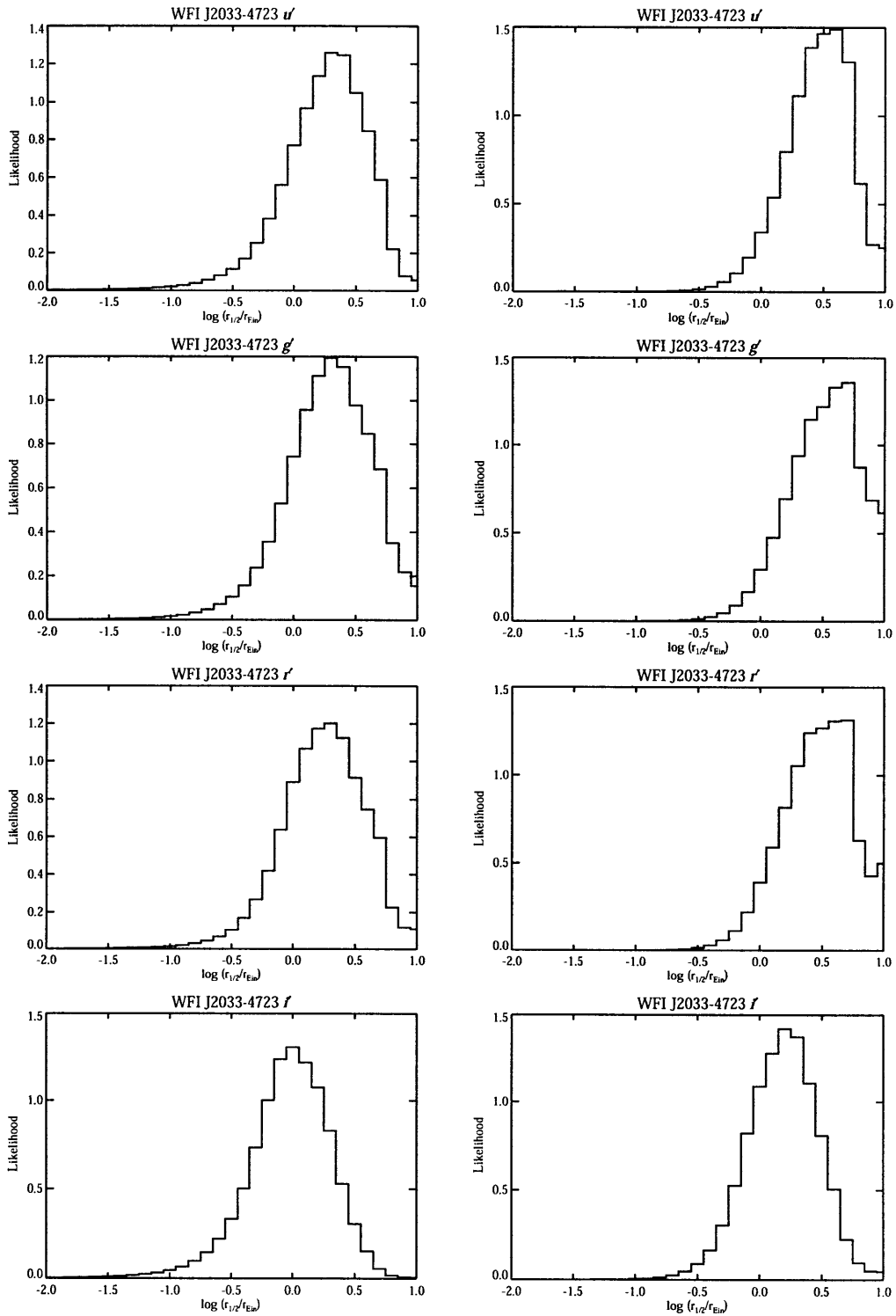
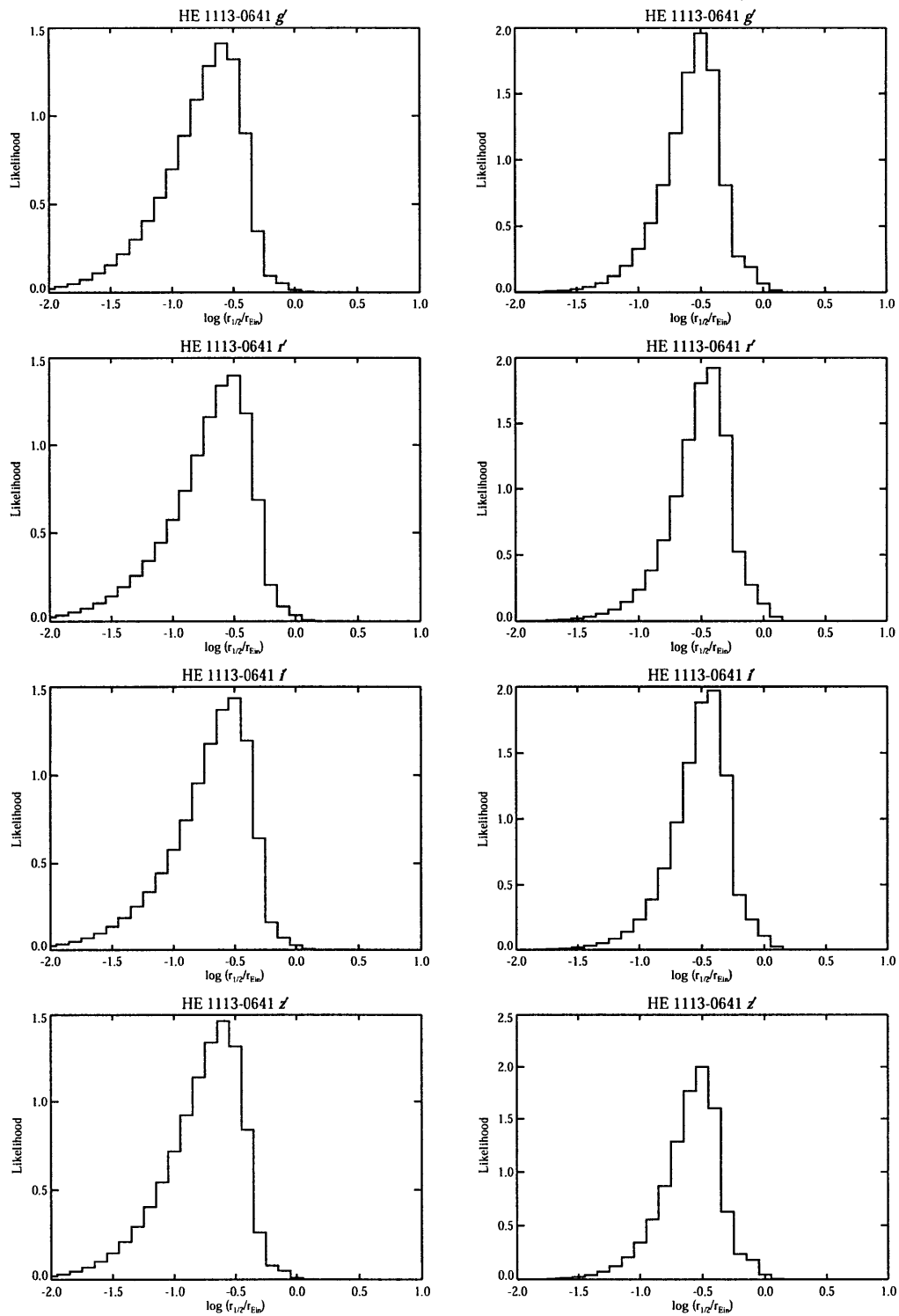Figure B-12 Likelihood distributions for the half-light radius of WFI J2033−4723 in the $u'g'r'i'$ filters, as a fraction of a $1M_\odot$ Einstein radius. Left column: logarithmic prior. Right column: Linear prior.
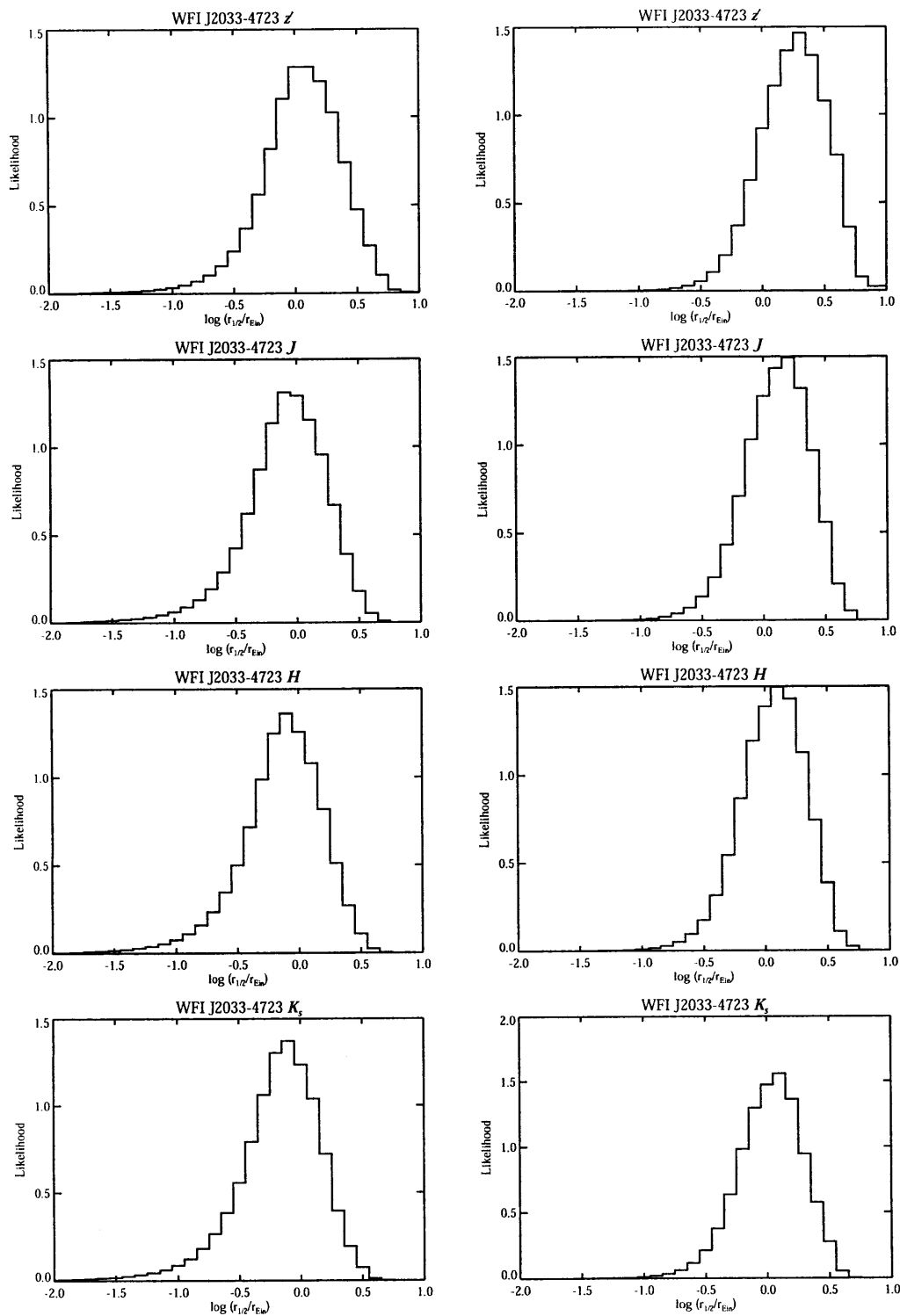
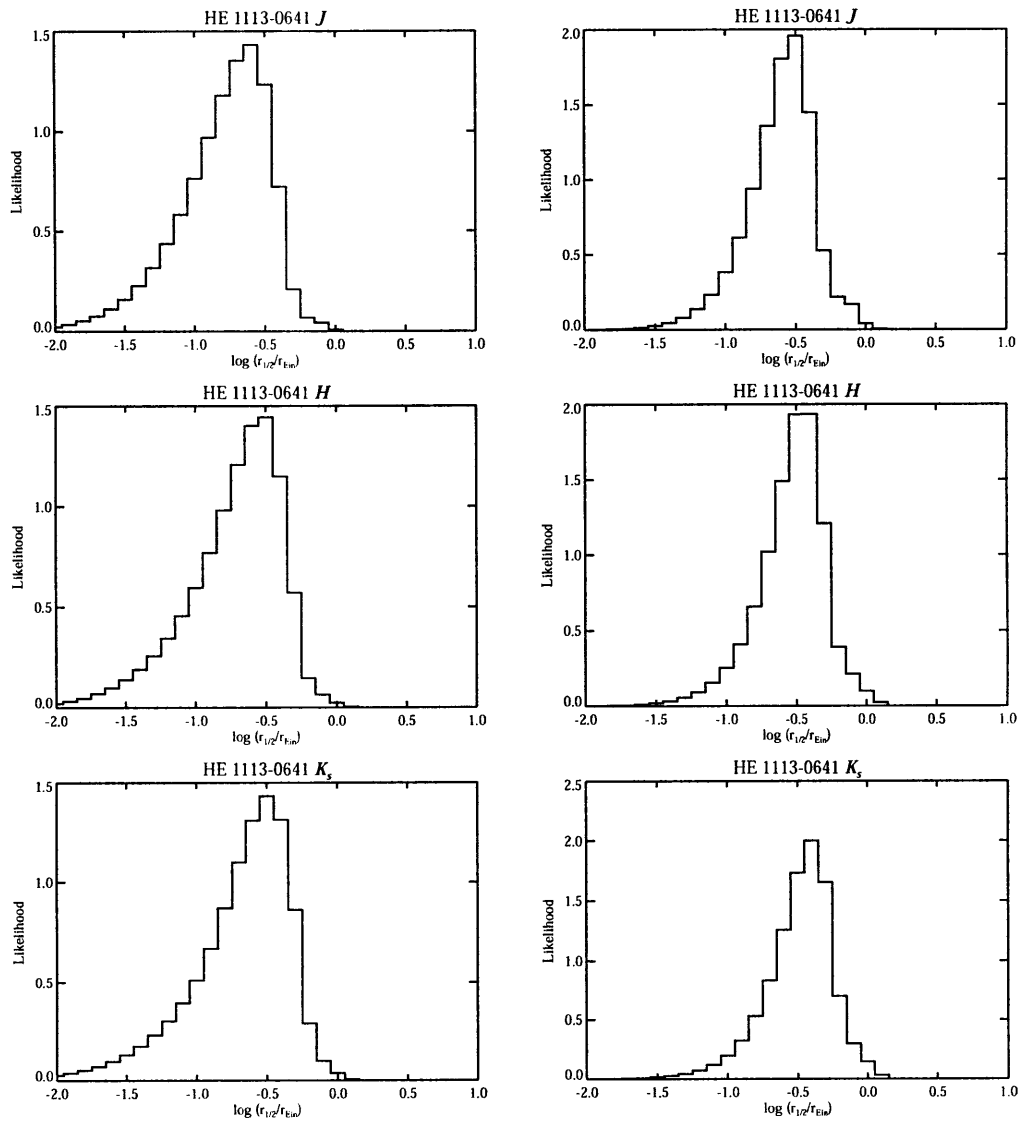Figure B-12 (cont'd) Likelihood distributions for the half-light radius of WFI J2033−4723 in the $z'JHK_s$ filters, as a fraction of a $1M_\odot$ Einstein radius. Left column: logarithmic prior. Right column: Linear prior.

215

Bibliography

E. Agol, S. M. Gogarten, V. Gorjian, and A. Kimball. Spitzer Observations of a Gravitationally Lensed Quasar, QSO 2237+0305. ApJ, 697:1010–1019, June 2009.

T. Anguita, C. Faure, A. Yonehara, J. Wambsganss, J.-P. Kneib, G. Covone, and D. Alloin. Integral field spectroscopy of four lensed quasars: analysis of their neighborhood and evidence for microlensing. A&A, 481:615–627, April 2008a.

T. Anguita, R. W. Schmidt, E. L. Turner, J. Wambsganss, R. L. Webster, K. A. Loomis, D. Long, and R. McMillan. The multiple quasar Q2237+0305 under a microlensing caustic. A&A, 480:327–334, March 2008b.

K. A. Arnaud. XSPEC: The First Ten Years. In G. H. Jacoby and J. Barnes, editors, *Astronomical Data Analysis Software and Systems V*, volume 101 of *Astronomical Society of the Pacific Conference Series*, pages 17–+, 1996.

N. Bade, J. Siebert, S. Lopez, W. Voges, and D. Reimers. RX J0911.4+0551: A new multiple QSO selected from the ROSAT All-Sky Survey. A&A, 317:L13–L16, January 1997.

S. A. Balbus and J. F. Hawley. A powerful local shear instability in weakly magnetized disks. I - Linear analysis. II - Nonlinear evolution. ApJ, 376:214–233, July 1991.

J. M. Bardeen. Kerr Metric Black Holes. Nature, 226:64–65, April 1970.

R. Barkana. Analysis of Time Delays in the Gravitational Lens PG 1115+080. ApJ, 489: 21–+, November 1997.

N. F. Bate, D. J. E. Floyd, R. L. Webster, and J. S. B. Wyithe. A microlensing study of the accretion disc in the quasar MG 0414+0534. MNRAS, 391:1955–1960, December 2008.

J. A. Blackburne, D. Pooley, and S. Rappaport. X-Ray and Optical Flux Anomalies in the Quadruply Lensed QSO 1RXS J1131−1231. ApJ, 640:569–573, April 2006.

J. A. Blackburne, L. Wisotzki, and P. L. Schechter. HE 1113−0641: The Smallest-Separation Quadruple Lens Identified by a Ground-Based Optical Telescope. AJ, 135: 374–379, January 2008.

O. Blaes. Accretion Disks in AGNs. In L. C. Ho and J.-W. Wang, editors, *The Central Engine of Active Galactic Nuclei*, volume 373 of *Astronomical Society of the Pacific Conference Series*, pages 75–+, October 2007.

R. C. Bohlin. Spectrophotometric Standards from the Far-UV to the Near-IV on the White Dwarf Flux Scale. In A. P. Koratkar and C. Leitherer, editors, *Calibrating Hubble Space Telescope. Post Servicing Mission*, pages 49–+, 1995.

R. C. Bohlin and R. L. Gilliland. Absolute Flux Distribution of the SDSS Standard BD +17°4708. AJ, 128:3053–3060, December 2004.

P. S. Broos, L. K. Townsley, K. Getman, and F. E. Bauer. *ACIS Extract, An ACIS Point Source Extraction Package*. University Park: Pennsylvania State University, 2002.

G. Bruzual and S. Charlot. Stellar population synthesis at the resolution of 2003. MNRAS, 344:1000–1028, October 2003.

W. Cash. Parameter estimation in astronomy through application of the likelihood ratio. ApJ, 228:939–947, March 1979.

G. Chartas. X-Ray Observations of Gravitationally Lensed Quasars: Evidence for a Hidden Quasar Population. ApJ, 531:81–94, March 2000.

G. Chartas, E. Agol, M. Eracleous, G. Garmire, M. W. Bautz, and N. D. Morgan. Caught in the Act: Chandra Observations of Microlensing of the Radio-loud Quasar MG J0414+0534. ApJ, 568:509–521, April 2002.

G. Chartas, X. Dai, and G. P. Garmire. Chandra and XMM-Newton Results on the Hubble Constant from Gravitational Lensing. In W. L. Freedman, editor, *Measuring and Modeling the Universe*, 2004a.

G. Chartas, M. Eracleous, E. Agol, and S. C. Gallagher. Chandra Observations of the Cloverleaf Quasar H1413+117: A Unique Laboratory for Microlensing Studies of a LoBAL Quasar. ApJ, 606:78–84, May 2004b.

G. Chartas, C. S. Kochanek, X. Dai, S. Poindexter, and G. Garmire. X-Ray Microlensing in RX J1131−1231 and HE 1104−1805. ApJ, 693:174–185, March 2009.

M. Chiba, T. Minezaki, N. Kashikawa, H. Kataza, and K. T. Inoue. Subaru Mid-Infrared Imaging of the Quadruple Lenses PG 1115+080 and B1422+231: Limits on Substructure Lensing. ApJ, 627:53–61, July 2005.

C. A. Christian, D. Crabtree, and P. Waddell. Detection of the lensing galaxy in PG 1115 + 080. ApJ, 312:45–49, January 1987.

M. Cohen, W. A. Wheaton, and S. T. Megeath. Spectral Irradiance Calibration in the Infrared. XIV. The Absolute Calibration of 2MASS. AJ, 126:1090–1096, August 2003.

G. D. Coleman, C.-C. Wu, and D. W. Weedman. Colors and magnitudes predicted for high redshift galaxies. ApJS, 43:393–416, July 1980.

X. Dai, G. Chartas, E. Agol, M. W. Bautz, and G. P. Garmire. Chandra Observations of QSO 2237+0305. ApJ, 589:100–110, May 2003.

X. Dai, C. S. Kochanek, G. Chartas, S. Kozlowski, C. W. Morgan, G. Garmire, and E. Agol. The Sizes of the X-ray and Optical Emission Regions of RX J1131−1231. *arXiv:0906.4342*, June 2009.

N. Dalal and C. S. Kochanek. Direct Detection of Cold Dark Matter Substructure. ApJ, 572:25–33, June 2002.

G. de Vaucouleurs and D. W. Olson. The central velocity dispersion in elliptical and lenticular galaxies as an extragalactic distance indicator. ApJ, 256:346–369, May 1982.

G. de Vaucouleurs, A. de Vaucouleurs, and J. R. Corwin. *Second reference catalogue of bright galaxies*. Austin: Univ. Texas Press, 1976.

W. H. de Vries, R. H. Becker, R. L. White, and C. Loomis. Structure Function Analysis of Long-Term Quasar Variability. AJ, 129:615–629, February 2005.

J. M. Dickey and F. J. Lockman. Hɪ in the Galaxy. ARA&A, 28:215–261, 1990.

S. S. Doeleman, V. L. Fish, A. E. Broderick, A. Loeb, and A. E. E. Rogers. Detecting Flaring Structures in Sagittarius A* with High-Frequency VLBI. ApJ, 695:59–74, April 2009.

A. Eigenbrod, F. Courbin, G. Meylan, C. Vuissoz, and P. Magain. COSMOGRAIL: the COSmological MOnitoring of GRAvItational Lenses. III. Redshift of the lensing galaxy in eight gravitationally lensed quasars. A&A, 451:759–766, June 2006.

A. Eigenbrod, F. Courbin, G. Meylan, E. Agol, T. Anguita, R. W. Schmidt, and J. Wambsganss. Microlensing variability in the gravitationally lensed quasar QSO 2237+0305 ≡ the Einstein Cross. II. Energy profile of the accretion disk. A&A, 490:933–943, November 2008.

M. Elvis, B. J. Wilkes, J. C. McDowell, R. F. Green, J. Bechtold, S. P. Willner, M. S. Oey, E. Polomski, and R. Cutri. Atlas of quasar energy distributions. ApJS, 95:1–68, November 1994.

S. M. Faber and R. E. Jackson. Velocity dispersions and mass-to-light ratios for elliptical galaxies. ApJ, 204:668–683, March 1976.

E. E. Falco, J. Lehar, and I. I. Shapiro. HST Observations and Models of the Gravitational Lens System MG 0414+0534. AJ, 113:540–+, February 1997.

D. J. E. Floyd, N. F. Bate, and R. L. Webster. The accretion disc in the quasar SDSS J0924+0219. *arXiv:0905.2651*, May 2009.

P. Freeman, S. Doe, and A. Siemiginowska. Sherpa: a mission-independent data analysis application. In J.-L. Starck and F. D. Murtagh, editors, *Society of Photo-Optical Instrumentation Engineers (SPIE) Conference Series*, volume 4477 of *Society of Photo-Optical Instrumentation Engineers (SPIE) Conference Series*, pages 76–87, November 2001.

M. Fukugita, T. Ichikawa, J. E. Gunn, M. Doi, K. Shimasaku, and D. P. Schneider. The Sloan Digital Sky Survey Photometric System. AJ, 111:1748–+, April 1996.

B. S. Gaudi and A. O. Petters. Gravitational Microlensing near Caustics. I. Folds. ApJ, 574:970–984, August 2002.

R. R. Gibson, W. N. Brandt, and D. P. Schneider. Are Optically Selected Quasars Universally X-Ray Luminous? X-Ray-UV Relations in Sloan Digital Sky Survey Quasars. ApJ, 685:773–786, October 2008.

C. E. Grant, M. W. Bautz, G. Chartas, and G. P. Garmire. Detection of X-Rays from Galaxy Groups Associated with the Gravitationally Lensed Systems PG 1115+080 and B1422+231. ApJ, 610:686–690, August 2004.

A. R. Green, I. M. McHardy, and H. J. Lehto. On the nature of rapid X-ray variability in active galactic nuclei. MNRAS, 265:664–+, December 1993.

F. Haardt and L. Maraschi. A two-phase model for the X-ray emission from Seyfert galaxies. ApJ, 380:L51–L54, October 1991.

J. N. Hewitt, E. L. Turner, C. R. Lawrence, D. P. Schneider, and J. P. Brody. A gravitational lens candidate with an unusually red optical counterpart. AJ, 104:968–979, September 1992.

J. Hjorth, I. Burud, A. O. Jaunsen, P. L. Schechter, J.-P. Kneib, M. I. Andersen, H. Korhonen, J. W. Clasen, A. A. Kaas, R. Østensen, J. Pelt, and F. P. Pijpers. The Time Delay of the Quadruple Quasar RX J0911.4+0551. ApJ, 572:L11–L14, June 2002.

D. W. Hogg, I. K. Baldry, M. R. Blanton, and D. J. Eisenstein. The K correction. *arXiv:astro-ph/0210394*, October 2002.

G. P. Holder and P. L. Schechter. External Shear in Quadruply Imaged Lens Systems. ApJ, 589:688–692, June 2003.

J. Huchra, M. Gorenstein, S. Kent, I. Shapiro, G. Smith, E. Horine, and R. Perley. 2237 + 0305: A new and unusual gravitational lens. AJ, 90:691–696, May 1985.

N. Inada, R. H. Becker, S. Burles, F. J. Castander, D. Eisenstein, P. B. Hall, D. E. Johnston, B. Pindor, G. T. Richards, P. L. Schechter, M. Sekiguchi, R. L. White, J. Brinkmann, J. A. Frieman, S. J. Kleinman, J. Krzesiński, D. C. Long, E. H. Neilsen, Jr., P. R. Newman, A. Nitta, D. P. Schneider, S. Snedden, and D. G. York. SDSS J092455.87+021924.9: An Interesting Gravitationally Lensed Quasar from the Sloan Digital Sky Survey. AJ, 126: 666–674, August 2003a.

N. Inada, M. Oguri, B. Pindor, J. F. Hennawi, K. Chiu, W. Zheng, S.-I. Ichikawa, M. D. Gregg, R. H. Becker, Y. Suto, M. A. Strauss, E. L. Turner, C. R. Keeton, J. Annis, F. J. Castander, D. J. Eisenstein, J. A. Frieman, M. Fukugita, J. E. Gunn, D. E. Johnston, S. M. Kent, R. C. Nichol, G. T. Richards, H.-W. Rix, E. S. Sheldon, N. A. Bahcall, J. Brinkmann, Ž. Ivezić, D. Q. Lamb, T. A. McKay, D. P. Schneider, and D. G. York. A gravitationally lensed quasar with quadruple images separated by 14.62 arcseconds. Nature, 426:810–812, December 2003b.

M. Karovska, S. J. Beikman, M. S. Elvis, J. M. Flanagan, T. Gaetz, K. J. Glotfelty, D. Jerius, J. C. McDowell, and A. H. Rots. The Chandra X-ray Observatory PSF Library. In F. R. Harnden, Jr., F. A. Primini, and H. E. Payne, editors, *Astronomical Data Analysis Software and Systems X*, volume 238 of *Astronomical Society of the Pacific Conference Series*, pages 435–+, 2001.

S. Kaspi, P. S. Smith, H. Netzer, D. Maoz, B. T. Jannuzi, and U. Giveon. Reverberation Measurements for 17 Quasars and the Size-Mass-Luminosity Relations in Active Galactic Nuclei. ApJ, 533:631–649, April 2000.

C. R. Keeton. Computational Methods for Gravitational Lensing. *arXiv:astro-ph/0102340*, February 2001.

C. R. Keeton, B. S. Gaudi, and A. O. Petters. Identifying Lenses with Small-Scale Structure. I. Cusp Lenses. ApJ, 598:138–161, November 2003.

C. R. Keeton, S. Burles, P. L. Schechter, and J. Wambsganss. Differential Microlensing of the Continuum and Broad Emission Lines in SDSS J0924+0219, the Most Anomalous Lensed Quasar. ApJ, 639:1–6, March 2006.

C. S. Kochanek. Do the redshifts of gravitational lens galaxies rule out a large cosmological constant? ApJ, 384:1–11, January 1992.

C. S. Kochanek. Quantitative Interpretation of Quasar Microlensing Light Curves. ApJ, 605:58–77, April 2004.

C. S. Kochanek and N. Dalal. Tests for Substructure in Gravitational Lenses. ApJ, 610: 69–79, July 2004.

C. S. Kochanek, N. D. Morgan, E. E. Falco, B. A. McLeod, J. N. Winn, J. Dembicky, and B. Ketzeback. The Time Delays of Gravitational Lens HE 0435−1223: An Early-Type Galaxy with a Rising Rotation Curve. ApJ, 640:47–61, March 2006.

A. M. Koekemoer, A. S. Fruchter, R. N. Hook, and W. Hack. MultiDrizzle: An Integrated Pyraf Script for Registering, Cleaning and Combining Images. In S. Arribas, A. Koekemoer, and B. Whitmore, editors, *The 2002 HST Calibration Workshop : Hubble after the Installation of the ACS and the NICMOS Cooling System*, pages 337–+, 2002a.

A. M. Koekemoer, S. Gonzaga, A. S. Fruchter, J. Biretta, S. Casertano, J.-C. Hsu, M. Lallo, and M. Mutchler. *HST Dither Handbook, Version 2.0*. Baltimore: STScI, 2002b.

J. A. Kollmeier, C. A. Onken, C. S. Kochanek, A. Gould, D. H. Weinberg, M. Dietrich, R. Cool, A. Dey, D. J. Eisenstein, B. T. Jannuzi, E. Le Floc'h, and D. Stern. Black Hole Masses and Eddington Ratios at $0.3 < z < 4$. ApJ, 648:128–139, September 2006.

J. Kristian, E. J. Groth, E. J. Shaya, D. P. Schneider, J. A. Holtzman, W. A. Baum, B. Campbell, A. Code, D. G. Currie, G. E. Danielson, S. P. Ewald, J. J. Hester, R. M. Light, C. R. Lynds, E. J. O'Neil, Jr., P. K. Seidelmann, and J. A. Westphal. Imaging of the gravitational lens system PG 1115+080 with the Hubble Space Telescope. AJ, 106: 1330–1336, October 1993.

P. Kroupa. On the variation of the initial mass function. MNRAS, 322:231–246, April 2001.

A. U. Landolt. UBVRI photometric standard stars in the magnitude range 11.5-16.0 around the celestial equator. AJ, 104:340–371, July 1992.

C. H. Lineweaver, L. Tenorio, G. F. Smoot, P. Keegstra, A. J. Banday, and P. Lubin. The Dipole Observed in the COBE DMR 4 Year Data. ApJ, 470:38–+, October 1996.

R. V. E. Lovelace. Dynamo model of double radio sources. Nature, 262:649–652, August 1976.

P. Magain, J. Surdej, J.-P. Swings, U. Borgeest, and R. Kayser. Discovery of a quadruply lensed quasar - The 'clover leaf' H1413 + 117. Nature, 334:325–327, July 1988.

S. Mao and P. Schneider. Evidence for substructure in lens galaxies? MNRAS, 295:587–+, April 1998.

R. B. Metcalf and H. Zhao. Flux Ratios as a Probe of Dark Substructures in Quadruple-Image Gravitational Lenses. ApJ, 567:L5–L8, March 2002.

G. Meylan, P. Jetzer, P. North, P. Schneider, C. S. Kochanek, and J. Wambsganss, editors. *Gravitational Lensing: Strong, Weak and Micro*, 2006.

T. Minezaki, M. Chiba, N. Kashikawa, K. T. Inoue, and H. Kataza. Subaru Mid-Infrared Imaging of the Quadruple Lenses. II. Unveiling Lens Structure of MG0414+0534 and Q2237+030. ApJ, 697:610–618, May 2009.

C. W. Morgan, C. S. Kochanek, N. D. Morgan, and E. E. Falco. The Quasar Accretion Disk Size - Black Hole Mass Relation. *arXiv:0707.0305*, July 2007.

C. W. Morgan, M. E. Eyler, C. S. Kochanek, N. D. Morgan, E. E. Falco, C. Vuissoz, F. Courbin, and G. Meylan. Simultaneous Estimation of Time Delays and Quasar Structure. ApJ, 676:80–86, March 2008a.

C. W. Morgan, C. S. Kochanek, X. Dai, N. D. Morgan, and E. E. Falco. X-Ray and Optical Microlensing in the Lensed Quasar PG 1115+080. ApJ, 689:755–761, December 2008b.

N. D. Morgan, G. Chartas, M. Malm, M. W. Bautz, I. Burud, J. Hjorth, S. E. Jones, and P. L. Schechter. Chandra X-Ray Observations of the Quadruply Lensed Quasar RX J0911.4+0551. ApJ, 555:1–6, July 2001.

N. D. Morgan, J. A. R. Caldwell, P. L. Schechter, A. Dressler, E. Egami, and H.-W. Rix. WFI J2026-4536 and WFI J2033-4723: Two New Quadruple Gravitational Lenses. AJ, 127:2617–2630, May 2004.

N. D. Morgan, C. S. Kochanek, E. E. Falco, and X. Dai. Time-Delay Measurement for the Quadruple Lens RX J1131−1231. *arXiv:astro-ph/0605321*, May 2006.

M. J. Mortonson, P. L. Schechter, and J. Wambsganss. Size Is Everything: Universal Features of Quasar Microlensing with Extended Sources. ApJ, 628:594–603, August 2005.

J. A. Muñoz, E. E. Falco, C. S. Kochanek, J. Lehár, B. A. McLeod, C. D. Impey, H.-W. Rix, and C. Y. Peng. The Castles Project. Ap&SS, 263:51–54, June 1998.

K. Mukai. PIMMS and Viewing: proposal preparation tools. *Legacy, vol. 3, p.21-31*, 3: 21–31, May 1993.

R. Narayan and M. Bartelmann. Lectures on Gravitational Lensing. *arXiv:astro-ph/9606001*, June 1996.

I. D. Novikov and K. S. Thorne. Astrophysics of black holes. In *Black Holes (Les Astres Occlus)*, pages 343–450, 1973.

M. Oguri, N. Inada, J. A. Blackburne, M.-S. Shin, I. Kayo, M. A. Strauss, D. P. Schneider, and D. G. York. Mass models and environment of the new quadruply lensed quasar SDSS J1330+1810. MNRAS, 391:1973–1980, December 2008a.

M. Oguri, N. Inada, A. Clocchiatti, I. Kayo, M.-S. Shin, J. F. Hennawi, M. A. Strauss, T. Morokuma, D. P. Schneider, and D. G. York. Discovery of Four Gravitationally Lensed Quasars from the Sloan Digital Sky Survey. AJ, 135:520–526, February 2008b.

D. N. Page and K. S. Thorne. Disk-Accretion onto a Black Hole. Time-Averaged Structure of Accretion Disk. ApJ, 191:499–506, July 1974.

A. R. Patnaik, I. W. A. Browne, D. Walsh, F. H. Chaffee, and C. B. Foltz. B1422+231 - A new gravitationally lensed system at $z = 3.62$. MNRAS, 259:1P–4P, November 1992.

P. J. E. Peebles. *The large-scale structure of the universe.* Princeton University Press, 1980.

M. S. Peeples, P. L. Schechter, and J. K. Wambsganss. Possible Futures for Quadruply-Imaged Quasar Systems due to Micro-lensing by Stars. In *Bulletin of the American Astronomical Society,* volume 36 of *Bulletin of the American Astronomical Society,* pages 1392–+, December 2004.

C. Y. Peng, C. D. Impey, H.-W. Rix, C. S. Kochanek, C. R. Keeton, E. E. Falco, J. Lehár, and B. A. McLeod. Probing the Coevolution of Supermassive Black Holes and Galaxies Using Gravitationally Lensed Quasar Hosts. ApJ, 649:616–634, October 2006.

B. A. Peterson, R. S. Ellis, G. Efstathiou, T. Shanks, A. J. Bean, R. Fong, and Z. Zen-Long. A complete galaxy redshift sample. III - Methods and catalogue. MNRAS, 221:233–255, July 1986.

S. Poindexter, N. Morgan, and C. S. Kochanek. The Spatial Structure of an Accretion Disk. ApJ, 673:34–38, January 2008.

D. Pooley, J. A. Blackburne, S. Rappaport, P. L. Schechter, and W.-f. Fong. A Strong X-Ray Flux Ratio Anomaly in the Quadruply Lensed Quasar PG 1115+080. ApJ, 648:67–72, September 2006.

D. Pooley, J. A. Blackburne, S. Rappaport, and P. L. Schechter. X-Ray and Optical Flux Ratio Anomalies in Quadruply Lensed Quasars. I. Zooming in on Quasar Emission Regions. ApJ, 661:19–29, May 2007.

D. Pooley, S. Rappaport, J. Blackburne, P. L. Schechter, J. Schwab, and J. Wambsganss. The Dark-matter Fraction in the Elliptical Galaxy Lensing the Quasar PG 1115+080. ApJ, 697:1892–1900, June 2009.

L. Č. Popović and G. Chartas. The influence of gravitational lensing on the spectra of lensed quasi-stellar objects. MNRAS, 357:135–144, February 2005.

G. T. Richards, M. A. Strauss, X. Fan, P. B. Hall, S. Jester, D. P. Schneider, D. E. Vanden Berk, C. Stoughton, S. F. Anderson, R. J. Brunner, J. Gray, J. E. Gunn, Ž. Ivezić, M. K. Kirkland, G. R. Knapp, J. Loveday, A. Meiksin, A. Pope, A. S. Szalay, A. R. Thakar, B. Yanny, D. G. York, J. C. Barentine, H. J. Brewington, J. Brinkmann, M. Fukugita, M. Harvanek, S. M. Kent, S. J. Kleinman, J. Krzesiński, D. C. Long, R. H. Lupton, T. Nash, E. H. Neilsen, Jr., A. Nitta, D. J. Schlegel, and S. A. Snedden. The Sloan Digital Sky Survey Quasar Survey: Quasar Luminosity Function from Data Release 3. AJ, 131:2766–2787, June 2006.

P. L. Schechter and J. Wambsganss. Quasar Microlensing at High Magnification and the Role of Dark Matter: Enhanced Fluctuations and Suppressed Saddle Points. ApJ, 580: 685–695, December 2002.

P. L. Schechter and J. Wambsganss. The dark matter content of lensing galaxies at $1.5R_e$. In S. Ryder, D. Pisano, M. Walker, and K. Freeman, editors, *Dark Matter in Galaxies*, volume 220 of *IAU Symposium*, pages 103–+, July 2004.

P. L. Schechter, M. Mateo, and A. Saha. DOPHOT, a CCD photometry program: Description and tests. PASP, 105:1342–1353, November 1993.

P. L. Schechter, C. D. Bailyn, R. Barr, R. Barvainis, C. M. Becker, G. M. Bernstein, J. P. Blakeslee, S. J. Bus, A. Dressler, E. E. Falco, R. A. Fesen, P. Fischer, K. Gebhardt, D. Harmer, J. N. Hewitt, J. Hjorth, T. Hurt, A. O. Jaunsen, M. Mateo, D. Mehlert, D. O. Richstone, L. S. Sparke, J. R. Thorstensen, J. L. Tonry, G. Wegner, D. W. Willmarth, and G. Worthey. The Quadruple Gravitational Lens PG 1115+080: Time Delays and Models. ApJ, 475:L85+, February 1997.

P. Schneider. A new formulation of gravitational lens theory, time-delay, and Fermat's principle. A&A, 143:413–420, February 1985.

P. Schneider and J. Wambsganss. Are the broad emission lines of quasars affected by gravitational microlensing? A&A, 237:42–53, October 1990.

P. Schneider and A. Weiss. The gravitational lens equation near cusps. A&A, 260:1–2, July 1992.

N. I. Shakura and R. A. Sunyaev. Black holes in binary systems. Observational appearance. A&A, 24:337–355, 1973.

I. I. Shapiro. Fourth Test of General Relativity. *Physical Review Letters*, 13:789–791, December 1964.

J. D. Silverman, P. J. Green, W. A. Barkhouse, D.-W. Kim, M. Kim, B. J. Wilkes, R. A. Cameron, G. Hasinger, B. T. Jannuzi, M. G. Smith, P. S. Smith, and H. Tananbaum. The Luminosity Function of X-Ray-selected Active Galactic Nuclei: Evolution of Supermassive Black Holes at High Redshift. ApJ, 679:118–139, May 2008.

D. Sluse, J. Surdej, J.-F. Claeskens, D. Hutsemékers, C. Jean, F. Courbin, T. Nakos, M. Billeres, and S. V. Khmil. A quadruply imaged quasar with an optical Einstein ring candidate: 1RXS J113155.4−123155. A&A, 406:L43–L46, July 2003.

D. Sluse, J.-F. Claeskens, B. Altieri, R. A. Cabanac, O. Garcet, D. Hutsemékers, C. Jean, A. Smette, and J. Surdej. Multi-wavelength study of the gravitational lens system RXS J113155.4−123155. I. Multi-epoch optical and near infrared imaging. A&A, 449:539–550, April 2006.

D. Sluse, J.-F. Claeskens, D. Hutsemékers, and J. Surdej. Multi-wavelength study of the gravitational lens system RXS J1131−1231. III. Long slit spectroscopy: micro-lensing probes the QSO structure. A&A, 468:885–901, June 2007.

J. A. Smith, D. L. Tucker, S. Kent, M. W. Richmond, M. Fukugita, T. Ichikawa, S.-i. Ichikawa, A. M. Jorgensen, A. Uomoto, J. E. Gunn, M. Hamabe, M. Watanabe, A. Tolea, A. Henden, J. Annis, J. R. Pier, T. A. McKay, J. Brinkmann, B. Chen, J. Holtzman, K. Shimasaku, and D. G. York. The $u'g'r'i'z'$ Standard-Star System. AJ, 123:2121–2144, April 2002.

J. A. Smith, S. S. Allam, D. L. Tucker, J. L. Stute, C. T. Rodgers, and C. Stoughton. The southern hemisphere $u'g'r'i'z'$ stars. AJ, submitted, 2007.

H. Sugai, A. Kawai, A. Shimono, T. Hattori, G. Kosugi, N. Kashikawa, K. T. Inoue, and M. Chiba. Integral Field Spectroscopy of the Quadruply Lensed Quasar 1RXS J1131−1231: New Light on Lens Substructures. ApJ, 660:1016–1022, May 2007.

R. B. Tully and J. R. Fisher. A new method of determining distances to galaxies. A&A, 54:661–673, February 1977.

C. Vanderriest, G. Wlerick, G. Lelievre, J. Schneider, H. Sol, D. Horville, L. Renard, and B. Servan. Variability of the gravitational mirage P.G. 1115+080. A&A, 158:L5–L8, April 1986.

M. Vestergaard. Determining Central Black Hole Masses in Distant Active Galaxies. ApJ, 571:733–752, June 2002.

C. Vuissoz, F. Courbin, D. Sluse, G. Meylan, V. Chantry, E. Eulaers, C. Morgan, M. E. Eyler, C. S. Kochanek, J. Coles, P. Saha, P. Magain, and E. E. Falco. COSMOGRAIL: the COSmological MOnitoring of GRAvItational Lenses. VII. Time delays and the Hubble constant from WFI J2033−4723. A&A, 488:481–490, September 2008.

J. Wambsganss and B. Paczynski. Expected color variations of the gravitationally microlensed QSO 2237 + 0305. AJ, 102:864–868, September 1991.

J. Wambsganss, B. Paczynski, and N. Katz. A microlensing model for QSO 2237 + 0305. ApJ, 352:407–412, April 1990.

J.-M. Wang, Y.-M. Chen, L. C. Ho, and R. J. McLure. Evidence for Rapidly Spinning Black Holes in Quasars. ApJ, 642:L111–L114, May 2006.

R. J. Weymann, D. Latham, J. Roger, P. Angel, R. F. Green, J. W. Liebert, D. A. Turnshek, D. E. Turnshek, and J. A. Tyson. The triple QSO PG1115+08 - Another probable gravitational lens. Nature, 285:641–643, June 1980.

J. N. Winn, D. Rusin, and C. S. Kochanek. The central image of a gravitationally lensed quasar. Nature, 427:613–615, February 2004.

L. Wisotzki, N. Christlieb, M. C. Liu, J. Maza, N. D. Morgan, and P. L. Schechter. The new complex gravitational lens system HE 0230−2130. A&A, 348:L41–L44, August 1999.

L. Wisotzki, N. Christlieb, N. Bade, V. Beckmann, T. Köhler, C. Vanelle, and D. Reimers. The Hamburg/ESO survey for bright QSOs. III. A large flux-limited sample of QSOs. A&A, 358:77–87, June 2000.

L. Wisotzki, P. L. Schechter, H. V. Bradt, J. Heinmüller, and D. Reimers. HE 0435−1223: A wide separation quadruple QSO and gravitational lens. A&A, 395:17–23, November 2002.

P. R. Woźniak, A. Udalski, M. Szymański, M. Kubiak, G. Pietrzyński, I. Soszyński, and K. Żebruń. The Optical Gravitational Lensing Experiment: A Hunt for Caustic Crossings in QSO 2237+0305. ApJ, 540:L65–L67, September 2000.

Q. Yu and S. Tremaine. Observational constraints on growth of massive black holes. MN-RAS, 335:965–976, October 2002.